Centre Val de Loire UNIVERSITÉ

UNIVERSITE D'ORLEANS

INSTITUTE OF GEOLOGY AND GEOPHYSICS, CAS

ÉCOLE DOCTORALE
ENERGIE, MATERIAUX, SCIENCES DE LA TERRE ET DE L'UNIVERS

Institut des Sciences de la Terre d'Orleans

THÈSE présentée par :

Xue Zhenhua

soutenue le **25 September, 2017**

pour obtenir le grade de : **Docteur de l'université d'Orléans**

Discipline/ Spécialité : Sciences de la Terre et de l'Univers

Mesozoic tectonic evolution of the Longmenshan thrust belt, East Tibet

THÈSE dirigée par :

Chen Yan	Professeur, Université d'Orléans
Faure Michel	Professeur, Université d'Orléans
Lin Wei	Professeur, Institute of Geology and Geophysics, CAS

RAPPORTEURS :

Li Haibing	Professeur, China University of Geosciences
Yan Danping	Professeur, Institute of Geology, CAGS

JURY *(y reporter tous les membres de jury présents à la soutenance)* **:**

Chen Yan	Professeur, Université d'Orléans
Faure Michel	Professeur, Université d'Orléans
Li Haibing	Professeur, Institute of Geology, CAGS
Lin Wei	Professeur, Institute of Geology and Geophysics, CAS
Hu Jianmin	Professeur, Insitute of Geomechanics, CAGS
Yan Danping	Professeur, China University of Geosciences

ABSTRACT

The Longmenshan Thrust Belt (LMTB) trending NE constitutes the northeastern boundary of the Tibetan Plateau, and separates the Songpan-Ganzi fold belt to the northwest and the Sichuan basin to the southeast, respectively. The LMTB is famous for its extremely steep topography, intensive activities as well as the abundant structures. As a typical composite orogen, the LMTB has had experienced intensive intracontinental deformation during the Mesozoic then is reactivated by the Cenozoic deformation, produced thin-skinned structures and basement-involved thin-skinned structures. The Mesozoic tectonic evolution of the LMTB is crucial to understand the intracontinental orogeny, uplifting of the Tibetan plateau and the alternation of the thin-skinned and thick-skinned structures.

The LMTB consists of three main thrusts, the Anxian-Guanxian thrust, the Beichuan-Yingxiu thrust and the Wenchuan-Maowen thrust distributed from SE to NW. A vertical cleavage belt has been delineated within the LMTB that divides the LMTB into a Western Zone and an Eastern Zone based on robust field structural analysis. The Eastern Zone characterized by NW-dipping foliation accommodated with NW-SE trending lineation, all shearing indicators show a top-to-the-SE shearing. All the foliations within the Western Zone are exclusively dipping to the SE with NW-SE trending lineation, and reveal the top-to-the NW shearing. Combined structural geometry and kinematics, the LMTB is actually a flower-liking structure. There is no horizontal lineation observed in the LMTB, which contradicts to the ductile strike-slip structure.

According to the structural level, the Eastern Zone can be further divided into four subunits, from SE to NW, the autochthon, the para-autochthon, the allochthon and the meta-allochthon. The autochthon is located to the east of the Anxian-Guanxian fault that is composed of Jurassic to Cretaceous rocks, weakly deformed as long wavelength fold. The para-autochthon bounded by the Anxian-Guanxian fault to the southeast and the Yingxiu-Beichuan fault to the northwest is mainly composed of Late Triassic rocks that is intensively folded and overturned to the southeast with the cleavage dipping to NW at local places. The allochthon includes the thrust belt between the Wenchuan-Maowen fault and the Yingxiu-Beichuan fault, the pervasive klippen distributes at the front of the LMTB. Extensive foliation and low greenschist

metamorphism assert its deeper structural level than the former two units. The meta-allochthon located between the vertical cleavage belt and the Wenchuan-Maowen fault, has had suffered the highest grade metamorphism from high greenschist to low amphibole facies. Detail structural level recorded in the meta-allochthon depicts a southeast-overturned antiform.

Combined redefined deformation, including the strata relationship based on pollen analysis, sedimentary characters of the Sichuan perpheral foreland basin and the zircon U-Pb age of the syntectonic granite, constrains this main deformation event in the Early Mesozoic around 219 Ma.

In the middle segment of the LMTB, there is a top-to-the-NW detachment fault developed along the western boundary of the Pengguan complex, which should be later stage superposition within the Eastern Zone. This detachment fault has been delineated along the southeastern boundary of the entire Songpan-Ganzi fold belt more 300 km in length by previous researchers. Integrated structural analysis, anisotropic of magnetic susceptibility study and gravity modeling suggest that the present architecture of the LMTB and its adjacent area is the result of basement slices extruding and stacking during the Late Mesozoic between 166-120 Ma.

The LMTB is far away from the contemporary plate boundary, devoid of ophiolite related material, could be an intracontinental orogen. On the basis of regional tectonic background, the Longmenshan area as the northwestern boundary of the Yangtze block, has had suffered extensive pre-Mesozoic extension that incidentally offer an ideal intracontinental weakzone. During the Early Mesozoic, the Yangtze basement underthrusts along the weakzone due to far-field effect of the Paleo-Tethys' obliteration and exhumated the different structural level material to the surface, presented as the southeastward thrusting and contemporaneous northwestward back thrusting. During the Late Mesozoic, the basement continues underthrusting due to the amalgamation of the Lhasa block to the Eurassia block, which lead to basement slices extrusion and stacking that resulted in couple developed detachment fault and thrust and crust thickening at the early stage. This process is a typical basement slice involved thin-skinned structure.

Keywords: Tibetan Plateau, intracontinental orogeny, thrust belt, thin-skinned structure

Contents

1. Introduction

1.1 Background and scientific issues

1) Intracontinental orogen

“造山作用”最早由 Gilbert (1890)提出，将其定义为特定时期内山链隆升作用。槽台学说中将造山带解释为“造山旋回中经受强烈褶皱作用和其他变形的地壳中的狭窄线性地带”(Schuchert, 1925)。板块构造理论提出后，加拿大学者 Wilson (1990)将造山带定义为“狭长的隆起地带”。现在，造山作用指板块俯冲碰撞过程中产生的一系列岩石变形、变质作用、岩浆活动、岩石圈增厚和地势隆升过程(Dewey and Bird, 1970; Sengör and Natal'in, 1996)，这些作用和现象以其特殊的组合方式记录于岩石圈中。板块理论中两个主要的角色为大陆岩石圈和大洋岩石圈，相比于大陆岩石圈，较重的大洋岩石圈沿活动大陆边缘俯冲再沿洋中脊新生，完成壳幔物质的循环，并在活动大陆边缘增生或产生新的岩浆物质完成大陆地壳生长过程 (Sutton and Watson, 1986)。

传统造山带定义局限于板块边缘，分为碰撞型和增生型(Figure 1.1 a 和 b)。碰撞型造山带指两个“漂浮”在岩石圈地幔上的刚性大陆块体在俯冲洋壳的拖拽力和洋中脊扩张的推挤力下发生碰撞，引起岩石圈的增厚和碰撞块体的强烈变形、变质和岩浆活动，如喜马拉雅造山带；而增生型造山带指在洋壳俯冲过程中海山、岛弧等物质逐渐向活动陆缘拼贴的，伴随强烈构造变形、变质作用以及地壳生长，两个陆块间几乎没有直接作用，如阿尔泰山脉(Brendan Murphy and Damian Nance, 1991; Windley, 1992, 1993; Windley and B.F, 1993; Nance and Murphy, 1994; Sengör and Natal'in, 1996; Sengor and Natalin, 1996; Cawood and Buchan, 2007)。以上两种造山带发生在洋壳俯冲或陆-陆碰撞大陆边缘，而非板块内部。

根据洋中脊、转换断层、俯冲消减带板块边界划分依据，具有古老陆核的刚性大陆板块拼合后形成一个新的更大的大陆块体，拼合产生的新陆块内不可避免的保留了先前构造的痕迹，成为构造薄弱带。因此，刚性板块理论被板块

内部广泛保留的古老造山带有关的地壳变形所打破(Molnar and Tapponnier, 1975)，由此提出第三种造山类型--陆内造山的研究。

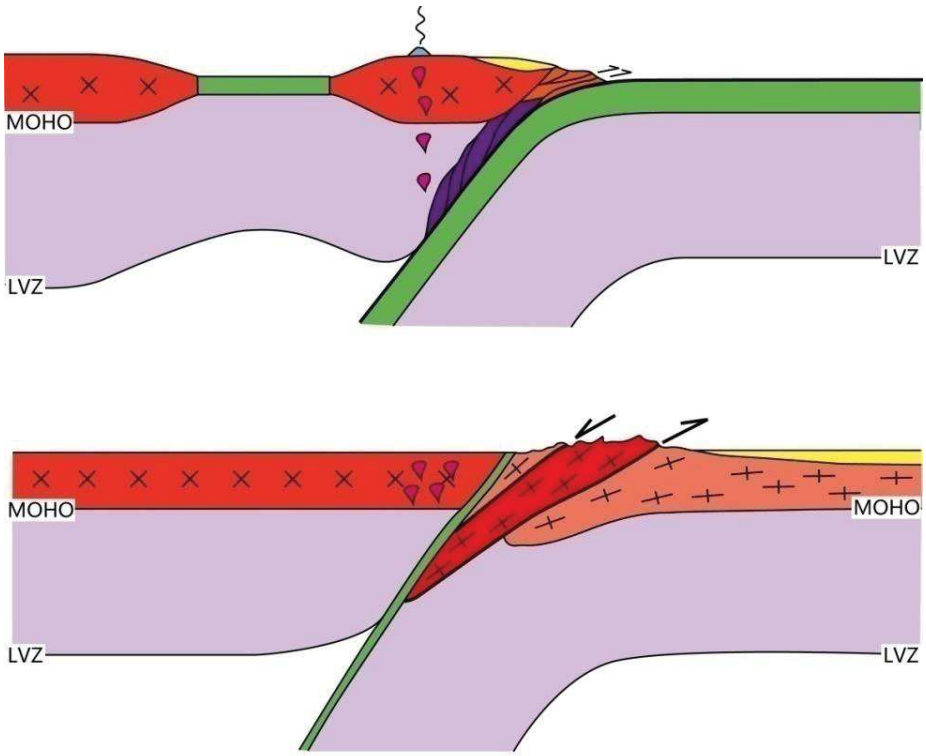

Figure 1.1 Classification of the orogens (Chu，2011)

(a) Collisional orogen；(b) Accretional orogen

陆内造山作用最早由德国学者在研究南非 Damara 造山带和欧洲华力西造山带时以 “陆内褶皱带”的概念提出(Intracontinental fold belt)概念时引出(Martin, 1983)。板内造山作用不同于板缘造山，不是板缘造山带继续发展的产物或板缘造山带演化的某一阶段，它有其独特的大地构造位置、形成演化历史及形成机制(张长厚和吴正文, 2002)。与板缘造山带类似，陆内造山带也存在大规模的构造变形、变质作用和岩浆活动。因此，学者可以通过应用在板缘造山带中的各地质、地球物理方法和方式来剖析陆内造山带。但陆内造山带的动力学机制一直存在争议。世界上典型的陆内造山带如南非 Damara 造山带、欧洲的比利牛斯山、澳大利亚的 Petermann 造山带和 Alice Spring 造山带、中国新生代的天山、华北的阴山-燕山褶皱冲断带和华南的雪峰山、北美洲的 Laramide 造山带以及西亚的 Zagros 等(Dickinson and Snyder, 1978; Martin, 1983; Choukroune, 1992; Allen et al., 1999; Hand and Sandiford, 1999; Sandiford et al., 2001; English and Johnston, 2004; McQuarrie, 2004; Raimondo et al., 2010; Chu et al., 2012a, c)。

这些造山带位于远离板块边界几百甚至上千公里的内陆地区，传统的板块俯冲模式无法解释这些造山带的形成。地幔柱活动、平板俯冲和板缘活动远程效应成为较为常用的三种解释机制(Molnar and Tapponnier, 1975; Dickinson and Snyder, 1978; Tapponnier and Molnar, 1979; Hendrix et al., 1992; Avouac et al., 1993; English and Johnston, 2004)，同时先前存在的薄弱构造带也是产生陆内变形的重要原因之一(Choukroune, 1992; M. Hand and M. Sandiford, 1999)。

例如雪峰山造山带位于我国华南板块核部，远离板块边界，其早中生代变形被解释成陆内造山作用(Chu et al., 2012a, b, c)。雪峰山地区以郴州-临武断裂带为界，东部区域主要保存早古生代构造变形；而西部区域则保留早中生代的构造特征。郴州-临武断裂带作为一个先期存在的陆内薄弱带，在古太平洋俯冲的远程效应下，华南西部的基底沿郴州-临武薄弱带向东南俯冲消减，而盖层沿着新元古代早期沉积的泥岩、粉砂岩等软弱岩层组成的滑脱带发生拆离、褶皱缩短，完成陆内造山过程，同时伴随广泛的造山后岩浆活动 (Figure 1.2)。

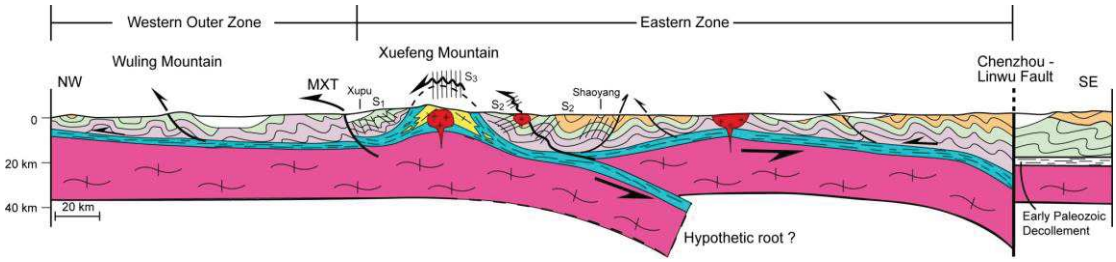

Figure 1.2 Structural cross section of the Early Paleozoic Xuefengshan orogen (Chu, 2011)

Alice spring 造山带是位于澳大利亚中部近东西走向经典的陆内造山带，它首先经历了中元古代之前的结晶基底形成和新元古代-泥盆纪时期稳定盖层发育过程。元古代结晶基底形成过程中保留的薄弱区域，经历晚古生代巨厚的沉积使得下部岩石圈升温软化，泥盆纪至石炭纪发生变形或重新活化了先存断裂，形成了切割岩石圈的逆冲断裂带，分隔南部的 Amadeus 盆地和北部的 Aruntal 结晶基底地块，两个块体在板内相互作用发生造山作用(Figure 1.2 a; Goleby et al., 1989; Martin Hand and Mike Sandiford, 1999; Sandiford et al., 2001)。构造变形主要发育于 Amadeus 盆地北部，而晚元古代造山产生的构造在这期陆内造山过程中同样经历了活化改造(Figure 1.3 b)。

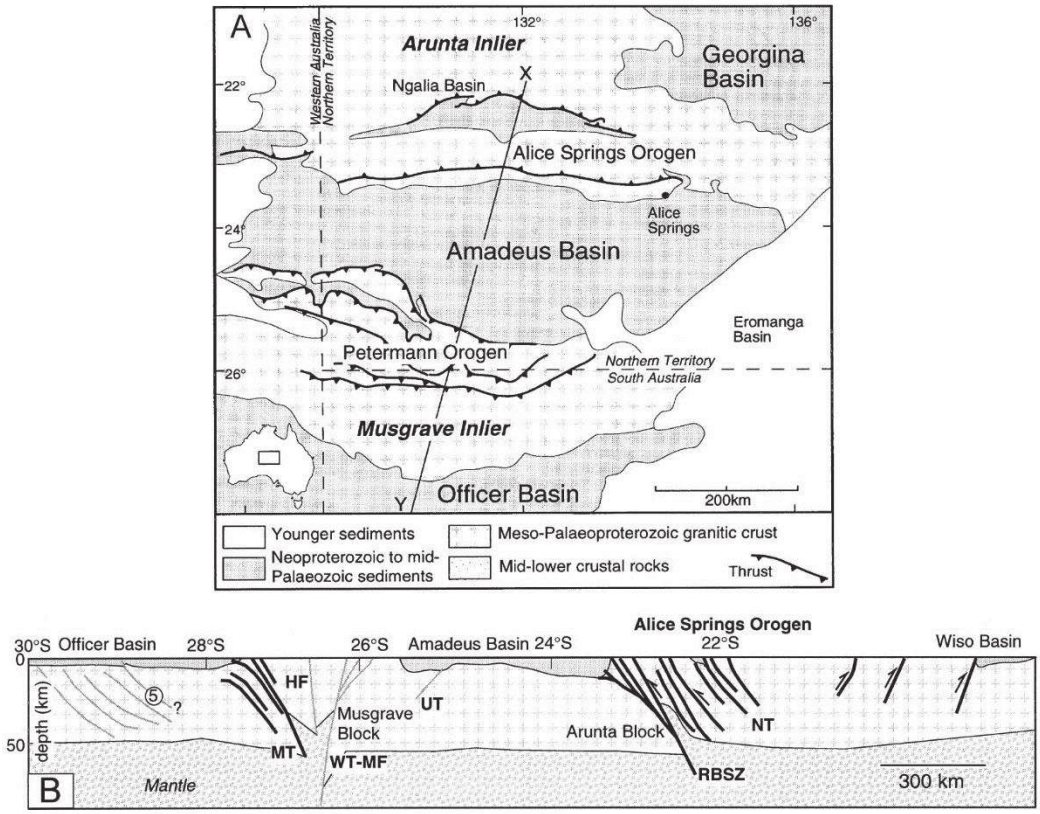

Figure 1.3 Alice Springs intracontinental orogen

(a) Geological map of Alice Springs orogen (Hand and Sandiford, 1999)；(b) Cross section of the Alice Springs (Hand and Sandiford, 1999; Sandiford et al., 2001)

由于陆内造山带大地构造位置的特殊性，其研究程度和关注度一直不如板缘造山带，其动力学机制和造山特征也有待进一步探讨。但是陆内造山也是板块构造的重要组成部分，也是研究板缘构造对板块内部影响的重要载体之一，因此它的形成、构造格架以及动力学机制越来越受到地质学家们的重视，各种研究手段诸如构造地质学、地球化学、地球物理等方法都被应用于分析陆内造山带的形成和演化过程。与板缘造山带不同，陆内造山带并不是板块间俯冲、增生或碰撞的直接结果，但是了解陆内造山过程对于研究板块内部构造变形、区域应力的传播以及板内构造对板缘变形的响应过程，都具有重要的科学意义。

2) Thickening mechanism of the Tibetan Plateau

龙门山作为青藏高原东缘，因其陡峭的地势和强烈的地震活动成为国际热点研究地区。垂直龙门走向的地势剖面表明，从四川盆地到青藏高原，在不到 100 km 的水平距离内，海拔由 500 m 左右直接攀升至 5000 m 以上(Figure 1.4)。

低温年代学数据和河流侵蚀速率表明龙门山地区在新生代以来经历了强烈而快速的隆升(Harrison, 1992; Tapponnier et al., 2001; Clark et al., 2005, 2010; Wang et al., 2012; Cook et al., 2013; Tian et al., 2013, 2014)。各种尺度的地球物理剖面均表明，地壳厚度由四川盆地的 45 km 左右向 NW 直接增厚至 60 km 左右(Robert et al., 2010b; Zhang et al., 2013; Guo et al., 2014)。但问题在于，龙门山山前缺乏新生代对应的前陆盆地(Burchfiel et al., 1995, 2008)，GPS 监测也表明靠近龙门山地表运移物质运移很慢(Zhang et al., 2002, 2004)，这种异常高的地势与物质运移特征和构造表现的不耦合引出龙门山新生代隆升和地壳的增厚机制的两种端元模型：1). 地壳脆性破裂，沿深入至岩石圈尺度的走滑-逆冲断裂活动，阶段性逆冲-增长导致地势的隆升和地壳增厚(Figure 1.5 a; Tapponnier et al., 2001; Hubbard and Shaw, 2009)；2). 下地壳通道流模式(channel flow)，即下地壳部分熔融为低粘滞系数的物质在重力作用和地表剥蚀共同作用下向外流动，遭遇刚性、冷的四川盆地后转变为垂直向上的流动，从而导致地势隆升和地壳增厚(Figure 1.5 a; Royden et al., 1997, 2008; Burchfiel et al., 2008)。

前人大多把龙门山地势隆升时间定在新生代，很少有人去探讨中生代龙门山地区的构造对地势隆升和地壳增厚的影响。前人对龙门山中段和南段的元古代杂岩体进行构造分析和同位素年代学分析认为，龙门山在白垩纪-早第三纪通过地壳尺度的楔形挤出或双重逆冲推覆造成龙门山地区早期的地壳增厚(Xu et al., 2008; Tian et al., 2016)。数值模拟结果进一步表明，龙门山主干边界断层上陡下缓的铲型断面形态不需要太多的水平缩短就能产生显著的地势隆升和地壳增厚(Feng et al., 2015)。目前只得到龙门山地区地表的岩片挤出证据，而了解这种构造特征和犁状的几何形态向地壳深部延伸方式，以及在松潘-甘孜褶皱带下部几何形态为我们探寻新生代以前龙门山地壳增厚提供重大理论依据，同时为青藏高原成因研究提供依据。

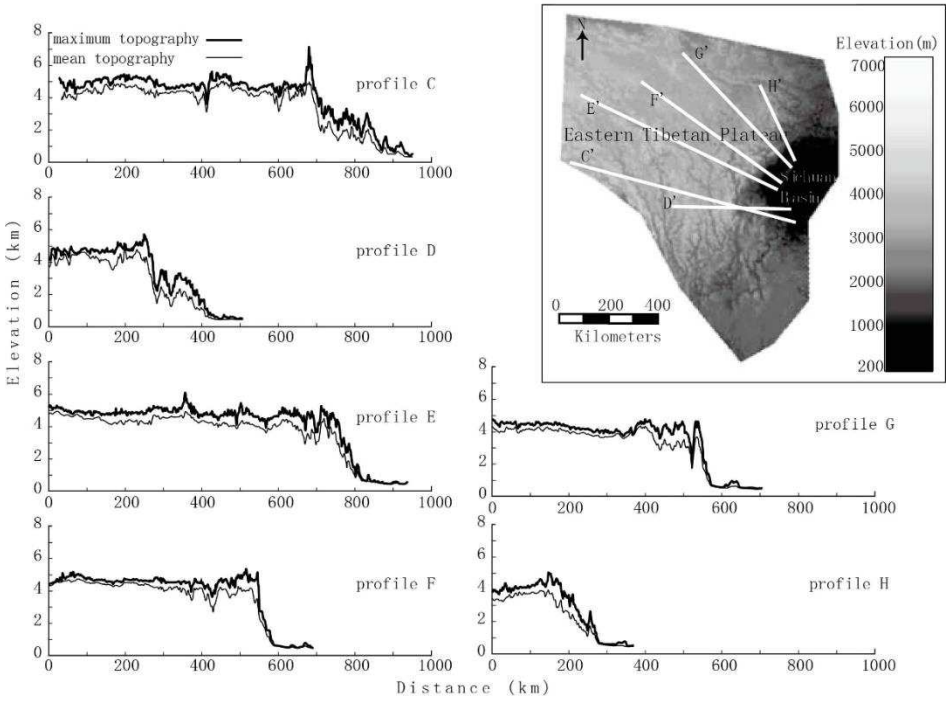

Figure 1.4 Topographic cross section of the Longmen mountain (Clark et al., 2005)

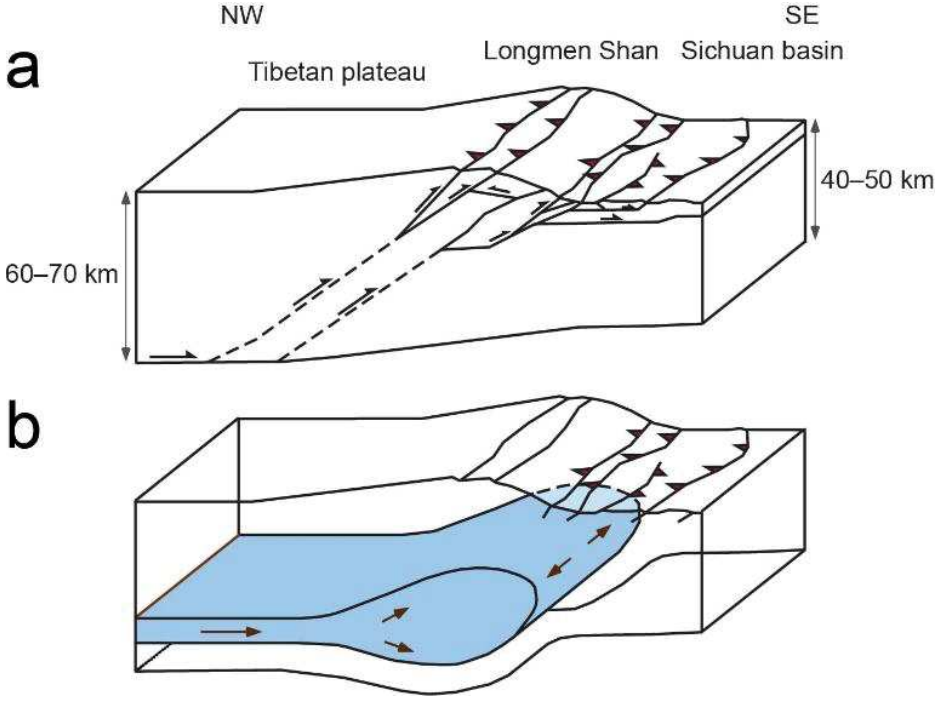

Figure 1.5 Two end-members model of the uplifting of the Tibetan Plateau

(a) Deep rooted thrust-slip fault piled up that lead to crustal thickening (Tapponnier et al., 2001); (b) Channel flow (Royden et al., 2008)

3) Thin-skined and thick-skined structure

薄皮构造最早由 Rogers (1849)在解释欧洲侏罗山式褶皱带时提出。造山带前陆典型薄皮构造指，沉积盖层与基底之间通过石膏、泥岩、页岩等软弱岩层

组成的拆离面与基底发生拆离，沉积盖层发生强烈的缩短、逆冲，各级逆冲断裂向下汇入主拆离断层之上，并表现为后端厚前端薄的楔形；而厚皮构造指在造山过程中，基底物质也卷入了逆冲推覆变形。最为典型的就是，在阿尔卑斯造山带，强烈逆冲推覆的薄皮构造和基底卷入变形的厚皮构造都广泛发育(Bellahsen et al., 2014; Pfiffner, 2016)。

龙门山逆冲推覆带前陆分布一系列的推覆体和飞来峰，推覆距离可达几十公里，表现为典型的薄皮构造特征；但沿龙门山同样分布着许多新元古代基底杂岩，被中生代的薄皮构造所围限。Burchfiel et al. (1995)在详细构造解析的基础上，将这些基底杂岩体归为强烈逆冲推覆带的原地系统，即将龙门山中生代变形定义为基底未卷入变形的薄皮构造。详细的地震反射剖面和前陆沉积盆地特征表明，龙门山南段，作为基底的宝兴杂岩卷入变形，属于典型的厚皮构造(Figure 1.6 a)；而龙门山北段，则仅表现为盖层强烈逆冲推覆的薄皮构造(Figure 1.6 b; Jia et al., 2006)。龙门山北段的薄皮构造和南段的厚皮构造在时间上也有差异，北段薄皮构造发生在早中生代，南段的厚皮构造发生在晚白垩世-早第三纪(Jia et al., 2006)。Robert et al. (2010a, b)根据在龙门山地区高精度地震反射剖面和典型剖面拉曼光谱测温结果提出龙门山地区印支期以薄皮构造的逆冲岩片为主，新生代以厚皮构造为主，同时伴随松潘-甘孜地壳增厚。龙门山的薄皮构造与厚皮构造更迭机制以及时间先后关系的厘定对理解造山带薄皮构造和厚皮构造产生机制及了解龙门山形成和演化过程有重大意义。

1.2 Research methods

本论文以“龙门山中生代构造演化”为主题，选取四川龙门山逆冲推覆带为研究区，通过中小尺度构造解析厘定研究区的构造格架、分区特点、主期构造事件的表现样式；进而通过对彭灌杂岩磁组构各向异性(AMS)、岩石显微组构分析及重力模拟，厘定出龙门山逆冲推覆带多期构造变形。根据卷入变形地层叠加关系、孢粉年代学、同构造岩体锆石 U-Pb 定年和韧性变形带内新生矿物 $^{40}Ar/^{39}Ar$ 定年确定龙门山主变形期和多期变形的时间。进一步厘定早中生代龙门山逆冲推覆带格架及晚中生代基底岩片挤出-逆冲改造早中生代格架过程。

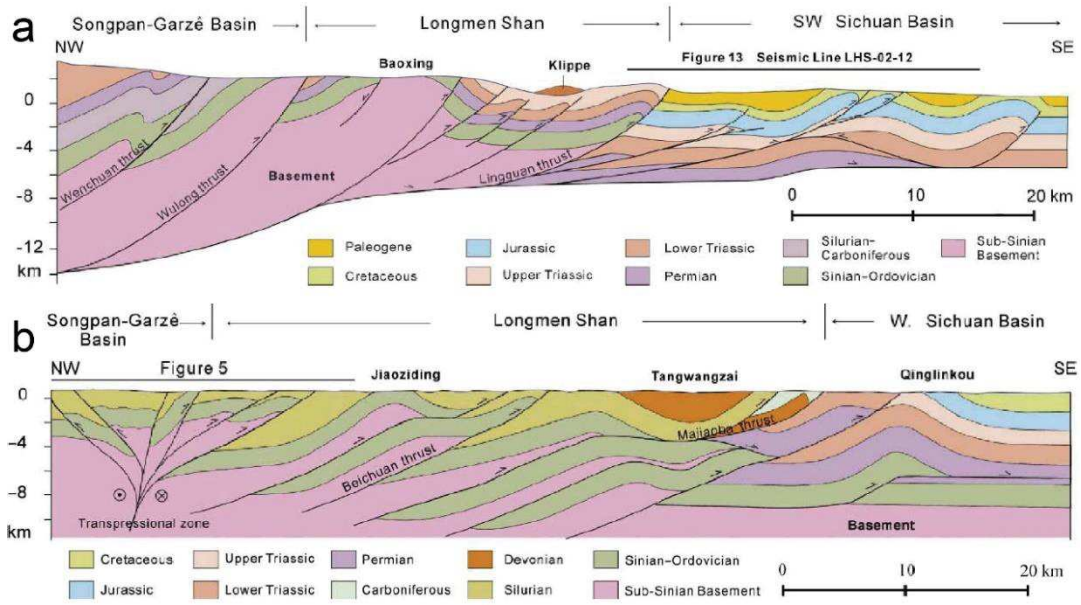

Figure 1.6 Cross section of the Longmenshan displaying thick-skinned and thin-skinned structures (Jia et al., 2006)

(a) Basement involved thick skinned structure of the south Longmenshan; (b) Thin-skinned structure of the north Longmenshan

1) Research content

a. Constructe the bulk architecture of the Early Mesozoic Longmenshan thrust belt

在大量调研前人研究成果的基础上，通过对龙门山逆冲推覆带及周边地区大范围、详细的野外考察，确定其构造几何学和运动学特征；根据对不同单元组成岩石的矿物组合和变形表现，确定龙门山的各个构造单元及其叠置关系。同时结合地震反射剖面、前陆盆地沉积特征等，完善对龙门山逆冲推覆带的构造演化认识。

b. Distinguish multiphase deformation of the Longmenshan thrust belt focusing on the emplacement mechanism of the Pengguan massif

彭灌杂岩作为研究区的元古代基底，其边界大多与古生代地层、中生代地层呈构造接触关系，足以表明岩体在新元古代侵位之后经历了后期的强烈改造作用。以磁化率各向异性精确厘定彭灌杂岩构造几何形态，岩石显微组构确定岩体变形级别；重力模拟揭示杂岩体及围岩的构造几何形态，通过多手段综合解析多期构造变形对认识龙门山构造演化过程的深化有重大意义。

c. The geochronological constraints of the Longmenshan thrust belt

在野外构造研究基础上确定卷入变形地层关系，确定主变形期相对年龄。对时代存在争议的重要地层单元，通过孢粉鉴定工作重新确定地层的时代，使变形的相对年龄更精确；对造山带内同构造花岗岩进行锆石 SHRIMP U-Pb 定年和强应变带内同变形矿物 $^{40}Ar/^{39}Ar$ 定年给出较为合理的绝对年龄。

d. Early Mesozoic intracontinental orogeny and Late Mesozoic modification of the Longmenshan thrust belt.

在对龙门山详细构造几何学、运动学和年代学认识基础上，结合研究区显生宙以来构造演化特征和同期区域构造背景，分析龙门山逆冲推覆带早中生代演化过程；以此为切入点，厘定晚中生代以来龙门山多期变形对早中生代格架的改造，从而为理解古特提斯洋闭合时在扬子板块边缘的构造响应提供帮助；晚中生代的多期变形，对龙门山后期作为青藏高原东缘地壳增厚也有一定的贡献。

2) Research routine

a. 资料搜集：全面收集和评估与论文相关的地质、地球化学、地球物理资料; 在及时了解和掌握研究领域的国内外前沿动态和研究区研究进展的基础上, 总结归纳, 为野外工作和室内分析提供指导和依据。

b. 野外地质调查和构造地质研究：以 1: 20 万区域地质资料为基础，同时结合局部地区 1: 5 万区域地质资料，以关键剖面重点开展详细的野外地质调查, 划分岩石构造单元，厘定几何学、构造学框架, 并系统采集岩石学和构造定向、定年样品。将野外露头-手标本-薄片不同尺度的构造变形特征有机地结合在一起，进一步确定不同构造单元的几何学和运动学；恢复不同层次变形发育的空间展布特征及其构造表现和叠加关系, 进而进行变形期次的划分; 探讨不同期次构造事件发生的区域构造背景，推出可能的动力学模型。

c. 磁化率各向异性(AMS)和矿物显微特征研究：对研究区重点岩体-彭灌杂岩进行了磁组构研究。彭灌杂岩野外表现为块状的花岗岩，露头尺度上不能识别出明显的韧性变形，很难开展传统的构造解析。彭灌杂岩地势险峻，仅有两条深切河沟纵横其中，交通很不便利。为了使 AMS 采样分布范围更广，只能背负工具徒步穿越岩体内的冲沟，然后使用钻机在野外系统采集定向样品。

AMS 能精确给出岩石的磁面理和磁线理，给出岩体几何学特征。通过矿物显微特征分析，确定岩体经历变形级别，从 AMS 所得出的几何框架中区分出构造成因和岩浆成因，结合区域几何学、运动学特征，完成岩体的构造解析。

d. 重力模拟：以区域小范围大比例尺布格重力异常图为基础，结合更大范围小比例尺布格重力异常数据，反演研究区中上地壳物质的重力信息；通过详细测量岩石各个层位的密度，结合前人对区域上各个地层密度的测试结果，以地球物理资料反映的深部形态为边界(断层深部延伸状态、盆地边界等)完成重力反演，获得更精细的深部几何学形态。

e. 年代学研究：根据地层中所含孢粉的，重新厘定相关岩石地层单元的时代；利用锆石 U-Pb 定年确定同构造花岗岩的年龄，从而标定构造事件发生的时间。在构造解析和矿物变形特征观察的基础上，选择研究区内的韧性剪切带或强应变带内同变形矿物(角闪石、白云母、黑云母、钾长石等)开展 $^{40}Ar/^{39}Ar$ 年代学分析，结合韧性变形的温压条件，确定多期次韧性变形发生的时间。

1.3 Main achievements and innovations of the thesis

1) Workload statistic

序号	工作内容	数量	单位	主要完成人
1	野外地质考察	3.5	月	薛振华、林伟
2	野外观测点	714	个	薛振华、林伟
3	实测剖面	20	条	薛振华、林伟
4	样品采集	130	块	薛振华、林伟
5	野外照片	825	张	薛振华
6	岩石学薄片鉴定	305	片	薛振华
7	构造定向薄片观察	280	片	薛振华
8	绘制地质图	10	张	薛振华、林伟
9	绘制剖面	12	条	薛振华、林伟
10	锆石阴极发光实验	6	件	薛振华、黎乐
11	锆石 SHRIMP U-Pb 定年	1	件	薛振华

12	锆石 LA-ICP-MS 测试	5	件	薛振华、黎乐
13	重力模拟剖面	2	条	薛振华
14	AMS 采样	36	点	薛振华
15	AMS 测试	339	个	薛振华
16	EBSD 测试	12	件	薛振华
17	单矿物云母温度计	7	件	薛振华

2）Main achievements of the thesis

1). A vertical cleavage belt (VCB) has been delineated along the Longmenshan thrust belt (LMTB), which divides the LMTB into an Eastern zone and a Western zone. The Eastern zone featured by the NW-dipping foliation and exclusively top-to-the-SE shearing along NW-SE trending lineation, while the Western zone display all the foliation dip to SE and display top-to-the-NW shearing along the NW-SE trending lineation. There is no imprint relationship between these two opposite kinematics and could happened contemporaneously. No ductile strike-slip structures have been found along the LMTB.

2). The Eastern zone can be further divided into four subunits based on roboust field observations and inner door anaysis, from SE to NW, autochthon, para-autochthon, allochthon and meta-allochthon, which are bounded by three main thrust of the LMTB and the VCB. These four subunits are characterized by enhancing deformation and deepening structural level from SE to NW. The highest metamorphism record in the meta-allochthon attained to low amphibole metamorphic grade, as a core of a SE-vergening anticline.

3). The LMTB suffered intensive shortening could be the result of the basement subduction. Both geophysical and geological evidences suggest a pre-T_2 rifting along the Longmenshan, the subsequent closure of the rift offers a potential soften zone where the basement subducted during the Early Mesozoic.

4). Pollen analysis of the brecciated limestone at the leading edge of the Tangbazi klippe, one of the klippen has a narrow tail covering concordantly deformed Jurassic-Cenozoic rocks, overthrough the strata evidence for Cenozoic thrusting of the klippen belt.

5). The Pengguan massif, one of the orogen-paralle proterozoic basement, could be the surface expression of the basement slice extrusion along the LMTB during the Late Mesozoic. The basement slices extruded southeastwards accommendated with the top-to-the-SE shearing at the foreland and the top-to-the-NW detachment at the hinterland, and the basement slices backstopped, piled up could lead to the crustal thickening.

6). Integrating previous research and new findings of the thesis, a Mesozoic evolutionary model of the LMTB has been proposed.

2. Geological settings of the Longmenshan and adjacent areas

2.1 Geomorphic location of the Longmenshan and brief introduction

龙门山主体位于于我国四川省西部地区，东北起自四川的广元，与米仓山相连，西南延伸至天全，被鲜水河断裂斜截，全长约 500 km，宽约 35-50 km(Figure 2.1)。龙门山陡峭的地势使得龙门山东西部气候发生差异，东部迎风坡雨水充足，是四川著名的暴雨区所在地；西部背风坡雨水稀少，气候十分干燥。大地电磁测量剖面和地震反射剖面表明松潘-甘孜褶皱带和四川盆地的深部地壳结构具有显著的差异，从四川盆地到松潘-甘孜褶皱带，地壳厚度从 44 km 突变至 60 km，表现为截然不同的两个单元(许志琴 , 1992; Robert et al., 2010a, b; Guo et al., 2013)，震惊中外的汶川地震(2008)和芦山地震(2013)便发生于此(Figure 2.1)。

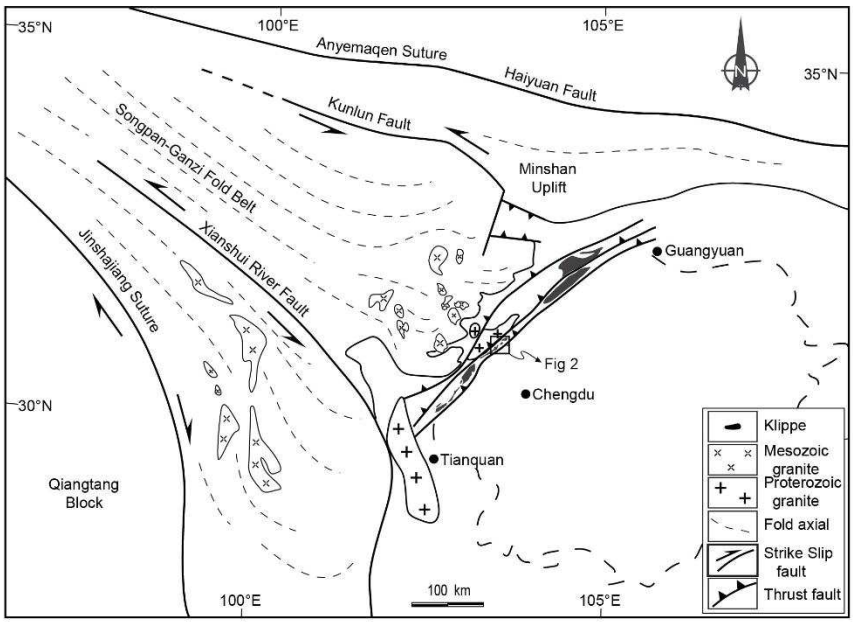

Figure 2.1 Simplified geological map of the Longmenshan thrust belt (Modified after Harrowfield et al., 2005)

龙门山逆冲推覆带区域上由三条倾向 NW 的逆冲断裂带组成，详细的构造解析表明，龙门山逆冲断裂带由 NW 向 SE 从韧性变形逐渐过渡为脆性，为典型的前展式传播方式(陈社发等, 1994a; Chen and Wilson, 1996)，地震反射剖面和地震余震震源深度位置均表明龙门山三条主干断裂向 NW 收敛于 15-20 km 深的滑脱面并向龙门山腹陆延伸(Li et al., 2010; Guo et al., 2013; Feng et al., 2015)。龙

门山逆冲推覆带为典型的复合型造山带，前中生代持续的伸展背景下，龙门山位于扬子板块稳定陆块 NW 缘(龙学明, 1991; 李月, 2008; 李佐臣, 2009)，在经历早中生代古特提斯洋闭合构造域下发生广泛的陆内造山事件后(许志琴等, 1992; Burchfiel et al., 1995; Chen and Wilson, 1996; Liu et al., 2013)，新生代新特提斯洋闭合碰撞下经历强烈活化(Clark et al., 2000; Kirby et al., 2002; Hubbard et al., 2009)，使龙门山逆冲推覆带不仅在 NW-SE 方向上变形层次表现不均一(Luo, 1991; Burchfiel et al., 1995; Chen et al., 1995; Worley and Wilson, 1996; Burchfiel et al., 2008)，沿龙门山 NE-SW 走向上也表现出分段特征(Jia et al., 2006; Jin et al., 2009; Xu et al., 2009; Jin et al., 2010)。

龙门山西北部的松潘-甘孜褶皱带为一东西向延伸、东宽西窄、平面上表现为倒三角形的复理石盆地(Yin and Nie, 1993; Chang, 2000)。北侧以阿尼玛卿-东昆仑缝合带为界，西南侧以甘孜-理塘缝合带为界，SE 边界则为龙门山逆冲推覆带(Figure 2.1)。松潘-甘孜褶皱带内分布厚达 10 km 的三叠纪西康群复理石(Figure 2.2)，为华南-华北碰撞时扬子板块边缘的被动沉积洋盆时期，广泛沉积来自华南、华北、西昆仑以及甘孜-理塘缝合带碎屑物质(Bruguier et al., 1997; Weislogel et al., 2006; Zhang et al., 2008; Weislogel et al., 2010)。沿松潘-甘孜褶皱带内多层次滑脱层(震旦-寒武泥质岩片岩、志留纪泥灰岩、早三叠石膏层)发生广泛的向南的剪切作用，造成了西康群强烈褶皱变形和大于 50%的缩短(许志琴等, 1992; Calassou, 1994; 王宗秀等, 1997; Roger et al., 2004; Harrowfield and Wilson, 2005)。

强烈褶皱的西康群复理石带内广泛侵入同造山或造山后 226-205 Ma 的埃达克质、A 型或钙碱性花岗岩，详细的地球化学分析表明岩浆主要来源于加厚地壳熔融，伴有古老基底熔融物质以及少量幔源物质加入，岩体内广泛记录具有古老锆石核部的物质。尽管最初研究认为松潘-甘孜为华南-华北板块碰撞时残留的古特提斯小洋盆，具有洋壳基底(Yin and Nie, 1993)，但更多研究者根据褶皱带内岩体的地球化学特征和高精度地震反射剖面结果认为松潘-甘孜褶皱带下部为扬子基底(Roger et al., 2004; 胡健民等, 2005; Zhang et al., 2006; 高锐等, 2006; Xiao et al., 2007b; Zhang et al., 2007; Yuan et al., 2010; Guo et al., 2013; Sigoyer et al., 2014; Guo et al., 2014, 2015)。

四川盆地作为扬子板块的重要组成部分，由古元古代-新元古代结晶基底和上覆的震旦-新生代盖层组成；震旦纪-奥陶纪碎屑岩和石灰岩之上广泛缺失志留系，随后被石炭纪-中三叠碳酸盐岩与火山岩不整合覆盖(四川省地质矿产局, 1991)。四川盆地西北缘在龙门山中生带以来持续的逆冲载荷作用下，形成周缘前陆盆地，精确记录了盆山耦合过程中，前陆盆地沉积中心及沉积物规律性迁移变化过程(崔秉荃和龙学明, 1991; Chen et al., 1994a; Li et al., 2003; Meng et al., 2005)。四川盆地内寒武纪泥页岩、志留纪页岩、晚三叠世蒸发岩充当多层次滑脱层，协调龙门山向四川盆地内传播变形(Yan et al., 2003b; Wang et al., 2014)，该套多层次滑脱体系与高精度地震反射剖面结果不谋而合(Hubbard and Shaw, 2009; Hubbard et al., 2010; Feng et al., 2015)。

2.2 Structural and geological history of the Longmenshan and adjacent areas

1) Proterozoic

龙门山沿扬子板块 NW 缘，由北向南分布元古代杂岩包括汉南杂岩、关口垭、平头山、刘家坪穹窿、轿子顶、雪隆包、牟托、彭灌、丹巴穹窿、宝兴杂岩、康定杂岩等(Figure 2.2)。精确年代学定年工作表明这些杂岩体就位于 840-750 Ma 之间(Li et al., 1999; 李献华等, 2001; Zhou and Michael, 2002; Yan et al., 2003a; Zhou et al., 2006; 李佐臣, 2006; Xiao et al., 2007a; Zhao and Zhou, 2007; Yan et al., 2008b; Pei et al., 2009; 李佐臣等, 2009)。杂岩体内分布一些基性-超基性侵入体，被解释为与地幔柱相关陆内裂谷下的产物，并与澳大利亚地区元古代基性岩浆对比(Li et al., 1999; 李献华等, 2001)；更多学者通过地球化学特征对比分析认为扬子板块 NW 缘这些新元古代杂岩体(轿子顶杂岩除外)为 Rodinia 大陆拼合时沿扬子板块活动边缘俯冲背景下产生的岛弧火山岩(四川省地质矿产局, 1991; 龙学明, 1991; Zhou and Michael, 2002; Yan et al., 2003a; Zhou et al., 2006; 李佐臣, 2006; 凌文黎等, 2006; Xiao et al., 2007a; Zhao and Zhou, 2007; Yan et al., 2008b; Pei et al., 2009; 李佐臣等, 2009)。

位于龙门山北段西北缘的碧口地块，分别以勉略缝合带、青川-阳平关断裂、虎牙断裂为界，与龙门山逆冲推覆带和松潘-甘孜褶皱带接壤。岩性组成上从北向南分别为董家河变质的蛇绿岩套(赖绍聪等, 2007)、横单群浊积岩、碧口

群火山岩、火山碎屑沉积岩(闫全人等, 2003, 2004)，被解释为元古代时期 Rodinia 超大陆拼合时，古板块由北向南向俯冲的一整套岛弧相关岩套。

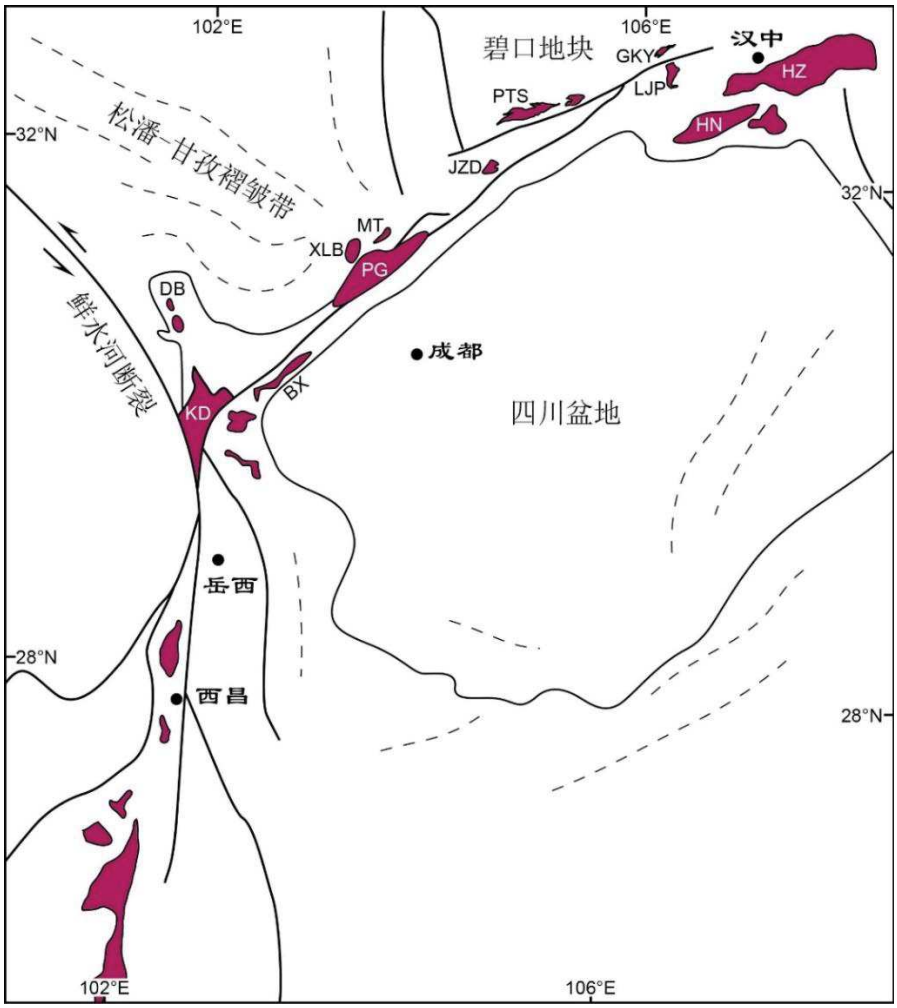

Fgiure 2.2 Proterozoic complex distributed along western boundary of the Yangtze bolock

HZ：Hanzhong complex; HN：Hannan complex; GKY：Guankouya complex; LJP：Liujiaping complex; PTS：Pingtoushan complex; JZD：Jiaoziding complex; MT：Moutuo complex; PG：Pengguan complex; XLB：Xuelongbao complex; DB：Danba dome; BX：Baoxing complex; KD：Kanding complex.

这些元古代花岗质岩石与新元古代变沉积岩共同构成龙门山地区沿线分布的基底杂岩。轿子顶穹窿核部由元古代花岗质岩石和通木梁群火山岩组成。通木梁群下段主要以火山熔岩为主，为一套玄武岩-安山岩-英安岩-流纹岩组合。其中保存的中酸性火山岩的岩浆锆石 LA-ICP-MS 年龄介于 829±6 Ma~1000±7 Ma，地球化学数据投图均落于亚碱性系列，地化特征对应于板块俯冲环境中岛弧火山岩(Pei et al., 2009; 李佐臣等, 2009, 2011)。而碧口群内岩石矿物组合与矿物组合反映的蓝片岩变质作用同样反映了洋盆闭合时所伴随的陆壳加厚或板块俯冲的结果(魏春景, 1994)。

810 Ma 之后进入 Rodinia 超大陆裂解阶段，地表产出以刘家坪穹窿核部刘家坪群为代表的酸性火山岩系。刘家坪群内火山岩岩浆锆石 LA-ICP-MS 年龄间于 809±11 Ma，稀土元素、微量元素配分曲线同样表明刘家坪群与典型的大陆裂谷流纹岩特征类似，形成于大陆边缘从挤压到伸展转变的裂谷构造背景(李佐臣等, 2009, 2011)。而 793 Ma 左右的轿子顶过铝质后碰撞型花岗岩，以及汉南杂岩中倪霞岩-碱性包体同样反映大陆裂谷环境下的岩浆活动(马润则等, 1997; Pei et al., 2009)。

因此，龙门山地区新元古代早期可能为 Rodinia 大陆聚合产生一系列沿扬子板块 NW 缘分布的岛弧岩浆岩和火山岩，随后进入到 Rodinia 大陆裂解阶段，区域上进入伸展构造背景。

震旦纪碳酸盐岩不整合盖在前震旦的花岗岩和微弱变质的火山岩、沉积岩上，沉积物特征及分布范围表明震旦纪时期继承了 Rodinia 裂谷空间，并且裂谷局限分布，整体上记录了稳定沉积过程。龙门山南段邛崃以西，晚三叠世砂岩甚至直接不整个盖在基底杂岩之上，表明至少在龙门山南段，元古代杂岩体在早中生代作为古陆块存在，具有稳定延伸的根部(Figure 3.1)。

2) Early Paleozoic

四川盆地内部，寒武系和奥陶系主要为海相或细粒陆源碎屑沉积岩，上寒武统局部地区出现蒸发岩。寒武系局部整合盖在震旦纪碳酸盐岩上，形成一套渐变过渡沉积体系。寒武-奥陶纪地层一般较薄，局部地区甚至缺失，但寒武-奥陶系中间并不存在明显的角度不整合。陈智梁(1987)认为扬子板块西缘在寒武纪时期为稳定大陆边缘裂谷环境。轿子顶杂岩东侧出露的毛塔子火山岩，地化特征和 SHRIMP 锆石 U-Pb 定年同样解释为 473.6 Ma 的陆内裂谷火山岩(李佐臣, 2009)，阐述了龙门山地区奥陶纪伸展裂陷环境。

龙门山逆冲推覆带寒武-奥陶系主要发育在彭灌杂岩 NE 以及龙门山北段轿子顶地区(Figure 2.3)。由于寒武-奥陶系发生强烈的褶皱变形，因此其沉积厚度具有不确定性。寒武系以粗粒碎屑岩为主，奥陶系由厚层大理岩和少量陆源碎屑岩组成，在龙门山北段表现为寒武-奥陶纪与上覆厚层志留系逆冲至变质的志

留系之上(Figure 3.1)，而龙门山南段奥陶纪地层主要为一套纯净的大理岩，记录了明显的韧性变形。

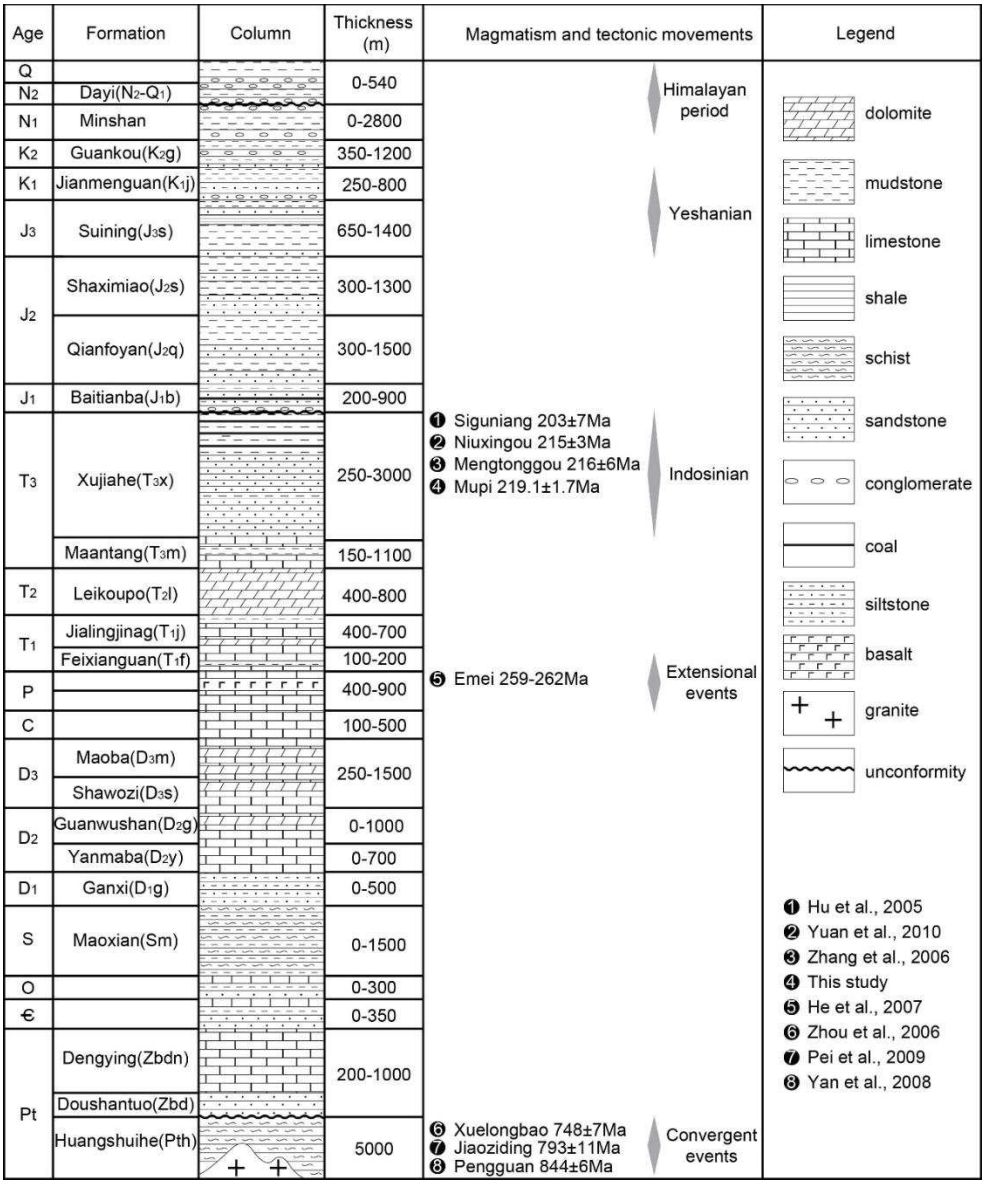

Figure 2.3 Lithostratigraphy of the Sichuan foreland basin and adjacent regions

志留纪以来，龙门山地区在稳定斜坡上发生持续拉张裂陷，并接受巨厚的志留系沉积(Figure 2.3)。龙门山逆冲推覆带广泛出露的志留系茂县群，主要分布在北川-映秀断裂西北侧，是一套变质程度不同的泥砂岩、千枚岩、泥质片岩和绢云母片岩，偶尔夹透镜状灰岩，厚度从 1000-4000 m 不等，如果这套沉积厚度准确，表明志留纪时期扬子板块 NW 缘发生了强烈快速沉降，很可能对应龙门山地区持续的伸展裂陷，产生平行扬子板块 NW 缘分布的巨大的沉积空间，并且初始形成的北川-映秀断裂很可能控制着志留系巨厚的沉积。在龙门山逆冲推覆带腹陆轿子顶、雪隆包、牟托等地，志留纪与下伏寒武-奥陶地层呈断

层或角度不整合接触(Figure 3.1)，指示明显的后期构造叠加改造作用。整套志留系茂县群内经历了低绿片岩相变质作用，局部地区达到低角闪岩相变质作用，并记录了完整的巴罗型变质带(Worley et al., 1995; Arne et al., 1997)。

总体来看，寒武-志留纪地层在龙门山地区分布具有局限性，在扬子板块北缘缺失早寒武世沉积，在轿子顶地区缺失中寒武世-奥陶纪沉积，而志留系又是一套巨厚沉积，这种厚度、岩相及地层缺失的东西方向变化，反映龙门山地区在早古生代经历了裂解-抬升-局部裂解的反复过程，但其沉积环境总体为伸展裂陷环境(龙学明, 1991; 李佐臣等, 2009, 2011)。

3) Late Paleozoic

晚古生代时期，扬子板块被动大陆边缘龙门山地区发生多期张性事件(韩克猷, 1984; 罗志立, 1984; 龙学明, 1991)，形成一系列 NE-SW 走向的同沉积正断层，控制泥盆纪近 6000 m 厚的沉积。龙门山逆冲推覆带下泥盆统为一套浅海相砂岩、粉砂岩、泥岩和泥灰岩，沉积厚度达到 3000 m 以上。中上泥盆统主要为一套碳酸盐岩，厚度从 300 m 到 2000 m 不等，主要分布在龙门山北段的唐王寨向斜和龙门山南段成都西部地区(Figure 3.1)，与石炭-下三叠统共同构成龙门山山前的飞来峰和逆冲推覆带，并经历了广泛变质和强烈的变形。在松潘-甘孜褶皱带东部边缘分布的下泥盆统厚度达 1000 m 左右，沉积特征显示为大陆架斜坡至深水沉积环境，局部地区甚至表现出复理石沉积韵律。

研究区大部分区域缺失石炭纪地层，仅在龙门山逆冲推覆带和松潘-甘孜褶皱带东部边缘有限产出。龙门山逆冲推覆带内石炭纪地层多为浅水环境下灰岩和白云岩，夹少量砂质灰岩和页岩，与泥盆纪地层一起以飞来峰和推覆体形式产出。松潘-甘孜褶皱带东缘，石炭系大多为灰岩、粉砂岩及深水环境的页岩，厚度仅有几百米。泥盆-石炭纪地层沉积特征表明龙门山地区沉积环境从志留纪以来一直保持着伸展背景下的深水环境。

四川盆地西部下二叠统主要由浅水相灰岩和白云岩组成，含砂质底砾岩，经历强烈褶皱变形作用。晚二叠世时期，龙门山西南部、云南地区广泛侵入玄武岩(峨眉山玄武岩)，局部地区厚度达 2000-4000 m(四川省地质矿产局, 1991)，并在龙门山逆冲推覆带发现与峨眉山地区相关的玄武岩(刘树根等, 1991)。晚二

叠世龙门山地区的伸展作用达到顶峰阶段，并沿扬子板块 NW 边缘广泛沉积碳酸盐重力流、浊积岩、深水硅质岩等伸展环境下的特征沉积物(罗志立, 1984, 1991, 1994; Chen, 1985; 罗志立和龙学明, 1992; 朱同兴和蒲心纯, 1994)。

松潘-甘孜褶皱带东缘的下二叠统厚度较薄，通常在 100 m 左右，由深水页岩、砂岩和灰岩组成，通常含有外来灰岩砾石团块。一些碎屑岩表现出浊积岩特征，可能沉积于大陆架和深水平原，地层层序中砾岩层与灰岩卵石层互层表明区域上强烈的伸展活动(Chen, 1985; 朱同兴和蒲心纯, 1994)。在松潘-甘孜褶皱带南部，产出海相枕状熔岩。无论是在扬子板块西北缘还是松潘-甘孜东南缘，与伸展同期的基性岩脉和小型侵入体切割晚二叠以前的地层单元。龙门山附近岩石圈内高密度、高电阻率的基性、超基性异常物质的存在，也表明该区曾发生过岩石圈的拉张破裂及熔融地幔物质的大量上涌(李立和金国元, 1987)。地震反射剖面也揭示出四川周缘前陆盆地二叠纪盖层下残存古生代裂谷盆地(Jia et al., 2006)。

4) Mesozoic

下-中三叠统在松潘-甘孜褶皱带出露有限，与四川盆地西北缘同层位岩性相似，均为一套浅海碳酸盐岩和硅质碎屑岩。碳酸盐岩，多为厚层灰岩、具有交错层理的鲕粒灰岩；硅质碎屑岩通常与粉砂岩、页岩与碳酸盐互层组成(Figure 2.4)。下三叠统最底部的飞仙关组由更深海相的薄层灰岩与浊积岩型砂岩组成。广泛分布的厚层浅色的碳酸盐岩指示大陆架沉积环境，而分布的交错层理的灰岩和鲕粒状灰岩表明逐渐向浅水环境转变。下三叠统飞仙关组的深海相岩石解释成深水裂谷沉积，可能为龙门山地区二叠纪裂谷以来持续的沉积物(罗志立和龙学明, 1992)。鉴于在整个四川盆地周边中-下三叠统并未观察到大陆架相关的珊瑚礁或浅海相珊瑚碎屑，以及泥岩、页岩、泥灰岩反映的沉积相，可以认为中-下三叠统四川盆地西北缘地区逐渐转变为稳定盆地沉积阶段而非珊瑚礁环岛(Read, 1985; Meng et al., 2005)。

无论在四川周缘前陆盆地还是松潘-甘孜褶皱带，两个单元内上三叠统沉积环境均发生显著变化：在四川前陆盆地内，上三叠统由最下部浅海相马鞍塘组向上不整合过渡到陆源碎屑沉积的须家河组(Figure 2.4)，且该不整合界面仅在周缘前陆盆地发育，表明严格受龙门山逆冲推覆带活动控制，四川盆地开始由

稳定的被动陆缘开始向前陆盆地活动陆缘转变。陆相须家河组主要由灰色砂岩、少量页岩及煤层以及不同层位的底砾岩组成，其沉积相和沉积厚度在横向上发生差异性变化，整体厚度远大于其下部海相的碳酸盐岩沉积(Chen et al., 1994a; Chen et al., 1995; Meng et al., 2005; Li et al., 2013; Luo et al., 2014; Zhang et al., 2015)。靠近龙门山逆冲推覆带，须家河组主要由粗粒沉积物、冲积砾岩组成，随着向四川盆地内迁移，逐渐转变为湖泊相细粒沉积。须家河组整体上为一垂直龙门山的楔形沉积体，厚度向四川盆地内部逐渐尖灭。这种沉积相由浅海相向陆相转变以及楔形的地层厚度，被解释为龙门山逆冲推覆带对四川盆地逆冲加载产生的前陆盆地沉积(崔秉荃和龙学明, 1991; Chen et al., 1994a; 曾允孚和李勇, 1995; 刘树根等, 1995; Li et al., 2003; 贾东等, 2003)。地球物理数值模拟也表明四川周缘前陆盆地在龙门山晚三叠世逆冲推覆加载下形成(Li et al., 2003; Meng et al., 2005; He, 2014)。龙门山北段，强烈褶皱的上三叠统须家河组被下侏罗统白田坝组不整合覆盖，向龙门山南段逐渐过渡为须家河组四段与须家河组三段的不整合接触关系(Figure 2.4)，表明龙门山逆冲推覆带在向四川盆地传播过程中的时空迁移性。前陆盆地汶川一号钻孔资料显示，映秀-北川断裂以西，彭灌杂岩与须家河组砂岩以构造岩片叠置的方式产出，且须家河早期沉积物也卷入这期逆冲变形，说明北川-映秀断裂的逆冲活动，使前陆盆地向四川盆地内迁移。上三叠统须家河组二段砂岩中出现彭灌杂岩基底杂岩、震旦纪火山岩和中-下三叠统砂岩砾石，指示龙门山地区元古代基底在晚三叠世时至少部分暴露在地表(崔秉荃和龙学明, 1991; Li et al., 2014)。

龙门山南段怀远西部，须家河组砂岩直接不整合覆盖在元古代杂岩之上，且元古代变质盖层和随后的寒武-二叠地层在宝兴地区连续产出，说明在龙门山南段元古代基底在晚三叠世时期以古陆形式存在(Figure 3.1)。

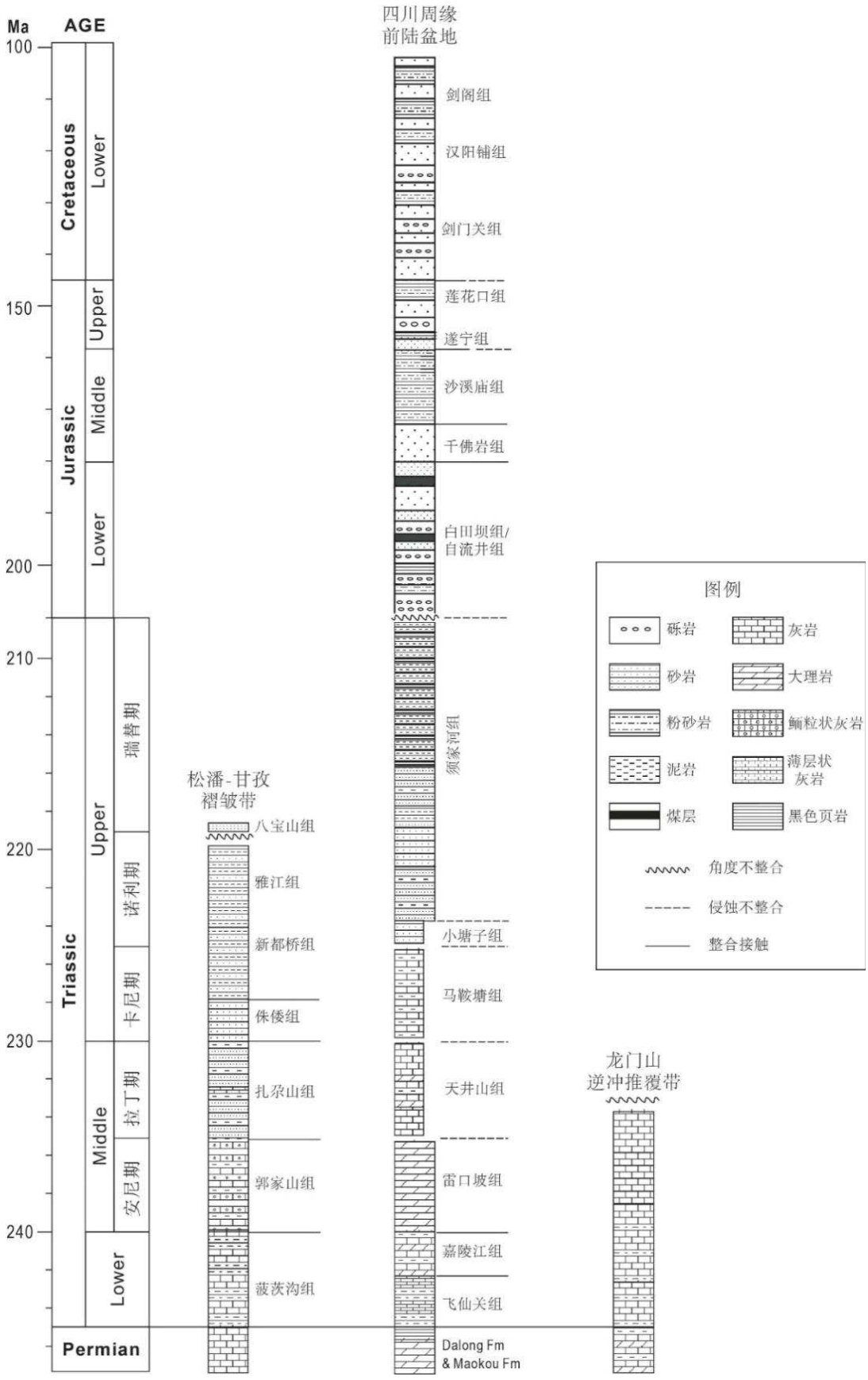

Figure 2.4 Mesozoic lithostratigraphy of the northwest Sichuan basin and adjacent regions (Meng et al., 2005)

松潘-甘孜褶皱带内，上三叠统为巨厚的复理石沉积，经历强烈褶皱变形，局部地区厚度可达 10 km，其中卷入变形最年轻的地层为诺利期雅江组，随后被晚三叠世末瑞替期八宝山组不整合覆盖(Figure 2.4)，标志着褶皱带活动的终结。褶皱带内广泛 NW-SE 走向的褶皱形迹表明变形早期 NE-SW 向挤压缩短，向 SE 靠近龙门山逆冲推覆带，褶皱轴迹呈弧形向南弯曲，随后变为 NE-SW 走向的褶皱形迹(Figure 2.1)。褶皱形迹的变化，被解释为晚三叠龙门山发生左行压扭性走滑的结果(Dirks et al., 1994; 陈社发等, 1994a, b; Chen et al., 1995; Arne et al., 1997; Meng et al., 2005)。松潘-甘孜褶皱带内侵入大量中生代 A 型、I 型、钙碱性和埃达克质花岗岩，年龄在 226-205 Ma 之间(Roger et al., 2004; 胡健民等, 2005; Zhang et al., 2006; Xiao et al., 2007b; Zhang et al., 2007; Yuan et al., 2010; Sigoyer et al., 2014)。大多数岩体切穿褶皱形迹并发育环状接触变质带，将松潘-甘孜强烈的褶皱变形进一步限定在晚三叠之前。然而，自生伊利石 K-Ar 年龄又表明整个褶皱带经历广泛 190-150 Ma 的变质作用(夏宗实, 1993)。

侏罗系白田坝组为一套单成分砾岩和发育板状交错层理的砂岩，向四川盆地内部逐渐变为细粒砂岩(Figure 2.4)，为一套陆相河流、湖泊沉积，主要分布在龙门山北段米仓山南部以及龙门山南段邛崃以西(Figure 3.1)。与上三叠统须家河组相比，下侏罗统显著特征是在整个四川盆地其厚度都比较均一，底砾岩也不厚，很多地方不超过 100 m，砾石主要由能干性较强的古生代石英岩、灰岩和大理岩，其良好的磨圆度表明经历较长距离的搬运。整套砾石中并未见元古代基底杂岩或中生代花岗岩物质。下侏罗统厚度均一，广泛发育的薄的底砾岩，砾石良好的磨圆表明早侏罗世龙门山处于造山后的宁静期。中上侏罗统千佛岩组和沙溪庙组为一套厚层砂岩、粉砂岩和页岩，盆地内以冲积扇沉积、河泛湖泊沉积为主，主要集中在龙门山北段米仓山南部和龙门山南段邛崃以西，碎屑锆石和古水流方向表明龙门山北段的中上侏罗统沉积物源主要来自龙门山西北段、米仓山和大巴山，而南段物源主要来自龙门山逆冲推覆带(崔秉荃和龙学明, 1991; 罗志立和龙学明, 1992; Luo et al., 2014)。这种厚层河泛沉积和冲积扇沉积表明前陆挠曲盆地载荷背景(Heller et al., 1988; Jordan, 1995)，说明晚侏罗世开始，龙门山逆冲推覆带开始新一轮向 SE 逆冲推覆并对四川前陆盆地加载。这一期的逆冲推覆可能导致龙门山沿线下侏罗统地层发生褶皱变形(Figure

3.1)。四川盆地内侏罗纪地层，在平衡剖面分析中作为重要的标志层证明龙门山山前强烈的褶皱、逆冲会产生显著的地势抬升(陈竹新等, 2005; Hubbard and Shaw, 2009; Hubbard et al., 2010)。

白垩纪地层在四川盆地西部广泛分布，在龙门山南段被广泛的第四纪覆盖(Figure 3.1)。沿龙门山逆冲推覆带，东北段白垩纪地层大多以单斜形式向四川盆地内延伸，而西南段白垩纪地层同样卷入褶皱和逆冲推覆变形，且上白垩统与下白垩统以角度不整合关系产出，下白垩统之后龙门山周缘前陆盆地再次加载沉积，龙门山西南段晚白垩纪-早第三纪时期的前陆盆地明显叠加在晚三叠世周缘前陆盆地之上，表现明显的再生前陆盆地特征，再生前陆盆地等厚图指示沉积中心集中在龙门山西南段，表明至少在龙门山西南段晚白垩世至早第三纪重新经历逆冲推覆活动(贾东等, 2003; 许志琴等, 2007; Xu et al., 2008; Tian et al., 2016)。精细地震剖面表明，龙门山南段再生前陆盆地内，白垩纪地层表现出典型的生长地层特征，结合宝兴杂岩西部糜棱岩带晚白垩世-早第三纪 $^{40}Ar/^{39}Ar$ 年代学结果，进一步表明龙门山西南段多期次叠加活动(Jia et al., 2006; Tian et al., 2016)。

5) Cenozoic

由于龙门山地区新生代地层不发育，新生代构造表现并不显著。低温年代学数据、河流侵蚀速率表明龙门山作为青藏高原东缘，受新生代印度-欧亚大陆碰撞影响，地势发生显著隆升，松潘-甘孜褶皱带内花岗岩与彭灌杂岩的磷灰石裂变径迹结果表明汶川-茂汶断裂两侧第三纪发生了显著的差异隆升，而映秀-北川断裂两侧物质中新世以来也发生了差异性隆升(Arne et al., 1997; Kirby et al., 2002; Clark et al., 2005; Godard et al., 2009; Wang et al., 2012; Cook et al., 2013; Furlong and Kirby, 2013; Tian et al., 2013)。新生代强烈的隆升使龙门山沿线的元古代基底杂岩大规模剥蚀，以广泛砾石沉积在第三纪大邑砾岩中(Chen et al., 1994b; Chen and Wilson, 1996)。在龙门山地区，新生代构造表现以脆性破裂为主，很难厘定新生代韧性变形。由于印度板块持续向北的挤压，导致青藏高原物质向东南逃逸(Tapponnier et al., 2001)，50-21 Ma 期间先沿哀牢山-红河左行走滑断裂侧向逃逸(Tapponnier et al., 1990; Harrison et al., 1992; Leloup and Kienast,

1993)，随后沿 NW-SE 走向的左行走滑鲜水河断裂发生侧向逃逸，并伴有 12 Ma 强烈的岩浆活动(Roger et al., 1995)。

2.3 Previous evolutionary models of the Longmenshan thrust belt

龙门山逆冲推覆带作为重要的地质界线，同时作为一个中生代-新生代多期变形的复合型造山带，其最典型的特征不仅表现为极高的地势、加厚的地壳，还表现出极大规模的逆冲推覆作用和与之伴生的周缘前陆盆地。经过几十年的研究，大家普遍认可的是龙门山作为一个复合型造山带，至少经历了中生代和新生代两期构造变形，并且新生代的变形对早期的起到构造活化作用(Burchfiel et al., 2008; Roger et al., 2010; Liu et al., 2013)。前人通过对龙门山和松潘-甘孜褶皱带构造学、同位素年代学工作，结合地球物理反射剖面以及四川周缘前陆盆地的演化历史，对龙门山逆冲推覆带的形成提出了不同的观点，对龙门山逆冲推覆带主要动力学模型主要集中在早中生代、晚中生代和新生代三个时间段。

1) Early Mesozoic

龙门山逆冲推覆带早中生代造山模式最早由罗志立(1984)提出的 C 型俯冲模式，不同于传统的洋壳向陆壳俯冲模式。该模式指出，龙门山位于稳定大陆相盆地边缘，由于正断层活动，使深部岩石圈减薄破裂，成为潜在的破裂面；经历晚古生代-早中生代稳定沉积作用，在数千到数万米厚的陆相沉积物加载、压实下，形成的沉积物厚度大于近代海洋沉积物的密度，巨大的重力势能使沉积盖层的基底甚至莫霍面发生错断、沉降，导致岩石圈发生错动，形成向龙门上倾斜的界面(Figure 2.5)。印支早期，龙门山地区的寒武纪-志留纪内广泛沉积的泥质岩内作为滑脱层，巨厚沉积物沿着滑脱层，在强大重力载荷作用下，向龙门山方向潜移，使早期的正断层反转为逆断层，该阶段强调物质自身重力势能的作用导致造山；印支晚期，由于松潘-甘孜已经固结，东部古太平洋板块俯冲的远程效应，使龙门山地区基底进一步消减和逆冲。松潘-甘孜褶皱带内的岩浆岩成分由东向西发生规律性变化，可能受扬子地壳和地幔向西倾斜俯冲过程中导致的岩浆分异。地震测深剖面和大地电磁给出的等温度结构图表明汶川-茂汶带以下，岩石圈等温线成舌状向西部下插，还未到达热均衡的状态。因此，C 型俯冲的本质是原先裂谷边缘在巨厚沉积物覆盖升温和自身重力作用下，古

太平洋板块俯冲的远程效应，使扬子板块向西发生了陆内消减俯冲作用，并在龙门山地表表现为一系列逆冲推覆构造(Figure 2.5; 罗志立, 1984, 1991, 1994; 罗志立和和龙学明, 1992)。

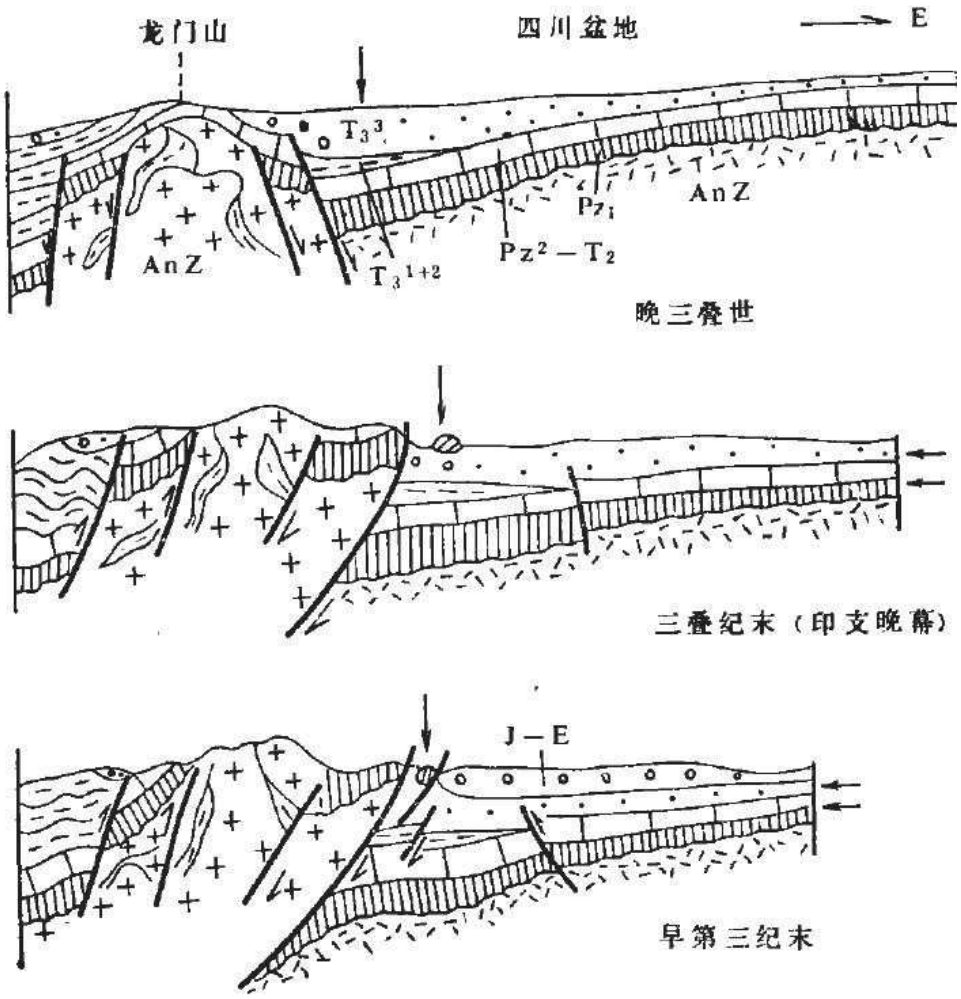

Figure 2.5 C-type subdcution model proposed by Luo 1984

许志琴通过对松潘-甘孜详细的构造填图提出三块体：即北部的劳亚陆块(昆仑块体)、东部的扬子板块及西部的昌都-羌塘微板块相互作用，导致扬子板块北部、西南部古特提斯洋两支俯冲碰撞及陆内汇聚，产生以松潘-甘孜褶皱带为主体的滑脱型山链(Figure 2.6; 许志琴等, 1991; 许志琴等, 1992; 王宗秀等, 1997)。首先，松潘-甘孜内，由于古特提斯洋经由阿尼玛卿缝合带向北俯冲，产生强烈的由北向南的挤压变形，构成近东西向向南凸出的弧形滑脱带；随后古特提斯洋南支沿甘孜-理塘缝合带向 SW 向义敦岛弧下面俯冲闭合，在松潘-甘孜内产生由西向东的挤压力，由此产生的 S-N 走向的褶皱形迹叠加在早期向 S 凸出的弧形构造上。在这种双向俯冲收缩机制下，沿着松潘-甘孜内部多层次

滑脱带，产生以洋壳为滑脱底面的羌塘-昌都主动大陆边缘三叠世复理石增生楔和以陆壳滑脱带为底的扬子被动陆源三叠系复理石楔，龙门山逆冲推覆带即为扬子被动陆缘增生楔的前陆褶皱带。

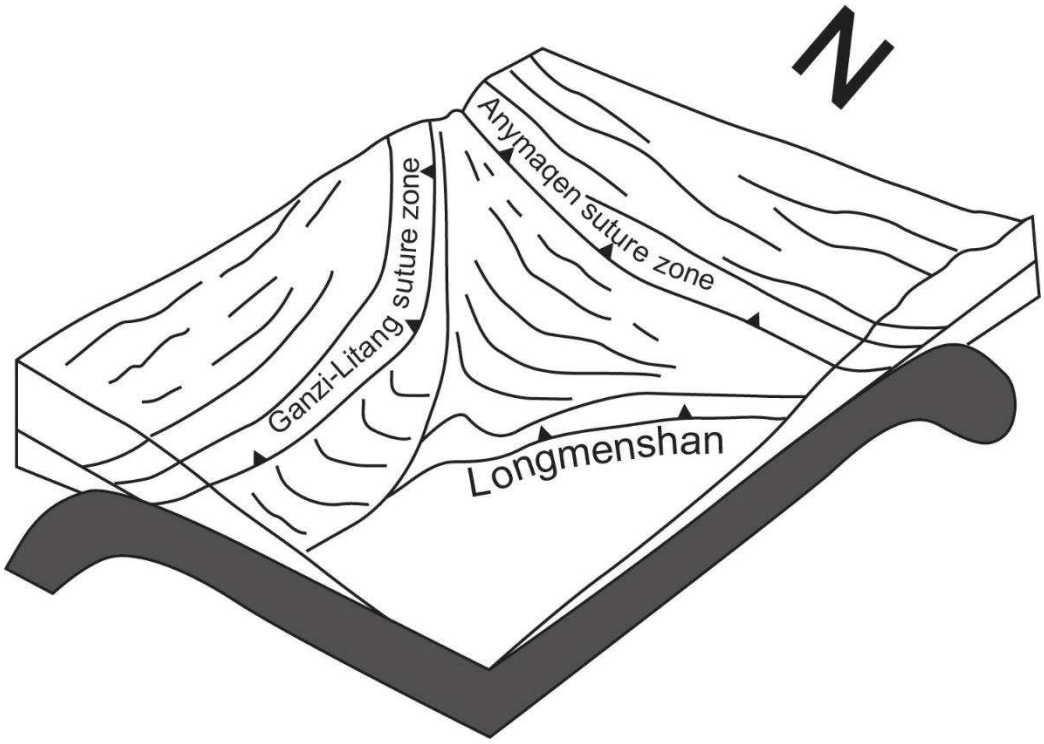

Figrue 2.6 Bivergent subduction and thrusting along Yangtz passive margin of the Early Mesozoic Longmen Shan (Xu et al., 1992)

很多学者认为早中生代华南华北板块碰撞时，松潘-甘孜北界阿尼玛卿洋向N 俯冲，在松潘-甘孜内产生一系列向 S 的剪切，而龙门山作为扬子板块和松潘-甘孜边界，经历左行走滑压扭并在龙门山地区产生广泛向 SE 的逆冲推覆作用，即松潘-甘孜带内现有 NE-SW 向挤压产生一系列 NW-SE 走向的褶皱，至龙门山地区，类似“陆内转换断层”，表现为左行走滑，使 NW-SE 走向的褶皱形迹向龙门山地区转变为 NE-SW 走向的褶皱；再向四川盆地方向，龙门山压扭性走滑传递为向 SE 逆冲推覆，形成龙门山广泛的逆冲推覆构造(Figure 2.7; Chen et al., 1994b; Chen et al., 1994a; Dirks et al., 1994; Chen et al., 1995; Worley et al., 1995; Worley and Wilson, 1996; Arne et al., 1997; Harrowfield and Wilson, 2005)。Mattauer (1992)提出松潘-甘孜褶皱带内巨厚盖层沿着底部滑脱带向 S 剪切，造成褶皱形迹向 S 凸出并在褶皱带南缘形成一系列逆冲推覆带。Worley et al. (1996)对汶川-茂汶剪切带内的石榴子石包裹体径迹三维切片研究表明，石榴子保存的包裹体径迹体现了水平方向的左行剪切，随后立即发生向 SE 的逆冲

推覆作用，矿物共生关系表明龙门山地区的峰期变质时间发生在走滑向逆冲转变期间，矿物共生关系也表明龙门山地区峰期变质作用发生在左行走滑向 SE 方向逆冲过程中发生。Burchfiel et al. (1995)对龙门山及周边地区详细构造分析认为，古特提斯洋不仅向北部的阿尼玛卿俯冲，同时沿甘孜-理塘缝合带向 SW 俯冲，两条俯冲带共同作用使松潘-甘孜洋盆向扬子板块斜向挤出产生龙门山广泛的逆冲推覆，同时表现出少量的左行走滑分量，他还认为华南华北碰撞时华南板块的顺时针旋转可能造成龙门山地区的走滑(Figure 2.7)。

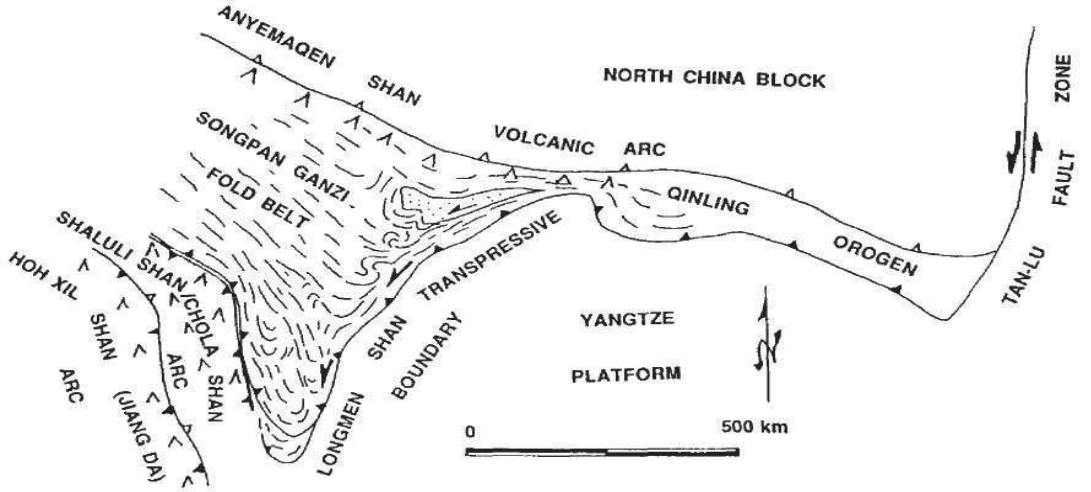

Figure 2.7 Interpretation of the Longmen Shan allochthon as part of a transpressive boundary along the major zone of early Mesozoic N-S convergence in central China (Burchfiel et al., 1995)

Chen et al. (1996)对龙门山早中生代走滑过程中产生向 SE 逆冲产生的推覆体和飞来峰展开了非常详细的构造几何学研究，提出晚三叠世以前扬子板块 NW 缘持续的伸展裂陷形成一系列 NE 走向的同沉积正断(Figure 2.8 a)；印支期由于松潘-甘孜褶皱带变形在龙门山地区产生向 SE 的逆冲推覆作用，使早期的正断层产生反转，形成汶川-茂汶断裂带和北川-映秀断裂带，早期正断过程中同沉积的巨厚沉积物以香水断裂为底断层被推覆至四川盆地，形成龙门山山前广泛的推覆体和飞来峰，并伴随产生四川周缘前陆盆地早期演化(Figure 2.8 b)；晚三叠至早白垩世阶段为阶段式逆冲推覆过程，也是龙门山逆冲推覆带由腹陆向前陆逐渐传递的过程，形成灌县-安县等后期的逆冲断裂，多期次的逆冲推覆活动与松潘-甘孜内的岩浆活动很好地对应(Figure 2.8 c)。

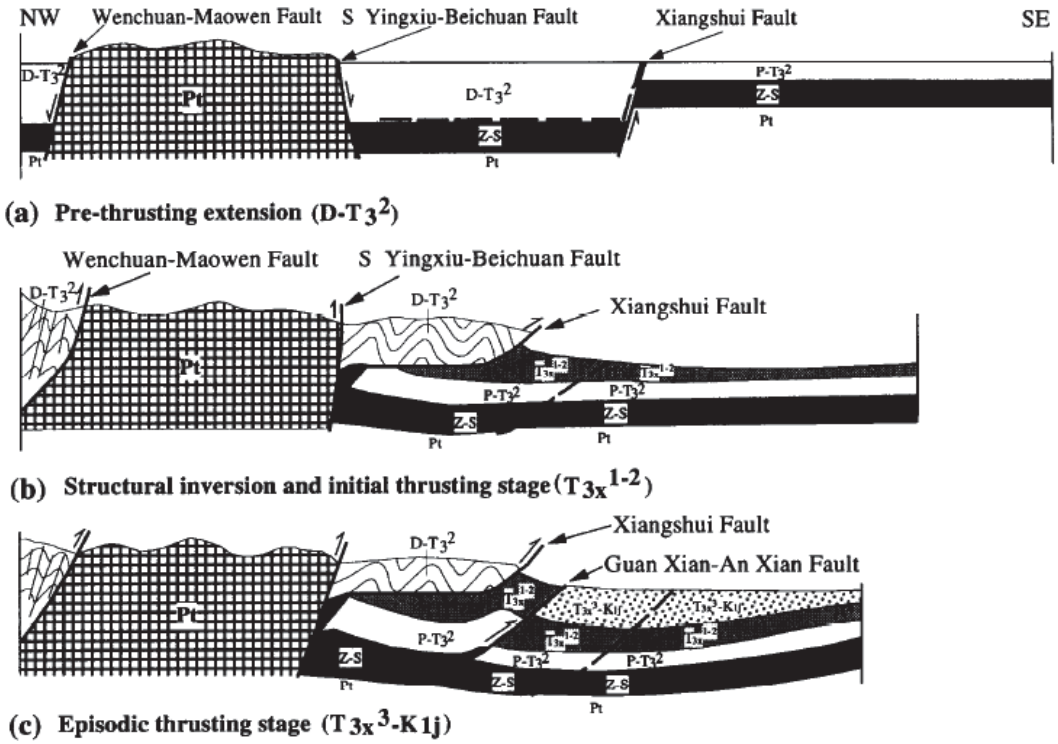

Figure 2.8 A simplified geological model illustrating the evolution of the Longmen Shan Thrust-Nappe Belt and relationship to the development of the Western Sichuan Foreland Basm.(Chen and Wilson, 1996)

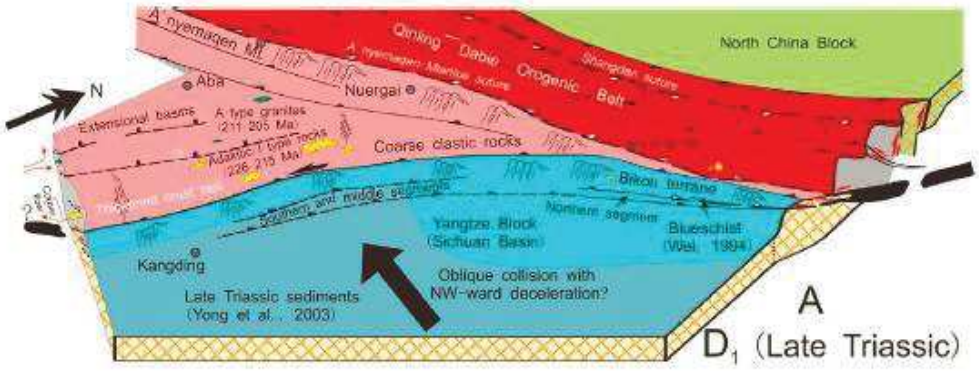

Figure 2.9 Northward subduction of the Yangtz Block (Yan et al., 2011)

Yan et al. (2011)根据构造要素差异和褶皱形态叠加，在龙门山逆冲推覆带识别出早中生代一期主要变形发生在 237-208 Ma 之间，在龙门山北段表现为上部向 WSW 的逆冲推覆，并在龙门山中段伴有左行走滑，这期时间导致松潘-甘孜地壳广泛增厚，上部向 WSW 的运动学为华南板块向华北板块碰撞时，俯冲板片上部地幔角流活动在龙门山地表的响应(Figure 2.9)。Zheng et al.(2016)通过对北川-映秀断裂内的假玄武玻璃和自生伊利石 K/Ar 定年，首次直观给出龙门山主干断裂早中生代活动的年代学证据。

2) Late Mesozoic

详细的构造解析表明扬子被动陆缘增生楔龙门山地区，不仅表现为广泛向SE 的逆冲推覆，在龙门山沿线的元古代杂岩体 NW 边界位置还发育着不协调的上部向 NW 剪切的糜棱岩带。糜棱岩带内新生云母氩氩年代学和四川盆地西部白垩纪再生前陆盆地分别限定元古代杂岩体 NW 边界正断剪切和向 SE 逆冲对四川盆地的加载作用在白垩纪，因而向 NW 的正断和向 SE 的逆冲具有同时性。因此提出由于欧亚大陆南部众多微弱块体的拼贴作用在强烈的挤压应力下，导致扬子板块向松潘-甘孜内发生陆内俯冲，进而松潘-甘孜下部物质沿龙门山逆冲推覆带向 SE 方向发生楔形挤出(Figure 2.10; 许志琴等, 1999)。挤出过程中产生龙门山前陆的逆冲推覆以及腹陆同时期正断，类似喜马拉雅造山带的主中央逆冲断层和藏南拆离系，使龙门山逆冲推覆带发生早期隆升(许志琴等, 2007; Xu et al., 2008)。

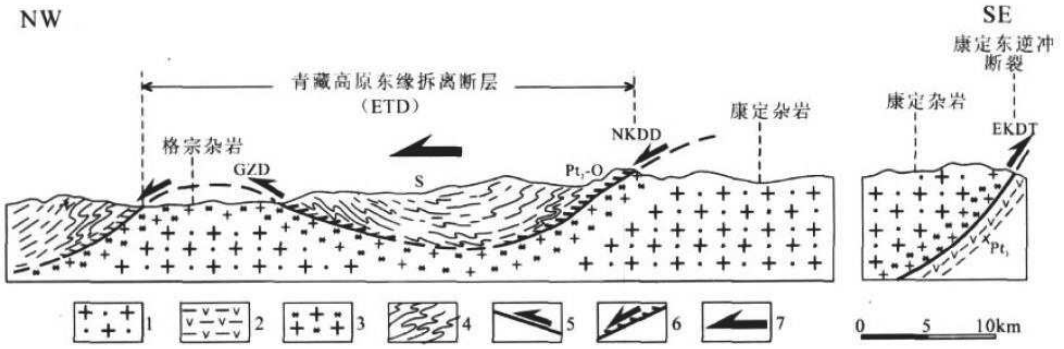

Figure 2.10 Crustal wedge extrusion of the Late Mesozoic Longmen Shan (Xu et al., 2007)

Tian et al.(2016)通过应力场分析，认为许志琴等(2007)白垩纪地壳楔形挤出模式会在龙门山腹陆地区出现局部的伸展应力场，野外应当表现出山间伸展盆地等，这与野外的观察不相符合。Tian et al.(2016)因而提出龙门山地区晚中生代仍然持续表现为挤压背景，向 SE 的逆冲推覆挤压过程中形成地壳尺度的 Duplex 构造，并指出在 Duplex 的顶界断层同样会形成元古代杂岩体 NW 界向 NW 的正断作用。

Yan et al.(2008)在龙门山逆冲推覆带元古代杂岩顶部和古生代与中生代盖层之间分别识别出两条上部向 SE 拆离的正断层，这两条拆离正断层中间形成一个“地壳通道流”，解释为造山带垮塌后的张性环境，位于松潘-甘孜褶皱带下部增厚、深变质的物质在龙门山地区以“地壳流”的形式向 SEE 方向挤出而垮塌

(2.11)，这期的伸展垮塌导致元古代杂岩之上志留系-奥陶系的普遍缺失，并且在整个扬子板块西缘元古代穹窿都有很一致的表现。对碧口地块、龙门山中段彭灌杂岩地区、丹巴地区的变质温压条件测试给出顺时针的 P-T-t 轨迹特征，对应着华南-华北板块碰撞增厚-垮塌的过程(Huang et al., 2003; Yan et al., 2003a, 2008a, b, Yan et al., 2008a, 2011, 2012; Zhou et al., 2008; 刘鹤等, 2008)；

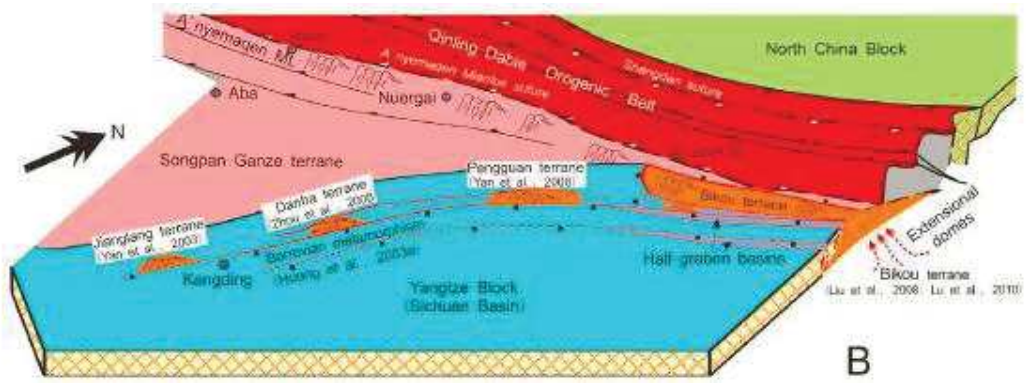

Figure 2.11 The Early and Middle Jurassic extensional in the Longmen Shan thrust belt indicates SE-ward retrograde migration of the South China Block (Yan et al., 2011)

在龙门山地区，重力均衡回弹对龙门造山带的构造演化也起着非常关键的作用(李勇等, 2005; 柯小平等, 2009; Li et al., 2013, 2014)。重力资料表明，松潘-甘孜褶皱带和四川盆地均表现出负均衡重力异常，而位于中间的龙门山地区则表现为显著的正均衡重力异常，根据艾利均衡模型，龙门山地区在调整过程中会产生向上隆升的力(李勇等, 2005)。重力均衡回弹响应在地表，转化为剥蚀的沉积物记录在四川周缘前陆盆地中。详细的盆地沉积特征分析将前陆盆地的沉积物分为两种类型四层样式：1)楔形构造沉积序列，前陆盆地的沉积处于饥饿状态，沉积空间大于物源的供给，整套沉积序列向上粒径逐渐变粗，沉积物源源不断向前陆盆地内部供给，可能对应龙门山强烈逆冲推覆对前陆盆地的加载过程；2)大型板状近等厚的构造沉积序列，表明盆地处于过饱和状态，沉积空间没有相应扩大，对应沉积环境相对稳定，可能对应构造加载间歇期龙门山地区重力均衡回弹，因而只提供物源而不产生沉积空间，两种类型的沉积序列交替产出，也体现了印支期龙门山向 SE 的逆冲推覆与宁静时期静态回弹相互交替作用(Li et al., 2013, 2014)。

3) Cenozoic

很多学者认为龙门山现今构造格架主要形成于新生代，包括地势隆升、地壳增厚以及龙门山广泛发育的飞来峰和推覆体构造(Meng et al., 2006; Royden et al., 2008; Burchfiel et al., 2008)。同样是龙门山沿线元古代杂岩体 NW 边界向 NW 的正断剪切，Royden et al.(2008)解释为 channel flow 在地表的响应(Figure 2.12)。该模式将彭灌杂岩解释成 channel flow 的盖层部分，其下部地壳流向外流出，将彭灌杂岩等元古代基底杂岩顶出，在其 NW 缘形成向 NW 的正断以及 SE 缘向 SE 的逆冲，类似青藏高原的主中央逆冲断裂和藏南拆离系。

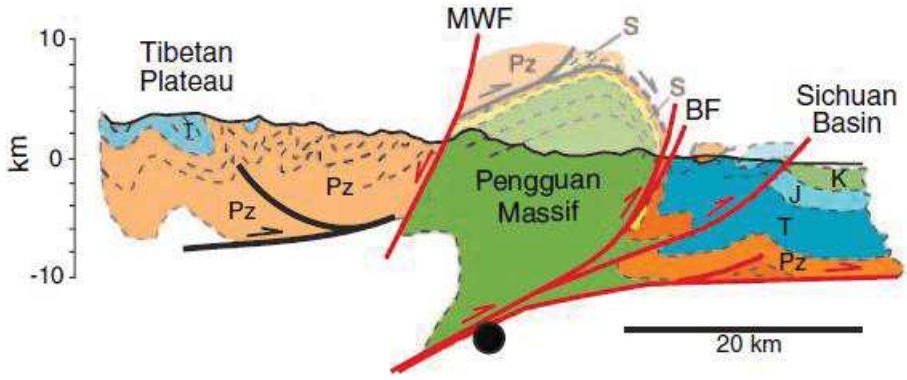

Figure 2.12 Geological structure along a profile through the Pengguan massif indicating the massif as the crest of the channel flow (Royden et al., 2008)

Meng et al. (2006)根据龙飞来峰的空间几何学形态、内部应变分析、分布空间位置与龙门地势的耦合关系等认为飞来峰的就位与新生代以来的重力滑覆相关。正是由于新生代 channel flow 的作用在龙门山地区产生强烈的地势差，形成在不到 100 km 的水平距离内，高程由四川盆地几百米向 NW 攀升至 5000 m 以上极陡的地势，并导致重力势能的累积(Richardson et al., 2008; Godard et al., 2009; Wang et al., 2012)。分布在龙门山中段的大型飞来峰，其尾部和中部表现为一系列正断，而在飞来峰前缘表现为向东南的逆冲推覆，这种野外观察的飞来峰内部“前压后拉”的构造表现，与垂直飞来峰剖面的应力分析结果一致；在龙门山南段飞来峰上部为老地层，下部新地层，且构成飞来峰的各个层位以构造关系接触；飞来峰的发育和分布范围与龙门山 NE-SW 走向上地势差异密切相关，地势高的彭灌杂岩、宝兴杂岩等东南缘，分布许多的飞来峰，而在龙门山北段飞来峰鲜有发育；龙门山中段的飞来峰盖在褶皱变形的侏罗-白垩纪-新

生代地层之上，表明飞来峰就位与新生代的事件密切相关。Meng et al. (2006)的模式中认为，新生代 channel flow 向 SE 挤出遭遇冷的刚性四川盆地时向上流动导致龙门山南北段不均一抬升，南段地势抬升较高，因而产生大规模的滑覆作用，龙门山北段地势相对较低，因而滑覆产生的飞来峰不明显。龙门山地区志留深海相的浅变质千枚岩、泥质岩以及元古代变质基底与震旦纪之间的不整合等岩性软弱界面在滑覆作用中充当滑脱层的作用，使基底上的盖层更容易顺着地势滑覆。滑覆作用剥蚀、卸顶更多的物质，更利于 channel flow 向地表的隆升，加上地表河流侵蚀作用，三者相互正向反馈，形成龙门山中段和南段山前广泛分布的飞来峰构造(Figure 2.13; Meng et al., 2006)。

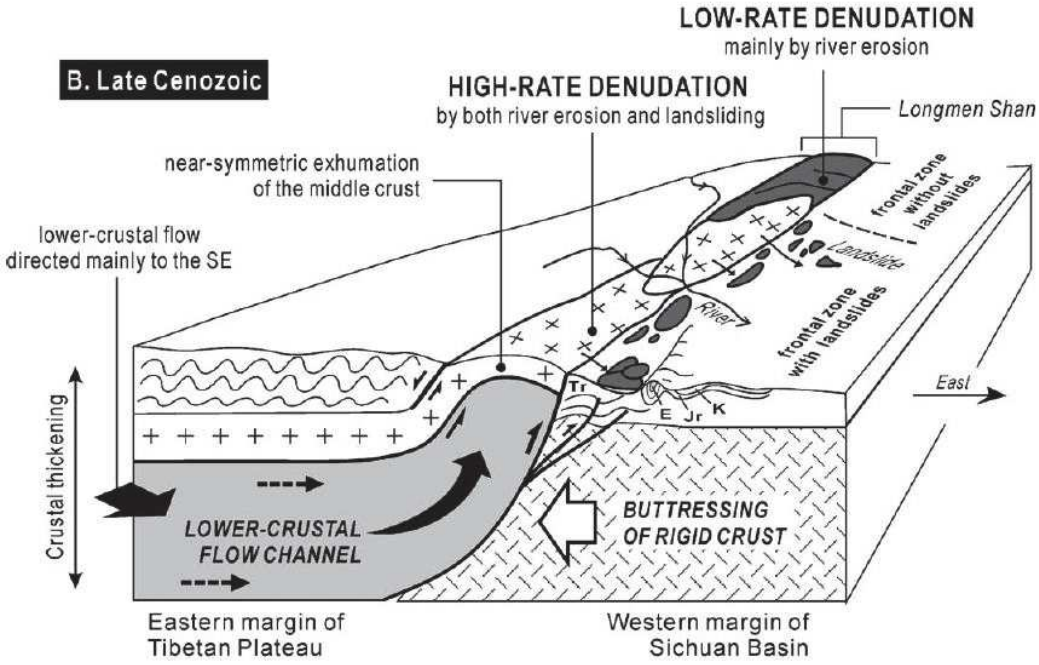

Figure 2.13 A model to illustrate possible links between surface processes and upward extrusion of lowercrustal flow channel at the eastern flank of the Tibetan plateau. It is suggested that a positive feedback existed between nearly symmetric exhumation and high-rate denudation by a coupled action of landslide and river erosion in the southern Longmen Shan. The lower-crustal flow is directed mainly to the southeast, and has exerted less influence on the northern Longmen Shan, which thus underwent neither marked denudation nor exhumation of crystalline basement rocks (Meng et al., 2006).

然而，Robert et al. (2010a)对龙门山地区的构造特征、精细地震反射剖面和典型剖面拉曼光谱测试结果更清晰地揭示了龙门山中生代薄皮构造和新生代厚皮构造格架 (Figure 2.14)。龙门山地区碳酸盐类物质拉曼光谱测试最显著的结果即在飞来峰底界测出 425℃以上的高温，表明飞来峰就位时底界断层处于一定深度的构造层次，为典型的印支期逆冲推覆加厚机制对应的产物，不支持上

述飞来峰新生代地表滑覆的观点；拉曼测温结果还显示，北川-映秀断裂作为一个深大断裂，其逆冲推覆活动使得 NW 界物质经历的温度明显高于 SE 界物质温度，形成两个截然不同的地质单元。地震反射剖面表明穿过龙门山地壳厚度发生显著增厚，从四川盆地 45 km 左右直接跳至松潘-甘孜 60 km 公里左右，地壳的增厚过程对应龙门山地区新生代广泛的厚皮构造，因而差异性快速隆升的元古代基底杂岩记录了比四川盆地更高的温度(Robert et al., 2010a, b)。事实上，前人对飞来峰底界断层泥内的自生伊利石 K/Ar 年龄定年，给出 171-180 Ma 的年龄，在时间上也不支持飞来峰新生代滑覆就位(Zheng et al., 2014)。

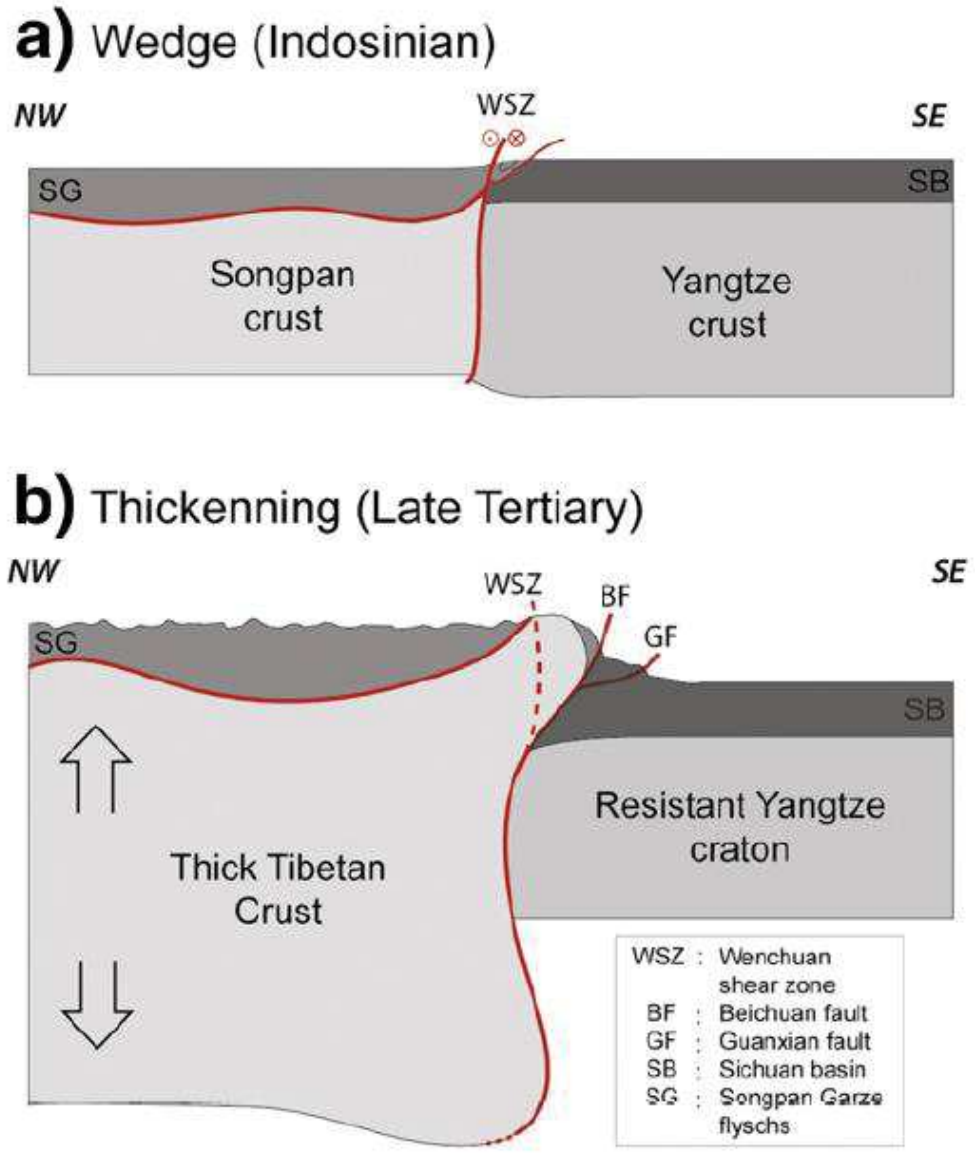

Figure 2.14 Schematic scenario envisaged for the Longmen Shan (Robert et al., 2010)

(a) During the early Indosinian event, the crust located west of the present Longmen Shan belonged to the margin of the Paleotethys and composed of a poorly known oceanic or thinned continental crust, and was adjacent to the continental crust of the Yangze block. A detachment

that separated the sedimentary units involved in a subduction wedge created sedimentary thickening and shortening; (b) Crustal thickening during the Neogene as a result from the India-Eurasia convergence overthrew material from the soft Tibetan crust and its upper part composed of the crystalline massifs onto the Yangtze block.

此外一些学者认为龙门山地区第四纪冰川作用对龙门山的构造框架起重要作用(韩同林等, 1994; 韩同林等, 1999; 周自隆, 2006; 周自隆和阮明德, 2006)。这些学者认为，以塘坝子地区为首的飞来峰，体现出典型的冰川漂砾的特征，提出飞来峰由“冰冻灰岩”组成，为第四纪龙门山及青藏高原地区广泛冰川活动产生。

2.4 Brief summary

龙门山位于松潘-甘孜褶皱带和扬子板块边缘，其构造属性和地球动力学演化，对理解古特提斯洋闭合乃至华南板块中生代地质历史演化至关重要；同时作为青藏高原的 NE 边缘，龙门山中生代构造样式对新生代构造的传承以及在此基础上理解新生代构造变形、地势隆升、地壳加厚等科学问题也非常关键。

龙门山地区作为扬子板块稳定大陆边缘，自 Rodinia 大陆拼合之后，早元古代-二叠纪持续伸展裂解，并在二叠纪伸展达到顶峰，持续的伸展过程使岩石圈地壳减薄的同时也沉积了巨厚的古生代沉积物。这些巨厚的沉积物如何通过构造运动抬升至地表，表现出构造样式和变质程度分带性，加上龙门山新生代强烈的地势隆升和构造叠加改造，给龙门山中生代构造解析提出了新的挑战。

早中生代作为龙门山地区重要构造背景转折期，从长期以来的伸展反转为挤压背景。龙门山地区并未记录蛇绿岩、岛弧岩浆岩等洋壳俯冲相关的物质证据，因此不同于传统定义的板块俯冲-碰撞造山。针对前人所提出的构造模式，可以确定的是，华南-华北碰撞及伴随的古特提斯洋闭合对龙门山的陆内变形起了至关重要的作用，而同期古太平洋的俯冲对龙门山的陆内变形可能也有远程效应。中生代以来从冈瓦纳大陆分离出来的小陆块渐次拼贴于劳亚大陆南缘，也在龙门山地区表现为多期构造样式叠加。在这些板缘、板内多期次活动背景下，成就了龙门山多期次造山的复合造山带格架，晚三叠世印支期造山作用明显，几乎奠定了龙门山地区的主要构造格架，以构建薄皮构造为主；新生代改造作用，造成印支期构造的活化以及松潘-甘孜地区地壳的广泛增厚；而在早中

生代和新生代的构造事件中，明显包含着晚中生代一期构造事件，这期事件也是争论最大的一期变形。

前人龙门山地区早中生代构造演化格架，前人的研究成果存在陆内俯冲消减变形、扬子被动陆缘的滑脱造山以及左行压扭走滑造山三种模型的争论，根本原因是龙门山逆冲推覆带的构造几何学框架还需要进一步厘定和解析，因此，对龙门山地区精细构造结构的把握、各期变形事件的叠加关系以及精细的深部地壳结构几何学特征对解析建立龙门山逆冲推覆带中生代的构造演化过程至关重要，本论文第一部分工作就是通过大量的野外观察和室内分析研究，通过中小尺度构造解析方法，对龙门山逆冲推覆带的构造格架有了更清晰的把握和认识；前人对龙门山晚中生代和新生代的动力学模式争议集中在地壳尺度楔形挤出、地壳的 duplex 模型、造山后地壳通道流垮塌模型以及 channel flow 模型等，这集中模型的提出都以龙门山沿线的元古代基底杂岩为研究对象展开，并进一步集中研究元古代基底杂岩 NW 缘向 NW 的正断作用，因此本论文第二部分工作以龙门山中段彭灌杂岩为研究对象，通过构造解析、磁化率各向异性、显微特征分析、重力模拟等多学科综合解析彭灌杂岩及沿线新元古代杂岩体的就位机制，进一步剖析龙门山逆冲推覆带晚中生代的构造演化过程。

3. Structural analysis of the Longmenshan thrust belt (LMTB)

龙门山逆冲推覆带区域上由三条倾向 NW 的逆冲断裂带组成(Figure 3.1)，晚三叠世以来持续向 SE 和 S 的逆冲推覆(许志琴等, 1992; Burchfiel et al., 1995, 2008; Jia et al., 2006)，以及新生代印度-欧亚板块碰撞产生的强烈抬升，使其成为青藏高原地势梯度最大的边缘之一(Clark and Royden, 2000; Kirby et al., 2002; Hubbard and Shaw, 2009)。龙门山逆冲推覆带主变形期主要表现为区域上非常一致的向 SE 的逆冲作用，并且从四川前陆盆地向龙门山腹陆表现出变形逐渐加强、变质逐渐加深的渐变特点(Chen et al., 1994a; Burchfiel et al., 1995; Chen and Wilson, 1996)。

这期主变形期主要表现为一系列向 SE 逆冲的褶皱及广泛的飞来峰带，及其一致倾向 NW 的褶皱轴面、劈理、面理以及 NW-SE 向矿物拉伸线理的几何学特征(Figure 3.2)。野外观察表明，无论在飞来峰、推覆体的下盘，还是飞来峰推覆体内部，均指示统一由 NW 向 SE 逆冲的运动学极性。关于龙门山逆冲推覆带这期主要的构造几何学、运动学表现样式，前人给出了多种解释模式。龙门山逆冲推覆带最早由罗志立(1984)提出 “C 型”俯冲模式，认为龙门山地区广泛的推覆逆冲构造是由于早期正断层反转形成的陆内俯冲导致，既不同于北美西部科迪勒拉型洋壳向陆壳俯冲，也不同于洋壳向洋壳俯冲的模式(罗志立, 1984)，属于陆内造山范畴。许志琴等(1992)通过对龙门山地区详细的构造填图，认为龙门山是在“双向”造山极性及“双向”变形构造体制下形成的薄皮逆冲楔构造，形成相应的前陆沉积盆地，这种大型的逆冲楔在白垩纪又经过挤出造成前陆盆地的活化加载作用(许志琴等, 2007; Xu et al., 2008)。

另一种观点认为特提斯闭合南北向挤压作用引起的松潘-甘孜与扬子板块差异性应变，在龙门山地区产生的挤压走滑作用是造成龙门山主变形期整体构造格架的真正原因，而区域上向 SE 的逆冲是左行走滑派生的一系列构造(Dirks et al., 1994; Worley et al., 1995; Chen et al., 1995; Burchfiel et al., 1995; Worley and Wilson, 1996; Arne et al., 1997)。Callassou et al. (1994)立足松潘-甘孜褶皱带底部大型滑脱带向 S 的剪切变形特征，提出松潘-甘孜褶皱带变形对龙门山逆冲推覆带的作用。

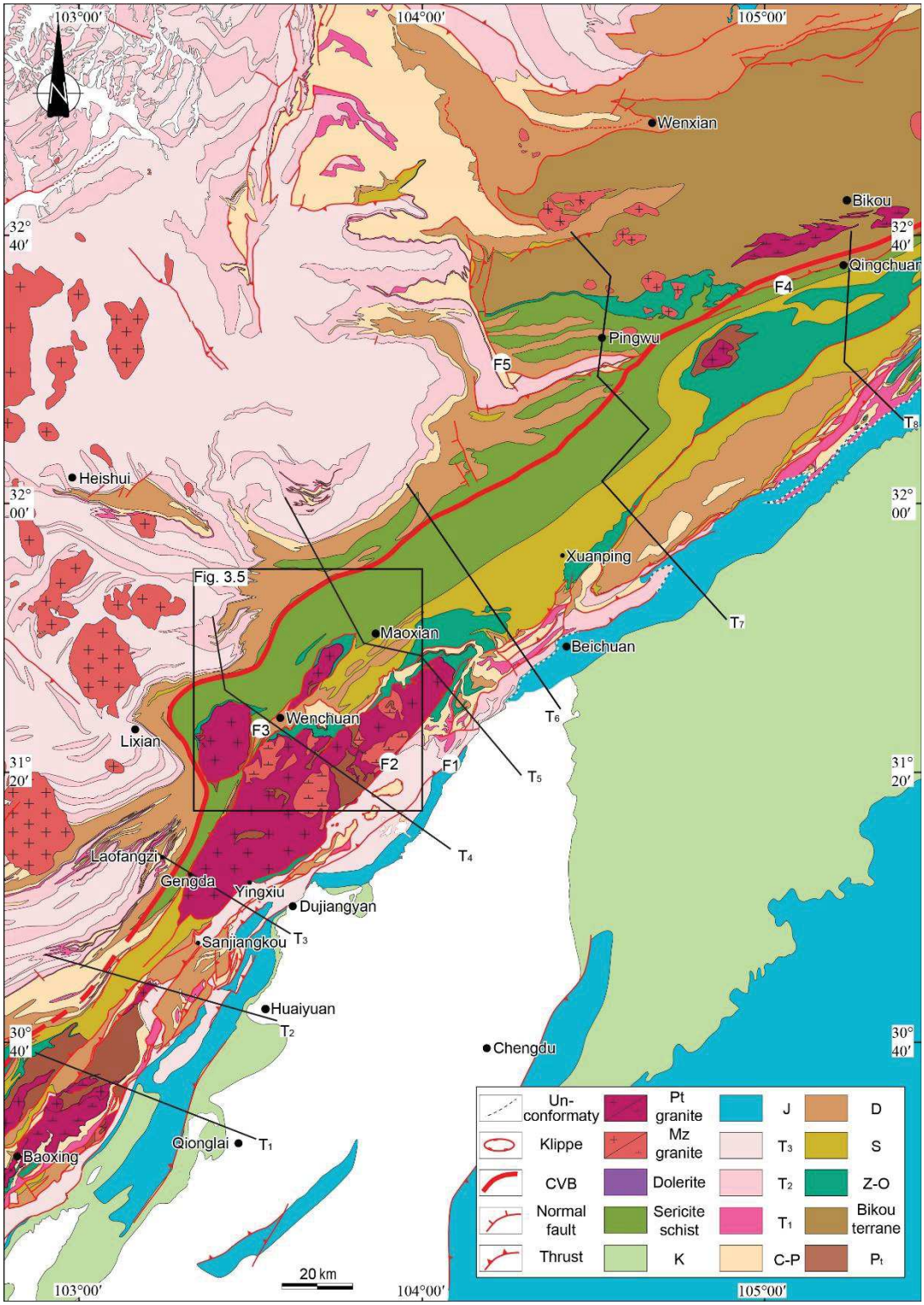

Figure 3.1 Geological map of the Longmenshan thrust belt (Modified from BGMRSP, 1991)

F_1: Anxian-Guanxian fault; F_2: Yingxiu-Beichuan fault; F_3: Wenchuan-Maoxian fault; F_4: Qingchuan fault; F_5: Huya fault

一些学者认为汶川-茂汶韧性剪切带高绿片岩相变质岩、碧口地块变质岩以及沿龙门山逆冲推覆带分布的变质岩带是古特提斯洋闭合后产生的造山后垮塌形成的通道流物质，这些变质岩带的出露产生了区域上一系列向 SE 的剪切变

形(Zhou et al., 2006; Yan et al., 2008b; Zhou et al., 2008; 刘鹤等, 2008; Yan et al., 2009; Yan et al., 2011)。

龙门山山前盆地研究结果表明，区域上重力均衡过程产生的地壳回弹对龙门山逆冲推覆带向 SE 的逆冲起着重要的作用(Li et al., 2003; 李勇等, 2005; Li et al., 2013; Li et al., 2014)。地震剖面解释结果进一步表明，受新生代印度-欧亚板块碰撞的影响，龙门山纵向上变形存在很大差异，北段以向 SE 逆冲的薄皮构造为主，南段以基底卷入变形的厚皮构造为主(贾东等, 2003; Jia et al., 2006; Jia et al., 2010)。鉴于以上争论，对龙门山逆冲推覆带的构造单元划分，构造几何学特征及运动学特征需要进行详细的重新厘定，以明确龙门山逆冲推覆带的构造属性及演化历史。本章选取垂直龙门山逆冲推覆带 8 条 NW-SE 走向的典型构造地质剖面图，详细解析龙门山逆冲推覆带这期主要变形期的构造岩石单元、构造几何学特征和运动学特征。

3.1 The main tectonic boundaries of the LMTB

地震反射剖面表明龙门山三条主干断裂带呈犁形向 NW 收敛于 15-20km 深的拆离带(Li et al., 2010; Guo et al., 2013; Feng et al., 2015)。从 NW 向 SE，三条断裂带表现出从韧性向脆性变化，可能对应造山带向盆地方向扩展趋势(陈社发等, 1994a; 金文正等, 2007)。

1) Anxian-Guanxian fault (F_1)

安县-灌县断裂 SW 起自都江堰市，向 NE 延伸至安县(今新北川县城)，再向 NE 变为一系列地表分支状产出的逆冲断裂，延至马角坝断裂(Figure 3.1)，是龙门山三条主干断裂的前锋断裂。地震反射剖面和汶川科学钻探揭示安县-灌县断裂带断层面倾向 NW，浅部倾角较陡，向地下深处逐渐变缓，为一铲型逆冲断裂。安县-灌县断裂整体表现为一条脆性断裂，钻孔岩心中断裂岩主要包括断层角砾岩、碎裂岩、断层泥，未见假玄武玻璃，主要在前期断裂上活化改造(郭瑞强, 2011; Li et al., 2012, 2015; 杨光, 2012; 杨光等, 2012)。Chen et al. (1996)在对龙门山地区详细构造解析基础上，指出安县-灌县断裂呈 NE-SW 展布于三叠纪须家河组地层之内或者界于上三叠统于下侏罗统地层之间，根据地层切割关系，认为该断裂为龙门山三条主干断裂最末期形成的断裂，并且在晚三叠世

区域上挤压变形形成后，经历后期强烈改造作用。在龙门山逆冲推覆向四川盆地传递过程中，该断裂作为边界断层，以晚三叠世须家河为主的上盘向 SE 逆冲至侏罗纪地层之上，兼具右行走滑分量(Li et al., 2013)，分隔龙门山逆冲推覆带与稳定的四川盆地，其逆冲活动导致山前地势隆升。在安县-灌县断裂下盘，前陆盆地盖层内上下两层滑脱面发育双重逆冲构造，很大程度上吸收了龙门山逆冲推覆带向 SE 的逆冲推覆作用(Lu et al., 2012, 2014, 2016)。

2) Beichuan-Yingxiu fault (F_2)

映秀-北川断裂经由 SW 的映秀镇，向 NE 至老北川县城，向 SE 延伸至宝兴杂岩西边的五龙断裂，断层走向 N30-55°E，以 50-80°角度倾向西北(Figure 3.2)，与安县-灌县断裂一样，均表现为上陡下缓的铲状几何学形态(Li et al., 2010; Wang et al., 2014; Li et al., 2015)。北川-映秀断裂地表由数条次级断裂共同组成叠瓦状构造样式，向 SE 逆冲的运动学特征野外表现为强烈变质的寒武系-志留系地层逆冲在未变质的泥盆-二叠系地层之上。断裂带内变形样式以脆性、脆韧性过渡为主，断层上盘透镜体同样指示断裂向 SE 逆冲的运动学特征。北川-映秀断裂沿彭灌杂岩的 SE 边界展布，是造成龙门山地势隆升最重要的断裂，多期次向 SE 的逆冲推覆作用，导致四川西部前陆盆地的加载和沉积作用(Chen et al., 1994a, 1995; Chen and Wilson, 1996; Li et al., 2013)。作为龙门山逆冲推覆带内重要的地质单元边界，映秀-北川断裂下盘的四川前陆盆地物质均未发生变质作用，而断层上盘元古代杂岩和古生代地层都经历了低绿片岩相变质作用，断层两侧的温压条件计算，表明映秀-北川断裂至少造成两侧物质 15 km 的差异性隆升(Robert et al., 2010; Airaghi et al., 2017)，断裂两侧的磷灰石裂变径迹结果也表明断裂两侧物质差异性隆升现象显著(Wang et al., 2012; Cook et al., 2013; Tian et al., 2013)。位于龙门山最南段宝兴县城附近的五龙断裂，低温年代学证据也表明其可能是北川映秀断裂向 SW 的延伸部分，本论文中统一命名为北川-映秀断裂(Figure 3.1 F_2; Richardson et al., 2008; Godard et al., 2009, 2010; Wang et al., 2012; Cook et al., 2013; Tian et al., 2013)。前人研究认为，沿龙门山山前分布的一系列推覆体和飞来峰均来自映秀北川断裂上盘彭灌杂岩的盖层物质，因而把映秀-北川断裂带一直延伸至飞来峰底界断层，整体呈波状起伏的特征(陈社发等, 1994a; b; Chen and Wilson, 1996)。

汶川 1 号钻和详细的野外填图工作表明汶川断裂带发育脆性断裂一套岩石组合，包括断层角砾、断层泥、碎裂岩带等，这些脆性的岩石组合在地表呈带状分布，指示 2008 年汶川地震的主滑移带并非在古老的北川-映秀断裂上发育，而是新产生的与古断面呈一定交角的震裂面(Li et al., 2010, 2012; Wang et al., 2014)，后期反复的脆性破裂和逆冲，造就了龙门山地势的抬升。

3) Wenchuan-Maoxian fault (F_3)

汶川-茂汶断裂带为龙门山腹陆最重要的一条边界断层，分隔松潘-甘孜褶皱带与龙门山逆冲推覆带，是龙门山地区韧性变形级别最高的主断裂，整体走向 25-45°，断面倾向 NW，具有向 SE 逆冲的运动学，地理位置上 SW 端穿过汶川县城，向 NE 端穿过茂县，但实际考察过程中发现，汶川-茂汶断裂带可能向 NE 延伸，稳定分布于志留纪绢云母片岩中。绢云母片岩发育均一的倾向 NW 的面理，而汶川-茂汶断裂可能在这套变质变形的志留系片岩中连续存在(Figure 3.1)。汶川-茂汶断裂带在龙门山中段表现样式非常复杂，在彭灌杂岩西界，耿达乡附近，以汶川茂汶断裂为界，雪隆包岩体和志留系变质岩整体逆冲至元古代彭灌杂岩之上；元古代牟托岩体逆冲于震旦系地层之上，整体又经过汶川-茂汶断裂逆冲至志留系片岩之上(Figure 3.1)。Dirks et al. (1994)将汶川-茂汶断裂定义为晚三叠世的韧性剪切带，由到达岩石圈地幔尺度的深大断裂将深部的变质变形物质抬升至地表，伴随明显的左行走滑；现今所识别出来的汶川-茂汶断裂是在韧性剪切带基础上叠加的脆性破裂。Arny et al. (1997)对剪切带内的变质云母氩氩定年，提出汶川-茂汶断裂在 120 Ma 发生差异性隆升，分隔 NW 部较高级的变质岩和 SE 部浅变质岩石。后期叠加的脆性断裂活动，使断裂带附近岩石强烈破碎、角砾岩化，局部地区可见断层泥。脆性断层擦痕与韧性剪切带的线理方向具有一致性，结合野外剪切指向，均反映断裂向 SE 逆冲的性质，伴随右行走滑剪切分量(Chen and Wilson, 1996; Xu et al., 2009; Fu et al., 2011)。

汶川-茂汶断裂带以东，紧邻该断裂带发育断面倾向 NW 的正断裂，仅围绕彭灌杂岩分布，向 NE 和向 SW 与北川-映秀断裂相交，称为“青藏高原东缘大型拆离带”，该拆离带的活动使浅变质的志留系茂县群直接盖在元古代基底之上，中间发生强烈的地层减薄缺失(Dirks et al., 1994; Burchfiel et al., 1995; 许志琴等, 2007; Xu et al., 2008; Burchfiel et al., 2008; Wang et al., 2012; Tian et al.,

2016)。藏东拆离带的发现，与北川-映秀断裂向 SE 耦合的逆冲活动，被解释成 channel flow 导致地势隆升在地表的响应(Burchfiel et al., 1995, 2008; Wang et al., 2012)、地壳挤出效应(许志琴等, 2007; Xu et al., 2008)或地壳尺度的双重逆冲构造(Tian et al., 2016)。

4) Qingchuan fault (F_4)

青川断裂东起自阳平关，向西经过青川，平武南部，及至虎牙断裂(Figure 3.1)。青川断裂曾被认为是汶川-茂汶断裂向 NE 的延伸部分，具有相似的运动学特征(王二七等, 2001)。地震反射剖面表明，青川断裂呈正花状构造，由深入地壳尺度分别向 SE 逆冲推覆和向 NW 的逆冲推覆体组合而成，兼具左行走滑特征，根据前陆盆地的演化特征，将青川断裂的左行压扭性走滑限定在中生代(Jia et al., 2006)。晚中生代青川断裂的左行走滑，被解释为碧口地块向西挤出时产生的边界断层(Burchfiel et al., 1995; Meng et al., 2005)或四川盆地发生顺时针旋转产生的边界效应(Wang et al., 2014)。然而新生代以来，横穿青川断裂的河流均发生显著的错段以及断裂带内脆性剪切的砾石，指示青川断裂明显的右行走滑特征(樊春等, 2008; Lin et al., 2014)。李勇等(2006)根据走滑断裂内断陷盆地内沉积特征、几何形态，将青川断裂右行走滑时间限定在 43-3.6 Ma 之间(李勇等, 2006)。

3.2 General zonation and structural geometry

龙门山逆冲推覆带及周边地区，以详实的野外构造观察为基础，以龙门山三条主干断裂和劈理直立带为边界，将龙门山逆冲推覆带分为五个构造岩石单元：原地系统，相对原地系统，相对外来系统，外来系统和西部带(Figure 3.2)。

沿龙门山逆冲推覆带稳定分布的劈理直立带将西部带与东部的四个单元分隔开。野外构造几何学形态详细剖析表明，劈理直立带两侧几何学形态对称。在劈理直立带东部，四个单元所有的面理均倾向 NW，与此相反的是，在劈理直立带西部的西部带，所有的面理均倾向 SE(Figure 3.2)。而面理面上所有的矿物拉伸线理的延伸方向在区域上具有一致性，均表现为 NW-SE 向或 N-S 向(Figure 3.2)。劈理直立带以东，无论宏观的倒转褶皱，剪切布丁还是微观的 σ

碎斑、云母鱼等，都指示上部向 SE 的剪切变形；反之在西部带，所有的剪切指向均指示上部向 NW 或 N 的剪切指向(Figure 3.2)。根据地层时代，龙门山边界断层的限定，地层变形样式及变质变形层次，进一步将东部带分为原地系统，相对原地系统，相对外来系统和外来系统(Figure 3.2)。

1) Autochthon

原地系统位于四川盆地西部安县-灌县断裂以东(Figure 3.2)，主要为一套侏罗纪-白垩纪地层，未见任何劈理构造，岩层产状较平缓，地层产状微向 SE 倾，向四川盆地内部延伸。侏罗纪地层区域上不整合盖在褶皱变形的上三叠统须家河组地层之上(Figure 3.1)。在龙门山北段，侏罗系地层本身也发生了褶皱作用并向 SE 倒转，作为主变形期后另一期事件叠加的证据。从变形层次来讲，原地系统的侏罗-白垩纪地层变形很浅，主要为浅表的脆-塑形变形，明显不同于主变形期(卷入变形的早侏罗世之前的地层)地层的变形和表现样式。

2) Para-autochthon

相对原地系统位于龙门山飞来峰群及推覆体之下，界于安县-灌县断裂与北川-映秀断裂之间(Figure 3.2)，主要为一套上三叠统须家河组地层，褶皱变形非常强烈，广泛发育构造透镜体，并在泥质岩夹层中发育劈理，层滑作用显著。在相对原地系统内部，向 NW 越靠近飞来峰及推覆体前锋带，表现出变形逐渐增强的特征，而在推覆体及飞来峰后缘构造窗位置，则记录了更强的褶皱变形和相对发育的劈理，反映飞来峰及推覆体在就位过程中对下伏地层拖拽推覆应力传播过程，并且轴面劈理大多倾向 NW(Figure 3.2)。

3) Allochthon

相对外来系统主要为一套志留系至二叠系古生代沉积及少量下三叠统灰岩地层(Figure 3.2)。其主体部分位于映秀-北川断裂与汶川-茂汶断裂之间，还包括龙门山山前广泛的推覆体和飞来峰。由于岩性差异，相对外来系统各个时代地层变形特征不尽相同。整体上都表现出强烈的褶皱变形和相对密集发育的劈理，而且志留系地层为一套泥质片岩、千枚岩，反映更深的变形层次。在飞来峰根带，常常可见较陡层理上密集发育的较缓的劈理，指示地层向 SE 倒转。

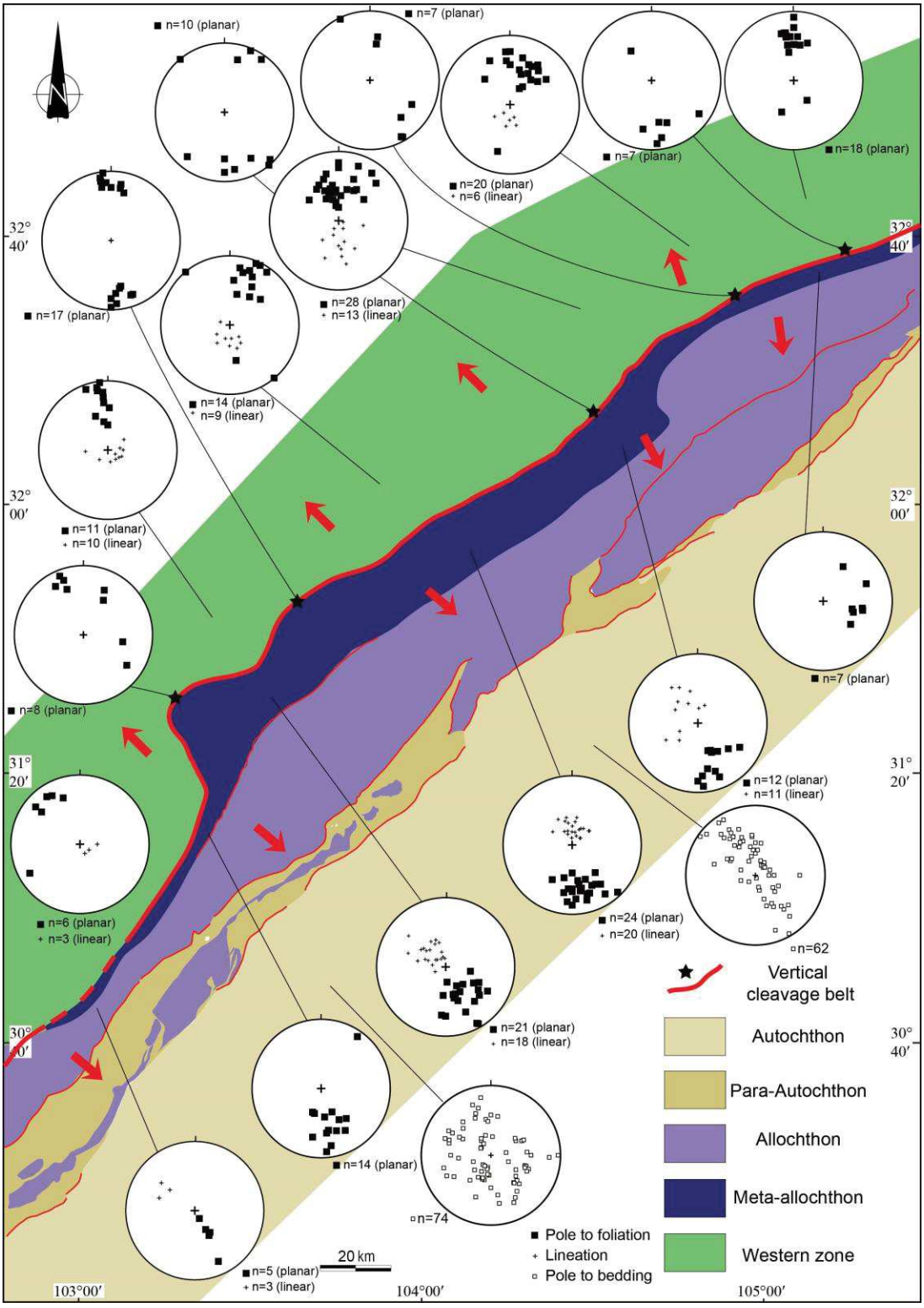

Figure 3.2 General zonation map of the LMTB (Lowerhemisphere projection)

4) Meta-allochthon

外来系统主要为一套志留系变质的绢云母片岩，分布于汶川-茂汶断裂带与劈理直立带之间(Figure 3.2)。整套系统是龙门山逆冲推覆带变质程度最高的构

造单元，整体上为绿片岩相变质，局部可达到低角闪岩相变质作用。其变形作用最强，原始层理不可见，能观察到石榴石、黄铁矿、云母甚至角闪石等变质矿物。外来系统内，沿 NW 倾的面理上发育的 NW-SE 向的矿物拉伸线理，奠定了龙门山逆冲推覆带区域上的几何学特征(Figure 3.2)。

5) Vertical cleavage belt (VCB)

劈理直立带西南起自宝兴县，向东北经过老房子，大致沿着志留系与泥盆系地质界线，绕过雪隆包杂岩西部，再与青川-阳平关断裂重合(Figure 3.1)。整条劈理直立带为一套志留系千枚岩或片岩，在整个龙门山逆冲推覆带稳定分布，劈理直立发育(Figure 3.2)不仅作为几何学界线分隔面理倾向 NW 的单元与面理倾向 SE 的单元，还从运动学上将上部向 SE 剪切的东部带与上部向 N 或 NW 的剪切的西部带分开。从各个单元变质变形程度来看，劈理直立带同时作为一个重要的地质界线，分隔变质变形层次浅的西部带与较深层次变质变形的外来系统单元(Figure 3.2)。劈理直立带在野外的表现以竖直的面理为主，在松溪、薛城等地表现尤为明显(剖面中会详细论述)。直立面理带夹有轴面近直立的无根褶皱以及平行面理的石英及方解石条带。整个劈理直立带未见与走滑相关的水平线理或擦痕构造，事实上整个劈理直立带由于变形层次较浅，并未发现任何明显的矿物定向或拉伸线理。在局部地区观察到面理上枢纽近竖直的细褶纹，可能有微弱的水平位移，但并不是龙门山逆冲推覆带的主要表现形式。

6) Western zone

位于龙门山劈理直立带西部的西部带主要由松潘-甘孜褶皱带和碧口地块组成。南部松潘-甘孜单元为一套强烈褶皱变形变质的晚三叠世浊积岩；在北段青川-碧口附近，西部带主要由元古代火山岩及志留系-泥盆系泥质片岩、云母片岩组成。位于松潘-甘孜褶皱带东部的西部带强烈褶皱变形，轴面劈理倾向 SE，碧口地区云母片岩及石英片岩均表现出倾向 SE 或 S 的面理，与东部带的四个单元呈相对形态。西部带与东部带的线理方向大致一致，为 NW-SE 向或 N-S 向(Figure 3.2)。

3.3 Kinematics analysis

根据野外岩石变质变形级别确定各个构造单元后和构造几何学后，根据可靠的运动学指向判断运动学对理解区域上的构造演化历史至关重要。

1) Traditional method

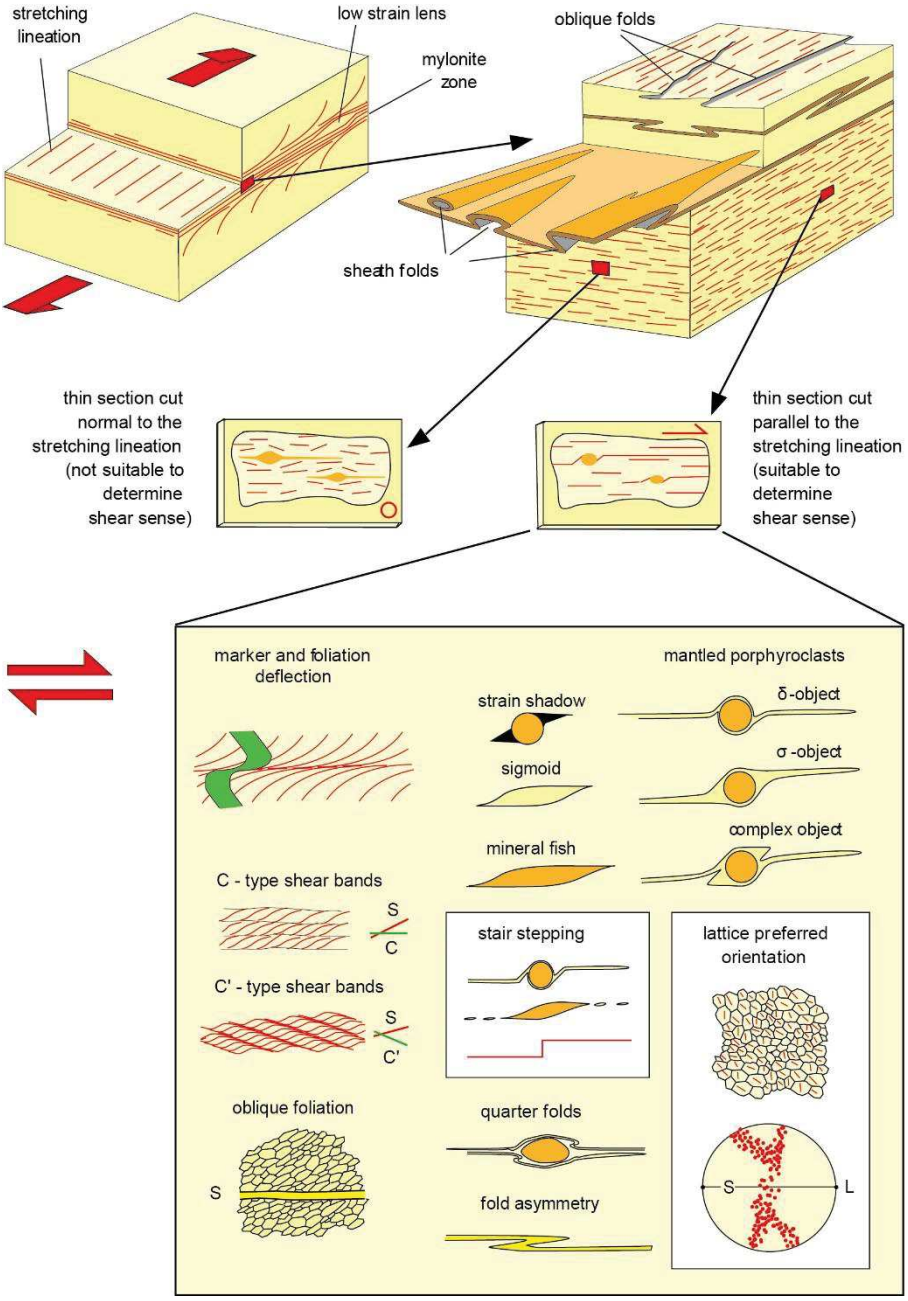

Figure 3.3 Shearing indicators in ductile shear zone

Top: Schematic diagram showing the geometry of a mylonite zone and the nomenclature used.

Bottom: The most common types of shear sense indicators (Passchier and Trouw 2005)

传统判断运动学剪切指向方法主要通过野外在垂直面理并平行线理的面(XZ 面)上观察一系列剪切标志，包括标志层和面理弯曲、S/C 组构、剪切条带、不对称压力影和旋转残斑等。室内观察垂直面理平行线理的定向薄片，通过微观的云母鱼、剪切条带等标志也能给出确定的剪切指向(Figure 3.3)。对颗粒大小比较均匀的石英含量很高的片岩，常可以通过测定石英光轴优选方位来确定剪切指向(Figure 3.3)。在确定区域上整体运动剪切方向后，局部变质变形较钱层次的倒转褶皱也能作为判断剪切指向的辅助证据(Figure 3.3)。

在龙门山逆冲推覆带，劈理直立带以东，无论是变质变形层次较高的外来系统内发育的不对称布丁、剪切压力影，还是相对原地系统倒转褶皱、层滑等标志都指示均一的上部向 SE 的剪切变形；反之，在陆内薄弱带以西的西部单元，所有的剪切指向，包括大型倒转褶皱、旋转残斑、云母鱼等剪切指向均指示统一上部向 NW 或向 N 的剪切变形。整体而言，劈理直立带不仅作为构造几何学界线分隔东部带和西部带，同样作为构造运动学分界，将上部向 SE 剪切的东部带与上部向 NW 或 N 剪切的西部带分开。

2) Electron Backscatter Diffraction analysis (EBSD)

Introduction

电子背散射衍射技术(Electron Backscatter Diffraction)实质是利用不同矿物、金属晶体结构和方位的背散射衍射图像来定性定量研究金属及矿物显微构造的技术。在地质学上的运用，主要是对任何对称系的晶体展开矿物晶格优选方位的研究，甚至可以研究光学显微镜无法研究的等轴晶系矿物和不透明矿物(Prior et al., 2015)。EBSD 测试原理是根据扫描电镜利用入射电子撞击在样品上，电子非弹性散射性使其能穿透样品表面与多层晶面平行碰撞，从不同晶面反射的电子束满足布拉格衍射条件后发生干涉衍射，形成菊池条带(Figure 3.4 a)。菊池条带的形状和几何属性在和已知数据库匹配时，就能得到矿物的空间方位，多点样品测试，最终得到统计学上矿物空间及晶格的几何学信息。EBSD 测出的矿物统计学上的几何学信息，可以给出矿物光轴的极密方向及滑移系，在定向薄片(XZ 面)测试时，根据光轴信息可以给出样品的剪切方向，以及变形过程中的温度条件。

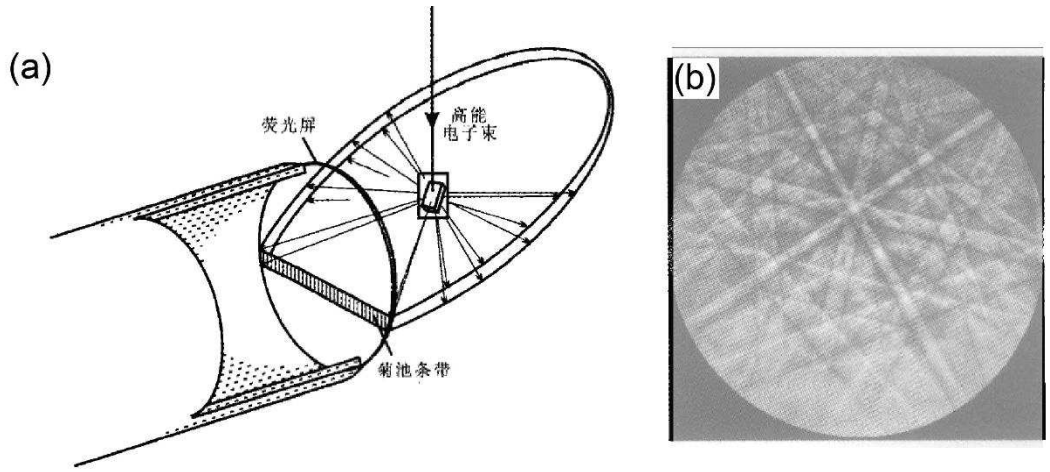

Figure 3.4 Schematic showing the theory of the EBSD

(a)电子束发出击打在矿物镜面，发生电子束反射被荧光屏接收；(b)荧光屏接收反射的菊池条带，该菊池条带特征反映矿物的种类及空间形态。

3.3.2.2 结果

为了更细致地研究龙门山逆冲推覆带的运动学特征和可能的剪切变形温度条件，我们在龙门山东部带和西部带总共选取 10 个样品(包括云母片岩、石英片岩和花岗质糜棱岩)在中国地质大学(北京)微区形貌、成分分析实验室进行了 EBSD 测试(Figure 3.5)。所有测试样品均选择垂直面理平行线理的切面，即最大剪切面作为测试面。

结果显示，陆内薄弱带东部带的样品，尽管表现出多点极密继承组构，除了 CX16 和 CX18 石英 C 轴给出上部向 NW 的剪切方向，其它样品的(CX11、CX10、CX8、CX6、CX33、CX109)石英 C 轴最大极密均给出一致的上部向 SE 的剪切指向(Figure 3.6)。CX16 和 CX18 位于彭灌杂岩西北缘，所给出的上部向 NW 的剪切指向将在第 4 章中详细论述。陆内薄弱带以西的样品，CX12 给出上部向 NW 的剪切变形，与野外观察和室内分析一致。

从石英 C 轴极密分布样式可以看出，CX6、CX8、CX11、CX33、CX109 表现出样品在变形过程中经历了相似的石英 C 轴中-低温滑移过程，而 CX12、CX18 则记录低温剪切滑移过程，CX109 也有类似低温滑移组构的记录。所有测试样品中，CX16 记录了最高剪切温度组构特征。

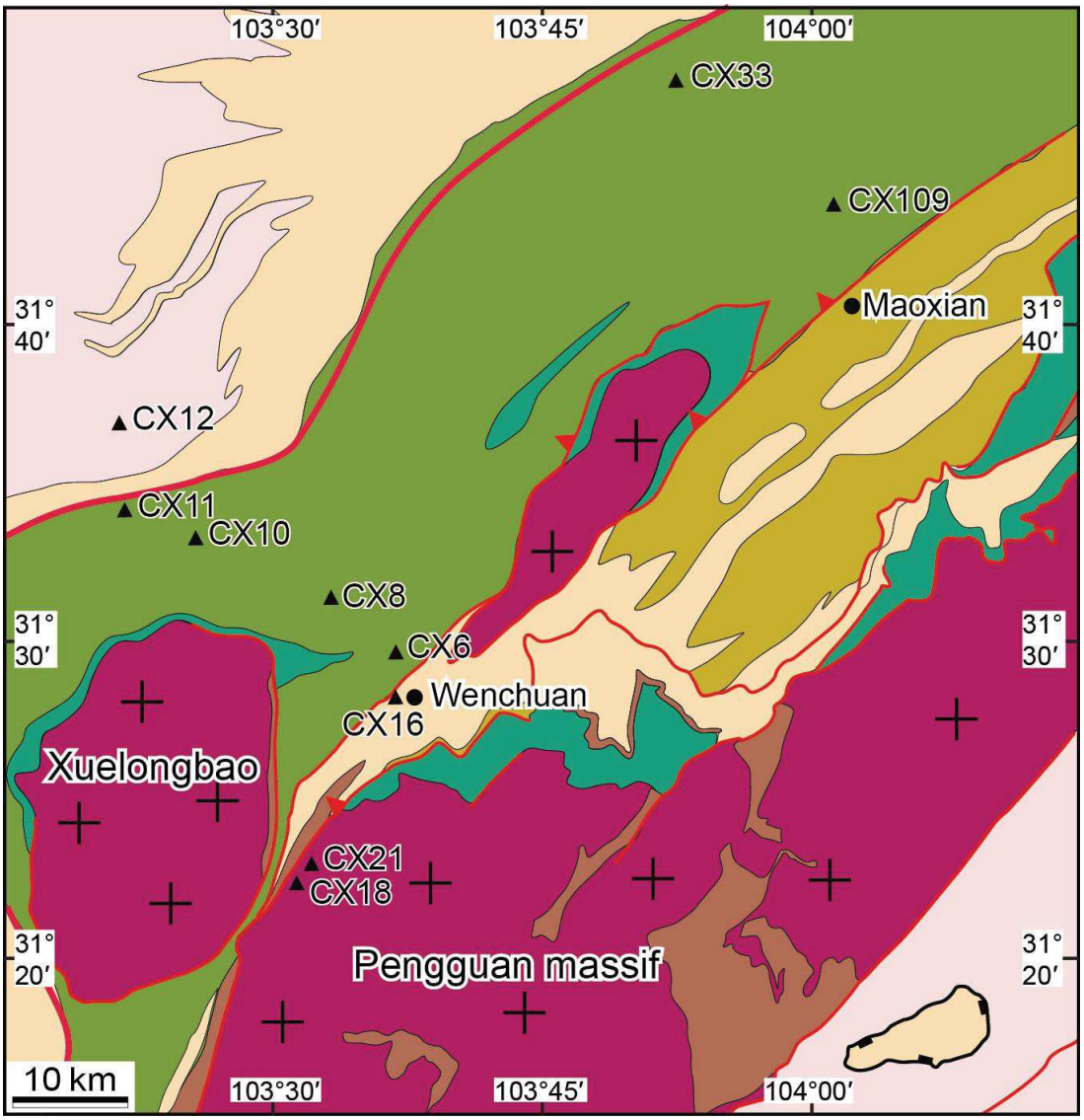

Figure 3.5 Location of the samples for EBSD test. Symbols and acronyms are the same as in Figure. 3.1.

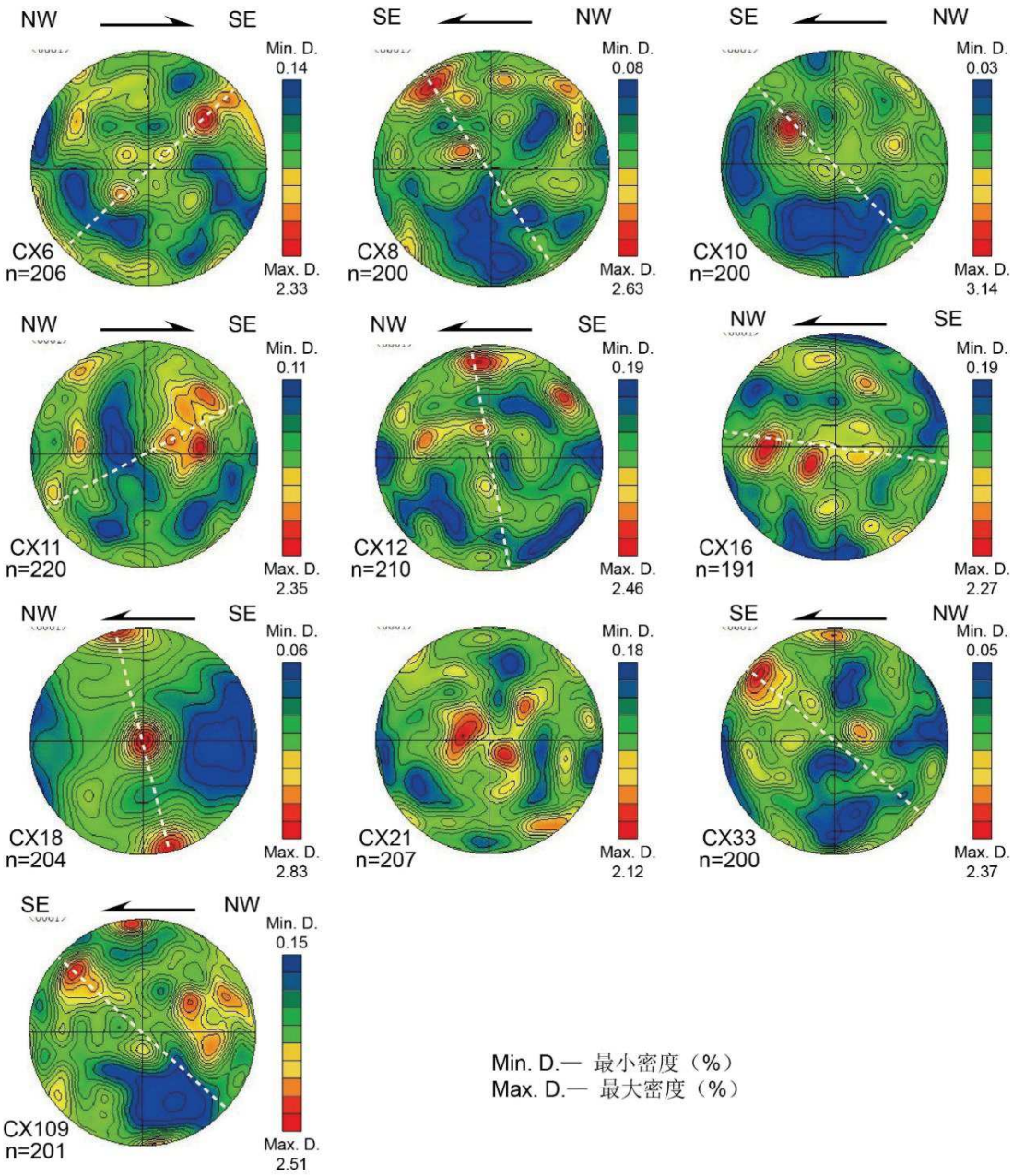

Figure 3.6 Quartz <c> axis distribution from EBSD testing

3.4 Detailed cross-section analysis

以上所划分的五个构造单元以及龙门山陆内薄弱带在龙门山整个造山带有非常一致的表现，劈理直立带，作为其中的构造界线也沿龙门山逆冲推覆带稳定分布。强应变带两侧相对的构造几何学特征和相背的运动学特征，在垂直龙门山逆冲推覆带 8 条 NW-SE 走向的剖面上都有非常详细和一致地记录(Figure 3.1)。

1) Qionglai-Baoxing corss section

邛崃-宝兴剖面位于研究区最南缘邛崃市以西，穿过龙门山逆冲推覆带东部带的原地系统、相对原地系统和相对外来系统(Figure 3.1 和 3.8)。原地系统为一套侏罗纪-新生代地层，侏罗纪地层地层平缓产出，原始层理清晰可见，未发育任何劈理构造(Figure 3.8 a)；白垩纪泥质岩整合盖在侏罗纪地层之上，与侏罗纪地层一起延伸至四川盆地内。侏罗纪-白垩纪-新生代地层局部地区形成宽缓褶皱，轴面近直立，无极性(Figure 3.7)。

相对原地系统主要为一套褶皱变形的晚三叠世-白垩纪地层(Figure 3.1 和 3.8)，产状近直立的白垩纪地层表明发生了强烈的褶皱变形，局部地区发育褶劈理(Figure 3.8 b)。根据野外测量层理产状表明，褶皱具有较陡的东南翼和较缓的西北翼(Figure 3.2)，给出向 SE 歪斜的褶皱极性。三叠-白垩地层之上还分布着由元古代-早三叠世地层组成的飞来峰。该单元中少量出露着元古代杂岩体-宝兴杂岩，被晚三叠世须家河组不整合覆盖(Figure 3.1)。该单元的宝兴杂岩主要为块状闪长岩，无面理化，极其破碎，反映后期强烈的脆性叠加，但与这期韧性主变形期并无太大关系，表明该系统内的彭灌杂岩属于准原地系统，处于浅表的构造层次。该单元整体表现出的变形程度高于原地系统，二者被安县-灌县断裂分隔(Figure 3.1)。

相对外来系统包括位于映秀-北川断裂 NW 的推覆体和叠置在相对原地系统之上的飞来峰(Figure 3.7)。该剖面上，飞来峰主要由元古代黄水河群-早三叠世地层组成。黄水河群变砂岩发生强烈的剪切变形并劈理化，原始层理已不可辨(Figure 3.8 c)。位于宝兴南边的灵关飞来峰由志留系-泥盆系岩石组成，飞来峰内部广泛的层滑作用、劈理产状都指示上部向 SE 的剪切变形。位于映秀-北川断裂 NW 的推覆体主要由元古代黄水河群和部分宝兴杂岩组成(Figure 3.1)。黄水河群强烈剪切变形为一套千枚岩、泥质片岩和石英片岩。层间滑动以及低温糜棱岩化非常明显，倾向 NW 的面理上清晰发育着 NW-SE 走向的线理(Figure 3.8 d)。沿平行线理垂直面理切面的定向薄片镜下观察，长石 σ 旋转残、长石书斜构造及其周边围绕的云母形迹均给出上部向 SE 的剪切变形(Figure 3.8 e-f)。该单元的宝兴杂岩发生明显的面理化，表明经历显著韧性变形，与相对原地系统的脆性破碎的宝兴杂岩不同。在相对外来系统内，无论是推覆体还是飞来峰，野外岩相学特征都表现出相对外来系统变形层次明显高于相对原地系统。

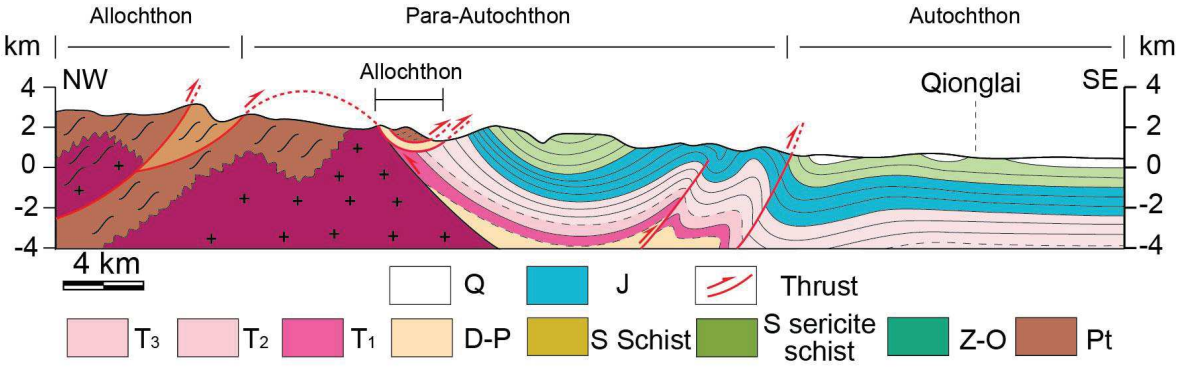

Figure 3.7 Qionglai-Baoxing cross section (Location is marked in Figure 3.1, T1)

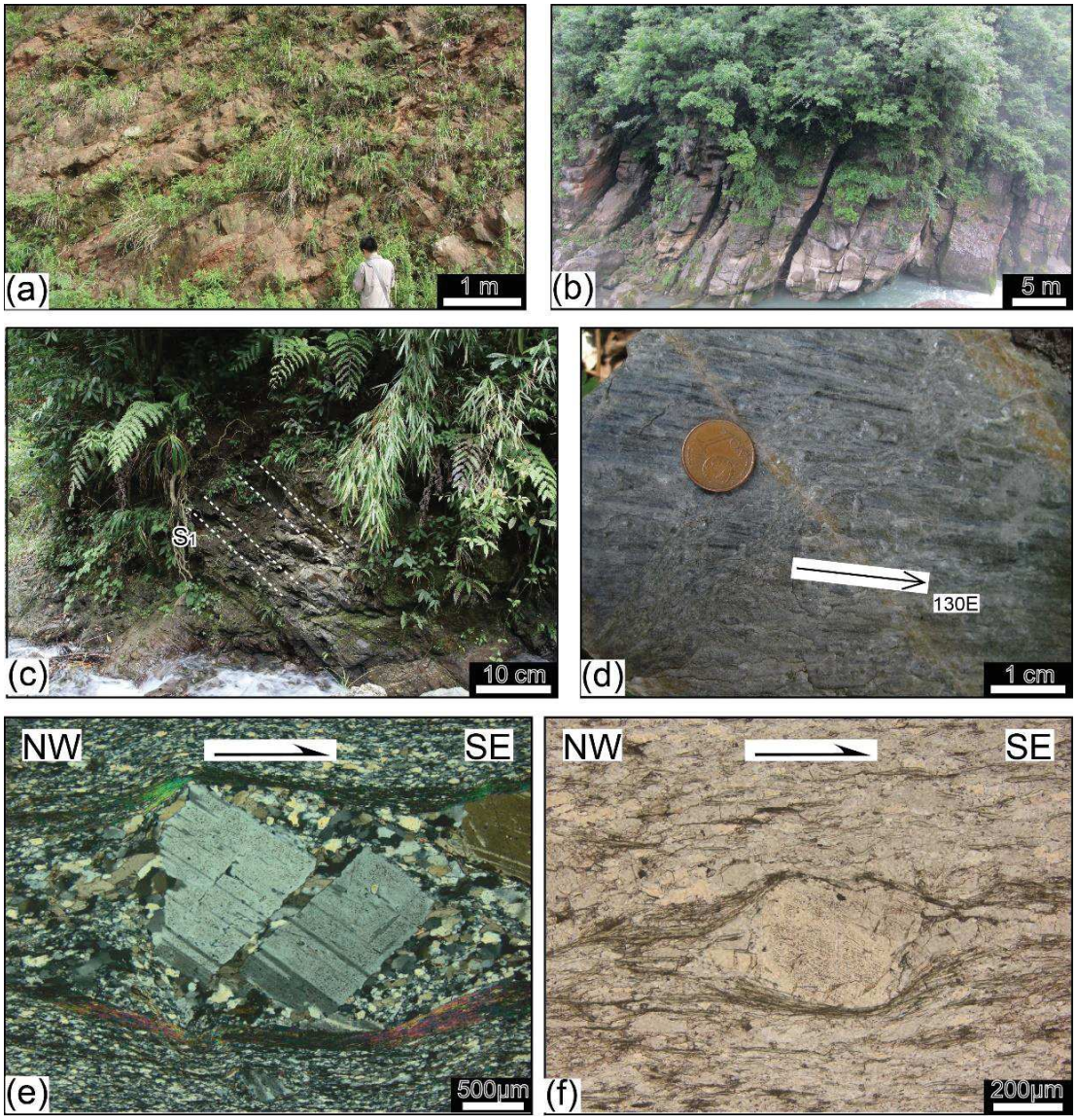

Figure 3.8 Petrological characteris and shearing indicators along the Qionglai-Baoxing cross section

(a) Autochthon, undeformed Jurassic rocks; (b)Para-autochthon, Cretaceous strata steep dip to SE indicating intensive folding; (c) Allochthon, klippe consist of Neoproterozoic rocks that is strongly foliated; (d) Ductile deformation within the allochthon presenting obvious foliation and lineation; (e-f) Allochthon, microscopic plagiolcase dominoand σ-type porphyroblast indicate top-to-the-SE shearing.

2) Huaiyuan-sanjiang cross section

怀远三江剖面东南起自怀远镇，向西北延伸至松潘-甘孜褶皱带内(Figure 3.1 T_2)。怀远剖面的原地系统、相对原地系统和相对外来系统都比较确定。该剖面整体变形层次较低，不发育外来系统。对于西部带，由于地势险峻并不能实地野外观察，只能根据区域地质图和图上的信息和我们的理解，给出剖面西部带的构造几何学信息，因而对该剖面劈理直立带仅以虚线表示(Figure 3.1)。

怀远镇西部侏罗-白垩纪一套宽缓褶皱构成原地系统，褶皱轴面近直立，不具有运动学指向意义。侏罗纪地层交错层理清晰可见，指示了正常的地层层序，倾向 SE，与白垩纪地层协调变形延伸至四川盆地内(Figure 3.1 和 3.11 a)。下侏罗统-白垩系地层同时以角度不整合盖在强烈褶皱变形的晚三叠世须家河组地层之上(Figure 3.9)。局部地区上三叠统须家河组地层又经过安县-灌县断裂逆冲至侏罗-白垩纪地层之上，反映了龙门山地区多期变形特征(Figure 3.9)。

安县-灌县断裂带以西的相对原地系统主要为一套强烈褶皱变形的晚三叠世须家河组地层和局部地区出露的元古代闪长质杂岩体(四川省地质矿产局, 1991)。无论是褶皱的倒转极性，还是剪切 σ 砂岩透镜体(Figure 3.10 b)，都指示上部向 SE 的剪切变形。位于飞来峰后缘构造窗，仍属于相对原地系统范畴，变形更加强烈。密集发育的倾向 NW 的劈理(Figure 3.11 a)、泥岩层夹砂质层中的剪切构造和 σ 砂质透镜体(Figure 3.11 b)、向 SE 倒转的褶皱(Figure 3.11 c)也同样指示上部向 SE 的剪切变形。而且，越向 NW 靠近推覆带根带，变形程度更加剧烈，反映飞来峰和推覆体在就位过程中对下伏系统-相对原地系统的拖拽作用(Figure 3.11)。

局部地区须家河组砂岩以不整合盖在元古代闪长质杂岩体上，表明这套元古代杂岩在早中生代时期作为古陆出露并接受须家河组地层沉积覆盖(Figure 3.1)，这与邛崃剖面相对原地系统内的元古代杂岩体浅层次脆性破裂很好地对应。在苟家桥下，晚三叠世须家河组地层砂质层与泥砂质层明显互层，类似复理石的沉积韵律特征(Figure 3.10 c)，地层中存在明显的塑形流变夹紧闭褶皱，但未见任何相关的褶劈理(Figure 3.10 d)，可能为晚三叠世地层还未完全固结便经历强烈的剪切变形形成；此外，露头尺度上，同沉积包卷层理十分发育，进一步佐证该套晚三叠世地层的同构造沉积属性。

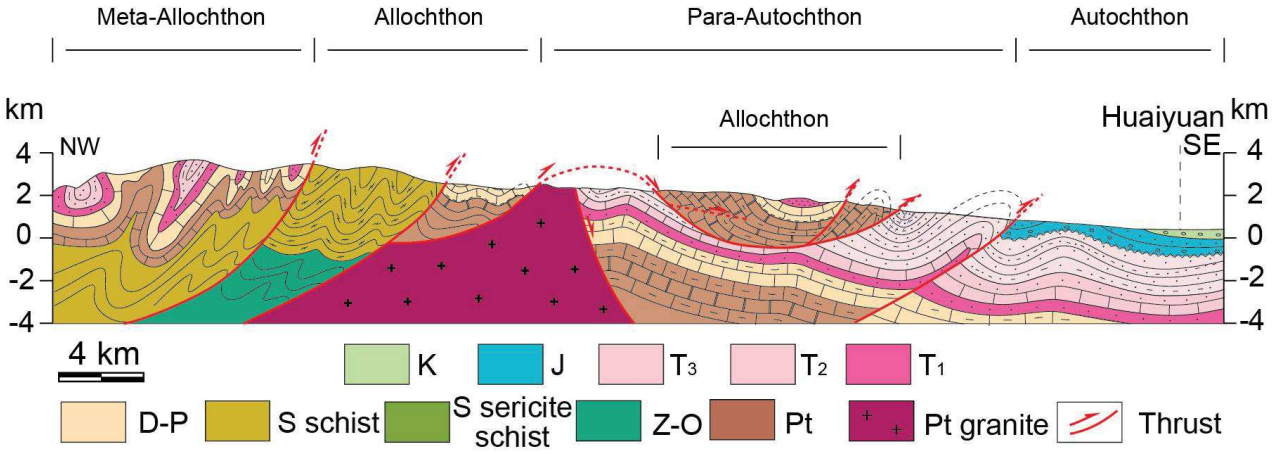

Figure 3.9 Huaiyuan-Sanjiang cross section (Location is marked in Figure 3.1, T2)

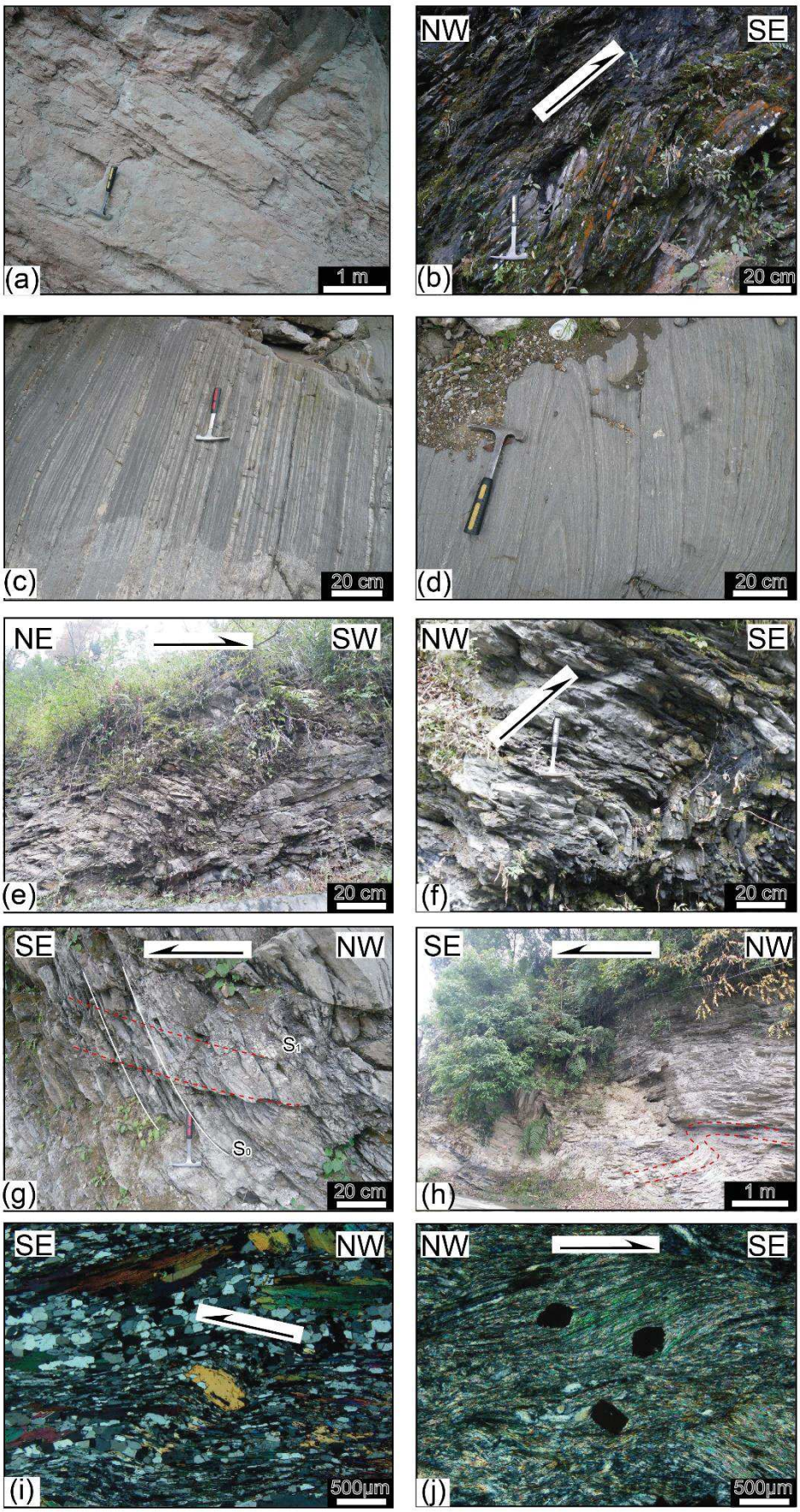

Figure 3.10 Petrological characteris and shearing indicators along the Huaiyuan-Sanjiang cross section

(a) Autochthon, the undeformed Jurassic strata characterized by cross bedding and dip to SE; (b) Para-autochthon, the Late Triassic Xujiahe formation is intensively deformed in which σ-type sandy lense indicate top-to-the-SE shearing; (c-d) Tightly folded Late Triassic strata without obvious cleavage; (e) Allochthon, the Devonian rocks inside the klippe records early phase of top-to-the-SW shearing; (e) Allochthon, the Devonian rocks of the klippe are intensively folded and overturn to SE; (f) Allochthon, the interrelation of the bedding and cleavage recorded in the Silurian rocks indicate the bedding overturning to SE; (h) Allochthon, enhancing deformation of the Silurian rocks indicate top-to-the-SE shearing; (i) Newly formed zoisite in σ-type indicate top-to-the-SE shearing; (J) Biotite formed S-C fabric indicating top-to-the-SE shearing.

相对外来系统主要包括映秀-北川断裂 NW 的推覆体和位于相对原地系统之上的大型飞来峰。飞来峰由泥盆系-下三叠统组成，作为相对原地系统，内部记录了早期 NW-SE 向枢纽的褶皱和褶皱传播断层(Figure 3.10 e)，被区域上向 SE 的逆冲推覆改造。飞来峰后缘，仍然表现为强烈穿切记录层理的褶皱及断层，并且强烈劈理化，指示了上部向 SE 的剪切变形(Figure 3.10 f)。野外宏观尺度上，映秀-北川断裂 NW 的相对外来系统主要为一套志留系-泥盆纪地层，发生褶皱并向 SE 倒转(Figure 3.10h)，强烈劈理化，局部地区出现“层陡劈缓”的几何学关系，指示了褶皱一翼向 SE 倒转(Figure 3.10g)，指示向 SE 的逆冲作用非常明显。与相对原地系统相比较，相对外来系统变形层次更深体现在局部地区有新生的云母矿物，剪切形成 S/C 组构(Figure 3.10 i)，以及显微镜下观察到帘石和石英的矿物组合(新生帘石和石英表明变质温度在 400℃左右)，帘石形成的 σ 残斑也指示了上部向 SE 剪切的运动学特征(Figure 3.10 j)。在整个相对外来系统中，根据构造几何学关系，所有的面理均倾向 NW，因而志留系岩石实际上位于泥盆系岩石之上，表现为年龄较老的岩石在年龄较新的岩石之上，地层层序发生反转，对应的变形层次也由志留系较深向泥盆纪较浅层次过渡，但整体上都表现出一致的上部向 SE 的剪切变形(Figure 3.11 d-f)。

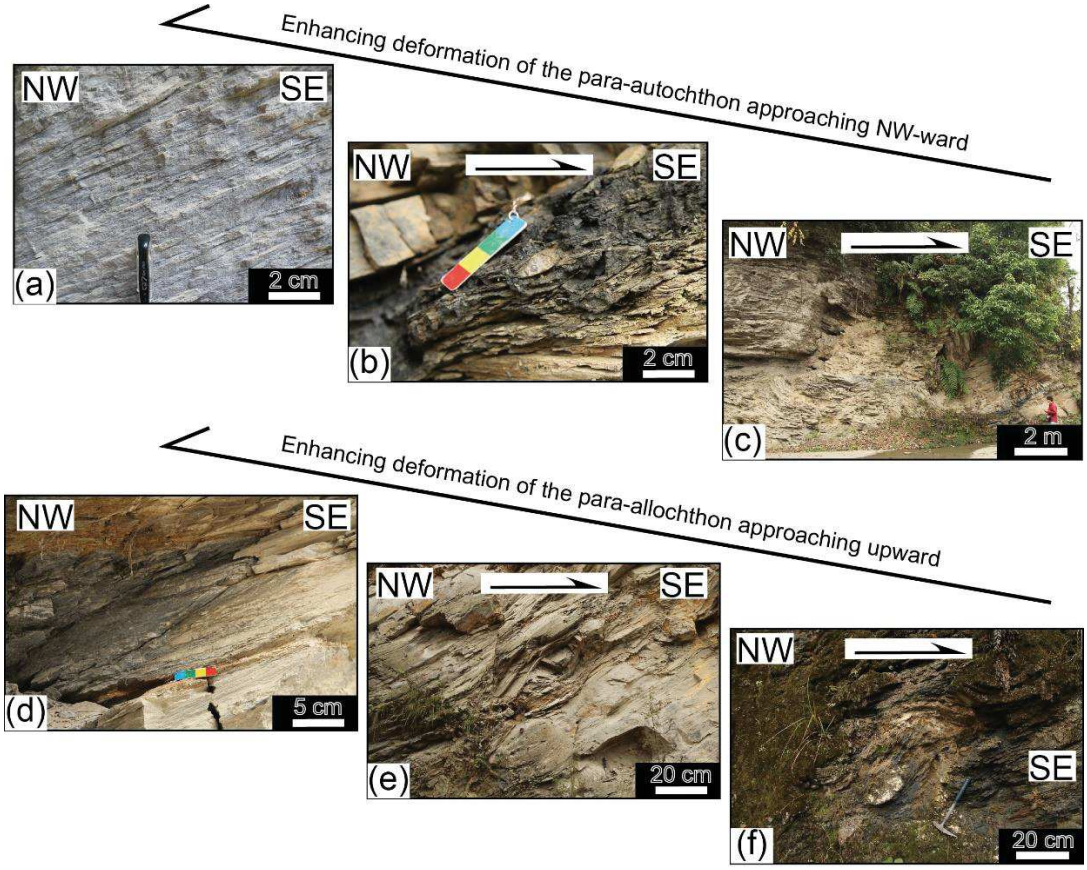

Figure 3.11 Progressive deformation of the para-autochthon and allochthon unit

(a) Silurian rocks located at the root of the klippe intensively foliated; (b) Para-autochthon, Late Triassic mudstone-sandstone interbeds and S-C fabric indicate top-to-the-SE shearing; (c) Para-autochthon, clear bedding of the Late Triassic Xujiahe formation featured by weaker deformation; (d) Allochthon, the Silurian rocks intensively foliated and the orignal bedding cannot be distinguished, the foliation dips to NW; (e) Allochthon, relative weak foliation of the Silurian rocks, the tectonic lens indicate top-to-the-SE shearing; (f) Allochthon, the geometric lowest unit of Devonian rocks characterized by low metamorphic grade, local tectonic lens indicate top-to-the-SE shearing.

3) Yingxiu-Laofangzi cross section

映秀-老房子剖面 SE 起自都江堰市，向 NW 穿过映秀到达老房子(Figure 3.1 T_3 和 Figure 3.12)。该剖面上原地系统、相对原地系统、相对外来系统以及外来系统的变质变形分带都很清楚，位于陆内薄弱带 NW 部的西部带，仍然表现倾向 NW 的面理，可能为后期构造事件改造了早期倾向 SE 的面理。安县-灌县断裂以东的原地系统仍然为一套微弱协调变形的侏罗-白垩纪地层(Figure 3.12)。

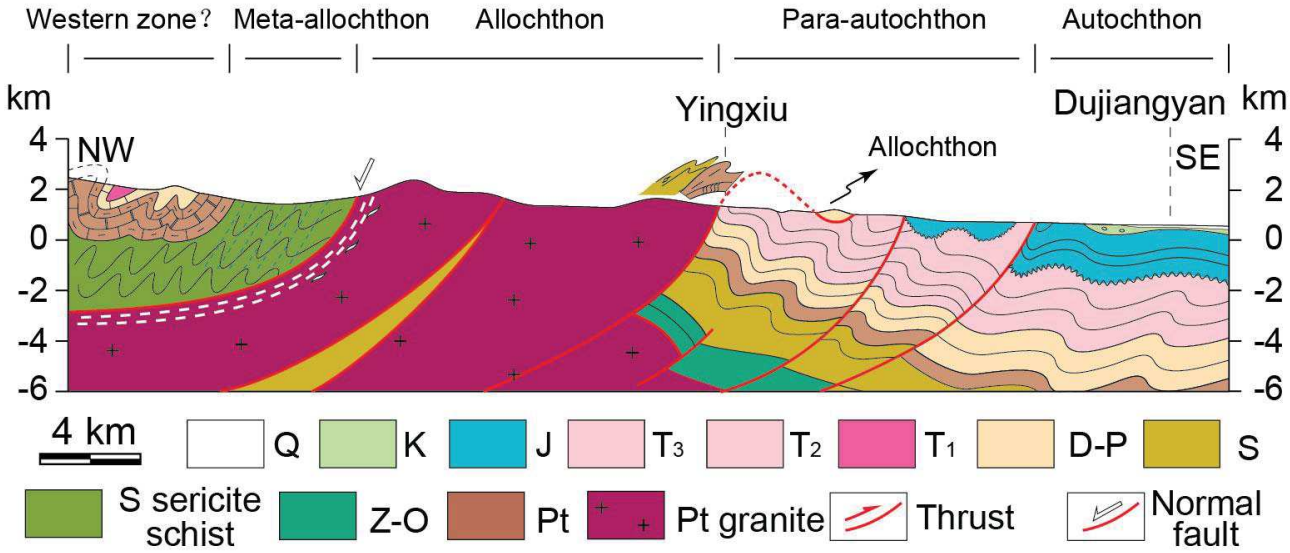

Figure 3.12 Yingxiu-Laofangzi cross section(Location is marked in Figure 3.1, T3)

相对原地系统主要为褶皱变形的晚三叠世须家河组地层，与侏罗纪地层一起褶皱形成向斜构造，核部的侏罗系西部为一条逆冲断裂，而侏罗纪系的褶皱可能为断层传播褶皱，为后期的叠加变形(Figure 3.1 和 Figure 3.12)。上三叠统须家河组为中-薄层砂岩夹泥岩层，泥质岩强烈劈理化，地层产状近直立，向 SE 陡倾，表明强烈的褶皱作用，褶皱极性向 SE(Figure 3.13 a)。

位于汶川-茂汶断裂和映秀-北川断裂之间的彭灌杂岩，与南部的宝兴杂岩具有相似的地球化学特性和年龄(Yan et al., 2008b)。在彭灌杂岩东南部，整体表现为块状闪长岩、花岗闪长岩(Figure 3.13 b)。显微构造特征分析表明，彭灌杂岩实际上由变形的 NW 块体与块状未变形的 SE 块体堆叠形成(Figure 3.12)(见第 4 章)。因而彭灌杂岩未变形的 SE 部分，对应着相对原地系统，而经历面理化变形的 NW 部分属于相对外来系统部分，这与南边邛崃剖面宝兴杂岩的几何学特征相对应。彭灌杂岩 NW 边界，还记录着后期向 NW 的正断(Figure 3.12)，将在第 4 章中详细论述。

位于汶川-茂汶断裂 NW 的外来系统--志留系岩石发生强烈剪切变形变质形成一套副片麻岩，广泛生长云母矿物。面理非常一致倾向 NW(Figure 3.2)，石英被韧性拉长组成 NW-SE 走向的线理(Figure 3.13 c)。露头尺度上长石 σ 残斑强烈剪切(Figure 3.13 d)以及砂质剪切透镜体(Figure 3.13 e)均指示上部向 SE 的剪切变形。微观尺度上，垂直面理平行线理薄片镜下观察(XZ 面)，副片麻岩中新生云母剪切形成的 S/C 组构以及剪切形成的 shearband 给出与露头尺度一致的运动学。相对外来系统还包括相对原地系统之上叠置的二叠纪地层构成的飞来峰(Figure 3.1 和 3.13)。

向 NW 靠近劈理直立带(陆内薄弱带)，志留纪片岩劈理渐变为直立产状，方解石布丁被拉长定向(Figure 3.13 f)。穿过劈理直立带，老房子石炭-二叠系发育平卧褶皱，不能确定给出运动学向 SE 还是向 NW，根据对区域上的认识，我们更倾向该平卧褶皱与西部带向 NW 的剪切变形相吻合。在西部带卧龙地区，尽管面理倾向 NW，表现为不协调的几何学形态。但运动学特征却指示上部向 NW 的正断，可能为早期向 NW 的逆冲，其几何学形态被后期松潘-甘孜褶皱带所改造。

Figure 3.13 Petrological characteris and shearing indicators along the Yingxiu-Laofangzi cross section

(a) Para-autochthon, Upper Triassic thick sandstone and thin siltstone interbeds vertically dippingto SE; (b) Undeformed Pengguan massif; (c) Allochthon, ductile deformed Silurian paragneiss with obvious foliation; (d) Allochthon, σ-type porphyroblast in Silurian paragneiss

indicate top-to-the-SE shearing; (e) Sandy lenses indicated top-to-the-SE shearing; (f) Meta-allochthon, carbonate budin in Silurian rocks strongly elongated due to intensive deformation; (g-h) Meta-allochthon, microscopic S-C fabric and shearband in Silurian paragneiss document a SE-ward vergence.

4) Tonghua-Wenchuan-Tangbazi cross section

塘坝子-汶川剖面东南起自塘坝子“飞来峰”向西北穿过九顶山，过汶川县城，很全面地记录了龙门山逆冲推覆带各个单元的表现样式(Figure 3.1 和 Figure 3.14)。原地系统为侏罗纪地层，不整合盖在褶皱变形的上三叠统须家河组地层之上。

相对原地系统为上三叠统须家河组地层，同样发生强烈褶皱，向 SE 倒转指示原地系统向 SE 方向逆冲推覆(Figure 3.14 和 3.16 a)。

作为相对外来系统的飞来峰，不整合盖在相对原地系统上，飞来峰后缘米级尺度的向 SE 方向的逆冲断裂仍然指示了强烈的挤压作用(Figure 3.15 b)，似乎不支持飞来峰滑覆就位模式中前缘挤压后缘伸张的应力机制(Meng et al., 2006)。塘坝子飞来峰主要由二叠系厚层灰岩组成，主体仍然在褶皱变形的晚三叠世地层之上，其中狭长拖尾盖在侏罗纪地层之上曾被解释为飞来峰新生代就位的关键地层学证据，详细工作表明其为新生代时期重新破碎胶结的产物(Figure 3.14)(章节 3.7.2)。映秀-北川断裂 NW 的元古代黄水河群地层，作为相对外来系统经历了强烈的剪切变形，劈理收敛于逆冲断裂以及剪切透镜体表明上部向 SE 的剪切变形。

外来系统主要为志留纪绢云母片岩，一致倾向 NW 的面理以及 NW-SE 向的线理稳定发育(Figure 3.2、Figure 3.16 d)。露头尺度上，石英 σ 剪切布丁(Figure 3.15 d)以及长石 δ 旋转残斑(Figure 3.15 e)都指示上部向 SE 的剪切变形。显微尺度下，观察 XZ 面定向薄片，云母鱼(Figure 3.16 a)、S/C 组构(Figure 3.16 b)均给出一致的上部向 SE 的剪切变形。

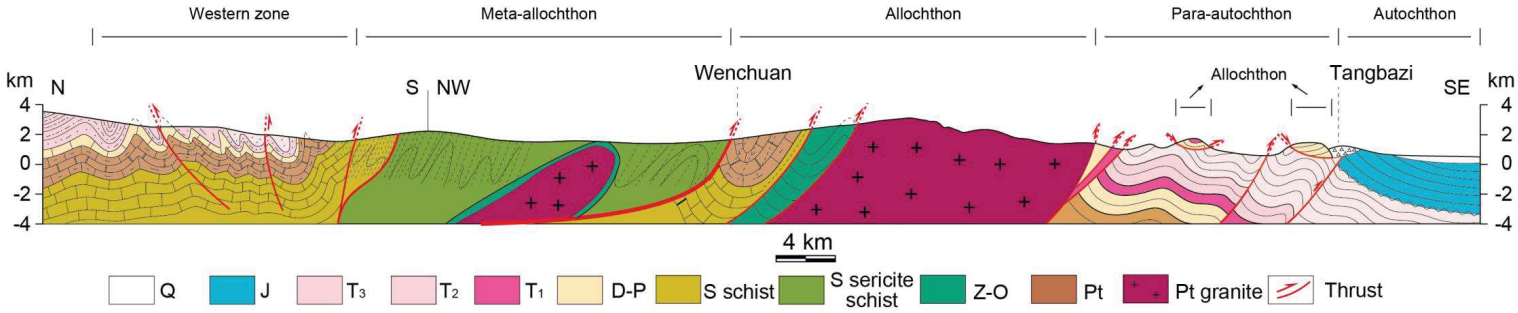

Figure 3.14 Tonghua-Wenchuan-Tangbazi cross section (Location is marked in Figure 3.1, T4)

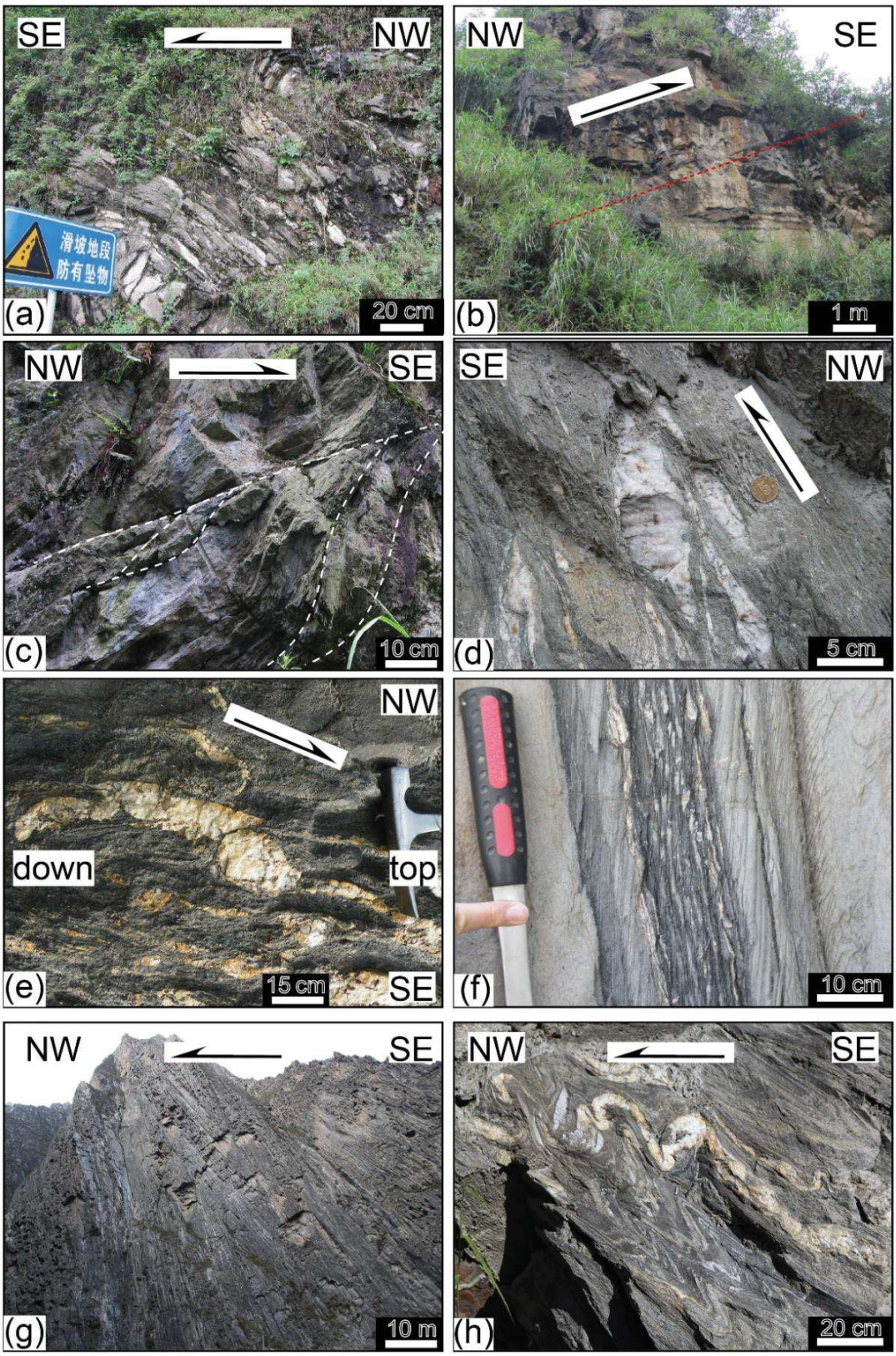

Figure 3.15 Petrological characteris and shearing indicators along the Tonghua-Wenchuan-Tangbazi cross section

(a) Folds para-autochthon overturn to SE; (b) Allochthon, the mesocopic thrust fault at the rear position of the klippe, showing top-to-the-SE thrusting; (c) Allochthon, the cleaved Proterozoic Huangshuihe group, in which deflected cleavage roots into a meter-scale SE-verging thrust

fault; (d) Meta-allochthon, the σ-type quartz budin indicate top-to-the-SE shearing; (e) δ-type feldspar in the allochthon indicate top-to-the-SE shearing; (f) Vertical cleavage developed alongthe vertical cleavage belt; (g)NW-ward overturned large scale chevron fold in the in the Western zone indicate top-to-the-NW shearing.

相对外来系统作为龙门山逆冲推覆带变形层次最高的单元，其内部变形层次也存在变化趋势。穿过汶川-茂汶断裂向 NW，刚进入相对外来系统，整座山为一套片岩，但局部地区可见原始层理指示向 SE 倒转的褶皱(Figure 3.16 c)；随后向 NW 可辨别出非常清晰的黑云母定向生长线理，成 NW-SE 展布(Figure 3.16 d)；进入相对外来系统中部位置，新生变质矿物出现角闪石，表明变质级别达到高绿片岩相或低角闪岩相，为整个龙门山变质级别最高的位置(Figure 3.16 e)；再向 NW 靠近劈理直立带，变形层次又开始略微降低，表现为绢云母片岩中石英脉强烈褶皱，向 SE 歪斜(Figure 3.16 f)。整体而言，相对外来系统依然变形层次最深，向两侧变形层次逐渐降低，形成一个背形构造，这与云母单矿物温度计测试所给出的空间几何学形态吻合的很好，为一个背形构造(Figure 3.3 d)。根据整个单元中均一向 NW 倾的面理判断，该背形整体上也给出上部向 SE 剪切的极性(Figure 3.3 d)。

劈理直立带为一套泥灰岩、炭质泥岩互层，成分层差异指示 S_0，直立劈理密集发育并在不同成分层间发生劈理折射现象，沿成分层分布的石英布丁反映强烈的水平缩短(Figure 3.15 f)。沿劈理直立带并未观察到任何与走滑相关的水平擦痕或者线理。

向 NW 穿过劈理直立带，西部带主要为松潘-甘孜褶皱带的上三叠统复理石和部分泥盆-二叠系地层。复理石发生强烈褶皱变形，百米级振幅的尖顶褶皱向 NW 歪斜，轴面倾向 SE，指示上部向 NW 的剪切变形(Figure 3.15 g)。中等尺度，泥盆系泥灰岩内方解石脉发生紧闭褶皱，褶皱极性同样指示上部向 NW 的剪切变形(Figure 3.15 h)。显微镜下，沿 XZ 切面薄片内云母鱼(Figure 3.16g)和不对称黄铁矿剪切压力影(Figure 3.16h)同样指示上部向 NW 的剪切变形。新生云母、长石等矿物组合特征表明，西部带整体上经历了低绿片岩相变质作用。

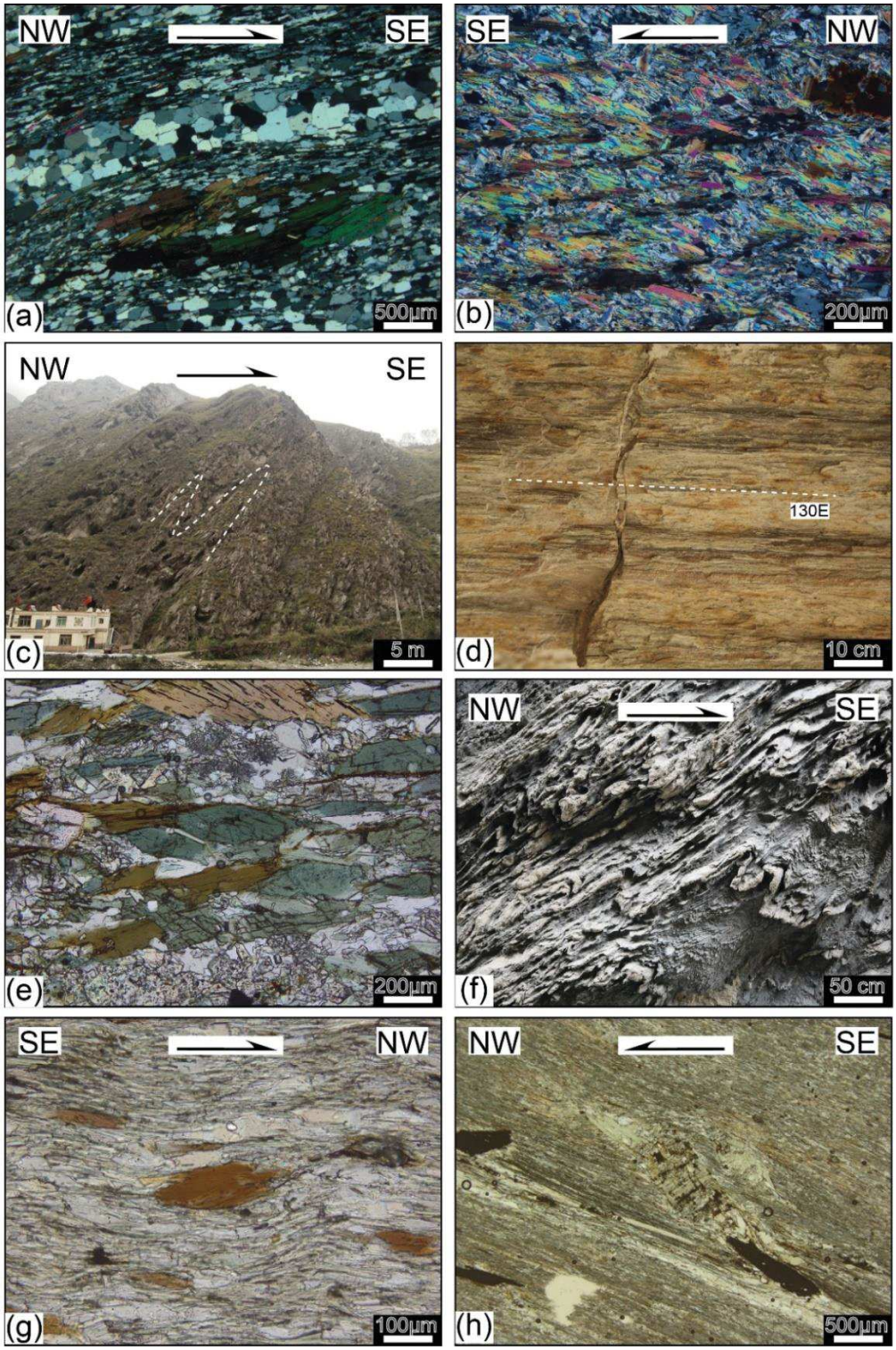

Figure 3.16 Microscopic shearing indicators and progressivedeformation in the allochthon along the Tonghua-Wenchuan-Tangbazi cross section

(a) Meta-allochthon, mica fish from the Silurian mica-quartz schist indicate top-to-the-SE shearing; (b) Mica schist from the meta-allochthon, microscopic S-C fabirc and shearband indicate top-to-the-SE shearing; (c) Silurian schist, original bedding in local place showing SE-verging fold; (d) Silurian schist, NW-SE trending lineation defined by aligned bitotite; (e) Mineral assemblage including biotite+amphibole in the meta-allochthon indicate high greenschist to low amphibolite metamorphic grade; (f) Allochthon, intensively folded quartz vein vergening to SE; (g) Mica fish from the Western zone indicate top-to-the-NW shearing; (h) Asymmetrical pyrite pressure shadow from the Western zone indicate top-to-the-NW shearing.

5) Hanwang-Qingping-Diexi cross section

汉旺-清平-茂县-叠溪剖面东南起自汉旺场，向西北经过茂县，到达叠溪镇(Figure 3.1 T_5 和 Figure 3.17)。该剖面上，第四纪松散堆积完全覆盖原地系统并超覆至晚三叠世须家河组地层之上，根据地质图观察，分隔原地系统与相对原地系统的安县-灌县断裂可能位于第四纪松散堆积之下(Figure 3.17)。

相对原地系统为褶皱变形的上三叠统须家河组地层，褶皱极性倒向 SE。在寒武系-二叠系组成的飞来峰 SE 缘，明显向 SE 的逆冲断层分隔飞来峰的二叠纪地层和下伏的晚三叠世地层，断层两盘地层产状表现显著不协调(Figure 3.18 a)。

相对外来系统主要由元古代至早三叠世地层和元古代彭灌杂岩体组成。位于须家河组地层之上的飞来峰以强烈褶皱产出，局部地区以寒武纪地层为核部形成向 SE 斜歪的背斜(Figure 3.18 b)，指示飞来峰作为相对外来系统的一部分在就位过程中遭受强烈向 SE 的剪切作用。相对外来系统推覆体部分，作为彭灌杂岩盖层的寒武纪变砂岩表现强烈的劈理化，反映了相对于相对原地系统更深层次的变形特征。劈理的收敛方向指示上部向 SE 的剪切变形(Figure 3.18 c)。

外来系统仍然作为变质变形最强的单元，在宏观和微观尺度上均给出明确的剪切标识。野外露头上，面理一致倾向 NW，面理上可见新生云母和长英质矿物定向形成 NW-SE 向线理(Figure 3.2)。志留纪绢云母片岩黄铁矿不对称压力影(Figure 3.18 d)以及强烈褶皱变形的石英脉(Figure 3.18 e)均给出稳定的上部向 SE 的剪切变形。薄片镜下观察，可见新生云母定向排列形成 S/C 组构或剪切形成 shearband 构造，指示上部向 SE 的剪切变形(Figure 3.19 a 和 b)。局部地区志留纪泥灰岩内，新生云母剪切形成云母鱼构造，给出相同的运动学特征(Figure 3.19 c 和 d)。新生的云母矿物表明较深层次的变形作用。

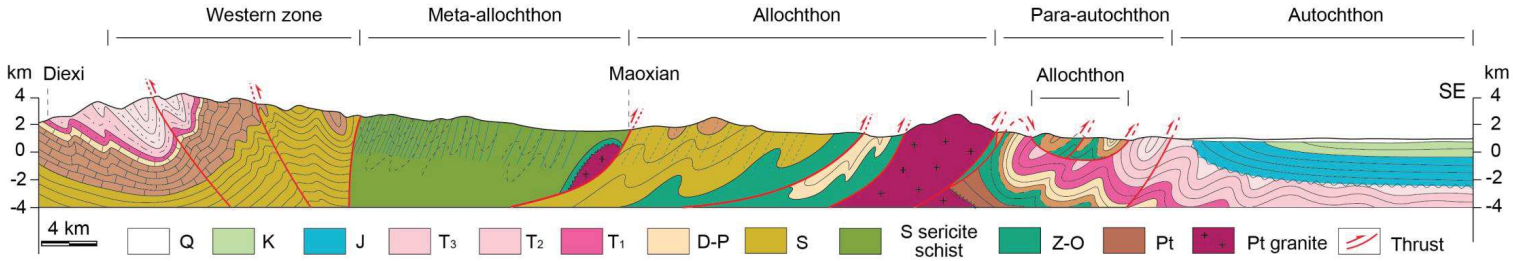

Figure 3.17 Diexi-Maoxian-Hanwang cross section (Location is marked in Figure 3.1, T5)

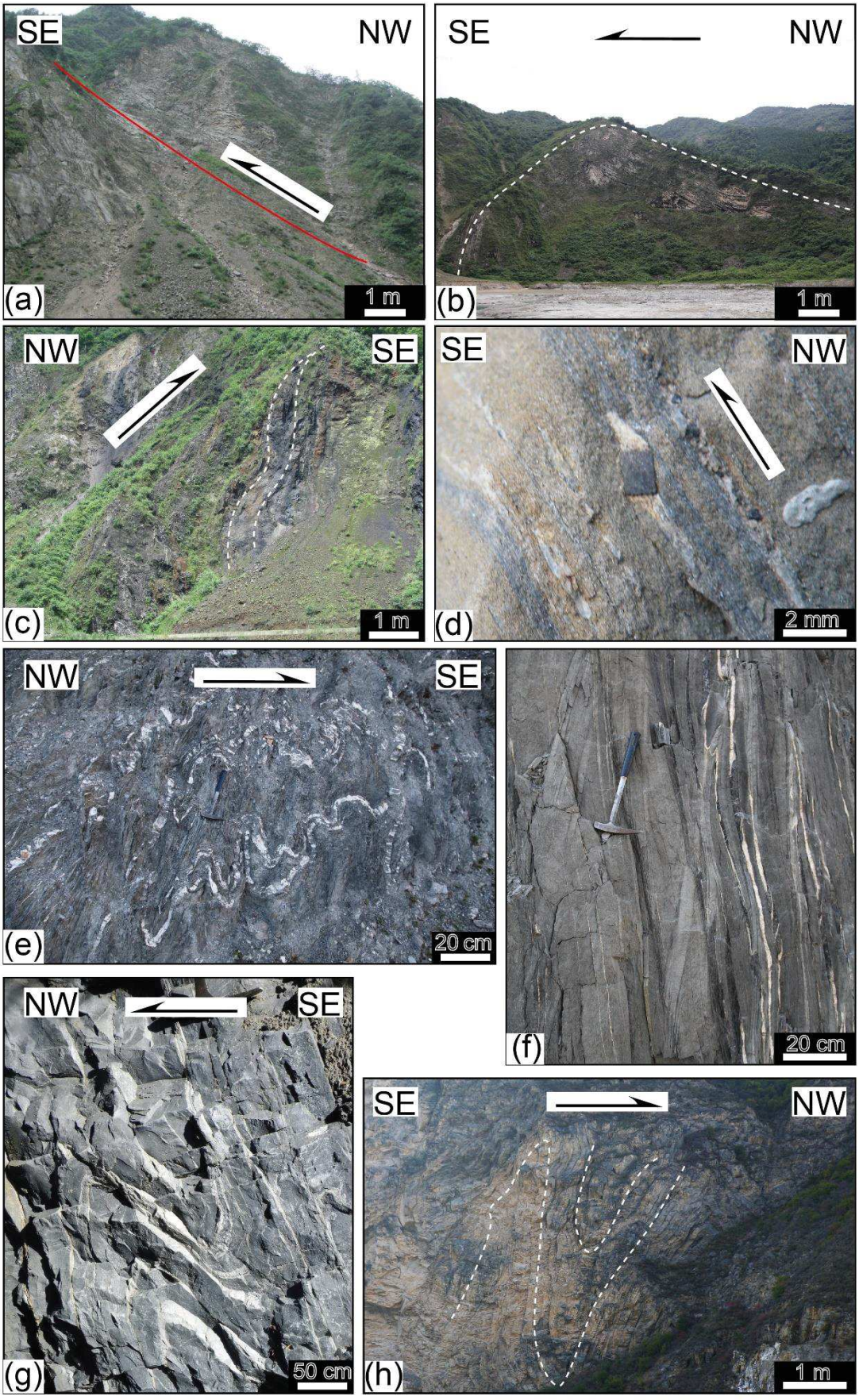

Figure 3.18 Petrological characteristics and shearing indicators along the Diexi-Maoxian-Hanwang cross section

(a) The boundary between the autochthon and the para-autochthon, a thrust fault separates the klippe from the Xujiahe formation and thrusting to SE; (b) Allochthon, klippe consists of Precambrian strata forming a SE-vergening anticline; (c) Allochthon, the Precambrian rocks suffering intensive deformation and strongly foliated; (d) Meta-allochthon, asymmetric pyrite pressure shadow from the Silurian schist indicate top-to-the-SE shearing; (e) Meta-allochthon, overturned quartz folding indicate top-to-the-SE shearing; (f) The vertical cleavage belt, the quartz vien suffered intensive folding and shortening, no sigh of ductile strike-slip structures; (g) The limestone in the Western zone folded and overturned to NW; (h) Large scale overturned chevron fold in the Songpan-ganzi belt indicate top-to-the-NW shearing.

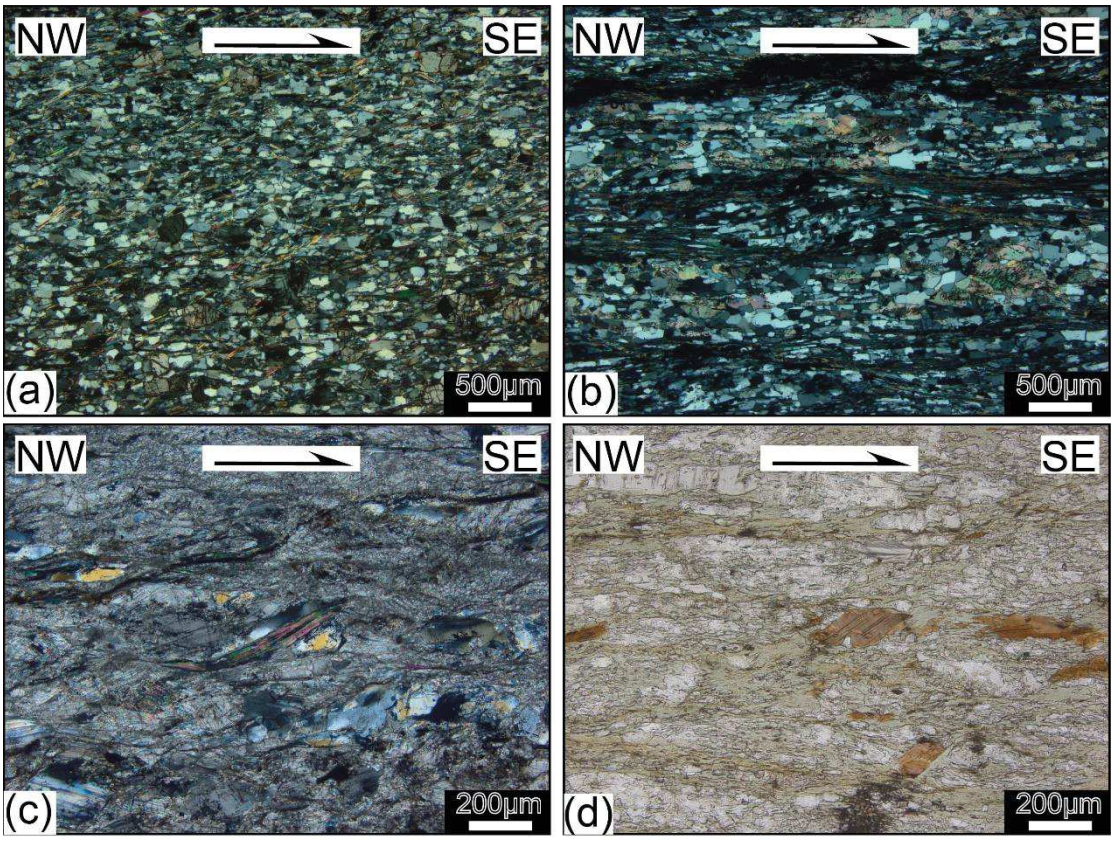

Figure 3.19 Microscopic shearing indicators along the Diexi-Maoxian-Hanwang cross section

(a) CX665, newly formed mica aligned and intersect with the shear plane of the quartzite that define top-to-the-SE shearing; (b) CX118, shearband in the mica-quartzite indicate top-to-the-SE shearing; (c-d) CX114-115, strongly foliated carbonates and mica fish in mica schist indicate top-to-the-SE shearing.

劈理直立带由强烈剪切变形的厚层砂岩、薄层灰岩及泥岩组成，泥岩已变质成绢云母片岩或绿泥石片岩(Figure 3.18 f)。石英脉剪切形成 σ 形态指示上部向 SE 的剪切变形，或挤压形成紧闭褶皱或无根褶皱。泥灰岩层广泛发育劈理，产状近直立。尽管发育枢纽近直立的细褶纹和小褶皱，但并未观察到水平的擦痕和线理，走滑的几何学特征仍然不显著。

西部带由少部分志留系-泥盆纪地层以及广泛的三叠纪地层组成。野外能观察到的面理和劈理均倾向 SE(Figure 3.2)。在泥盆纪地层中，强烈剪切变形并劈

理化的灰岩、大理岩指示上部向 NW 的剪切变形(Figure 3.18 g)；而在松潘-甘孜褶皱带内，复理石强烈褶皱变形为 W 型褶皱向 NW 歪斜指示同样的运动学特征(Figure 3.18 h)。

6) Beichuan-Xuanping cross section

北川-漩坪剖面东南起自新北川县城南部，向 NW 穿过马角坝断裂系，东部带四个单元、劈理直立带与西部带完整出露(Figure 3.1 T_6 和 Figure 3.20)。原地系统出露微弱褶皱变形的侏罗系和第四系松散堆积。侏罗系地层发育板状交错层理，指示由 NW-SE 的古水流方向，表明龙门山在侏罗纪时期已有一定的隆升(Figure 3.21 a)。侏罗系砂岩与上三叠统须家河组砂岩之间的不整合界线分隔原地系统与相对原地系统。相对原地系统为中三叠统-上三叠统砂岩(Figure 3.1)，地层陡立表明发生了强烈褶皱或掀斜作用，并发育少量垂直层理的劈理，标志层发生错段指示向 SE 的逆冲推覆作用(Figure 3.21 b)。

相对外来系统包括马角坝地区广泛分布的由二叠系-下三叠统组成的飞来峰以及映秀-北川断裂以西由寒武系石英砂岩及志留系泥质片岩组成的推覆体。飞来峰由泥盆-早三叠世地层组成，内部发育多条向 SE 逆冲的次级断裂，使泥盆纪地层为核部的背斜向 SE 逆冲推覆(Figure 3.20)。泥盆系地层发生强烈褶皱变形的同时，还广泛发育劈理，反映更深层次的变形，褶皱的极性指示上部向 SE 的剪切(Figure 3.21 c)。

该剖面外来系统主要志留纪绢云母片岩组成，面理极其发育并倾向 NW(Figure 3.2)，成分层指示 S_0 为强烈褶皱并向 SE 歪斜的向斜(Figure 3.21 d)，指示在向 SE 剪切变形过程中发生轴面劈理与层理的置换。劈理密集发育以及新生云母矿物表明该剖面外来系统属于变形层次最深的产物。

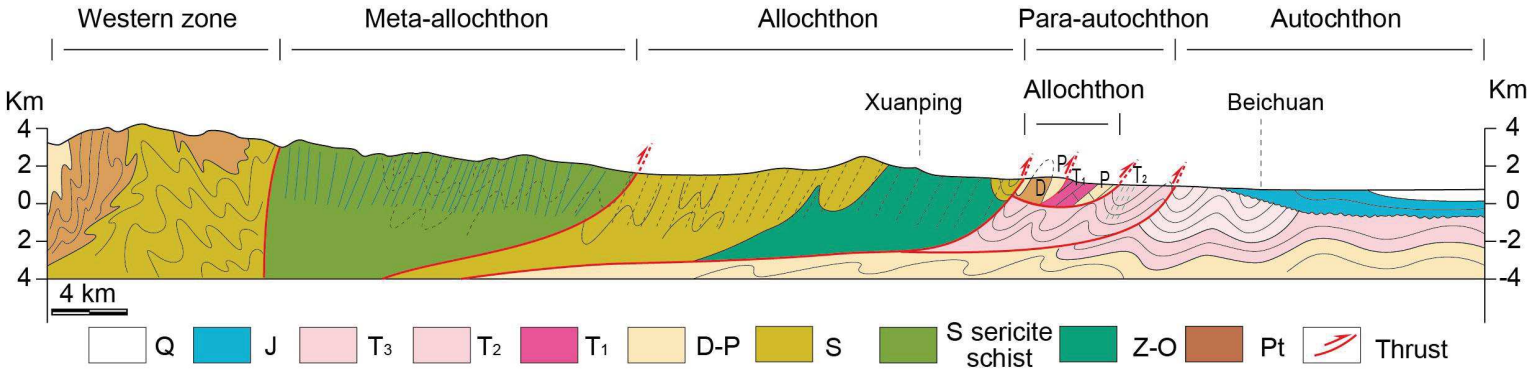

Figure 3.20 Beichuan-Xuanping cross section (Location is marked in Figure 3.1, T6)

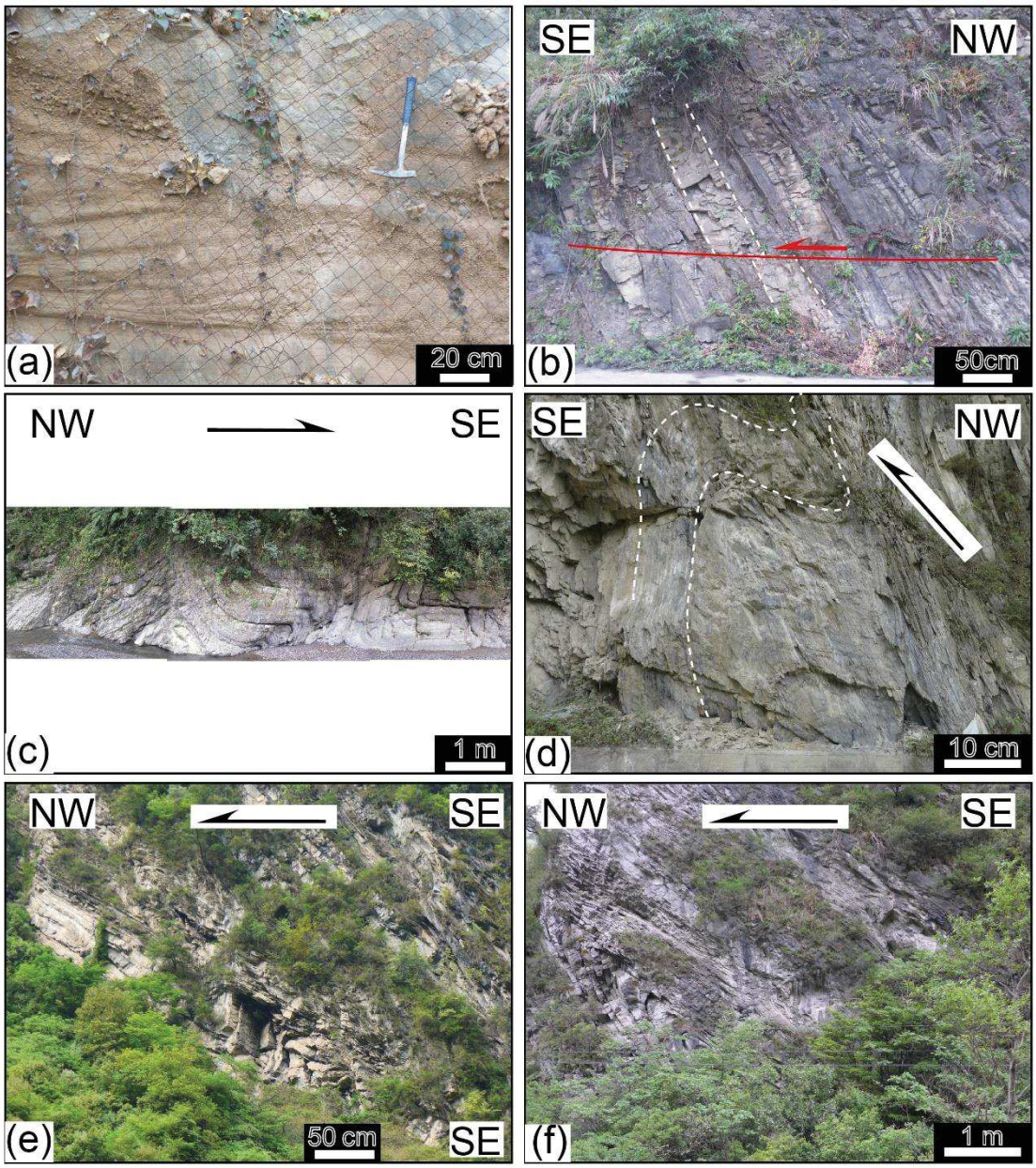

Figure 3.21 Field charateristics and shearing indicators along the Beichuan-Xuanping cross section

(a) Autochthon, undeformed Jurassic strata with cross-bedding; (b) Para-autochthon, bedding dislocated to SE indicate top-to-the-SE shearing; (c) Allochthon, Devonian rocks are intensively deformed and overturned to SE; (d) Meta-allochthon, the original beding totally transposing to foliation accompany SE-ward thrusting; (e-f) Western zone, Permian thin limestone and Triassic flysch are intensively foldedand overturned to NW.

向西北穿过劈理直立带，西部带由志留系-二叠系地层组成。在志留系-泥盆系地层中，劈理密集发育，大多呈高角度向 N 或 S 陡倾，体现劈理直立带相对较宽的分布范围。在二叠系薄层灰岩中，向 NW 强烈倒转的褶皱确定了西部带特有的上部向 NW 的运动学特征(Figure 3.21 e 和 f)

7) Jiangyou-Pingwu cross section

江油-平武剖面是研究区跨度最长的剖面，东南起自江油市向 NW 到达平武县城，直至碧口地区，囊括龙门山地区所有构造单元(Figure 3.1 T_7 和 Figure 3.22)。原地系统仍然由侏罗-白垩系地层组成。野外观察和剖面图上可以看出，侏罗纪地层不整合盖在强烈褶皱变形的上三叠统须家河组之上。但侏罗系自身也发生了褶皱和地层的倒转，局部地区受安县-灌县断裂的逆冲，表明侏罗系被后期构造叠加改造(Figure 3.22)。侏罗系虽然以褶皱样式表现出后期变形，但其变形层次明显不同于主变形期。相对原地系统在该剖面以上三叠统须家河组砂岩为主，仅在唐王寨向斜东南方位出露，大部分区域被唐王寨推覆体覆盖(Figure 1 和 Figure 3.22)。须家河组强烈褶皱变形，向 SE 倒转，并发育褶皱传播断层，指示上部向 SE 的剪切变形，比原地系统的侏罗纪-白垩纪地层变形更强，原始层理清晰可见，劈理不发育(Figure 3.23 a)。层间劈理广泛发育，劈理与层理的交切关系同样也指示了上部向 SE 的运动学。

相对外来系统主要由志留纪泥质片岩、千枚岩和唐王寨推覆体组成，唐王寨推覆体为少量志留纪千枚岩、泥质片岩和泥盆纪-石炭纪砂质岩和厚层灰岩组成的大型向斜(Figure 3.23 b)，其中志留纪泥质片岩中所有的面理都一致地倾向 NW(Figure 3.2)。志留纪片岩作为较弱层，在唐王寨向斜推覆就位过程中作为底界滑脱层协调变形。吴山和林茂炳(1991)对唐王寨中做脆性应力应变分析认为唐王寨向斜为中生代滑覆就位(吴山和林茂炳, 1991b)。但唐王寨向斜后缘的韧性-塑形变形均表现为逆冲-褶皱等挤压构造，并不支持唐王寨向斜滑覆就位模式(Figure 3.23 c)。更多详细野外几何学和运动学特征都表明唐王寨在挤压背景中就位(许志琴等, 1992; Burchfiel et al., 1995; Chen and Wilson, 1996)。因而飞来峰后缘脆性的伸展应力场(吴山和林茂炳, 1991b)可能对应龙门山后期隆升后的局部改造作用。位于唐王寨向斜和北川-映秀断裂 NW 方向的志留纪泥质片岩构成了相对外来系统另一重要组成部分。

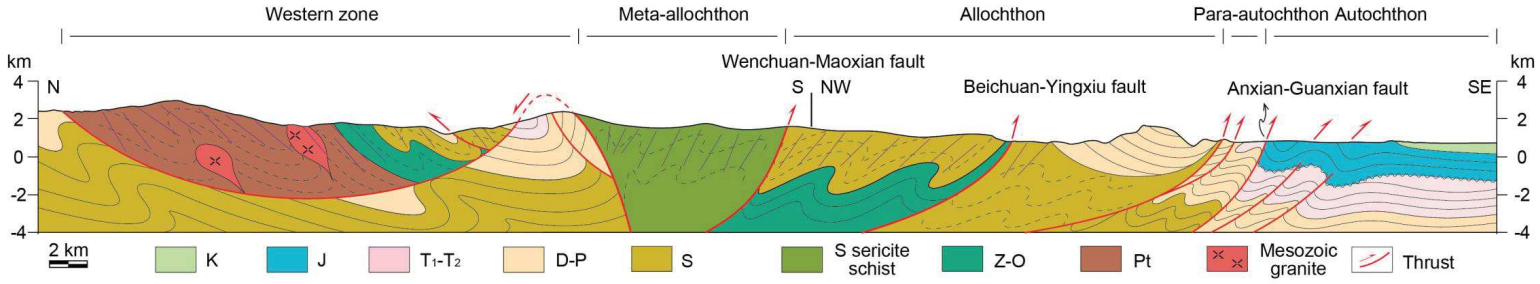

Figure 3.22 Jiangyou-Pingwu cross section (loation is marked in figure 3.1, T_7)

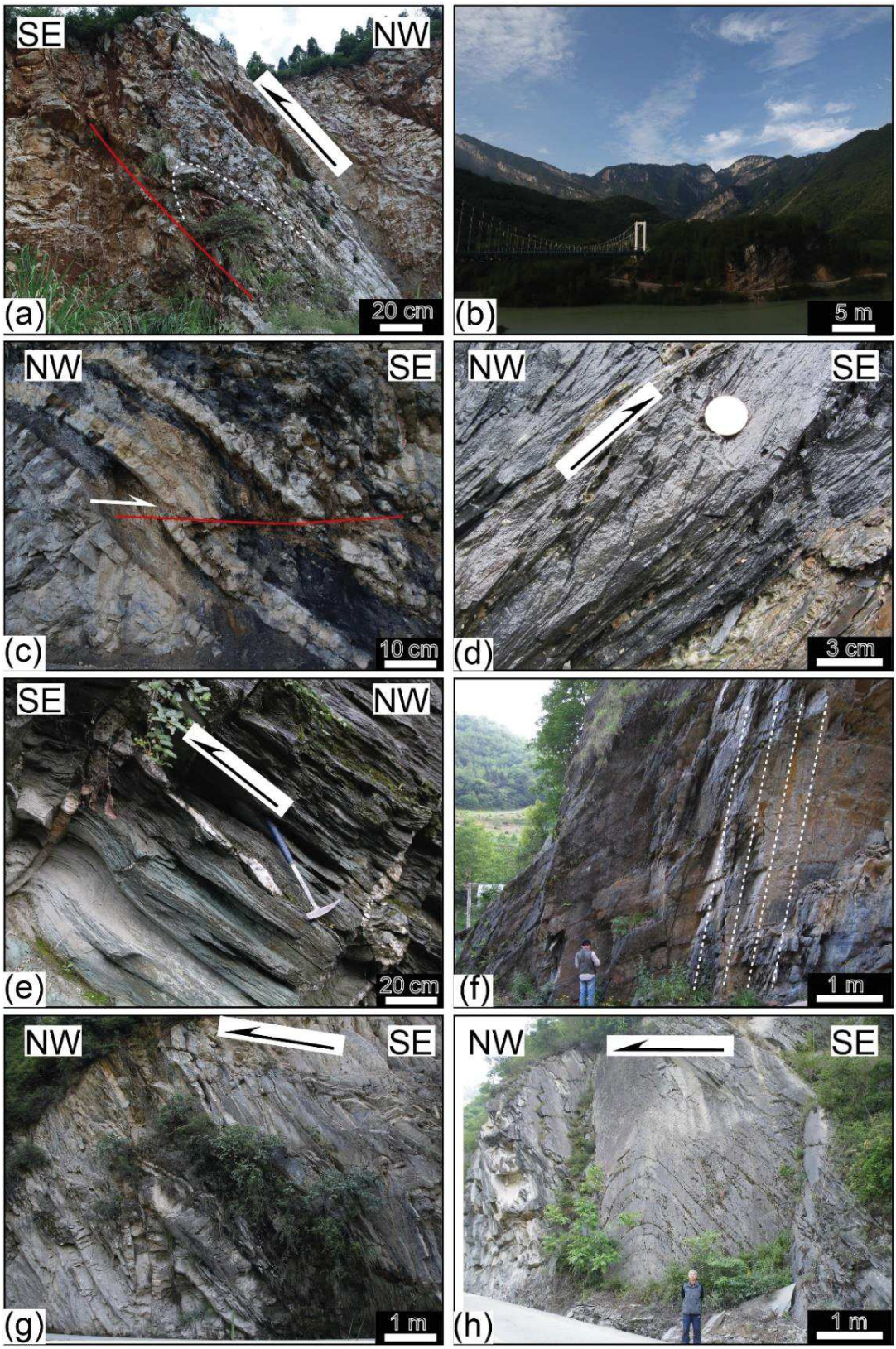

Figure 3.23 Field petrological characteristics and shearing indicators along the Jiangyou-Pingwu cross section

(a) Para-autochthon, fault –propagated fold thrust to SE recording in the Late Triassic sandstone; (b) Allochthon, the giant Tangwangzhai syncline; (c) dislocation of the thin limestone inside the Tangwangzhai syncline indicate top-to-the-SE shearing; (d) Allochthon,

Silurian pelitic schist enveloping sandy lense indicate top-to-the-SE shearing; (e) Meta-allochthon, σ-type quartz budin from the Silurian sericite-bearing schist indicate top-to-the-SE shearing; (f) Vertical cleavage belt, well-developed foliation obliterate the original bedding that depicted by the composition layer; (g) The Devonian overturned fold in the Western zone indicate top-to-the-SE shearing; (h) Western zone, well-developed foliation in the Silurian rocks dipping to the SE, the original bedding documented by the vegetation as an fold verging to NW.

野外观察几何学特征表明作为相对外来系统的志留纪片岩被映秀-北川断裂逆冲至同样作为相对外来系统的唐王寨向斜之上，表明映秀-北川断裂多期向 SE 的逆冲变形活化改造作用(Figure 3.22)。在豆叩地区，志留纪泥质片岩中砂质夹层被剪切形成连续的 σ 透镜体，指示上部向 SE 的剪切变形。整体上变形特征指示的变形层次高于相对原地系统。

外来系统中云母等新生矿物出现，为一套绢云母片岩，变形层次最深，并在倾向 NW 的面理上稳定发育向 NW 陡倾的线理(Figure 3.2)。XZ 剖面剪切拉伸的 σ 石英布丁指示上部向 SE 的剪切(Figure 3.23 e)。

劈理直立带主要发育在泥盆纪炭质千枚岩中，原始成分层以西可见，表现为大型轴面劈理近直立褶皱，表明经历强烈缩短变形(Figure 3.23 f)。劈理直立带内发育粒径在 1cm 左右的黄铁矿，可能为热液活动所致。带内并未观察到走滑相关的水平擦痕、线理或枢纽近直立的褶皱构造。区域上，劈理直立带与 NEE 走向的青川断裂合并为同一条地质界线。青川断裂地震反射剖面表明其为一条花状构造的走滑断裂(贾东等, 2003; Jia et al., 2006)，这与劈理直立带两侧似花状的结合学形态吻合的很好。

西部带在平武剖面中主要由上元古界碧口群和早古生代地层组成，该西部带的分布范围在整个龙门山逆冲推覆带中最广泛。我们根据野外的观察和室内分析，将西部带解释为一个可以与东部带类比的大型飞来峰构造(Figure 3.22)。西部带内广泛发育的面理一致倾向 SSE(Figure 3.2)，并可见 NNW-SSE 的矿物拉伸线理(Figure 3.2)平武县城向 N 出城，泥盆纪砂岩发生紧闭褶皱并向 N 歪斜，指示上部向 N 的剪切变形(Figure 3.23 g)。志留纪片岩中，由于强烈剪切作用，原始层理已完全被置换成倾向 SSE 的面理，原始成分层由顺层生长的植物指示出来，为一向 NNW 斜歪的大型褶皱，结合 XZ 面野外剪切指向，上部向 N 的剪切变形非常确定(Figure 3.23 h)。沿 XZ 面制作的薄片尺度观察，长石斑

晶生长形成 σ 碎斑以及石英碎斑形成书斜构造均指示上部向 N 的剪切变形(Figure 3.24)。

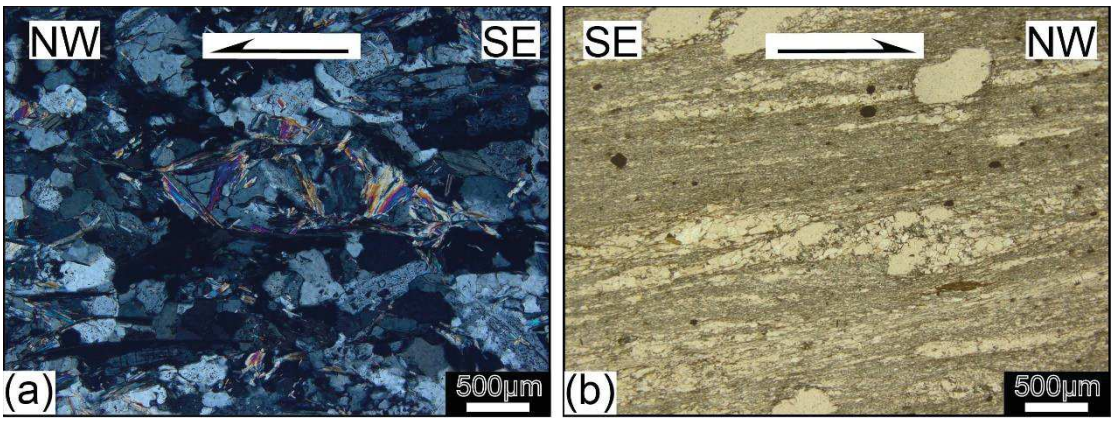

Figure 3.24 Microscopic shearing indicators along Jiangyou-Pingwu-Mupi cross section

(a) CX396, σ-type porphyroblast from quartz schist and wraping mica indicate top-to-the-NW shearing; (b) CX412, quartz blast assemble in domino structure indicate top-to-the-NW shearing.

8) Tianjingshan-Qingchuan cross section

天井山-青川剖面东南起自天井山-矿山梁以北，向 NW 穿过马角坝断裂(安县-灌县断裂北延段)，再向北穿过青川断裂到劈理直立带附近(Figure 3.1 T_8 和 Figure 3.25)。相对原地系统仍然为微弱变形的侏罗-白垩系，不整合盖在褶皱变形的上三叠统须家河组之上(Figure 3.25)。

相对原地系统主要由早三叠世砂岩组成，砂岩层中广泛发育的剪切透镜体指示上部向 SE 的剪切(Figure 3.26 a)。原始层理清晰可见，劈理仅在局部地区发育，显示变形层次比原地系统深。

相对外来系统主要由寒武纪-志留纪片岩组成。局部地区观察到向 SE 歪斜的背斜被强烈劈理化，劈理倾向 NW，指示上部向 SE 的剪切变形(Figure 3.26 c)。志留纪片岩中，剪切形成的 σ 石英布丁给出一致上部向 SE 的剪切指向(Figure 3.26 d)。

外来系统分布范围较窄，局部地区见新生石榴子石，表明其较高变质层次。

劈理直立带露头表现为大量石英脉强烈剪切变形，类似于糜棱岩(Figure 3.26 e)。该剖面上劈理直立带变形层次较其它剖面都高，反映了劈理直立带在横向上表现不均一性。地质位置上，劈理直立带同时对应青川断裂带，作为重要地质界线分隔了向 N 和向 SE 剪切单位。

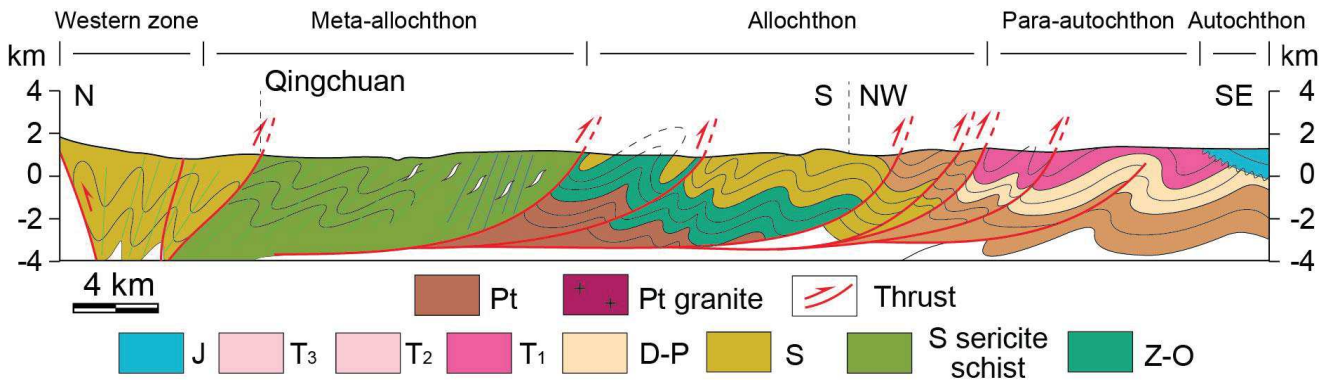

Figure 3.25 Qingchaun-Tianjingshan cross section (loation is marked in figure 3.1, T_8)

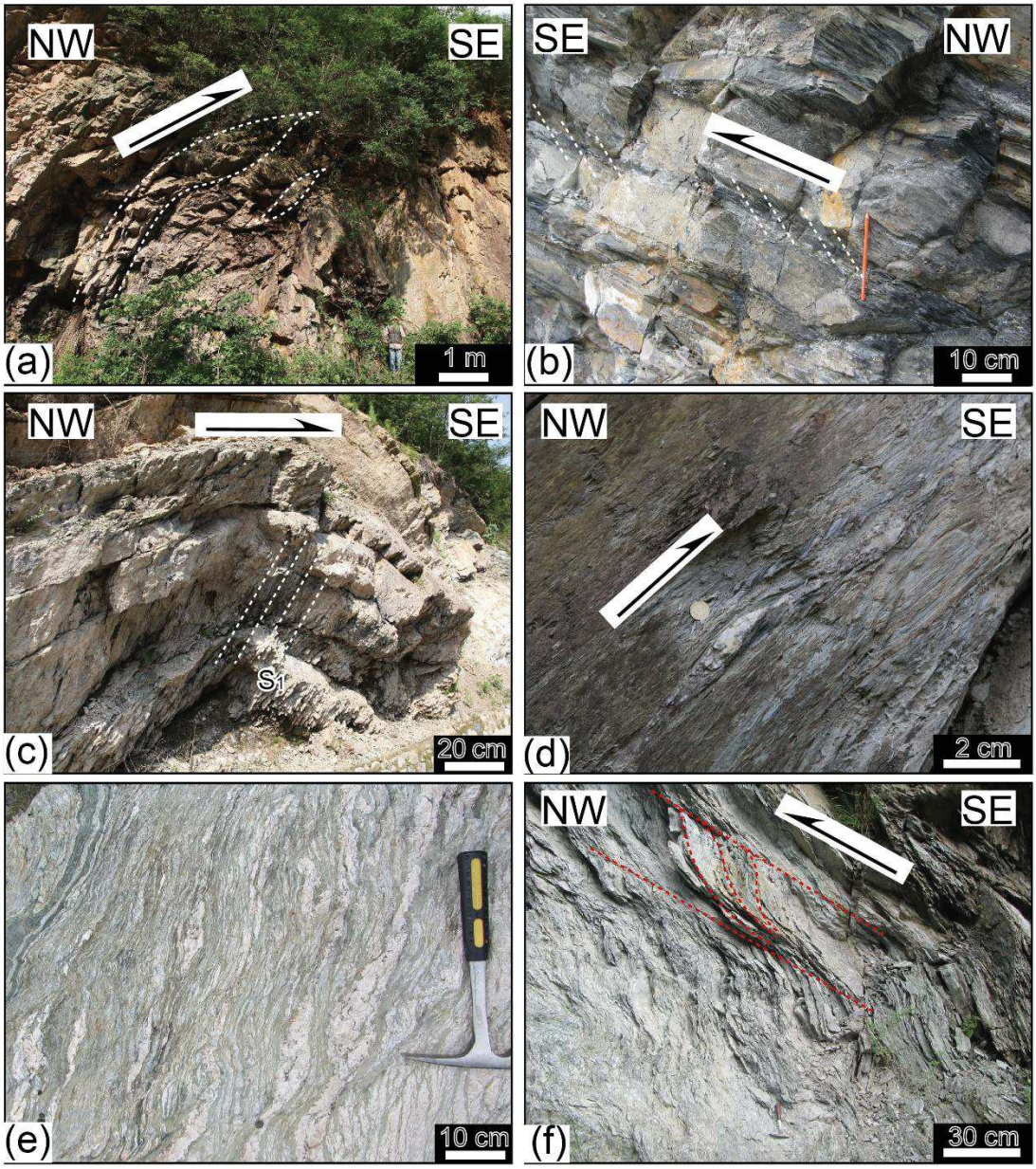

Figure 3.26 Deformation characteristics and shearing indicators along the Qingchuan-Tianjingshan cross section

(a) Para-autochthon, sandy lense within the Early Triassic sandstone indicate top-to-the-SE shearing; (b) Allochthon, cleavage deflection between Cambrian sandstone-silt interbeds indicate layer-parallel slip, accomdated to SE-vergening; (c) Allochthon, Silurian pelitic schist develop foliation dipping NW, the original bedding depicts SE-vergening fold; (d) Allochthon, calcite σ-type lense indicate top-to-the-SE shearing; (e) Top view of the vertical cleavage belt of the interlayered quartz vein and mica schist, no sign of horizontal striation and lineation; (f) Mica schist from the western zone wrapping sigmoidal shearing structure indcate top-to-the-NW shearing.

西部带主要为一套石英绢云母片岩，表现一致的倾向 SE 的面理(Figure 3.2)。云母片岩剪切形成的 S/C 组构指示上部向 NW 的剪切(Figure 3.26 f)。

3.5 The involving domain of the vertical cleavage belt (VCB)

龙门山南段，宝兴县以北，劈理直立带沿奥陶系大理岩展布(Figure 3.1，章节 3.5.1)，由于大理岩较纯，其成分单一易变形，因而记录不了较高级别的变质和较强的变形特征。在劈理直立带东南侧，宝兴杂岩分为相对原地系统和相对外来系统两部分，两者均表现出一致的上部向 SE 的剪切变形。在灵关镇附近，由泥盆系泥质灰岩和志留系薄层灰岩组成的飞来峰，作为相对外来系统的一部分，盖在褶皱变形的上三叠统之上(Figure 3.1)，能与龙门山中段和北段很好地对应。在龙门山南段，劈理直立带东南侧变形的广度和宽度可以与龙门山中段的变形相吻合，但是劈理直立带西边的变形表现则相对较弱，几乎没有上部向 NW 剪切的表现形式。

龙门山北段，在平武以北的碧口地块以青川-平武断裂为界，碧口地块主要为绢云母片岩、片岩、副片麻岩、泥质片岩，局部地区震旦纪冰碛砾石定向拉伸，可以确定为线理方向，平行线理垂直面理的砾石剪切变形的 σ 碎斑 (Figure 3.27 a)、紧闭褶皱(Figure 3.27 b)以及镜下 σ 型旋转残斑(Figure 3.27 c)均指示上部向 N 或 NW 的剪切变形，与劈理直立带北侧的运动学特征一致。

Figure 3.27 Top-to-the-N shearing in Bikou Terrane north of the vertical cleavage belt

(a) σ-type gravel in the Sinian tillite show top-to-the-N shearing; (b) Foliation-parallel tight fold overturned to north; (c) σ-type porphyroblast on XZ plane thin section indicate top-to-the-N shearing.

从平武向北，靠近平武县城为一系列向 N 倒转的褶皱，夹云母片岩和石英片岩，发育面理 (章节 3.5.7)，是变形较强的地区；继续向北，变形逐渐减弱，表现为一系列宽缓褶皱，无极性，原始层理清晰，发育半透入性劈理，表明其变形温度和强度都发生了减弱，在向北的推覆体底界断裂处表现为一平卧褶皱，向 N 倒转(Figure 3.28 c)；向 N 到白马藏族乡，向 N 的逆冲变形逐渐减

弱，渐变为轴面近直立的宽缓褶皱(Figure 3.28 b)；再向北，则几乎看不见与向N 逆冲相关的变形(Figure 3.28 a)。

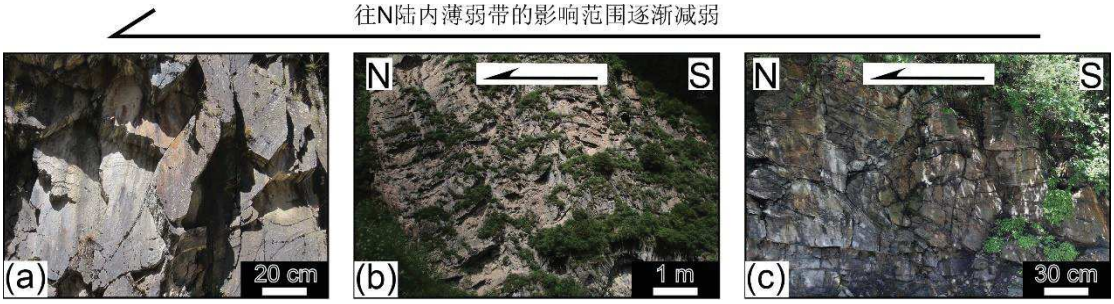

Figure 3.28 Attenuated deformation north of the vertical cleavage belt

(a) Undeformed Devonian sandstone showing no sign of northward shearing; (b) The unit below the nappe of the Western zone showing weakly N-ward vergening fold; (c) Tectonic boundary between the nappe and autochthon of the Western zone, the autochthonous Devonian sandstone presenting recumbent fold vergening to the north.

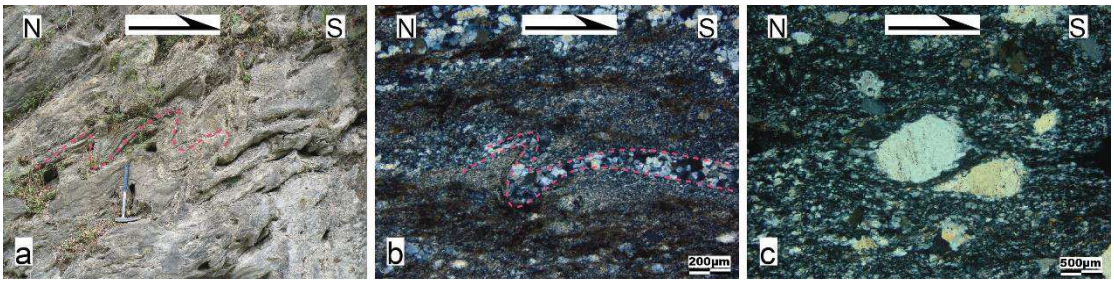

Figure 3.29 Top-to-the-S shearing due to the Mianlve suture zone

(a) S/C indicate top-to-the-S shearing; (b) Asymmetric pressure shadow wrapping opaque mineral indicate top-to-the-S shearing; (c)σ-type quartz porphyroblast indicate top-to-the-S shearing.

穿过碧口地块向北，尽管面理产状大多数倾向 S 或 SE 方向，但是局部地区野外露头尺度的 S/C 组构和薄片镜下尺度的压力影拖尾和石英 σ 碎斑开始表现出向 SE 的运动学极性(Figure 3.29)，这与劈理直立带北侧向 N 的运动学极性不相吻合。由此说明碧口地块北部逐渐受到勉略洋缝合带的影响(Meng and Zhang, 2000)，表现出向 S 的运动学极性。

劈理直立带不仅向 N 影响一定范围后逐渐消亡，向 NE 也逐渐表现出减弱的趋势。

沿着青川-阳平关断裂，一直向 NE 方向，劈理直立带的表现形式逐渐减弱。首先是劈理直立带南侧的变形程度开始大幅度降低，在阳平关镇南边为一套寒武-奥陶纪的泥岩、页岩，几乎看不出变形，地层保存完好，倾角较缓，随着向 N 靠近薄弱带附近，变形样式表现为紧闭的褶皱，继而表现出极性向 SE

倒转的褶皱(Figure 3.30)，从表现形式来看，与汶川茂县地区运动学极性可以对应，但是该处的构造系统划分已经不明显，以劈理直立带为中心的构造活动影响范围延至阳平关镇已经接近尾声，变形也已经非常弱，可能已经到了龙门山主造山带影响范围的末端，故而变形表现不如之前典型地区强烈，再向 NE 方向，即进入米仓山的影响范围内。

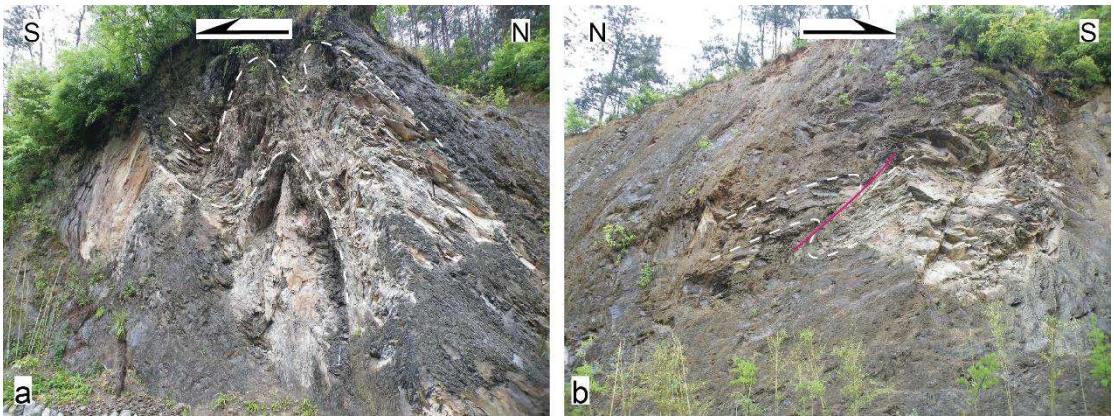

Figure 3.30 Top-to-the-SE shearing south of the vertical cleavage belt

(a) Tight folded Silurian rocks display weak SE-ward vergence; (b) Fold-propagated thrust in the Silurian schist indicate top-to-the-SE shearing.

综上所述，在龙门山北段，劈理直立带向 NE 延伸至阳平关镇表现已经不明显，显示出龙门山主变形期造山作用向 NE 方向的尖灭，而在碧口地块东部，受到勉略缝合带的影响，已将薄弱带北侧的变形部分改造，而表现出向 S 的运动学特征。

3.6 Timing of the main phase deformation

1) Relationship of strata involving deformation

龙门山这期强烈的逆冲推覆构造形成时间存在很大争议。龙门山地区卷入韧性变形最年轻的地层为上三叠统须家河组，下侏罗统白田坝组不整合盖在褶皱变形的须家河组地层之上(Figure 3.31)，这期角度不整合在龙门山北段尤其显著。根据地层卷入变形关系表明这期主变形期发生在 T_3-J_1 之间(四川省地质矿产局, 1991; 许志琴等, 1992; Burchfiel et al., 1995; Jia et al., 2006)。此外，在四川西部周缘前陆盆地沉积环境在晚三叠世由浅海碳酸盐台地逐渐转变为陆相碎屑岩沉积环境，同样指示晚三叠世龙门山逆冲推覆带向 SE 方向的逆冲作用(Chen et al., 1994a; Li et al., 2003)。

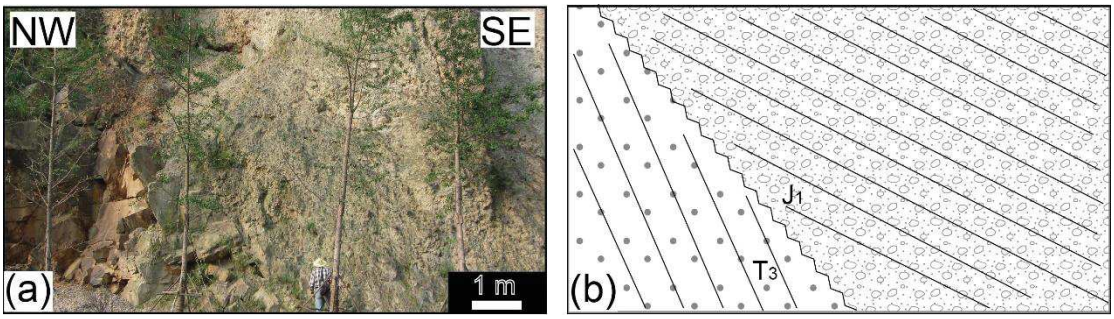

Figure 3.31 Early Jurassic unconformable cover on the deformed Late Jurassic Xujiahe formation

在松潘-甘孜褶皱带，上三叠统西康组经历强烈褶皱变形后，大部分地区上升隆起成为剥蚀区，但在局部地区发育有晚三叠世晚期的沉积(八宝山组)，不整合覆盖在褶皱变形的西康组地层之上(陈社发等, 1994a)，明显早于龙门山主变形期。

如前所述，无论是龙门山北段侏罗纪地层自身发生变形，还是龙门山南段安县-灌县断裂逆冲至侏罗纪地层之上，均表明龙门山地区叠加了侏罗纪后期的改造作用(Burchfiel et al., 1995; Jia et al., 2006)。但关于主变形期构造几何学形态最终定性于新生代还是中生代一直存在很大争议(Meng et al., 2006; Burchfiel et al., 2008)。

2) Pollen analysis of the bricciated limestone at the leading edge of the Tangbazi klippe

Introduction

As typical representations of a thin-skinned structure, klippen have gained much attention from structural geologists all over the world. The Longmenshan belt is an important geological boundary that separates the greatly deformed and metamorphosed rocks of the Songpan-Ganze Fold belt to the NW from the relatively less deformed sediments in the Sichuan Basin (Figure 3.1). Since the devastating earthquake that occurred in Wenchuan and Lushan, Longmenshan has drawn even more interest from researchers. The Longmenshan belt has developed a series of NE-SW trending fold-and-thrust structures represented by a series of nappes and klippes, which is the best natural laboratory for thin-skinned tectonics. Dozens of klippes are distributed in the center section of Longmenshan belt, such as the Jianfengding, Dayudong, Tiantaishan, Tangbazi, etc. (Shi, 1994; Figure 3.32). These thrusts have important significance for the tectonic evolution of the southeast Yangtze block and

the uplift process of the Tibetan Plateau. The timing of the emplacement of these klippes is very important; it would greatly contribute to the elucidation of the emplacement mechanism and might even allow an explanation of the uplift process of the Longmenshan and the whole Tibetan Plateau. The Bailuding klippe, the Tangbazi klippe and the Gexianshan klippe, located in the center of Longmenshan, are considered as typical klippes in the area, and provide a perfect location to research their timing and emplacement mechanism as well as the uplift scenario of the entire Longmenshan belt.

Regional geological setting and research status

The Longmenshan thrust belt originates in Guangyuan city and merges with the Micangshan to the northeast, ends at Tianquan city and is truncated by the Xianshui river fault to the southwest. The Longmenshan belt is about 500km long and 35-50km wide and regionally composed of three faults that strike northeast and steeply dip to the northwest (Figure 3.1). A continuous southward (Yan et al., 2011) or southeastward thrust since the late-Triassic (Luo, 1991; Xu et al., 1992; Chen et al., 1994a) and extensive uplifting induced by the collision of the Eurasian and the Indian plates during the Cenozoic formed the highest mountains and caused the landscape to exhibit greater relief than anywhere else on the Tibetan Plateau (Clark et al., 2000; Kirby et al., 2002; Hubbard et al., 2009). Field observations have shown that both overturned folds and thrusts intra nappe and klippe consistently demonstrated a southeastward thrust (Burchfiel et al., 1995; Xu et al., 1992; Jia et al., 2006). Seismic data further revealed that the collision of Eurasian and Indian plates during the Cenozoic resulted in different deformation characteristics along the Longmenshan belt (Jia et al., 2006).

The klippe and nappe along the Longmenshan belt are mainly composed of Devonian to early-Triassic strata and each klippe has different types of strata (Figure 3.32). The Tangbazi and Gexianshan klippe are mainly composed of Permian light grey of medium thickness massive limestone and dolomitic limestone and contain micro-fossils such as Fusulinid, Brachiopoda, Bryozoa, etc. Further west, the Dayudong and Jianfengding klippe contain different tiny early-Triassic strata, and its biostratigraphic age has been determined by Lamellibranchia such as *Claraia* (Figure 3.32; BGMRSP, 1991).

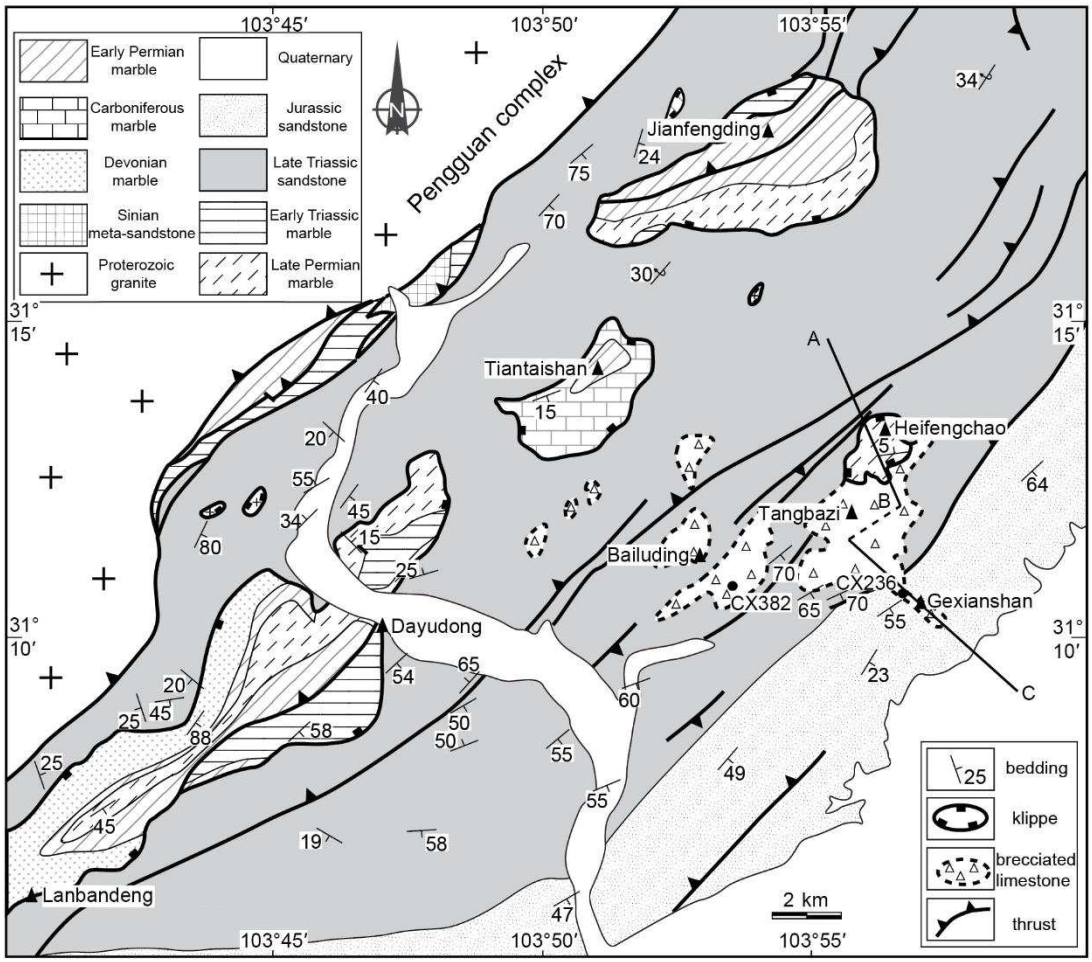

Figure 3.32 Geological map of the Pengguan klippes (modified after a regional 1:200 thousand geological map of Guanxian)

The timing of these klippes is still in dispute (Xu et al., 1992; Burchfiel et al., 1995; Meng et al., 2006). Traditionally, a Mesozoic thrust model has been proposed, based on following evidence: 1) the newest strata evolving in the thrust belt is a late-Triassic Xujiahe formation (Xu et al., 1992; Dirks et al., 1994; Chen et al, 1996; Worley et al., 1996), 2) the sedimentary environment confirmed that the Xujiahe formation is a typical foreland basin (Chen et al., 1994b; Li et al., 2003), 3) the results of $^{39}Ar/^{40}Ar$ dating of the newly formed mica and U/Pb dating of the syn-tectonic granite zircon in Longmenshan area are exclusively between 153-232Ma (Zhou et al., 2002; Huang et al., 2003; Yan et al., 2008, 2011; Lu et al., 2010), 4) isotopic dating of authigenic illite isolated from the bottom boundary fault of the largest Baishi-Goujia klippe combined with zircon fission track dating of the hanging wall of the Yingxiu–Beichuan fault zone that constrained the emplacement age of the Longmenshan klippe fall between 171-180Ma (Zheng et al., 2014), 5) regional unconformity between extensively folded late-Triassic strata and relatively weak deformed Jurassic strata

exists in the center and north segment of the Longmenshan belt (BGMRSP, 1991; Xu et al., 1992; Burchfiel et al., 1995; Chen et al., 1996; Jia et al., 2006). 6) both overturned fold and layer-parallel slip in each klippe and nappe consistently exhibit top-to-SE movement (Xu et al., 1992; Chen et al., 1996; Burchfiel et al., 1995; Jia et al., 2006; Yan et al., 2011), and 7) the thermal characteristics revealed by Raman spectroscopy of carbonaceous material just beneath the klippe indicate a temperature greater than 400 °C, suggesting that the klippes have a tectonic origin (Robert et al., 2010). In addition, the Longmenshan lacks a typical Cenozoic foreland basin and a massive Cenozoic deformation record (Xu et al., 1992; Burchfiel et al., 1995). Most of the klippes, such as the Tiantaishan klippe, the Jianfengding klippe and the Dayudong klippe, etc., occur on folded late-Triassic strata (Figure 3.32). Taken together, the evidence cited above strongly suggests that the emplacement of the Longmenshan klippes are intrinsically related to an extensive regional thrust.

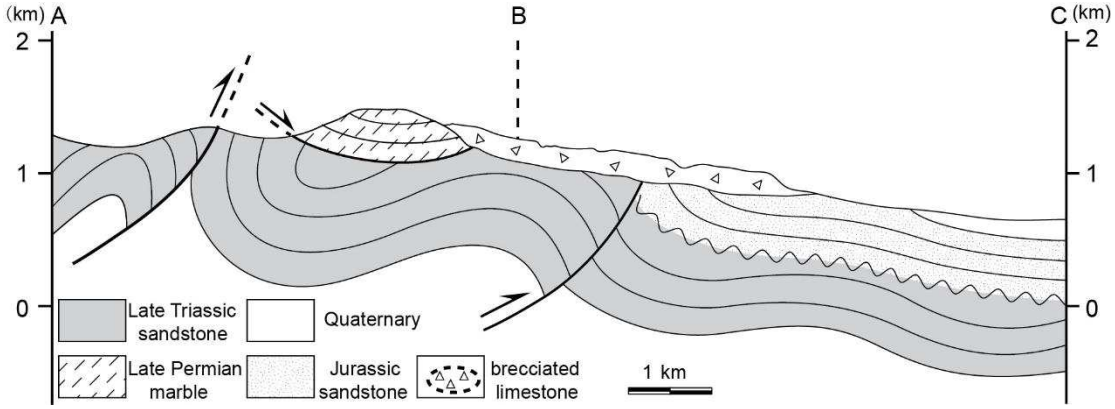

Figure 3.33 Cross-section of the Tangbazi area (the location is shown in Figure 3.32)

The Tangbazi-Gexianshan klippe is composed of Permian limestone, which forms a long narrow tail extending eastward and sits on Upper Jurassic strata overlaying continuous Cretaceous-Eocene sequences (Figures 2 and 3). This phenomenon clearly shows that the klippe must have been emplaced post-Eocene, which is the foundation that supports the argument that the entire klippe belt in Longmenshan was formed during the Cenozoic (Bian, 1980; Li, 1989; He, 1992; Shi, 1994; Han et al., 1994, 1999; Burchfiel et al., 1995; Meng et al., 2006; Jia et al., 2006; Han et al., 2006, 2008, 2009; Zhou et al., 2006a, 2006b). Actually, Bian et al. (1980) first reported this special “tail”; their field observations and detailed structural analysis almost demonstrated the Indosinian (Triassic) deformation in Longmenshan, except for this strange “tail”. Finally, they proposed a Cenozoic modification to explain the reason for this unusual strata. Burchfiel et al. (1995) claimed that the main

deformation period of the Longmenshan occurred between late-Triassic to the Jurassic, giving the same reasons as Bian (1980), a partial reactivation during the Cenozoic. The narrow "tail" of Gexianshan is a suite of brecciated limestone (Shi, 1994; Han et al., 1994, 1999; Burchfiel et al., 1995; Meng et al., 2006). Shi (1994) suggested this brecciated limestone was formed by a southeastward gravitational slip induced by a large gravitational gradient (because of the extreme altitude on the margin of the Tibetan Plateau). A combined strain variation from the extension in the rear to a contraction in the leading edge of the klippe has led to the proposal of a gravity-driven generation during the Cenozoic (Wu et al., 1991, 1999; Han et al., 1994, 1999; Shi, 1994; Meng et al., 2006). Other researchers think that the characteristics of the brecciated limestone in Gexianshan are approximately similar to glacial erratic boulders and they think that the Longmenshan klippe is the result of glaciation in Qinhai-Tibet during the Pleistocene (Han et al., 1994, 1999; Zhou et al., 2006a, 2006b).

In summary, the composition, timing and mechanism of the Gexianshan narrow "tail" are of vital importance to explain the timing and the emplacement mechanism of the Longmenshan klippe. In order to clarify these issues, detailed field observations, petrological analysis and paleontological analyses have been done.

Petrological characteristics

Field observations show that the leading edge of Tangbazi and Bailuding "klippe" is completely brecciated limestone and the diameter of the breccia ranges from 0.5-15 cm (Figure 3.34a b). Some of the breccia are lightly rounded while the majority have a conserved angular shape (Figure 3.34a b). Although the shallow ground allowed extensive weathering, several outcrops could be seen and fresh breccia was common. All of the brecciated limestone is uniform and devoid of any sign of a stack rhythm or layer characteristics. Especially in a cross-section from a cement quarry near the Biluding "klippe", similar brecciated limestone was evident everywhere (Figure 3.34a). The breccia is completely angular and relatively depth of color than the agglutinate. Both the breccia and agglutinate are composed of pure limestone plus a minor pelitic component; however, impurities cannot be recognized with the naked eye.

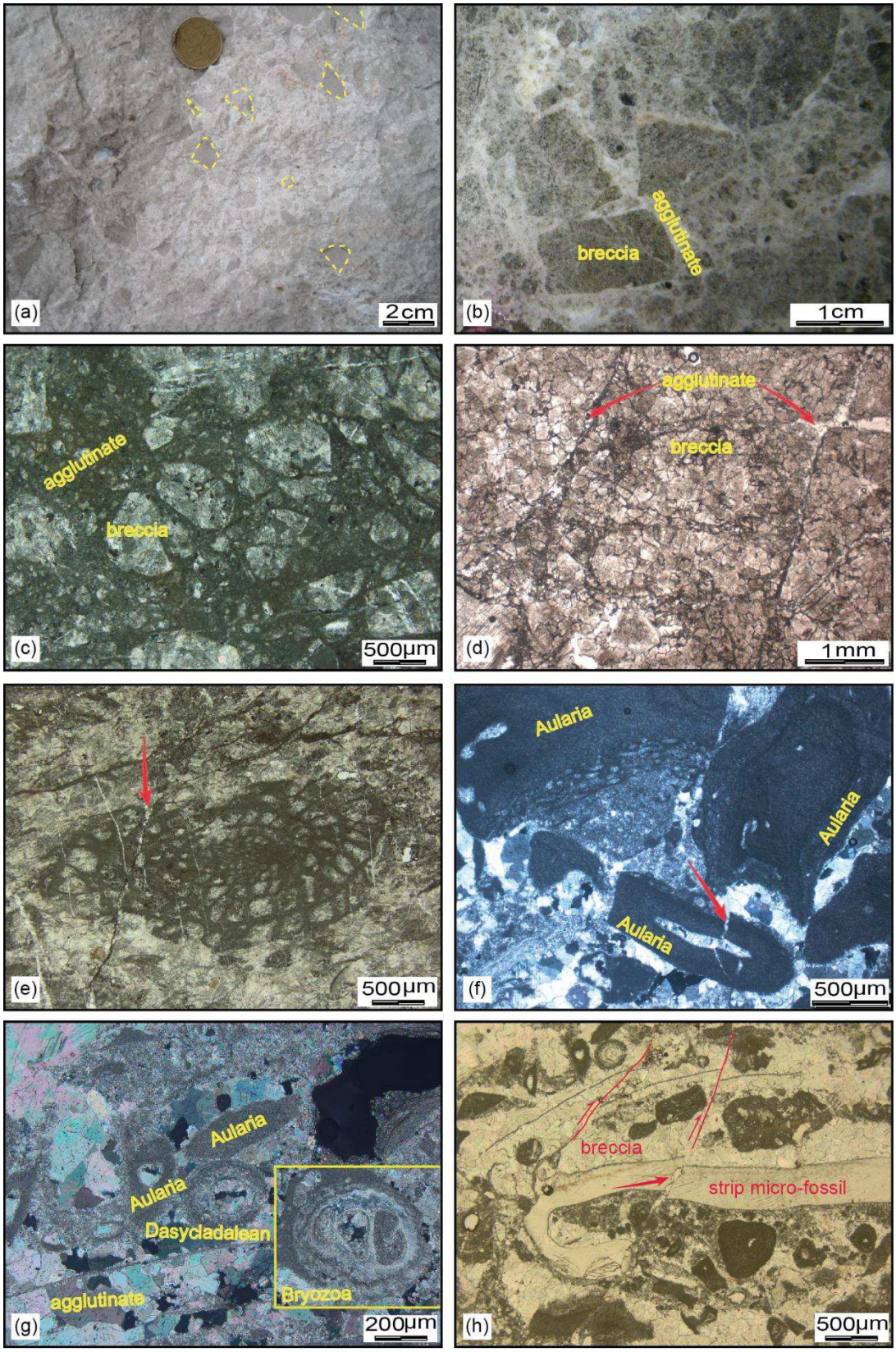

Figure 3.34 Photographs of the crumbled breccia.

a、field photograph of CX382 breccia; b、field photograph of CX236 breccia; c、micrograph of CX236, CPL; d、micrograph of CX382, PPL; e、fusulinid in the breccia of CX236 with micron fracture (marked with red arrow), PPL; f、Aularia in the breccia of CX236 with micron extension fracture (marked with red arrow), CPL; g、Bryozoa and Dasycladalean in the breccia

of CX236, CPL; h、strip micro-fossil in the breccia of CX236 with zigzag fracture (marked with red arrow), PPL

Samples collected from the leading edge of the Tangbazi and Biluding klippe were designated as CX236 and CX382, respectively (Figure 3.32). Thin sections were made from these two samples and observed under a polarization microscope. A characteristic high white interference color could be recognized under Crossed Polarized Light (CPL). The breccia was mainly composed of bioplastic limestone and partially composed of micro-crystal and dolomitic limestone. The agglutinate was mainly calcareous with a tiny pelitic component (Figure 3.34c). Numerous micro-paleontological fossils had developed in the CX236 breccia, such as Fusulinid (Figure 3.34e), *Aularia* (Figure 3.34f g), Bryozoa (Figure 3.34g), Dasycladalean (Figure 3.34g) and a long strip of micro-fossils (Figure 3.34h), which confirmed the protolith of the breccia was classified as a typical bioplastic limestone; the fossil assemblage and characteristics indicate that the protolith breccia is from the upper Permian Changxing stage or Wujiaping stage (Yang, 1988; Sha et al., 1990; BGMRSP, 1991). Some Fusulinid and *Aularia*s evidence micro-cracks with no evident relative displacement from filling carbonates (Figure 3.34e f). A strip micro-fossil had a tiny crack with a displacement of approximately tens of microns and the fracture had a zigzag shape (Figure 3.34h). The fossil in the breccia was nearly preserved in its original sedimentary status with no sign of any ductile deformation or evident displacement (Figure 3.34e f h). No micro-fossils were found in thin sections of CX382 and its optical characteristics suggest dolomitic limestone properties (Figure 3.34d). Both the optical characteristics of the breccia and the fossil abundance in the breccia definitely indicate that CX236 and CX382 are different, which indicates that the protoliths of these two breccias belong to strata from different ages. The protolith of the breccia of CX382 is composed of dolomitic limestone without any fossils and might indicate early-Triassic strata in the Longmenshan area (Sha et al., 1990).

Pollen analysis

The timing and mechanism of the generation of the brecciated limestone are of vital importance in understanding the timing and the emplacement mechanism of the Longmenshan klippe. In order to identify its actual age, we extracted pollen from the samples CX236 and CX382 (the sample locations are shown in Figure 3.32). In order

to avoid pollution from modern pollen, all brecciated limestones were sampled from the inner core of a cement quarry.

The brecciated limestone was smashed to pieces with a hammer, sifted (diameter of 0.45μm), and the 100g of powder that passed through the sifter was collected. Lycopodium spore tablets (27637 grains) were added to the samples to facilitate pollen concentration calculations. To improve the sample clarity, the samples were treated with hydrofluoric acid (Moore et al., 1991) and the residues were further concentrated by centrifugation. The pollen residues were suspended in glycerol. A Leica DM 4000 B microscope at ×400 was used to count pollen grains.

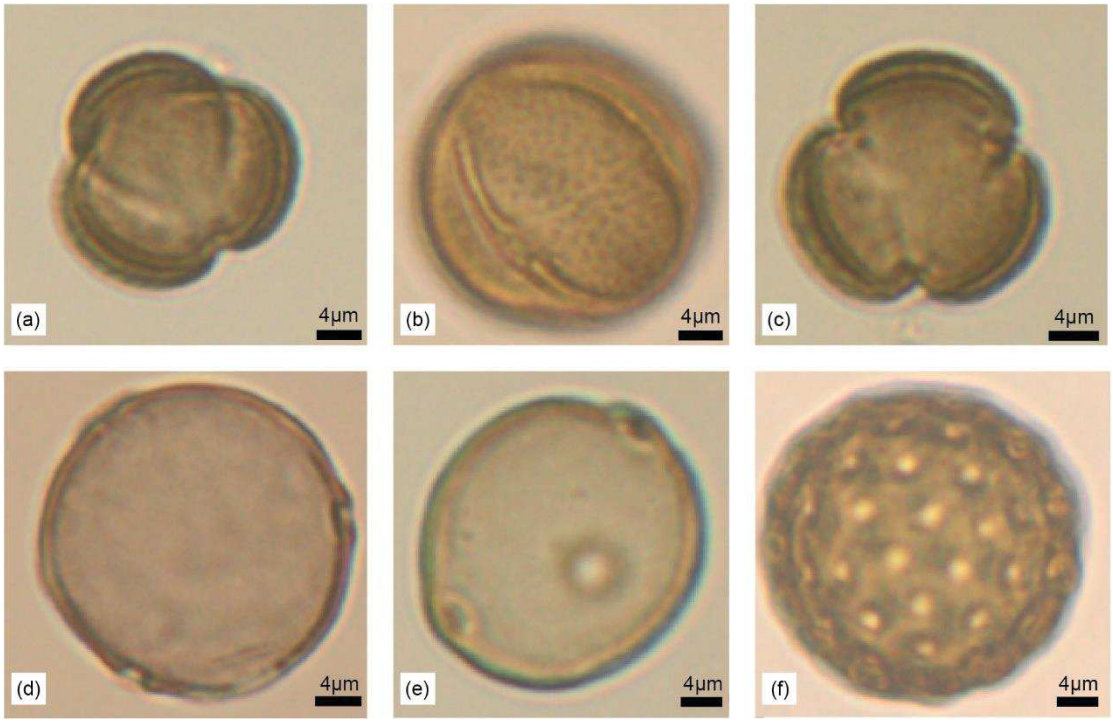

Figure 3.35 Photographs of pollen extracted from the crumbled breccia.

a、side view of Artemisia; b、equatorial view of Artemisia; c、polar view of Artemisia; d、polar view of Chenopodiaceae; e、equatorial view of Chenopodiaceae; f、Moraceae

Both CX236 and CX382 contained the same species of pollen, varying only in diversity and quantity. Three principal types of pollen were recognized: *Artemisia*, Moraceae, and Chenopodiaceae. *Artemisia* has short spines on its thick-walled cypselasis, nearly rounded with three colporates (Figure 3.35a b c) and the colporates gradually narrow toward the poles (Figure 3.35b). Moraceae are nearly rounded or elliptical with an average size of 25.5×28μm and contain 3 to 4 colporates (Figure 3.35d, e). The grains usually appeared on the cypselasis and a bit beyond the pollen outline (Figure 3.35d). Chenopodiaceae is rounded or semi-rounded with a diameter

between 12-30μm. Approximately 16 to 90 holes are well-distributed on its thin and transparent cypselasis; the outline of this pollen has a wave-like contour. Measurements of these three pollen grains obtained by detailed microscopic counting at a 400 × magnification and equal proportion calculation are shown in Figure 3.36.

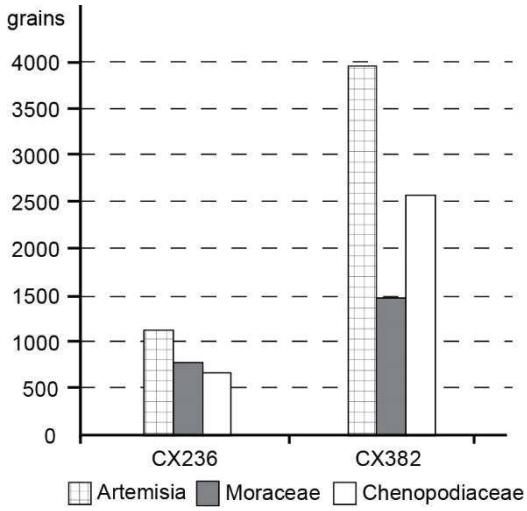

Figure 3.36 Histogram showing the statistical quantities of the pollen

The columns in Figure 3.36 show that the maximum grains of *Artemisia* in CX236 and CX382 were greater than 1000 and 4000, respectively, which is sufficient to prove that the pollen was contained in the brecciated limestone. The pollen was colored and uniform, which is completely different than the modern pollen (Sun et al., 1997). The similarity of the pollen status in CX236 and CX382 allows the further conclusion that the vegetal assemblage that prevailed in the Longmenshan area was exclusively arid or subarid vegetation (Miao et al., 2011), totally unlike the modern vegetation in this area.

The earliest reported Asteraceae fossils recorded are probably those found in the Eocene of the western Tarim basin, south Xinjiang (Zhang & Zhan, 1991), which are characterized by medium to long spines. Nevertheless, the *Artemisia* pollen in this study had short spines and thick-walled cypselas, which appeared slightly later (Wang et al., 2004; Figure 3.35). Wang et al. (2004) suggested there were three major stages in *Artemisia*'s evolutionary history based on its morphological data: 1) *Artemisia* did not become abundant until the Middle to Late Miocene, 2) it became highly developed during the Pliocene and became the principal genus in north China and 3) the quaternary was a major period for the diversification and further worldwide expansion of *Artemisia*. *Artemisia* became abundant from the Miocene to the Pliocene in Tibet, Tarim and Ningxia (Wang, 1996; Zhang et al., 2000; Wu et al., 2002). Since

the protolith of the breccia is Permian bioplastic limestone, we can conclude that the *Artemisia* originates exclusively from the agglutinate. That is to say, the timing of the brecciated limestone and the appearance of the Artemisia is simultaneous. The origin and development of plants are considered to be closely related to environmental trends. Artemisia grows mainly in arid and semiarid temperatures and is usually considered as an indicator of moderate to low precipitation (Wu, 1995; Wang et al., 2004; Miao et al., 2011), whereas Chenopodiaceae indicates a saline to non-saline desert environment (Miao et al., 2011). These two taxa have been often used as an indicator of an arid or semiarid paleo-climate (Miao et al., 2011).

Discussion

Detailed field observations and petrological analysis indicate that the brecciated limestone of the Tangbazi and Gexianshan have some typical characteristics as follows: 1) the majority are angular-shaped breccia but fewer weak rounded breccia also exist and the diameter of the breccia range from several millimeters to tens of centimeters (Figure 3.34a, b) and 2) the breccia and the agglutinate are totally consumed when sufficient hydrochloric acid is added, leaving only a thin pelitic film floating on the solution, combined with a characteristic high white interference color observed under CPL (Figure 3.34c). We believe the breccia and the agglutinate are composed of carbonate with a small pelitic component. Post-Eocene *Artemisia* extracted from this suite suggest that the "tail" is a product of breccial re-sedimentation in the Cenozoic rather than a Permian strata as depicted on the regional geological map.

Breccia can be classified as explosion breccia, karst breccia, fault related breccia, glacial drift breccia or crumbled breccia according to its genesis. The genesis of the Bailuding and Tangbazi breccia by explosion is the last consideration because of its location far away from magmatism. Karst breccia usually appear where carbonates are well distributed, originating from the collapse of karst caverns or from water transportation. However, the appearance of arid to semiarid *Artemisia* and Chenopodiaceae is unlikely in such a humid karst water environment, so breccial generation via karst collapse is also unlikely. The breccia in Tangbazi and Bailuding share nearly the same characteristics; a few researchers think that the breccia is a kind of fault cataclasite at the bottom boundary fault of the klippe (Shi, 1994). However, we discovered many Permian fossils in the breccia, such as Fusulinid (Figure 3.34e),

Aularia (Figure 3.34f g), Bryozoa (Figure 3.34g), Dasycladalean (Figure 3.34g) and long strip micro-fossils (Figure 3.34h). The fossils in the breccia were almost preserved in their original sedimentary status with no sign of any ductile deformation nor evident displacement which would indicate a cataclysm (Figure 3.34e f h). The zigzag shape fracture preserved in the strip fossil (Figure 3.34h) is an index of instantaneous transtension in place. If the cataclasite fault movement model is correct, straighter boundaries and more fragile displacement should exist in these micro fossils, which is not compatible with their observed characteristics (Figure 3.34e f h). More importantly, *Artemisia* in CX382 is nearly four times more abundant than CX236 (Figure 3.36). There are two possible reasons for the difference in abundance during the formation of the brecciated limestone: 1) pollen abundance is differentiated by the distance between the regions (Miao et al., 2011), however, the distance between Bailuding and Tangbazi is less than 3 kilometers, which is too short to account for the observed differences, and 2) the morphology and quantity of the *Artemisia* has been evolving since the Eocene (Miao et al., 2011). This evolution of the diversity might be the only reason for the difference in abundance in one area. The huge pollen differences observed in CX382 and CX236 indicate a different timing of the breccia in these two sites, which is at odds with a bottom boundary fault movement model that requires synchronous timing of the breccia along the whole fault.

Another possible mechanism is glacial drifting. The brecciated limestone could have arisen from massive pieces of limestone smashed by large ice sheets on the Qinhai-Tibet and frost-splitting during the Quaternary before the re-sedimentation and cementing of the breccia (Han et al., 1999). However this explanation is contested by the following facts: 1) A great deal of Carboniferous to Permian limestone is exposed in the hinterland of the Longmenshan at higher elevations and lower temperatures, which is a condition likely to form glacial breccia, but no sign of such brecciated limestone has been found until now, and 2) *Artemisia* isolated from the brecciated limestone is definitely unlike the Quaternary pollen, but the glaciation in Qinhai-Tibet Plateau occurred during the Pleistocene (Li et al., 2004). This mechanism does not make sense with respect to time.

Crumbled breccia refers to generation by a gravitational collapse or landslide because of a scarp or a steep slope. Weakly rounded and angular breccia coexsit in the

samples. The components of the agglutiante were governed by the environment while the crumbling occurred. Only this mechanism could cause the instantaneous extension to form a zigzag fracture (Figure 3.34h). Immediate sedimentation and cementation are the key factors that allowed the preservation of these micro-structures. No further continuous deformation and movement occurred so the fragile relative displacement in the micro-fossils is not very evident. So we can conclude that the brecciated limestone in the research area is crumbled breccia.

The micro-fossil assemblage in CX236 date its protolith to the late-Permian, which is concordant with the nearby intact limestone from Heifengchao (Figure 3.32; Figure 3.34; Sha et al., 1990; BGMRSP, 1991). The protolith of CX382 may indicate low-Triassic strata due to the dolomitic interference color and lack of fossils in the breccia (Sha et al., 1990). The different time reflected by the *Artemisia* abundance differences indirectly indicate that at least two collapse events occurred in the Longmenshan area. A high gravity gradient was required for crumbling to occur. Furthermore, a large scale collapse along the Longmenshan belt (Figure 3.32) was required for a quick uplifting during this time. So, we arrive at the conclusion that the elevated topography in this area required at least a two-phase growth, which agrees well with the low temperature dating results (30-25Ma and 15-10Ma; Wang et al., 2012).

According to the field observations, we redefined the distribution of the brecciated limestone and separated the Cenozoic crumbled breccia from Permian limestone in the Tangbazi and Bailuding areas (Figures 2, 3). The intact Permian limestone showed the original bedding while the breccia was distributed irregularly. Part of the brecciated limestone has a narrow “tail” extending southeastward and covering Jurassic-Quaternary rocks, creating an anomalous stratigraphic relationship of Permian limestone sited on a Jurassic strata (Figures 2, 3), which is a phenomenon caused by a Cenozoic gravitational collapse. Coincidently, the boundary of the “tail” in Gexianshan agrees well with the isoheight contour line (BGMRSP, 1991), which indicates that the timing of the “tail” is too recent to have been destroyed by weathering. After the removal of the brecciated limestone, the main part of the Tangbazi klippe just rests on a folded late-Triassic strata and is far away from the Jurassic rock (Figure 3.33). It is unreasonable to postulate a Cenozoic emplacement of the klippe based on the aforementioned stratigraphic overlay relationship. In our opinion, the timing and emplacement mechanism of the klippe in the Longmenshan

belt is more likely intrinsically related to the regional thin-skinned structural during the Mesozoic.

An updated model of the brecciated limestone and the klippe is shown in Figure 3.37. First, a southward (Yan et al., 2011) or southeastward thrust beginning in the late-Triassic (Xu et al., 1992; Burchfiel et al., 1995; Chen et al., 1996) pushed the Permian strata covering onto the folded late-Triassic rock (Figure 3.37a). The main thrust activity did not cease until the Jurassic. Then the folded Triassic rocks unconformity overlain by Jurassic sandstone. The elevated topography began to grow because of the high angle thrust beginning in the early-Cretaceous (Chen et al., 1994b; Zeng et al., 1995; Yan et al., 2011), which accelerated the erosion of the earlier placed Permian limestone sheet (Figure 3.37b). By the Eocene, the topography of Longmenshan has achieved a high altitude and a limestone collapse caused the incorporation of contemporary pollen (Figure 3.37c). Finally, the brecciated limestone was naturally selected, presenting the aspects seen today (Figure 3.37d).

Conclusion

According to detailed field observations and petrological analyses, we recognized totally two different parts of the Gexianshan and Tangbazi klippe: crumbled breccia and a massive klippe (Figures 2, 3). The post-Eocene age of the brecciated limestone could be verified by the plethora of Cenozoic pollen contained in the agglutinate, which is contradictory to the Permian dating annotated on the geological map. Furthermore, the large-scale of the crumbled breccia in the Longmenshan area indicated rapid uplifting and the achievement of high altitude.

The pollen abundance differences demonstrated a different age for the crumbled breccia in Bailuding and Tangbazi, further indicating the existence of at least a two-phase growth of the elevated topography, which agrees well with the low temperature dating reported (30-25Ma and a 15-10Ma rapid uplifting).

After removal of the Cenozoic brecciated limestone, the massive klippe, the main part of the Heifengchao klippe was sited on a folded late-Triassic strata (Figure 3.33). The leading edge of the klippe is far away from the Jurassic boundary. A conclusion that a previous Cenozoic emplacement should be based on the relationship between the crumbled breccia and the underlying concordantly deformed Jurassic-Eocene rocks is unreasonable. A combination of regional isotopic data and field observations indicate a Mesozoic thrust model of the klippe in the center of the Longmenshan.

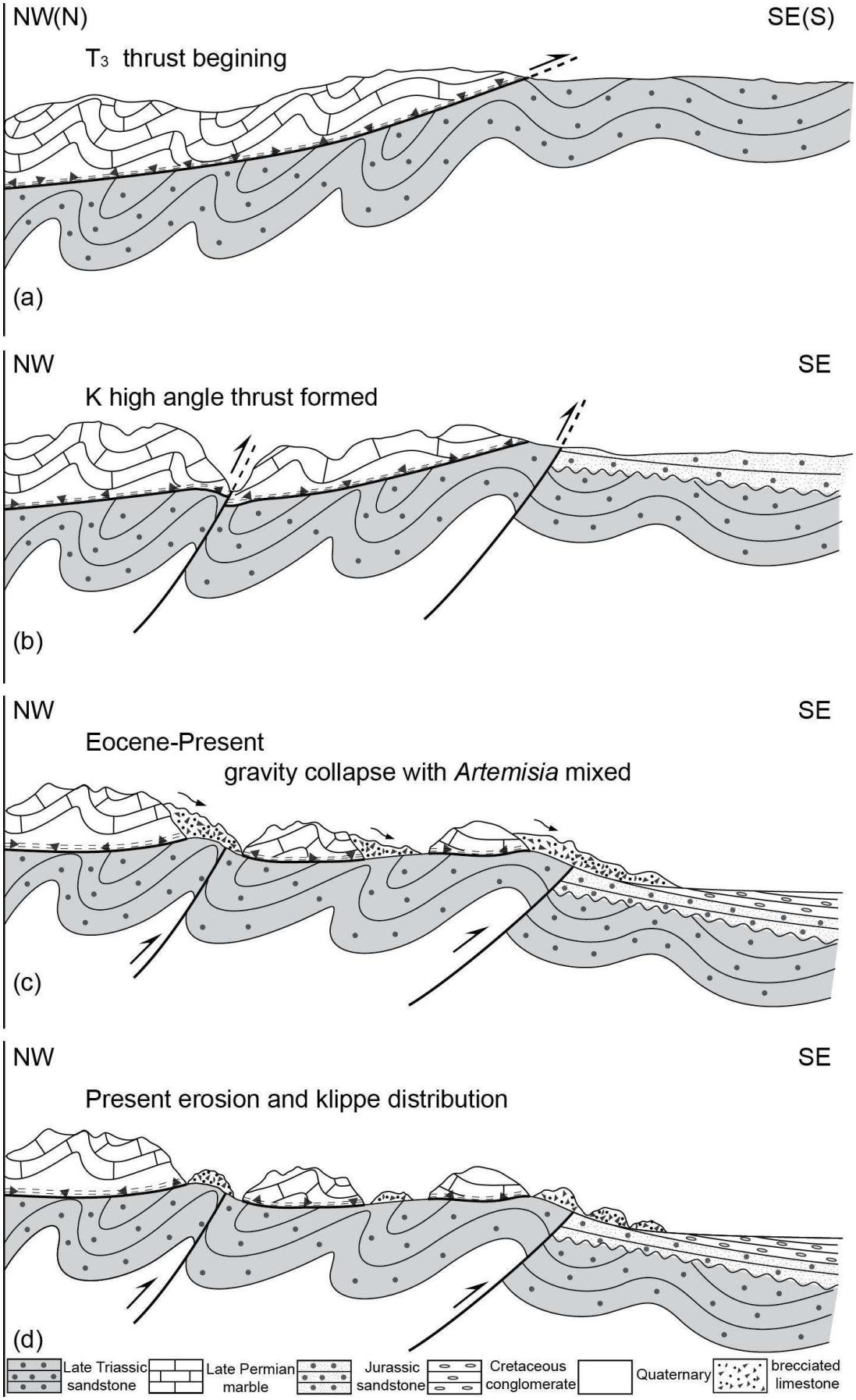

Figure 3.37 The evolutionary model of the Longmenshan belt

3) Geochronological constraints

Previous results

龙门山以西松潘-甘孜褶皱带发生经历 T_3 末期的强烈褶皱作用后被广泛的岩浆岩侵入切割(Figure 3.1)。前人对松潘-甘孜内广泛分布的岩浆岩进行了详细的地球化学成分分析和年代学工作。大量工作表明，松潘-甘孜内广泛的岩浆作用，主要源于下地壳剪切生热的部分熔融，伴有扬子古老基底物质，部分岩体还混有新生幔源成分(黄永健等, 2002; Roger et al., 2004; 胡健民等, 2005; Zhang et al., 2006; Xiao et al., 2007b; Zhang et al., 2007; 赵永久等, 2007; Sigoyer et al., 2014)。对松潘-甘孜褶皱带及龙门山沿线的岩体锆石 U/Pb 结果统计后给出两个非常明显的峰值：211.7Ma 和 811.2Ma(Figure 3.38 a)。其中新元古代年龄主要对应龙门山 NE-SW 走向的杂岩体年龄。部分新远古带年龄来自松潘-甘孜岩体内寄生锆石核部年龄，从侧面论证松潘-甘孜下部存在古老扬子基底的物质(Roger et al., 2004; 胡健民等, 2005)。

龙门山西部松潘-甘孜褶皱带内大规模岩体切穿褶皱带内广泛的褶皱形迹，并发育烘烤边和环状接触变质带，表明岩体侵位于强烈褶皱变形之后(四川省地质矿产局, 1991; Worley and Wilson, 1996; Roger et al., 2004)。因此，211.7Ma 的峰值年龄可作为松潘-甘孜强烈褶皱变形的时间上限。此外，在松潘-甘孜褶皱带南部，丹巴穹窿的马奈岩体，该岩体北部发生强烈糜棱岩化，其几何学和运动学与区域上大型向南的褶皱拆离变形相吻合，但向南，岩体逐渐过渡为块状未变形状态，因此被解释为同构造侵入体，年龄为 195Ma (Calassou, 1994)。Sigoyer et al.(2014)在对松潘-甘孜地区岩浆岩进行综述性研究时认为，可能由于方法的原因导致马奈岩体 195Ma 的年龄偏年轻，因此同构造变形的时间还要更老一些，这与广泛构造后期侵入的岩浆岩年龄相吻合。

前人对龙门山北段碧口地区、中段彭灌杂岩地区、南段宝兴杂岩地区以及丹巴穹窿地区进行了广泛详细的云母、角闪石的 $^{40}Ar/^{39}Ar$ 工作(Dirks et al., 1994; Huang et al., 2003; Zhou et al., 2008; Liu et al., 2010; Yan et al., 2011; Weller et al., 2013)。对所有已发表 $^{40}Ar/^{39}Ar$ 年代学结果进行统计后，给出许多年龄峰值(Figure 3.38 b)。比较典型的一组结果在 236-258Ma 之间，可能对应峨眉山玄

武岩喷发事件(Yan et al., 2011)。随后自 200Ma 以来，一直都有 $^{40}Ar/^{39}Ar$ 年龄的冷却记录，可能代表多期构造事件。

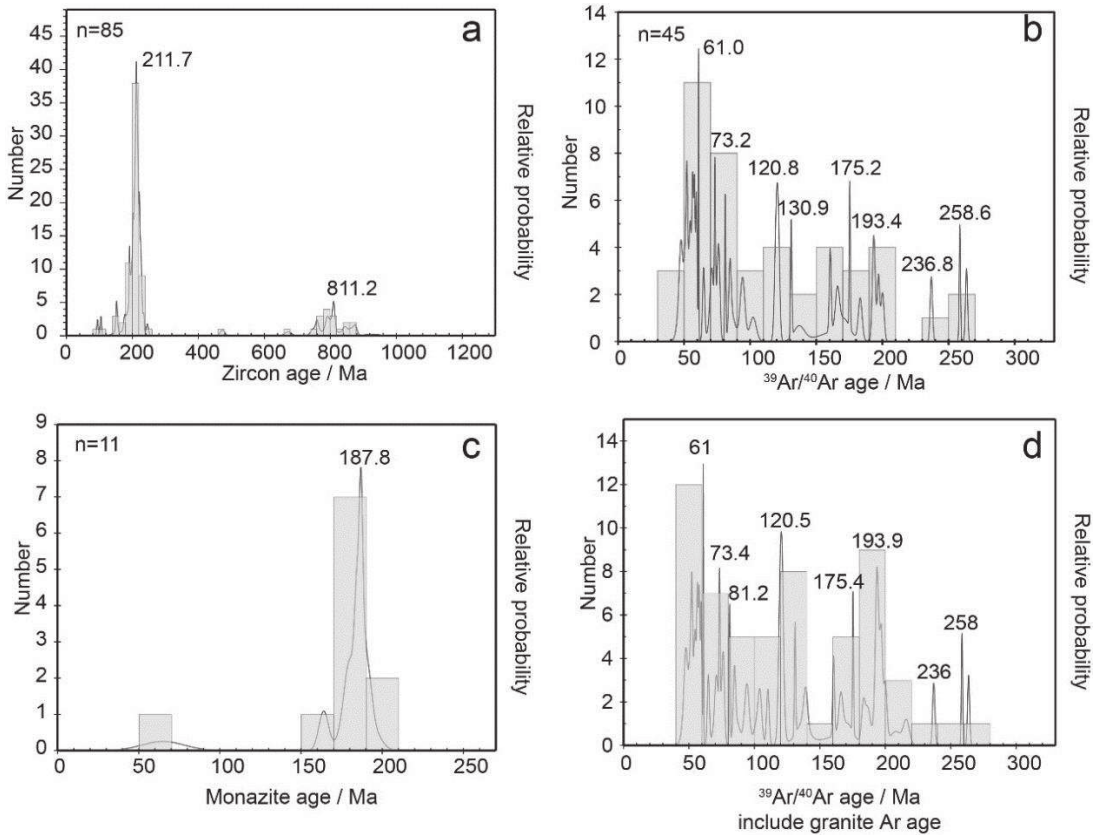

Figure 3.38 Geochronological result statistics of the Longmenshan and adjacent areas

(a) Zircon U-Pb dating of the granites in the Songpan-Ganzi terrane and the Longmenshan thrust belt; (b) $^{40}Ar/^{39}Ar$ dating on newly formed Amphibole, micas; (c) U-Th-Pb dating on monazite from the Longmenshan and adjacent areas; (d) $^{40}Ar/^{39}Ar$ dating on metamorphic minerals of the Longmenshan and adjacent areas.

以丹巴穹窿为核心的巴罗型变质带内强烈变质的片岩也有研究者做过详细的独居石测年工作，从夕线石带到周边的黑云母变质带内独居石原位 U-Th-Pb 定年结果给出 187.8Ma 的峰值年龄(Figure 3.38 c; Huang et al., 2003; Weller et al., 2013)，可能代表这期主变形期后的冷却年龄。

Syntectonic granite—Mupi granite

在江油-平武北段(Figure 3.1T_7 和 3.22)，平武县城向 N 出城 10km，木皮岩体也表现出显著的同构造岩浆岩特性。平武以北属于龙门山构造带的西部带，整体上表现倾向 S 的面理和上部向 N 的运动学特征。木皮岩体主要为二长花岗岩，含斜长石巨斑晶。野外露头上，木皮岩体南部发生明显的面理化，其几何学形态与围岩非常一致，都表现出一致的向 S 倾的面理(Figure 3.39 a)。采集定

向样品，沿 XZ 切面的手标本尺度上，长石的 σ 旋转残斑指示上部向 N 的剪切变形，与围岩运动学特征一致(Figure 3.39 c)。这种强烈的面理化变形，向岩体北部逐渐减弱，并最终完全变成块状未变形岩体(Figure 3.39 b)。因此，从岩体的几何学和运动学特征表现形式来看，我们将木皮岩体解释为同构造岩体。显微镜下，长石发生破裂，并灌入石英(Figure 3.39 d)，进一步佐证在岩体未完全固结时经历了同期变形，导致已结晶的长石发生脆性破裂。

鉴于对木皮岩体构造指示意义的认识，我们对木皮岩体进行了采样，从木皮岩体中挑选出锆石，研究了其显微特征和阴极发光图像，对其中具有清楚振荡环带的锆石进行了 SHRIMP 定年分析。锆石分选采用重液浮选和电磁方法完成，锆石 U-Pb SHRIMP 定年在中国科学院地质与地球物理研究所离子探针实验室完成。

样品中锆石多为短柱状或长板状，长宽比在 1:1 到 3:1 之间(Figure 3.40)。锆石多具有明显的岩浆成因的振荡环带，且 Th/U 比值多大于 0.1，为典型的岩浆锆石。一部分锆石含有明显的继承核，CL 照片显示核部比边部明亮，其幔部也具有典型的岩浆生长锆石特征，CL 图片较暗(Figure 3.40)。显著的 CL 照片差异显示出明显两个不同世代的锆石。

其中 20 颗锆石给出非常协和的年龄在 219.1±1.7Ma，指示了木皮岩体冷凝结晶年龄，而锆石核部的年龄为 729 Ma 左右的新元古带年龄，这与龙门山广泛分布的新元古代杂岩体的年龄一致，可能为岩浆就位过程中捕获的锆石(Zhou et al., 2006; Xiao et al., 2007a; Yan et al., 2008b; Pei et al., 2009)。

因此，根据我们的分析认为，木皮岩体就位年龄 219.1±1.7Ma 对应西部带大规模向 N 逆冲推覆的年龄。

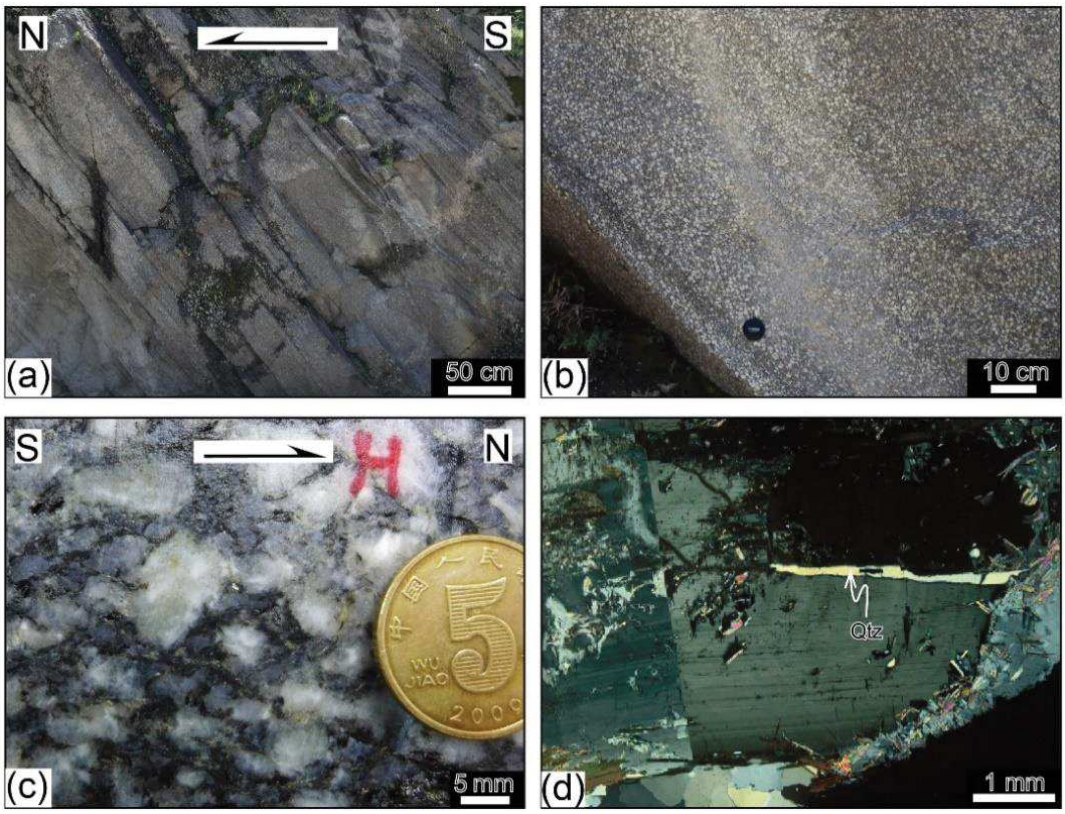

Figure 3.39 Petrological characters of the syntectonic Mupi grainte, noth of Pingwu city

(a) Strongly mylonitisation at the south margin of the granite and deformation accommdate into the country rock; (b) Blockage rocks at the north part of the granite, totally undeformed; (c) σ-type plagioclase in hand speciman indicate top-to-the-N shearing; (d) Microscopic view, the quartz vein infill the brittle cracked plagioclase.

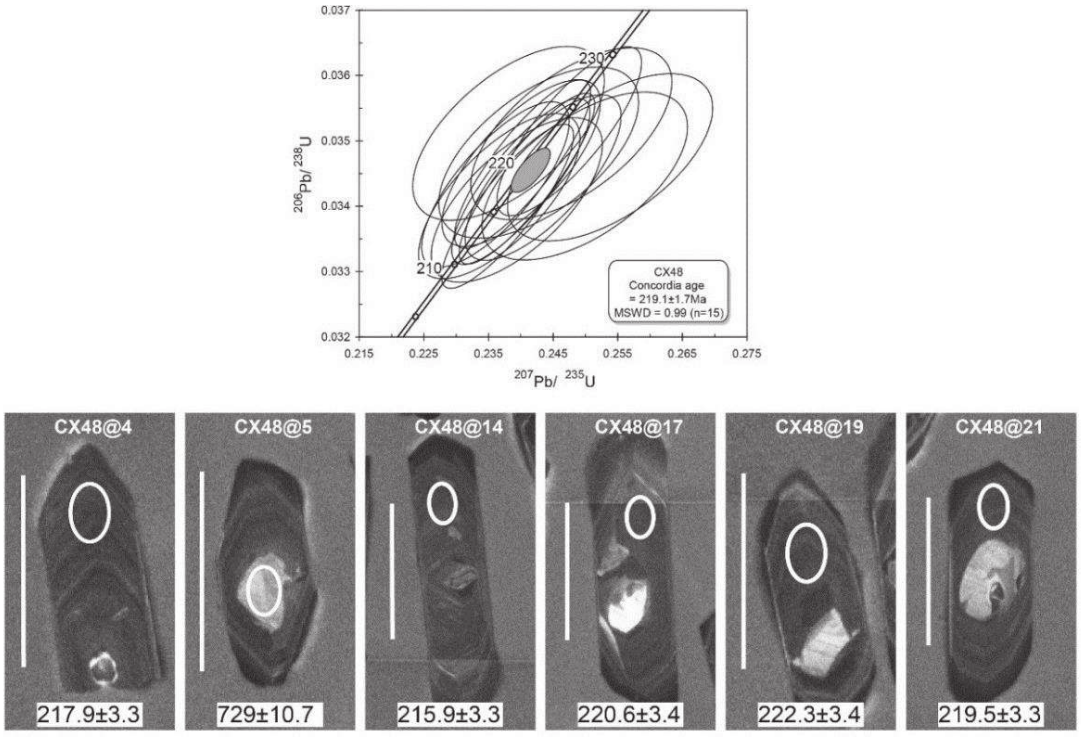

Figure 3.40 Zircon Climage and SHRIMP U-Pb dating of the Mupi granite

3.7 Thermal structure of the meta-allochthon—Mica geothermometer measurements

为了进一步验证龙门山造山的构造单元，我们对典型剖面进行了黑云母、白云母的温度计测试，揭示剖面各个位置变质岩所记录变形期间经历的变形温度，对各构造单元的变形层次有直观的定量的判断依据。尤其在研究造山带构造热演化历史时，精确获得各个单元的变质条件起着非常重要的作用。针对黑云母或白云母单矿物 Ti 饱和温度计的提出，很大程度上解决了低级泥质变质岩变质温度测定问题(Wu and Chen, 2015a; b)。尤其针对像龙门山逆冲推覆带整体上只经历低绿片岩相变质作用而并无合适矿物对来测定经历变形的温度条件，是非常有效的。

1) Introduction of the Mica geothermometer

云母 Ti 温度计测试方法实质上是根据自然界中多件泥质样品测试结果所拟合出来的经验公式。用于计算的变泥质岩变质温度，必须保证 TiO_2 达到饱和，以观察到与云母共生的钛铁矿或金红石为标准(Wu and Chen, 2015a)。在运用白云母单矿物温度计测试前，同时还需保证过铝质矿物，如 Al_2SiO_5，以及石英同时存在(Wu and Chen, 2015b)。黑云母 TiO_2 饱和条件下温度根据经验公式 $\ln[T(℃)]=6.313+0.224\ln(X_{Ti})-0.28\ln(X_{Fe})-0.449\ln(X_{Mg})+0.15P(GPa)$，该公式适用于温度在 450-840℃，0.1-1.9GPa 范围，并保证黑云母中 Ti 百分数含量在 0.02-0.14 之间(Wu and Chen, 2015a)。白云母 TiO_2 饱和、Al 饱和单矿物温度计经验公式为 $\ln[T(℃)]=7.258+0.289\ln(X_{Ti})+0.158[Mg/(Mg+Fe)+0.031\ln[P(Kbar)]$，其中各元素含量比值要求 Ti =0.01-0.07，Fe=0.03-0.16, Mg=0.01-0.32 且 Mg/(Fe+Mg)=0.05-0.73。该温度计使用变泥质岩经历温压条件界于 450-800 °C 和 0.1-1.4 GPa 之间(Wu and Chen, 2015b)。

2) Sample description and results

经过详细镜下观察，在通化-汶川剖面选取了 6 个志留系云母片岩样品(CX6、CX8、CX9、CX10、CX16、CX32)进行黑云母单矿物测试以及一个绢云母片岩(CX7)进行白云母单矿物温度计测试(Figure 3. 41 a)。电子探针测试工作在中国科学院地质与地球物理研究所电子探针与扫描电镜实验室完成。

为保证用于测试的样品满足温度计适用条件，我们在镜下对待测样品进行了详细分析。所有用于测试的样品，均观察到明显的云母鱼钛铁矿或者金红石共生的特征，多表现为黑云母中聚集生长金红石或钛铁矿，表明测试样品 TiO_2 达到饱和，且有石英共生(Figure 3. 41 b、c)，矿物组合特征满足云母单矿物测试条件。详细数据见附表 3.1。

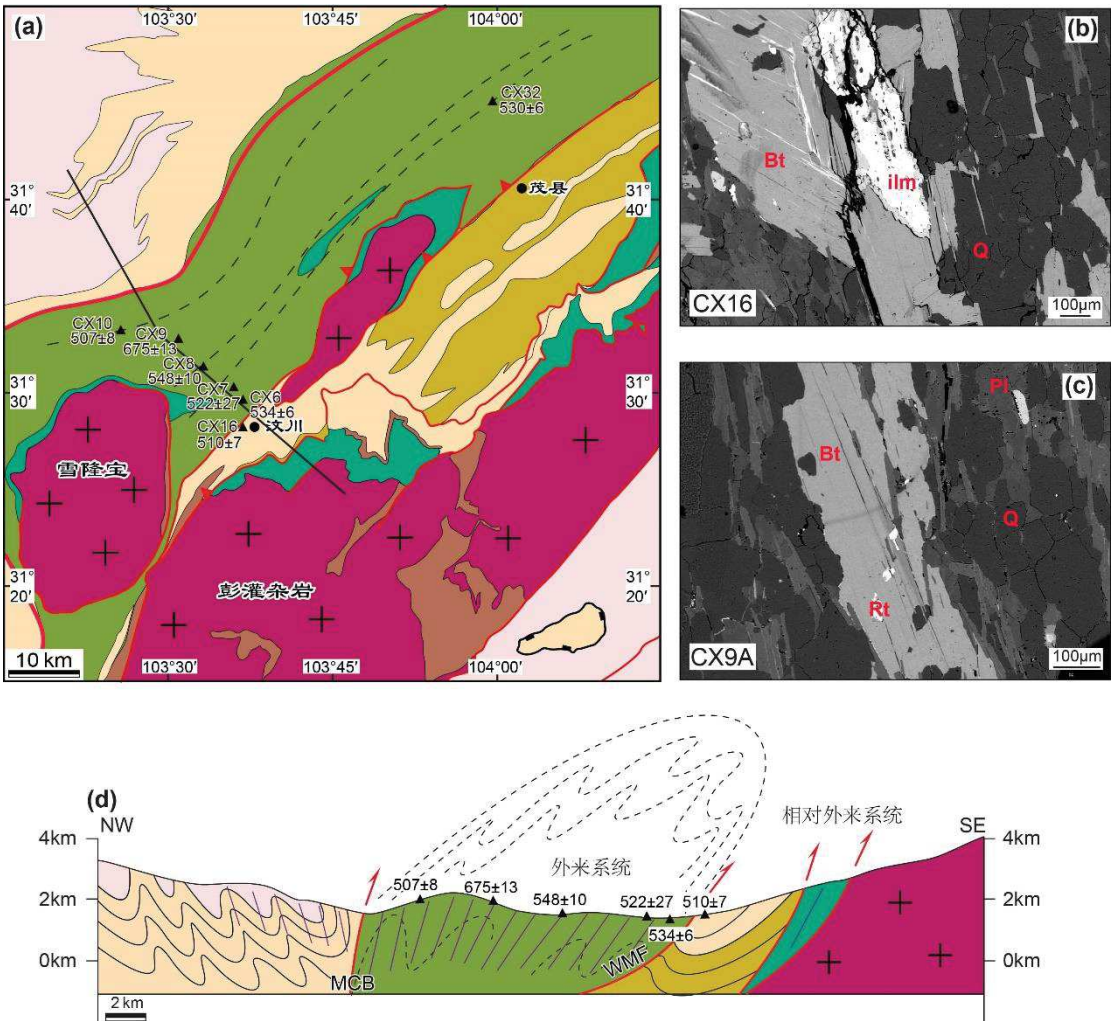

Figure 3.41 Location and structural profile of the Longmenshan thrust belt (location of the profile marked in Figure 3.1)

(a) Geological map with testing temperature results; (b) and (c) Back scattered image under SEM show the paragenesis of ilmenite and biotite or rutile and bitotite, indicating the saturation of TiO_2 in the system; (d) Structural profile with the temperature results. Symbols and acronyms are the same as in Figure 3.1. WMF: Wenchuan-Maowen fault. Q: quartz ; Pl: plagioclase; Bt: biotite; R: rutile.

地质温度计测试结果表明，在通化-汶川剖面外来系统内部，虽然整体温度呈现偏高趋势，但岩石所记录的变质温度呈规律性分布。剖面上看，最高变质温度并不在陆内薄弱带附近，而在外来系统内部，达到 675±13℃，然后分别向

NW 和 SE 方向变质温度递减，形成一个背形构造(Figure 3.41 d)。位于汶川-茂汶断裂下盘的 CX16，属于相对原地系统，给出明显低于其它样品的温度结果，显示温度跳跃降低的情况(Figure 3. 41 d)。茂县北部的 CX32，温度计测定结果为 530±6℃，该结果与沿龙门山构造走向向的 CX7 测试结果相近，表明在外来系统中岩石温度特征给出的向 SE 倒转的背形构造样式稳定连续分布。

3.8 The evolutionary scenario of the LMTB during the Early Mesozoic

垂直龙门山走向的 8 条构造剖面让我们对龙门山整体的构造格架有了非常清楚的认识(章节 3.5)。每条剖面的详细的几何学、运动学以及变形层次分析在龙门山整个造山带都稳定分布，其中劈理直立带作为西部带与东部带重要的几何学和运动学的界线，在龙门山逆冲推覆带沿线也稳定存在。东部带根据变形层次和变形程度进一步划分的四个单元在整个龙门山逆冲推覆带也稳定分布。在对龙门山整体构造格架理解基础上，我们给出了龙门山主变形期的构造框架模式图(Figure 3.42)。

如图所示，东部带四个系统中的原地系统为一套侏罗-白垩纪地层，整体变形微弱，呈宽缓褶皱，未见任何劈理，整体属于地表变形层次，不整合盖在强烈褶皱变形的地层之上；相对原地系统主要为强烈褶皱变形的上三叠统须家河组砂岩，褶皱极性向 SE，通过安县-灌县断裂逆冲至原地系统之上，局部地区发育褶劈理表明其变形层次比原地系统深；相对外来系统以映秀-北川断裂为界向 SE 逆冲至相对原地系统之上形成推覆体和飞来峰，主体由志留系千枚岩、泥质片岩组成，还包括少量寒武-奥陶纪薄层灰岩以及泥盆纪-早三叠世岩石，志留纪片岩强烈剪切变形，面理非常发育并一致倾向 NW，无论是砂质剪切透镜体还是剪切石英脉都指示上部向 SE 的剪切变形，变形程度和面理发育程度都表明相对外来系统从更深层次推覆上来；外来系统主要由志留纪绢云母片岩组成，除了表现出与相对外来系统一致的构造几何学和运动学特征以外，新生云母以及局部地区新生石榴子石的矿物组合表明外来系统是整个龙门山地区变质级别最高的单元，且在外来系统内部，云母单矿物温度计结果反映外来系统内部也呈现向 SE 倒转的背形构造。劈理直立带作为重要的界限，分隔上部向 NW 或 N 运动的西部带。

岩浆岩地球化学特征和高精度地震反射剖面，都表明松潘-甘孜褶皱带下面存在与扬子板块相同性质的基底(Roger et al., 2004; 胡健民 et al., 2005; Guo et al., 2013; Sigoyer et al., 2014)。而沿龙门山逆冲推覆带，并未发现蛇绿岩和中生代岛弧相关的岩浆活动，同时龙门山地区远离板块边界，可以将龙门山逆冲推覆带划分为陆内造山带。正如 Figure 3.42 所展示的，无论是东部带还是西部带，寒武-晚三叠盖层都发生了强烈的缩短变形，表现为强烈的逆冲、褶皱和挤压；而扬子基底作为刚性的块体，不太可能像上地壳一样发生褶皱和缩短，必然存在一个薄弱的地方发生扬子基底的消减来耦合盖层的缩短(Figure 3.42)，因此我们将劈理直立带这个地表重要的地质边界对应岩石圈尺度的“陆内薄弱带”—扬子基底沿陆内薄弱带发生消减伴随盖层的逆冲缩短，产生广泛向 SE 的逆冲和上部向 NW 的逆冲。

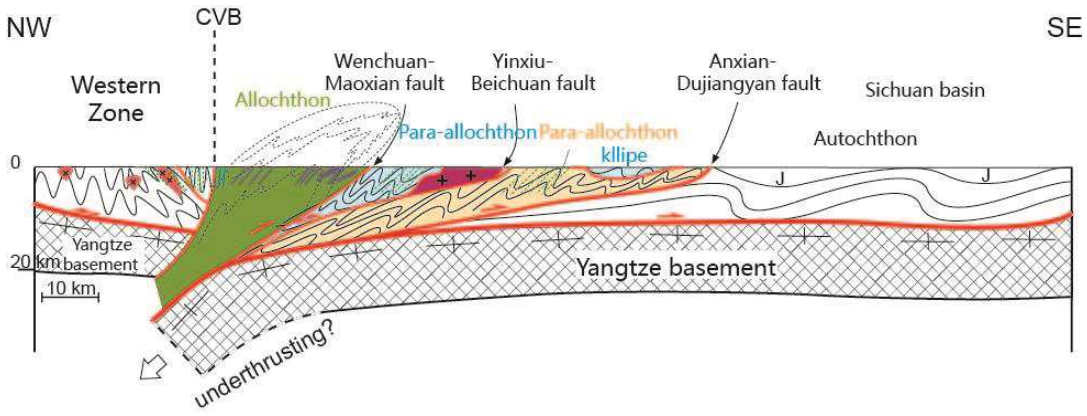

Figure 3.42 The architecture profile of the Early Mesozoic Longmenshan thrust belt

发生陆内俯冲的陆内薄弱带可以是先存的古老造山带，如澳大利亚中部的 Alice spring 造山带，经历区域上晚元古代 Peterman 造山事件后，在泥盆纪-石炭纪时期重新活化陆内俯冲造山(Goleby et al., 1989; Hand and Sandiford, 1999; Sandiford et al., 2001)，或者是前期地壳伸展后闭合形成陆内薄弱带，如分隔法国和西班牙的比利牛斯山，在经历海西期持续到早白垩世广泛伸展作用后，形成陆内裂谷，晚白垩世开始挤压，在裂谷位置发生板内俯冲，形成比利牛斯山(Choukroune, 1992)。龙门山逆冲推覆带东部带，物质变形层次有规律地分布，整体上从 SE 向 NW 变形层次逐渐加深。龙门山作为扬子板块 NW 缘，先经历了自寒武纪-奥陶纪稳定裂谷断裂时期沉积，志留纪时期裂谷局部扩大，沉积形成巨厚的志留系，伸展作用一直持续至二叠纪达到顶峰，表现为广泛出现的基性玄武岩和碳酸盐重力流等。长期的断裂伸展，使龙门山地区在接受寒武-二叠

的沉积同时，地壳发生显著减薄。尽管松潘-甘孜东部出现少量枕状熔岩，但并未出现与蛇绿岩相关的超基性岩，持续的伸展拉伸并未产生新的洋壳，岩石圈地壳显著减薄成为一个可能的薄弱带。早中生代在松潘-甘孜和扬子块体相互作用下，扬子基底经由裂谷闭合的薄弱带发生陆内基底消减，使裂谷内的物质由浅至深通过多条逆冲断裂逐渐至浅表并堆叠起来，部分物质卷入到基底消减变形中，形成龙门山逆冲推覆带内变质级别最高的单元。随着基底的不断消减，基底上的盖层也发生大规模逆冲褶皱缩短，向 SE 逆冲加载在四川盆地上形成周缘前陆盆地，并在前陆盆地上形成一系列推覆体和飞来峰。随着基底的消减和盖层的挤压缩短变形，最终形成龙门山现今所表现的构造格架。而龙门山构造框架中西部带，则对应基底沿裂谷薄弱带消减时，发生的同期向 NW 的反冲构造。通过对比野外观察和室内分析，上部向 SE 逆冲的范围远大于向 NW 的逆冲，我们倾向认为是东部扬子基底向西部松潘-甘孜扬子基底下面消减，形成向 SE 的逆冲推覆和同期向 NW 的反冲(Figure 3.42)。

4. Emplacement of the Pengguan complex—multiphase deformation

4.1 Introduction

At the northeastern margin of the Tibetan Plateau, the Longmenshan belt is remarkable for its steep topographic gradient with a thickened crust of *ca*. 60 km as well as the intensive seismic activity, such as the devastating M_w 8.0 Wenchuan (2008) and M_w 7.0 Lushan (2013) earthquakes (Fig. 4.1a) (*Guo et al.*, 2013). Numerous investigations have been carried out to study the formation of the thickened crust and elevated topography (*Yin and Harrison*, 2000; *Tapponnier et al.*, 2001; *Royden et al.*, 2008; *Hubbard and Shaw*, 2009).

The Longmenshan Thrust Belt (LMTB) is a composite orogen that records multiphase southeastward thrusting in Mesozoic and Cenozoic (*BGMRSP*, 1991; *Burchfiel et al.*, 1995; *Chen et al.*, 1995), and a period of top-to-the-NW shearing (*Burchfiel et al.*, 1995; *Xu et al.*, 2008; *Tian et al.*, 2016). The widespread top-to-the-SE shearing has been interpreted as the consequence of the Mesozoic continental collision between the North China block (NCB) and South China block (SCB) imprinted by Cenozoic continental collision between the India and Eurasia blocks (*Burchfiel et al.*, 1995; *Xu et al.*, 2008). The top-to-the-NW shearing mostly developed associated with the orogen-parallel Neoproterozoic complexes (*Xu et al.*, 2008; *Tian et al*., 2016); yet, both of them remain controversial in terms of mechanism, scale and timing (*Burchfiel et al.*, 1995; *Xu et al.*, 2008; *Zhou et al.*, 2008; *Tian et al.*, 2016). On the basis of extent and timing of the top-to-the-NW shearing and the emplacement of the Neoproterozoic complexes, several models have been proposed: i) Cenozoic lower crust channel flow bounded by NW- and SE-directed shear zones, buttressed to the SE by the old and resistant lithosphere of the Sichuan basin that sustains the high topography of the Longmenshan (*Burchfiel et al.*, 2008; *Royden et al.*, 2008), ii) crustal shortening by thrust faults rooted in the lithosphere that formed duplex structure of the LMTB (*Tapponnier et al.*, 2001; *Hubbard and Shaw*, 2009; *Tian et al.*, 2016), and iii) the extrusion of a crustal wedge during the Cretaceous (*Xu et al.*, 2008). The understanding of the top-to-the-NW

shearing and the emplacement of the Neoproterozoic complexes therefore is crucial to unravel the evolution of the LMTB as well as the uplifting of the Tibetan Plateau.

The Neoproterozoic Pengguan complex, located in the middle segment of the LMTB and is cored by granitic rocks, and involved into the top-to-the-NW shearing that provides a perfect place to unravel the tectonic history of the LMTB (Fig. 4.1b). For this study, we conducted a field-based structural analysis, Anisotropy of Magnetic Susceptibility (AMS) measurements, and microstructural analysis, aiming to constrain the structural geometry and deformation intensity of the Pengguan complex. This is complemented with gravity modeling of the Pengguan complex and adjacent areas, which provides a high-resolution image of the upper crust structures. Integrating published geochronological data and lithological characteristics of the sediments inside the Sichuan foreland basin to the SE, the new multidisciplinary results from this study provide a comprehensive understanding of the tectonic evolution of the LMTB.

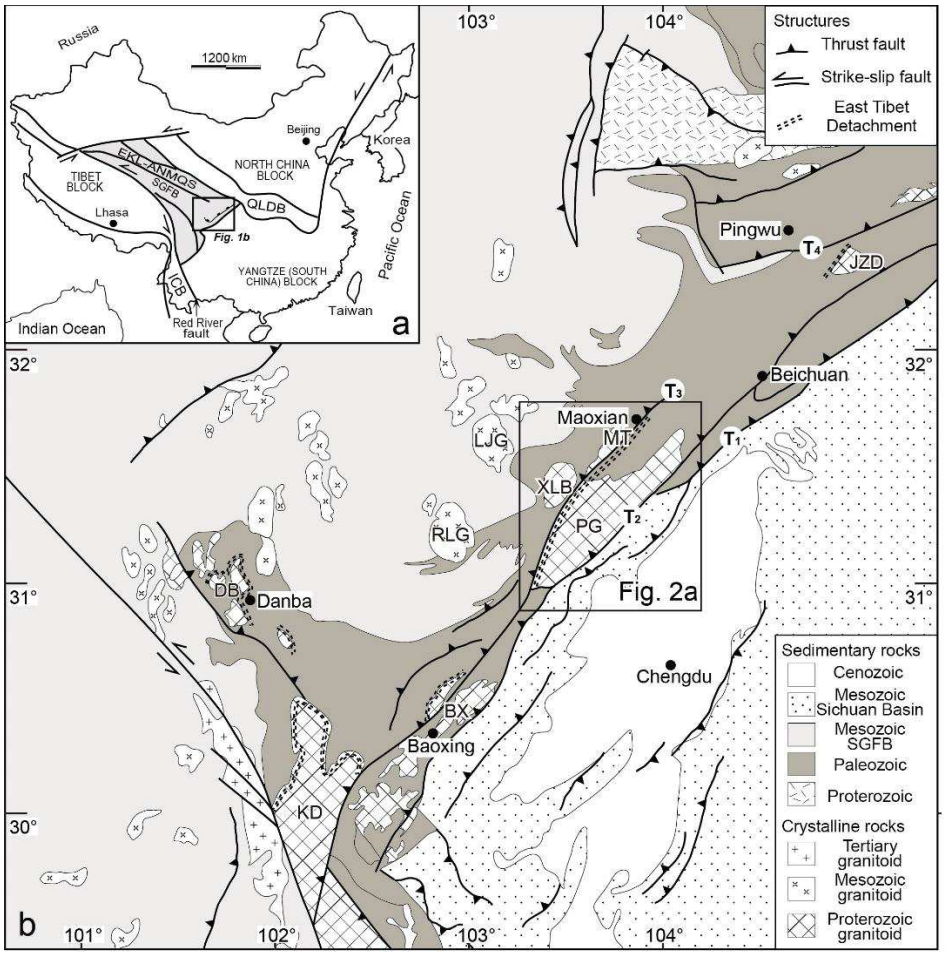

Fig. 4.1 (a) Simplified tectonic sketch of China.

QL: Qingling-Dabie orogenic belt; EKL-ANMQS: East Kunlun-A'nyemaqen suture; SGT: Songpan-Ganzi terrane; LMTB: Longmenshan thrust belt; ICB: Indochina block; (b) Simplified geological map of the Longmenshan thrust belt, modified after BGMRSP (1991), Burchfiel et al. (1995) and Xu et al. (2007). T1: Anxian-Guanxian Fault (AGF); T2: Yingxiu-Beichuan Fault (YBF); T3: Wenchuan-Maowen Fault (WMF); T4: Qingchuan Fault (QCF); JZD: Jiaoziding complex; PG: Pengguan complex; XLB: Xuelongbao complex; BX: Baoxing complex; KD: Kangding complex; DB: Danba dome; RLG: Rilonguan granite; LJG: Laojungou granite; MT: Moutuo complex.

The regional structure of the LMTB is defined by three listric thrust faults that strike northeast and steeply dip to the northwest, namely from northwest to southeast, the Wenchuan-Maoxian Fault (WMF, T_3 in Fig. 4.1b), the Yingxiu-Beichuan Fault (YBF, T_2 in Fig. 4.1b) and the Anxian-Guanxian Fault (AGF, T_1 in Fig. 4.1b) (*Xu et al.*, 1992). A set of orogen-parallel Neoproterozoic complexes, *e.g.,* the Jiaoziding complex, the Pengguan complex, the Xuelongbao complex, the Baoxing complex, the Kangding complex, the Danba dome, are distributed from NE to SW along the LMTB (Fig. 4.1b).

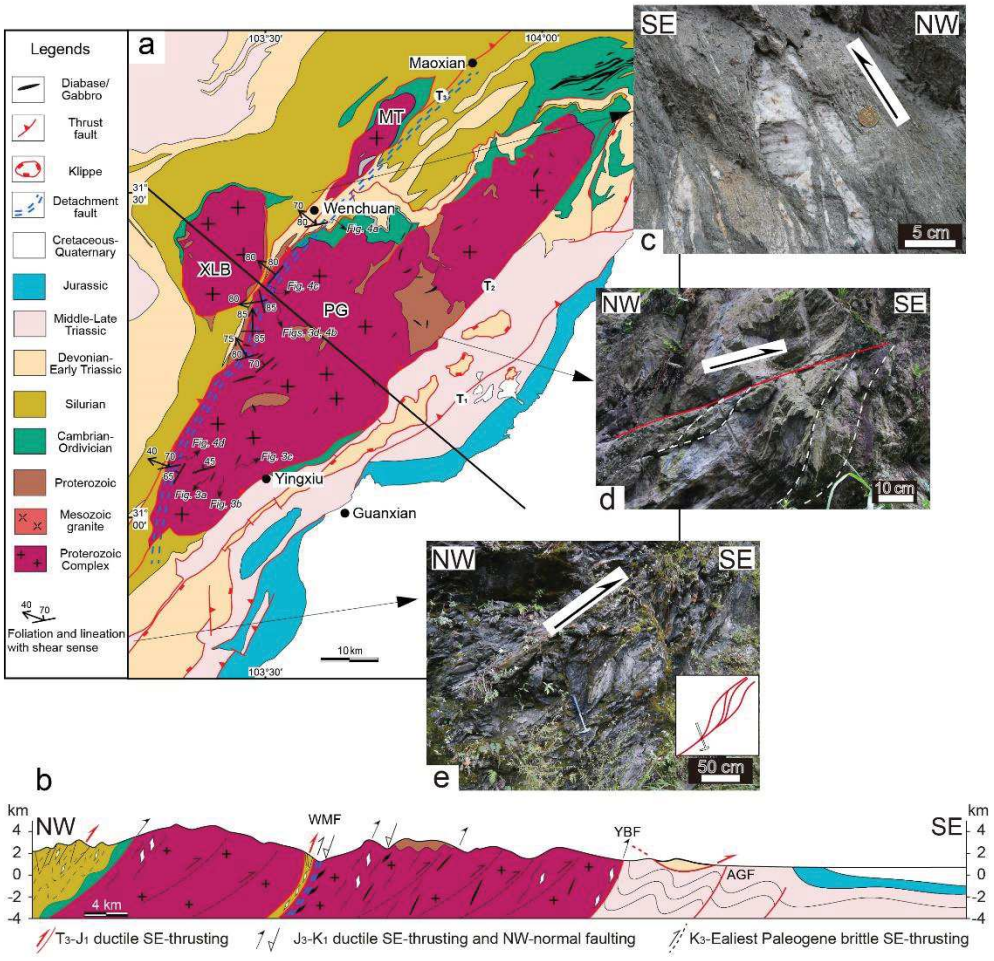

Fig. 4.2 (a) Structural map of the Pengguan complex and its adjacent area; (b) Cross-section crossing the Pengguan complex and Xuelongbao complex; (c) Quartz boudin wrapped in the Silurian schist indicates a top-to-the-SE shearing, northwest to the Wenchuan city (31°29.758

´ N, 103°34.535 ´ E); (d) Shear zone developed in the Proterozoic meta-sandstone display a top-to-the-SE sense of shear, immediately in the hanging wall of the Beichuan-Yingxiu fault (31°15.62 ´ N, 103°46.96 ´ E); (e) Sigmoidal lens in the Late Triassic sandstone-mudstone interbeds indicates a top-to-the-SE shearing (30°47.843 ´ N, 103°14.615 ´ E). Symbols and acronyms are the same as in Fig. 4.1.

To the NW of the LMTB, the Songpan-Ganzi Terrane (SGT) is characterized by an extensively folded turbidite of Middle-Late Triassic age, more than 7 km in thickness. This folded unit is intruded by tens of syn- and post-tectonic granites that dominantly derive from the partial melting of the SGT Neoproterozoic basement and a variable proportion of sedimentary rocks as well as negligible amounts of material of mantle source (Fig. 4.1b; *Roger et al.*, 2004; *Hu et al.*, 2005; *Zhang et al.*, 2006, 2007). The Paleozoic-Late Triassic sedimentary cover is separated from the Neoproterozoic basement by a regional décollement and transported southwards (*Calassou*, 1994; *Harrowfield and Wilson*, 2005). To the east of the LMTB, the Sichuan foreland basin, underlain by a Neoproterozoic basement, records flexural subsidence due to the thrusting of the LMTB (*Chen et al*., 1994a).

In the LMTB, both Early Mesozoic and Cenozoic shortenings have been documented. The Early Mesozoic shortening is the result of transpressional interaction between the SGT and the SCB, which resulted in structural inversion of the western margin of the Yangtze block from a pre-Middle Triassic rift to a SE-verging fold-and-thrust belt. Pervasive SE/SSE-ward thrusting developed at different scales in (i) the Sichuan foreland basin and (ii) the hinterland in the west of the WMF (*Xu et al.*, 1992; *Burchfiel et al.*, 1995; *Worley and Wilson*, 1996; *Yan et al.*, 2011). In the foreland basin, the orogen-parallel klippen and nappes were transported SE-ward and tectonically overlie on the extensively folded Late Triassic rocks (Fig. 4.2a). Most of the klippen are exposed as synclines overturned to the SE. SE-ward thrusting is also indicated by SE-verging folds and locally developed sigmoidal tectonic lenses in the Late Triassic sandstone-mudstone interbeds (Figs. 4.2b and e). In the hinterland, macroscopic scale sigmoidal quartz boudins, asymmetric pressure shadow and microscopic scale of shear-bands, mica fishes, and asymmetric plagioclase porphyroclasts on the XZ plane indicate an unambiguous top-to-the-SE shearing (Figs. 4.2b and c).

The timing of the Mesozoic shortening is firstly constrained by the unconformity between the Lower Jurassic conglomerates and the intensively folded Upper Triassic sandstone in the Sichuan foreland basin, which indicates a deformation age during T_3-

J_1 (*BGMRSP*, 1991). Secondly, most plutons intruded in the SGT yield a peak age around 211 Ma that postdates the folding of the SGT and the SE-verging folds of the LMTB (*BGMRSP*, 1991; *Roger et al.*, 2004; *Hu et al.*, 2005; *Zhang et al.*, 2006; *Xiao et al.*, 2007; *Sigoyer et al.*, 2014). Thirdly, $^{39}Ar/^{40}Ar$ dating of metamorphic rocks from the northern segment of the LMTB provides a range of ages between 237 and 208 Ma that were interpreted as minimum timing constraints for this deformation (*Yan et al.*, 2011). Due to SE-ward propagation of the LMTB, the Sichuan foreland basin initiated during the Late Triassic with depositional environment changing significantly from shallow marine carbonate platform to terrestrial clastic basin (*Chen et al.*, 1994b).

The Mesozoic thrust belt and underlying autochthon were reactivated and thrusted southeastwards during the Cenozoic (Fig. 4.2b). This was interpreted as the response to the northward indentation of India into the Eurasia Block (*Tapponnier et al.*, 1982; *Burchfiel et al.*, 2008; *Yan et al.*, 2011). This brittle, SE-directed Cenozoic deformation is expressed by brittle faults with slicken lines, and SE-ward overturned Jurassic rocks in the LMTB. Low-temperature geochronology reveals fast exhumation of the LMTB during the Cenozoic, controlled by the main listric thrusts (*Arne et al.*, 1997; *Enkelmann et al.*, 2006; *Godard et al.*, 2009; *Wang et al.*, 2012; *Cook et al.*, 2013; *Tian et al.*, 2013). The absence of coeval adjacent foreland basin may be due to narrowly distributed and predominantly vertical displacements along the high angle listric reverse faults in the LMTB (*Feng et al.*, 2015).

However, between the Early Mesozoic and Cenozoic shortening, there is an intermediate phase of deformation during the Late Jurassic to Early Cretaceous (Fig. 4.2b). Structural analysis and $^{39}Ar/^{40}Ar$ dating reveal a NW-SE directed compressional phase along the belt, to the west of the WMF this resulted in crustal thickening and associated Barrovian-type amphibolite facies metamorphism around 133-120 Ma (*Dirks et al.*, 1994; *Worley et al.*, 1995; *Arne et al.*, 1997). In the Pengguan complex, the top-to-the-SE shearing was dated at 140-135 Ma or *ca.* 166 Ma (*Yan et al.*, 2008; *Airaghi et al.*, 2017). A belt characterized by top-to-the-NW/N shearing is named East Tibet Detachment, mainly developed at the N or NW boundary of the Neoproterozoic complexes that extend from the Danba dome to the middle Longmen shan and may extend to the Jiaoziding complex (Fig. 4.1b) (*Xu et al.*, 2007). It is worth noting that this fault formed at *ca.* 166-120 Ma (*Huang et al.*,

2003a, 2003b; *Xu et al.*, 2008; *Li*, 2009; *Tian et al.*, 2016), and therefore overlaps with the top-to-the-SE tectonics. In the LMTB, both top-to-the-SE and top-to-the-NW shearing were developed with steeply NW-dipping foliation and steeply NW-plunging lineation (*Dirks et al., 1994; Xu et al., 2008*). The SGT exhibits low regional cooling rates of *ca.* 2-3℃/Myr since Late Triassic to Tertiary (*Huang et al.*, 2003a; *Roger et al.*, 2011), and thus the deformation during Late Jurassic to Early Cretaceous is more likely restricted to the periphery of the SGT.

In the Sichuan foreland basin, sediments display cyclicity of wedge-shaped and tabular mega-sequences that indicate three stages of SE-motion of the LMTB during i) Late Triassic-Early Jurassic, ii) Late Jurassic-Early Cretaceous, and iii) Late Cretaceous-Eocene (*Chen et al.*, 1994a; *Li et al.*, 2013). The episodic sedimentation in the Sichuan foreland basin has been interpreted as the response to the aforementioned three periods of events.

4.2 Structural analysis of the Pengguan complex

1) Litho-tectonic units and bulk architecture

The NE-SW trending Pengguan complex, bounded by the YBF to the southeast and the WMF to the northwest, is composed of Neoproterozoic granitic rocks and sedimentary rocks of Huangshuihe group (Fig. 4.1b) (*BGMRSP*, 1991). The Neoproterozoic granitic rocks are coarse-grained biotite tonalite, fine-grained biotite granodiorite and two-mica granodiorite which yield an emplacement age of 809±3 Ma by zircon U-Pb dating (Fig. 4.3a) (*Yan et al.*, 2008). From base to the top, the Huangshuihe group consists of pyroclastic rocks, spilite, crystalline limestones, graphitic schists, sericite quartz schists, and quartzites (*BGMRSP*, 1991). Lastly, a set of NE-SW trending mafic diabase and gabbro sills intruded the Pengguan complex during 195-186 Ma (Figs. 4.2a and 4.3c) (*Chen et al., 2015*). Several NE-trending and SE-directed thrusts are developed at the NE and SW periphery of the complex (Fig. 4.2a).

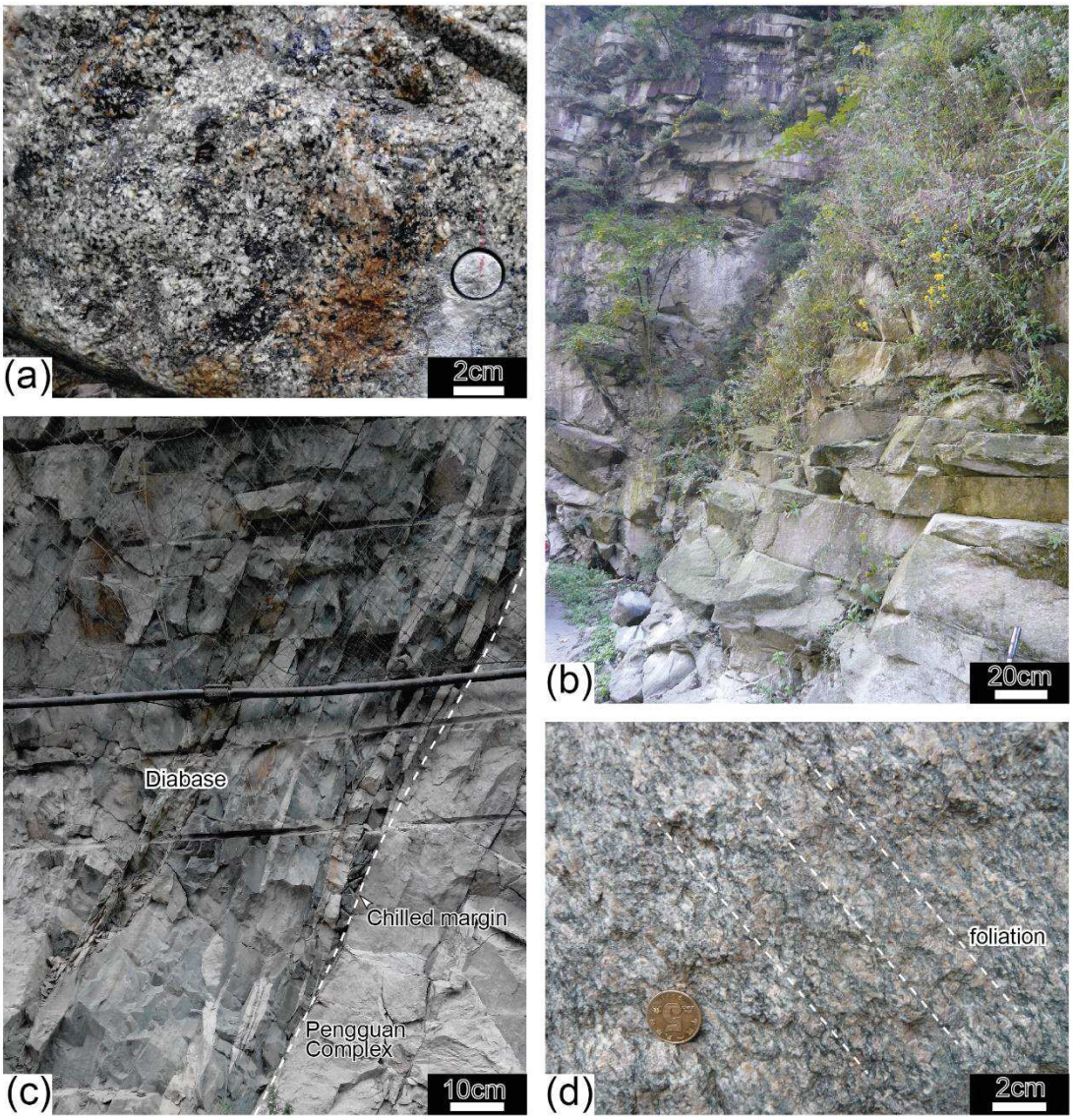

Fig. 4.3 Photographs showing field characters of the Pengguan complex.

(a) Undeformed massive diorite (31˚3.77´N, 103˚23.19´E); (b) Undeformed granodiorite with well-developed subhorizontal joints (31˚04.315´N, 103˚26.520´E); (c) Diabase dyke intruding the diorite (31˚06.66´N, 103˚28.88´E); (d) Intensively mylonitized diorite (31˚22.931´N, 103˚30.364´E). Locations are presented in Fig.2a.

Subhorizontal joints represent the main structural pattern of the Pengguan granitic rocks (Fig. 4.3b). Although previous work documented several NE-SW trending shear zones developed inside the complex (*Ma et al.*, 1996), the ductile planar and linear structural elements are not clearly expressed in the field. Even when a planar fabric can be observed in the field, a mineral lineation is not always visible. Only in the NW boundary of the complex, the ductile deformation is evidently characterized by NW-dipping foliation and NW-plunging lineation (Fig. 4.2a). On its

SE margin, the metamorphic rocks of the Huangshuihe group suffered extensive folding and shearing that are consistent with the YBF activity.

2) Kinematic analysis

Macro- and mesoscopic- structural analysis document two opposite senses of shear in the Pengguan complex, namely a top-to-the-SE, and a top-to-the-NW shearing.

The top-to-the-NW shearing is obvious in the NW boundary of the Pengguan complex, at the footwall of the WMF. This NW-dipping fault separates Silurian rocks to the NW from Neoproterozoic ones to the SE, with a consistent normal component of movement (Fig. 4.2a). The shear foliation dips steeply to the NW, and the lineation plunges steeply to the NW. The rare foliation steeply dipping to the SE/S is probably formed by tilting of the original foliation during the Cenozoic deformation (Fig. 4.2a). In thin sections, mica fish, quartz ribbon aggregates, sigmoidal clasts, and shearbands on XZ plane of the sericite-quartz schist and granitic mylonite from the western boundary of the Pengguan complex indicate a consistent top-to-the-NW shearing (Figs. 4.4a-d). Within the mylonite, the mineral assemblage that defines the foliation and the lineation includes quartz + feldspar + biotite + muscovite + chlorite, suggesting that the shearing was developed under greenschist facies metamorphic conditions (Fig. 4.4).

In the southeastern boundary of the Pengguan complex, in the hanging wall of the YBF, a top-to-the-SE sense of shear is demonstrated by the extensively folded and cleaved Proterozoic Huangshuihe group, in which deflected cleavage roots into a meter-scale SE-verging thrust fault (Fig. 4.2d). Compared to the top-to-the-NW shearing, the SE-verging shearing in the SE boundary, developed under a low metamorphic grade since no porphyroblasts crystallized there. However, both the top-to-the-SE shearing and top-to-the-NW shearing under greenschist facies metamorphism conditions were distributed in the NW part of the Pengguan complex as constrained by AMS and petrofabric study in Section 4.4 below.

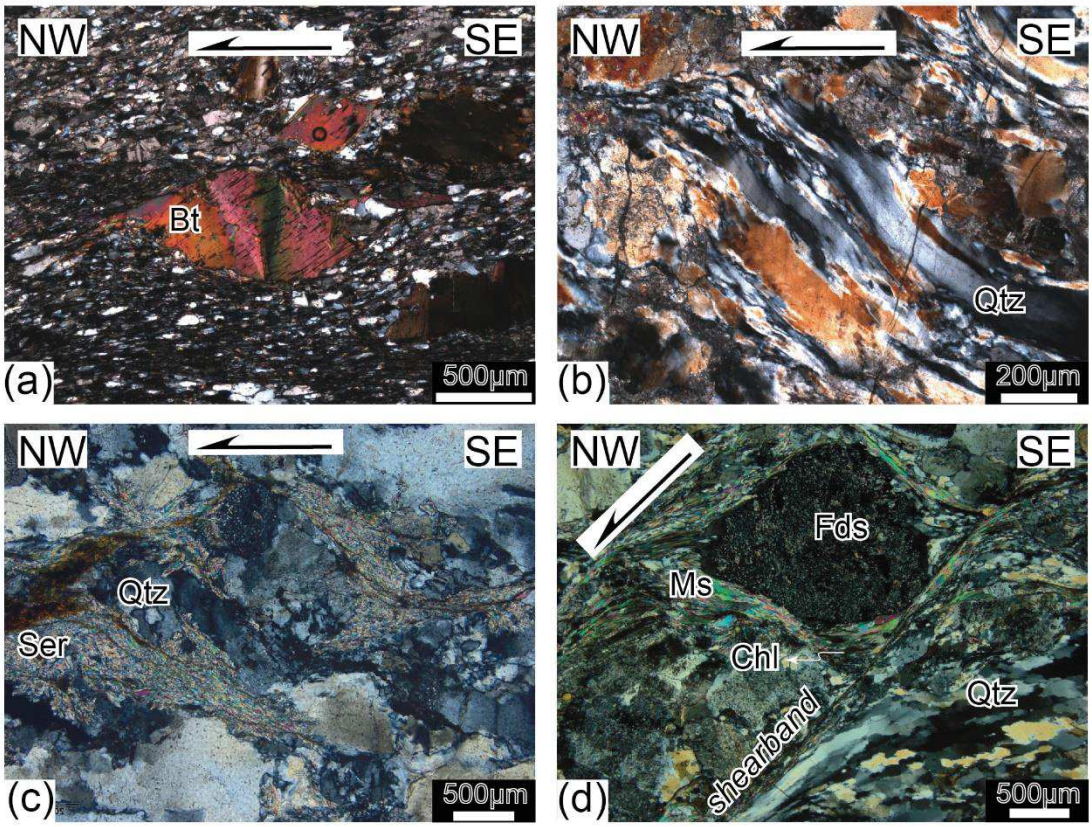

Fig. 4.4 Microscopic features indicate top-to-the-NW shearing in the NW boundary of the Pengguan complex.

(a) Mica fish in the Devonian sericite-quartz schist (31˚28.445´N, 103˚34.479´E); (b) Ribbon quartz aggregates in the granitic mylonite (31˚22.444´N, 103˚30.551´E); (c) Sericite aggregates wrap quartz porphyroclasts in the granitic mylonite (31˚23.39´N, 103˚30.99´E); (d) Shear band and sigmoidal porhyroblasts in the granitic mylonite (31˚05.193´N, 103˚18.730´E). Qtz: Quartz; Cal: Calcite; Bt: Biotite; Ms: Muscovite; Ser: Sericite; Chl: Chlorite; Fds: Feldspar

4.3 Anisotropy of Magnetic Susceptibility (AMS) and petrofabric study

Granitic rocks are often used as a proxy to study regional tectonics due to their ability to record their emplacement setting and their post-solidus deformation. However, it is difficult to distinguish secondary post-solidus fabrics from primary magmatic ones preserved in granitic rocks merely by field observation, especially when the granite is weakly deformed and/or fine-grained. Fortunately, the anisotropy of magnetic susceptibility (AMS) has been proven as an efficient method to reveal the fabrics of granitic rocks (*e.g., Borradaile and Henry*, 1997; *Bouchez*, 2000; *Talbot et al.*, 2005), and a combined microstructural analysis has been applied to the Pengguan granitic rocks in order to decipher its emplacement mechanism and posterior deformation.

Magnetic susceptibility (*K*) is the ratio of the induced magnetization (*M*) of a specimen to the externally applied magnetic field (*H*) (*Borradaile et al., 2004, 2010*). The anisotropy of magnetic susceptibility (AMS) is a second rank tensor that describes directional variation of a specimen's magnetic susceptibility, which can be used as deformation proxy if the contributing factors (mineral content, mineral shape fabric, and crystallographic fabric) are determined (*Borradaile and Jackson*, 2004, 2010; *Kruckenberg et al.*, 2010; *Parsons et al.*, 2016). The AMS is geometrically represented by an ellipsoid defined by three orthogonal principal axes, K_1 (maximum), K_2 (intermediate), and K_3 (minimum) (*Tarling and Hrouda*, 1993). K_1 and K_3 corresponding to the magnetic lineation and the pole of the magnetic foliation, respectively. The mean magnetic susceptibility (K_m) is computed as $(K_1+ K_2+ K_3)/3$, which represents the sum effect of the magnetic carriers of the specimen.

Three types of magnetic carriers (namely diamagnetic, paramagnetic and ferromagnetic) have been classified based on their induced magnetization strength and direction (*Tarling and Hrouda*, 1993). Induced magnetization of paramagnetic (*e.g.,* phyllosilicate) and ferromagnetic (*e.g.,* magnetite) minerals display same direction as the externally applied field while the ferromagnetic minerals exhibit much higher susceptibility. Conversely, induced magnetization of diamagnetic (*e.g.,* quartz and calcite) minerals is opposite to the external field but with a low intensity.

The overall rock magnetic fabric is determined by all magnetic minerals, including but not limited to, their abundance, the grain shape preferred orientation, the crystallographic preferred orientation, presence of high susceptibility inclusions and extent of magnetostatic interaction of ferromagnetic minerals (*Borradaile and Jackson*, 2004). The grain size of the ferromagnetic minerals also influences the magnetization by determining the number of magnetic domains (regions display identical magnetic dipole). The magnetite has been classified as single domain (SD), pseudo single domain (PSD), and multi domain (MD) based on its grain size varying from smallest to largest (*Tarling and Hrouda*, 1993). The MD and PSD magnetite display 'normal AMS' (the shape of the magnetic ellipsoid resembles the grain), while the SD magnetite display 'inverse AMS' (*Ferré et al*., 2002). Generally, the most abundant, high susceptibility, and strongly anisotropic minerals control the whole-rock AMS fabrics (*Borradaile and Jackson*, 2004, 2010). Magnetostatic interactions between ferromagnetic grains also influence the AMS that depends on the

spatial distribution and concentration of the ferromagnetic grains (*Parsons et al.*, 2016).

The corrected anisotropy degree describes eccentric extent of the AMS ellipsoid from a sphere (P_J=1) to an ellipsoid (P_J>1) (*Jelinek*, 1981).

$$P_J = \exp\sqrt{2\sum(\ln K_i - \ln K_m)^2} \qquad (1)$$

K_i refers to the three susceptibility axes, K_1, K_2, and K_3. The shape parameter T defines the shape of the magnetic ellipsoid ranging from prolate ($T=-1$) through neutral ($T=0$) to oblate ($T=+1$) (*Jelinek*, 1981).

$$T = \frac{\ln(F) - \ln(L)}{\ln(F) + \ln(L)} \quad \text{where} \quad L = \frac{K_1}{K_2} \quad \text{and} \quad F = \frac{K_2}{K_3} \qquad (2)$$

1) Methods of AMS analysis

A sampling of 299 oriented cores from 36 sites regularly covering the southern Pengguan complex with an interval of 1.5 km has been carried out along the main N-S and W-E trending valleys and several small ones inside the complex, and also at its periphery (Table 4.1; Fig. 4.7). Due to the high topography and access difficulty, the sampling coverage in the northeastern part is relatively low. Approximately six cores about 4 to 6 cm in length and 2.5 cm in diameter and separated by nearly 2 meters intervals were collected from each site. Cores were oriented by compass and, when possible, by solar compass. To avoid the shape effect on the magnetic anisotropy, all cores were cut into 2.2 cm in length to mimic the spherical shape with respect to the 2.5 cm diameter.

Table 4.1 Results of AMS measurements from the Pengguan granitic rocks

Magnetic fabric measurements were performed at the Institute of Geology and Geophysics of Chinese Academy of Sciences. Specimens cut from each sample were analyzed using AGICO Kappabridge (MFK1) magnetic susceptometer operating in low field (300 A/m) to construct the AMS ellipsoid orientation and corresponding magnetic fabric parameters. Measurements include 1) thermomagnetic experiments, 2) isothermal remanent magnetization, and 3) hysteresis properties of small rock fragment on the Micro 3900 Vibrating Sample Magnetometer to determine the magnetic carriers that contributed to the magnetic susceptibility.

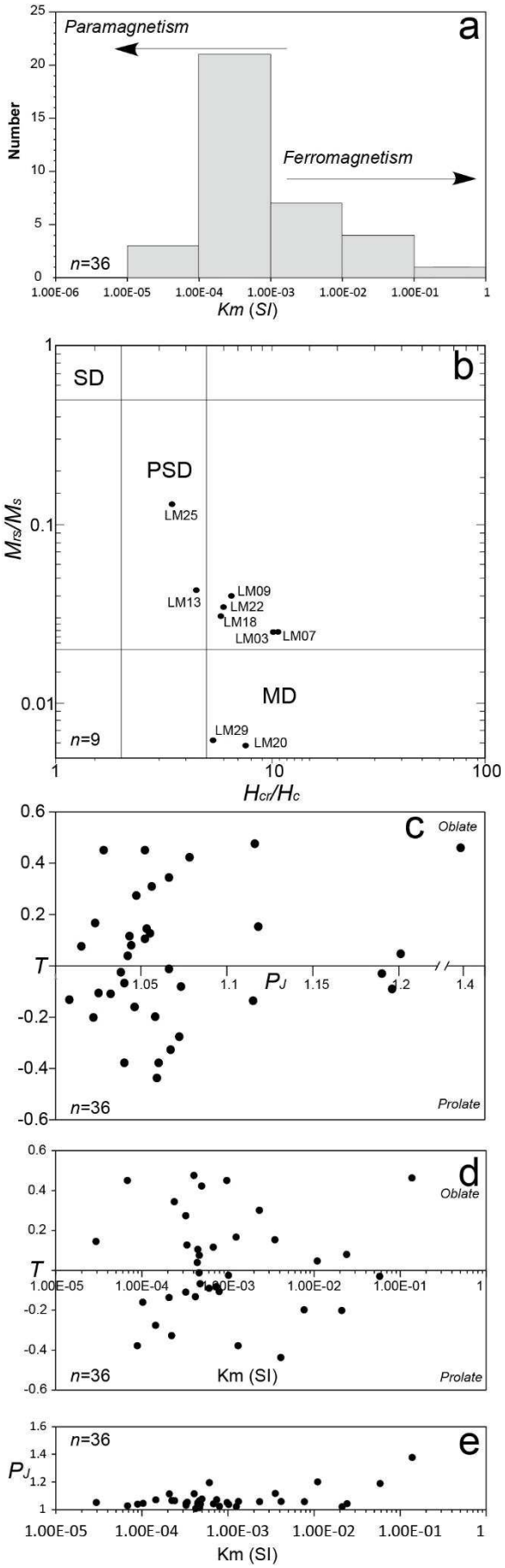

Fig. 5. AMS scalar parameters of the Pengguan granodiorite and diorite.

(a) Histogram of site-mean magnetic susceptibility (Km); (b) Mrs/Ms vs. Hcr/Hc diagram from selected samples of the Pengguan granitic rocks to define the size of magnetite. Mrs: remanence of saturation magnetization after removing the applied field; Ms: saturation magnetization under applied field; Hcr: coercivity of remanence after removing the applied field; Hc: coercivity under applied field; SD: single domain; PSD: pseud-single domain; MD: multi-domain; (c) Shape parameter T vs. anisotropy degree PJ value; (d) Bulk magnetic susceptibility Km vs. shape parameter T; (e) Anisotropy degree PJ value vs. Km.

2) Magnetic mineralogy

The site magnetic susceptibility value (*Km*) are given in Table 4.1 and their related distribution histogram is presented in Fig. 4.5a. For the Pengguan granitic rocks, *Km* mostly varies from 30 μ SI to more than 130 m SI among which 75 percent of the sites have Km < 1500 μ SI and two sites have extremely high susceptibility (*LM07* and *LM13*).

The representative magnetic mineralogy measurements, including hysteresis loop, isothermal remanent magnetization and thermo-magnetic experiments are presented in Fig. 4.6 (Detailed nine groups of results are presented in Table S1 and Fig. S1). Most sites display a linear relationship between the applied magnetic field and the induced magnetization (Fig. 4.6a), a quick saturation but a weak intensity of IRM (Fig. 4.6b) and a sharp drop of *Km* at about 580°C (Fig. 4.6c), indicates that paramagnetic minerals are the principal susceptibility carriers with a weak concentration of the ferromagnetic minerals. A few samples representing a small number of sites are characterized by a non-linear hysteresis curve (Fig. 4.6d): a quick saturation with a higher intensity of IRM (Fig. 4.6e) and a sharp drop of the Km at 580°C (Fig. 4.6f) reveal the presence of magnetite as the main susceptibility carrier. According to the hysteresis curves (*Dunlop*, 2002), the presence of pseudo-single domain (PSD) and multi-domain (MD) magnetite has been estimated (Fig. 4.6b).

In summary, the magnetic susceptibility carriers of the Pengguan granitic rocks mainly consist of paramagnetic minerals (biotite) with a small part of the PSD/MD magnetite, which display a normal correlation to the tectonic or magmatic fabrics (*Rochette et al.*, 1992). The magnetic carriers of the Pengguan granitic rocks are consistent with the consensus since long that, in granitic rocks, the paramagnetic behaviour is mainly carried by the micas while the ferromagnetic one is carried by magnetite (*Bouchez*, 1995, 1997; *Kruckenberg et al.*, 2010; *Wei et al.*, 2014a)

3) AMS Results

A lack of consistent correlation between P_J, T and Km (Fig. 4.5c and 4.5d) implies that AMS, at least for the paramagnetic susceptibility carrier, varies independently from the magnetic minerals (*Borradaile and Henry*, 1997). The sites of *LM07* and *LM13* with extremely high P_J, could be the result of extremely high susceptibility (*Rochette et al.*, 1992). These sites may be affected by enrichments of magnetic minerals due to posterior hydrothermal fluid circulation, and will be ignored in the following discussion.

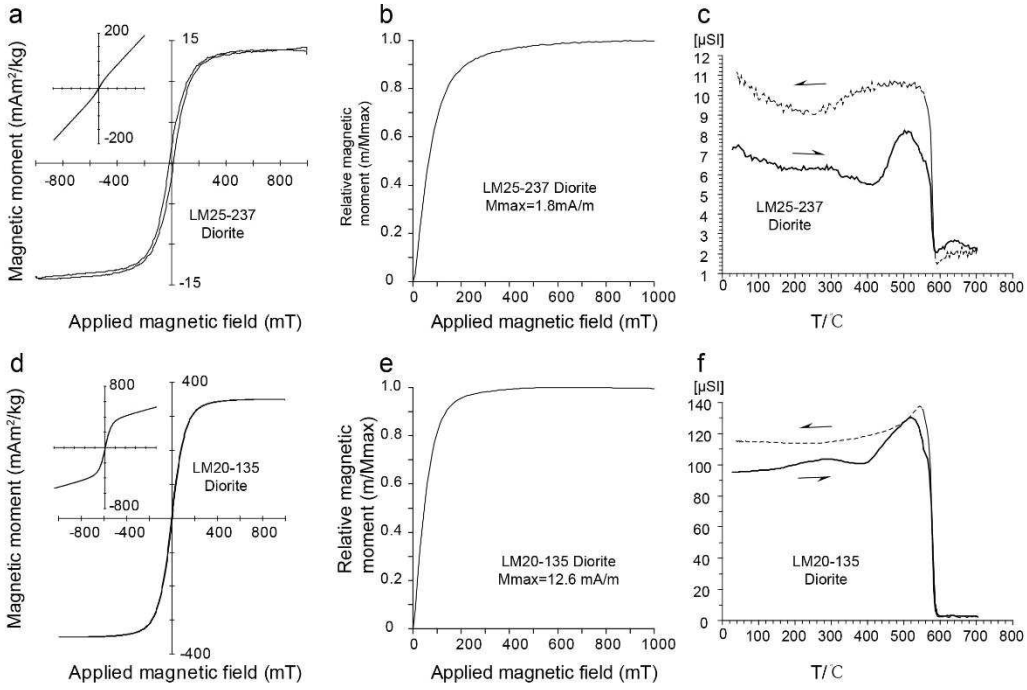

Fig. 4.6 Magnetic mineralogical measurements of representative specimens from the Pengguan granitic rocks.

Magnetic hysteresis loop diagram (a, d; small insects are those before removing paramagnetic component), measurements of Isothermal Remanent Magnetization (b, e), and thermomagnetic experiments (c, f) of the Pengguan granitic rocks

The equal-area projection of the magnetic principal axes with their confidence ellipses at 95% level are given in Fig. 4.7. Most magnetic principal axes are well defined with low α_{95max} values (Fig. 4.7; Table 4.1). The sites of *LM23, LM24* and *LM27* display poorly defined magnetic fabric and will be ruled out in the following discussion. Some fabrics indicate that K_2 and K_3 have a girdle distribution on the same plane (*LM10, 21, 23, 31,* and *33*) that reflects a prolate fabric and corresponds to a negative T value (Table 4.1) (*Kruckenberg et al.*, 2010).

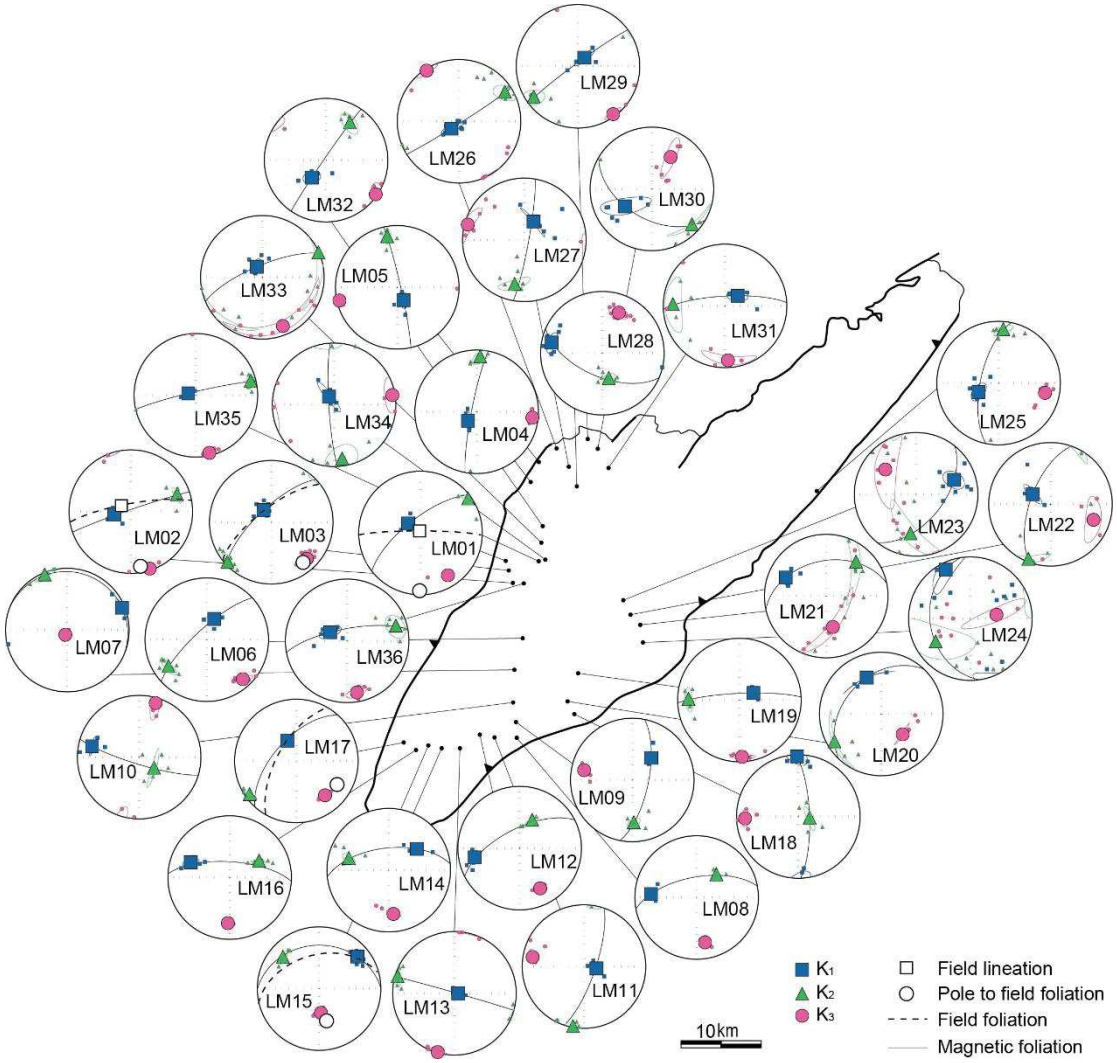

Fig. 4.7 AMS fabrics for each site of Pengguan granitic rocks and compare to the field measured fabrics.

K1: magnetic lineation, K3: pole of magnetic foliation. All projections are equal area lower hemisphere projection.

The orientation contour diagrams of the magnetic fabrics distinguish a prevailing group of foliations dipping steeply to the NW (with an average direction of 53° NW 76°) and lineations plunging steeply to the NW (with an average direction of 315° NW 75°; Fig. 4.8a). The orientation diagrams also reveal a subset of sites with moderately N-dipping or steeply E-dipping foliations and moderately NE-plunging lineations.

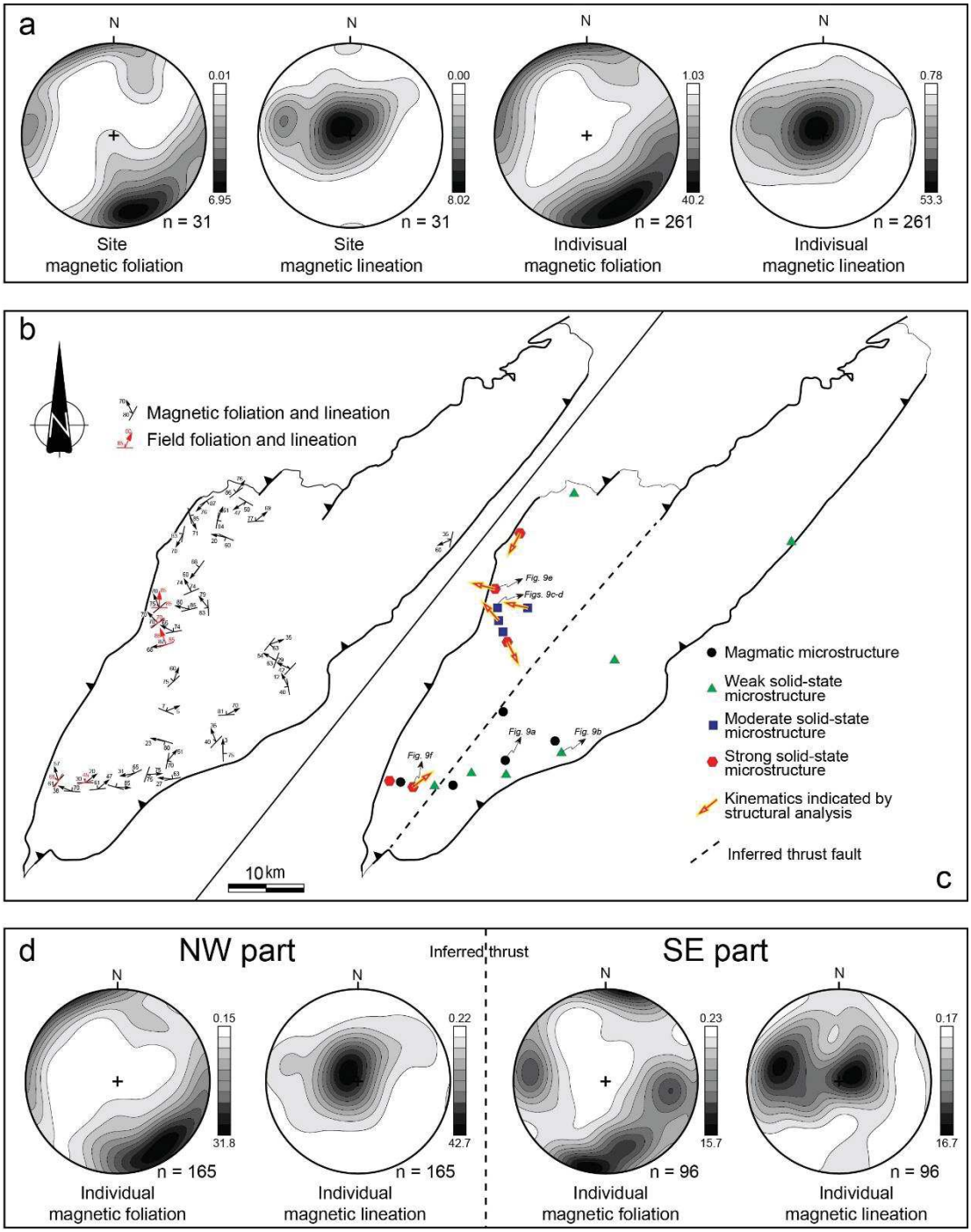

Fig. 4.8 Data analysis after removing the extremely high Km sites of LM07, 13 and poorly defined sites of LM23, 24, and 27.

(a) Orientation contour diagrams of site-mean and individual magnetic fabircs; (b) Site-mean magnetic and field fabrics of the Pengguan complex; (c) Deformation intensity zonation based on microstructural study; (d) Orientation contour diagrams of individual magmatic fabrics partitioning based on deformation zonation. All projections are equal area lower hemisphere projection.

Magnetic structures of the complex in map view display that the steeply NW-dipping foliations generally associated with the steeply NW-plunging lineations are

mostly distributed in the NW part of the complex. While the N-dipping foliations and associated moderately NE-plunging lineations, and other magnetic fabrics having random azimuth are mostly distributed in the SE part of the complex (Fig. 4.8b). It is worth noting that the AMS fabrics of the NW part of the complex is consistent with the tectonic ones measured in the field.

Specimens cut from samples of five representative sites (*LM01*, *02*, *03*, *15*, and *17*) that had well-clustered magnetic fabrics were selected to evaluate the relationship between the principal AMS directions and macroscopic fabrics observed in the field. The magnetic foliation in all five selected samples corresponds well with the mylonitic foliation measured in the field, and when the lineation could be observed in the field, it corresponds well with the orientation of K_1 (Figs. 4.7 and 4.8b). In the XZ plane thin sections, aligned biotite or aligned magnetite wrapping in the oriented chlorite defines the field foliation that also defines the magnetic foliation (Figs. 4.S2a and b).

4) Microstructural analysis

Microtextural and microstructural analyses are based on the observation of mineral relationships, subgrains and intracrystalline microstructures. This is intended to qualitatively assess the deformation of the granitic rocks, and to distinguish the solid-state fabrics from the magmatic ones by comparison of the mineral structures with the AMS fabrics (*Paterson et al.*, 1989, 1998; *Nédélec and Bouchez*, 2015). 21 thin sections coming from 19 AMS sites and 2 hand samples, cut parallel to the magnetic/tectonic lineation and perpendicular to the magnetic/tectonic foliation, were observed under the optical microscope. The systematic examination on these thin sections allowed us to discriminate four types of microstructures including: i) magmatic, ii) weak solid-state, iii) moderate solid-state, and iv) strong solid-state microstructures. The incipient gneiss and mylonite suffered strong solid-state deformation will be discussed with respect to their spatial distribution in the complex.

(1) Magmatic microstructure. The magmatic microstructure does not exhibit visible solid-state deformation. Despite the plagioclase partially altered to sericite, the rock primary structures are defined by well-preserved euhedral amphibole, weak undulose extinction in quartz, and euhedral pseudomorphose of feldspar depicted by sericite aggregates (Fig. 4.9a). The amphiboles with a rhombic shape are randomly

distributed in the groundmass of quartz and feldspar with magmatic microstructures. Biotite grains, with sharp boundaries, are neither kinked nor bent.

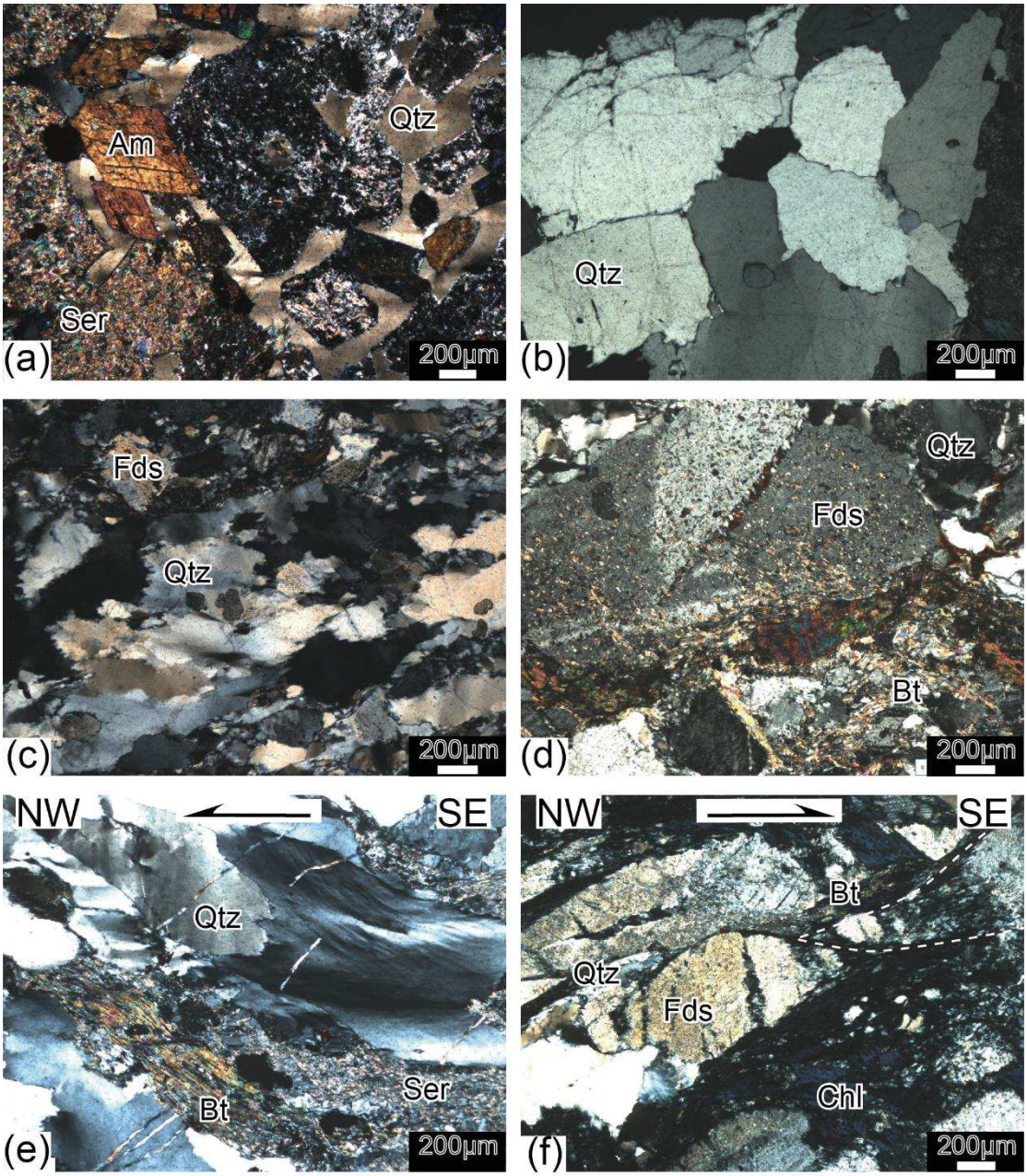

Fig. 4.9 Microstructures observed in the granitic rocks of the Pengguan complex.

(a) Magmatic microstructures with euhedral amphiboles and altered plagioclase grains (31˚16.661´N, 103˚28.322´E); (b) Weak solid-state deformation, lobate quartz boundaries and a few buldging neograins indicate partial recrystallization (31˚05.812´N, 103˚33.763´E); (c) and (d) Moderate solid-state deformation: (c) Quartz-quartz serrated boundaries and recrystallization with similar grain shape preferred orientation, subgrain rotation is the dominant recrystallization mechanism (31˚16.661´N, 103˚28.321´E); (d) Feldspars flexured like sand clock with biotite and chlorite wrapped around (31˚16.661´N, 103˚28.321´E); (e) and (f) Intensive solid-state deformation: (e) Recrystallized quartz grains organized into ribbons and mica aggregates form sigmoidal structures that indicate top-to-the-NW shearing (31˚22.391´N, 103˚20.848´E); (f) Fine-grained quartz and feldspar forming tails around residual feldspar phenocrysts that indicate top-to-the-SE shearing (31˚03.536´N, 103˚30.588´E). Qtz: Quartz;

Cal: Calcite; Bt: Biotite; Ms: Muscovite; Ser: Sericite; Am: Amphibole; Chl: Chlorite; Fds: Feldspar

(2) Weak solid-state microstructure. The quartz grains have undulose extinction and sub-grain walls are developed (Fig. 4.9b). Quartz-quartz boundaries are lobate or slightly serrated, and small newly-formed grains appear with the same grain shape preferred orientation, arguing for the onset of dynamic recrystallization. Biotite grains are slightly elongated due to glide along their basal plane. Such a microstructure indicates that some deformation took place during the transition from magmatic to solid-state.

(3) Moderate solid-state microstructure. Moderate solid-state microstructure is attested by the ubiquitous serrated grain boundaries and uniform grain size that replace the primary quartz grains with slight lattice misorientation. Subgrain rotation becomes the main dynamic recrystallization mechanism in quartz (Fig. 4.9c). The biotite grains record extensive kinking and the feldspars displays like a sand clock due to fracture or flexure (Fig. 4.9d).

(4) Strong solid-state microstructure. In the intensive solid-state deformation microstructures, the aggregates and recrystallized grains display obvious mylonitic characteristics. The quartz grains become ribbon-shapped and the mica aggregates form sigmoidal structures (Fig. 4.9e). Fine-grained quartz and feldspar form tails around residual feldspar phenocrysts (Fig. 4.9f).

Although merely 21 sites were conducted for microstructural observations for the whole Pengguan complex, the above defined types of deformation state display a well-defined distribution (Fig. 4.8c). The moderate and strong solid-state deformed microstructures are exclusively distributed in the NW part of the complex, while the weak solid-state and magnetic fabrics are distributed in the SE part.

5) Interpretation of AMS and microstructures of the Pengguan granitic rocks

The magnetic susceptibility of the Pengguan granitic rocks mostly arises from paramagnetic biotite and partly ferromagnetic magnetite (PSD or MD) based on *Km*, thermo-magnetic, hysteresis loop and isothermal remanent magnetization measurements. Numerous previous studies have demonstrated that this kind of paramagnetic minerals carry comparable magnetic fabrics in terms of orientation with

the mineral petrofabrics (*e.g., Rochette*, 1992; *Bouchez et al*. 1995, 1997; *Ferré*, 2002; *Borradaile and Jackson*, 2004). As mentioned above, the sites of the mylonite of within the Pengguan complex display well clustered magnetic fabrics that are consistent with the field ones according to the stereonet projection and microscopic characteristics (Figs. 4.7, 4.8b, S2a and S2b). Thus the subfabrics of the biotite and magnetite contribute to the normal magnetic fabrics.

The well-grouped magnetic fabrics characterized by steeply NW-dipping foliations and steeply NW-plunging lineations, from these rocks with moderate solid-state deformation, are consistent with those from ductilely deformed ones as well as the regional field fabrics, which are mostly distributed in the NW part of the Pengguan complex. While, the SE part of the complex, characterized by magmatic and weak solid-state microstructures, displays randomly oriented magnetic fabrics (Fig. 4.8d). Thus, it is reasonable to suggest that most of the magnetic fabrics of the NW part of the complex arise from ductile deformation.

In addition to the kinematics described in Section 3.2, the asymmetric quartz ribbon, the sigmoidal structures of micas and feldspars on thin sections (perpendicular to the field foliation and parallel to the magnetic lineation) indicate both top-to-the-NW and top-to-the-SE shearing in the NW part of the Pengguan complex (Figs. 4.8b and 4.9e-f). The mineral assemblage that defines the foliation includes quartz + feldspar + biotite + chlorite; it suggests the top-to-the-SE shearing under greenschist facies metamorphism conditions, which is similar in metamorphic grade to the top-to-the-NW shearing in the NW boundary of the complex (Figs. 4.4 and 4.9f).

4.4 Gravity modeling

Gravity modeling has long been used to depict the bulk architecture of deep structures; it is especially well-suited to decipher the geometry of plutonic massifs (*e.g., Talbot et al.*, 2005; *Turrillot et al.*, 2011; *Lin et al.*, 2013; *Wei et al.*, 2014a). In order to complement our field structural and AMS observations, we applied this approach to constrain the deep structure of the Pengguan complex and adjacent areas.

1) Gravity map

In the study area, a detailed Bouguer anomaly map (1:200000) was acquired from the Geological Survey of China, complemented regionally by a lower resolution

(2'x2') Bouguer grid acquired from the International Gravimetric Bureau database (*Bonvalot et al*., 2012). In order to highlight the short wavelengths gravity signatures of the upper crust, the long wavelengths gravity anomaly were subtracted from the complete Bouguer anomaly at the regional scale. After several trials, the regional component was extracted using a low-pass Butterworth filter with a 70 km cut-off which i) fitted well the gravity trends at the regional scale, ii) properly outlined residual anomalies over known outcropping geological structures. In Fig. 4.10, main geological contours are superimposed on the residual gravity anomaly map (*BGMRSP*, 1991).

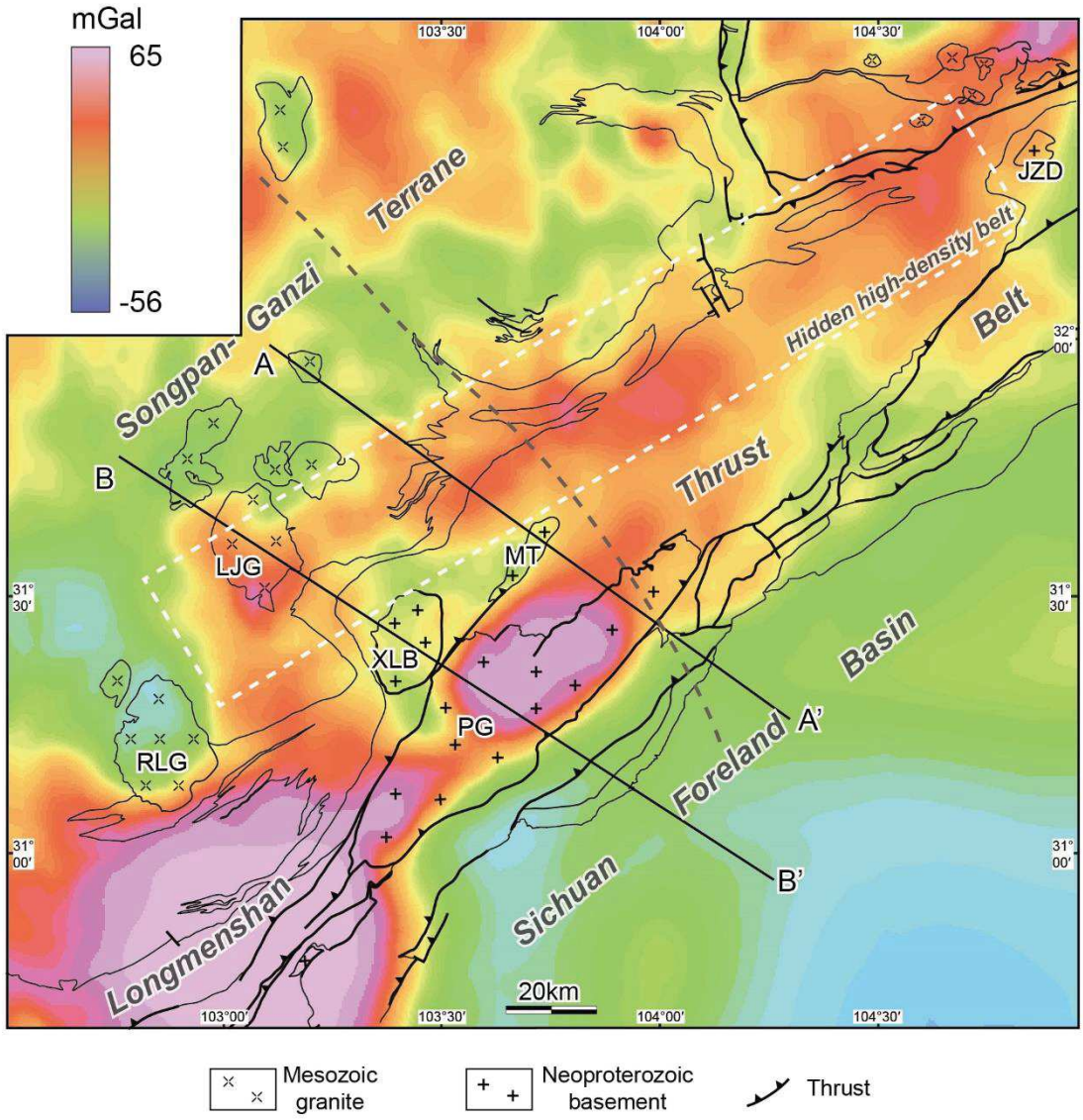

Fig. 4.10 Residual Bouguer gravity anomaly of the Pengguan complex and adjacent areas after substraction of a 70km wavelength regional trend from the complete Bouguer anomaly.

Grey dashed line represents the location of the seismic profile processed by Guo et al. (2013). PG: Pengguan complex; XLB: Xuelongbao complex; MT: Moutuo complex; JZD: Jiaoziding complex; RLG: Rilonguan granite; LJG: Laojungou granite.

The general architecture of the residual gravity map is structured along three main NE-SW-trending units: in the center, the LMTB predominantly outlined by high gravity anomalies, separates the Sichuan foreland basin to the SE, marked by well-defined low gravity anomalies, and the SGT to the NW, marked by intermediate gravity signatures. In the residual anomaly, several Mesozoic granites intruded in the SGT display well-defined negative anomalies due to their low density relative to the country rocks (Fig. 4.10). A significant positive anomaly appears at the position where the Pengguan complex is located (Fig. 4.10). To the northwest of the Pengguan complex and nearly parallel to the LMTB, there is a well-defined positive gravity anomaly belt, which does not associate with any outcrop of high density material (Fig. 4.10).

2) 2D gravity modeling

To feature the deep geometry of the Pengguan complex within the LMTB tectonic context, 2D gravity modeling was performed. Two NW-SE trending profiles perpendicular to the LMTB were modeled using Geosoft-GM-SYS software (Fig. 4.10). Density of rocks considered in the modeling is derived partly from laboratory measurements. We concentrated our density determinations on rocks outcropping in the Pengguan complex and surrounding areas (Fig. 4.11), concerning the more peripheral or non-outcropping geological units, we complemented our dataset with densities from a previous study (*Zhang et al*., 2009). For non-outcropping deep units, the density of the undifferentiated upper crust was chosen at 2.72 g/cm^3 following *Turrillot et al*. (2011), and we considered the existence of a deep low density material (density 2.65 g/cm^3) imbricated with the Pengguan rocks that we discuss in a next stage. We also took into account very dense basic/ultrabasic material (density 3.0 g/cm^3) intercalated in the Pengguan complex. This is consistent with the NE-SW trending diabase/gabbro intrusions (*ca*. 195-186 Ma) reported in the Pengguan complex (Figs. 4.2a and 4.3c) (*Chen et al., 2015*). Also, we assumed that the NE-SW trending hidden high density belt northwest of Pengguan complex share the same density as the Pengguan complex. In our profiles, the overall tectonic style and structural dips were made consistent with surface geological observations and

information available in nearby seismic profiles. In particular, the three main listric thrust faults were constrained by the seismic reflection data, two of them bound the Pengguan complex (*Jia et al.*, 2006; *Li et al.*, 2010; *Guo et al.*, 2013; *Feng et al.*, 2015).

3) Interpretation of the gravity model

In Fig. 4.11, the two modeled gravity profiles display similar geological architectures that portray the western Sichuan foreland basin and the SGT, taking into account the overall strata thicknesses constrained by regional geological mapping (*BGMRSP*, 1991). According to our models, the SGT, intruded by several Mesozoic plutons, is underlain by a very structured basement, while the strata in Sichuan basin are rather flat, as shown in the seismic profile (Fig. 4.11C) (*Guo et al.*, 2013; *Feng et al.*, 2015). In our models, on both sides of the Pengguan complex, the significant thickening of certain sedimentary units is interpreted as the result of folding and thrusting due to the bulk shortening in the LMTB since the Late Triassic. The simplified density applied in the modeling could also partly contribute to the variations in strata thickness. The gravity modeling suggests that the Xuelongbao complex is a 2-3 km thick rootless batholith and the Moutuo complex is even thinner (Fig. 4.11). On the contrary, the Pengguan complex is thick (*ca.* 20 km), which is partly due to tectonic stacking, according to the gravity model (Fig. 4.11).

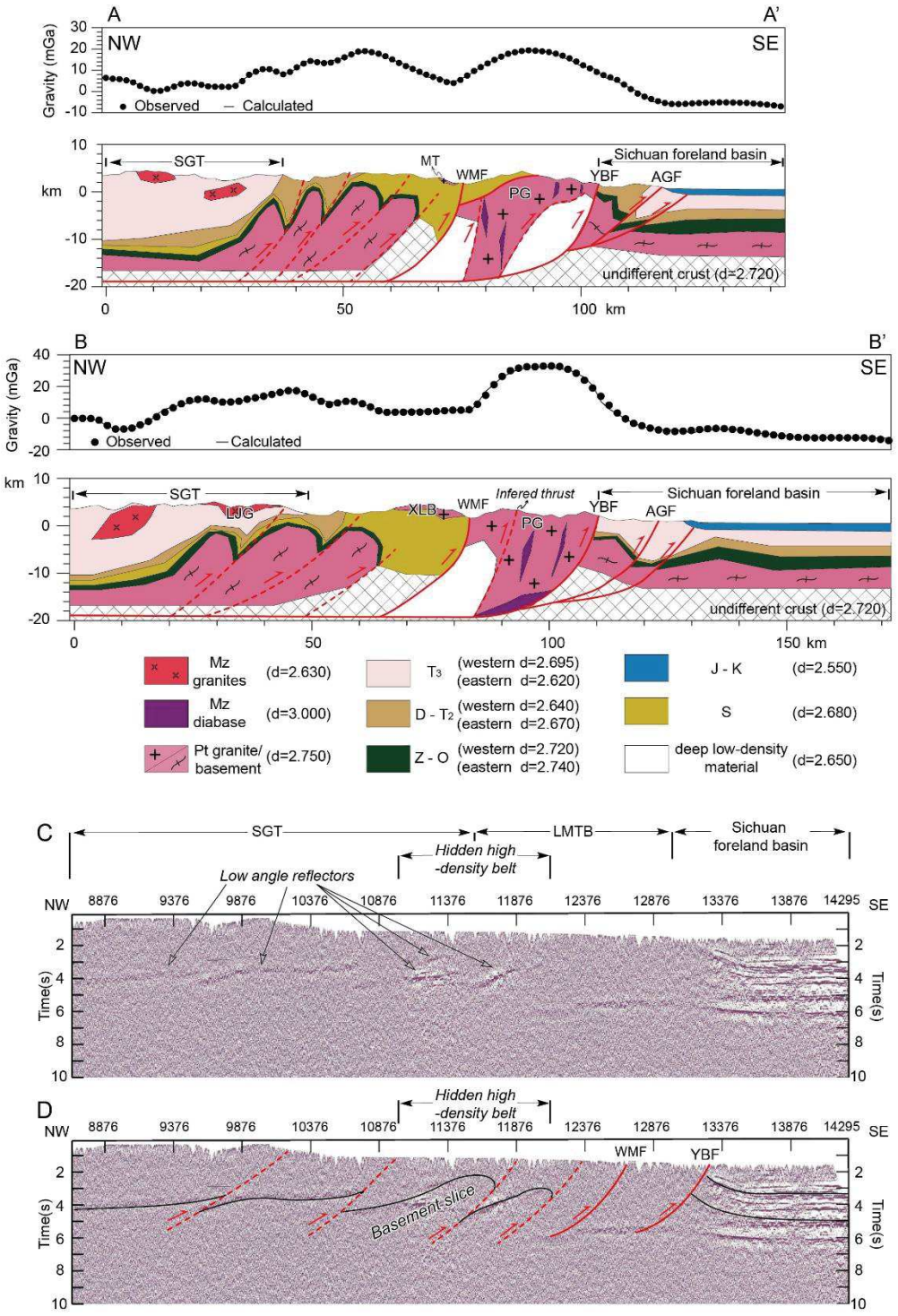

Fig. 4.11 (A-B) Forward gravity models across the LMTB range. The effect of the model, represented by the black continuous line, matches the observed residual Bouguer gravity values represented by the black dots; (C) Seismic profile processed by Guo et al. (2013); (D) Schematic reinterpretation of the seismic profile. Location of these profiles are marked in Fig. 4.10. Thick red lines refer to the thrust faults constrained by seismic reflection data. The dashed red lines represent interpreted thrust faults. Symbols and acronyms are the same as in Fig. 4.1.

As indicated by the gravity model, the Pengguan complex would be strongly tectonized and the NW part of the complex would be underlain by low density material, likely implying that a thrust fault separates the NW part from the SE part of the complex. This structure is consistent with the zonation of the AMS fabrics and microstructures (Figs. 4.8b-d and 4.11). In accordance with the structural observations, the profiles suggest that the NW part of the Pengguan complex is an allochthonous basement slice, thrusted SE-ward onto the autochthonous SE part. Further to the NW, the hidden high-density belt is considered as an equivalent of the Pengguan complex, but still not outcropping, strongly tectonized and folding the overlying Paleozoic sediments. The gravity model indicates that this high-density belt is associated with an undulated residual Bouguer anomaly, and we match this gravity pattern featuring a series of imbricated basement slices (Fig. 4.11). Either thrusting or normal movement could form such stacked structure. We favor the thrusting as a result of compressional tectonics because field observations show exclusively compressional structures in the study area (*Xu et al*., 1992; *Burchfiel et al*., 1995; *Worley and Wilson*, 1996).

Two possible reasons could account for the low density material right upon the YBF featured in profile A-A': i) low density Late Triassic sediments tectonically imbricated with granitic rocks during thrusting (*Lu et al.*, 2014), or ii) the indirect effect due to relatively less mafic intrusions inside the northeastern Pengguan complex compared to its southwestern part (Fig. 4.11).

4.5 Discussion

1) Summary of our new results

Our microstructural analysis of the Pengguan complex indicates that the ductile deformation developed in its NW part and is absent in its SE part. The AMS fabrics of the ductilely deformed NW part display steeply NW-dipping foliations associated with steeply NW-plunging lineations, which are consistent with the field-observed fabrics. The SE part displays N-dipping foliations associated with lineations moderately plunging to the NE or randomly oriented magnetic fabrics (Figs. 4.8b-d). Thus the ductile deformation in the NW part was strong enough to erase the primary magmatic fabrics. A top-to-the-NW and a top-to-the-SE shearing with a greenschist facies metamorphism were developed along the NW and SE boundary of the NW part

of the Pengguan complex (Fig. 4.8b). These observations let us suppose that the NW and SE parts of the complex are separated by a thrust fault. The NW part of the complex acted as an allochthonous basement slice that imbricated southeastwards and overlaid the autochthonous SE part (Figs. 4.2b and 4.8c).

Two orogen-perpendicular gravity profiles reveal that i) the imbricated slices of the Pengguan complex are consistent with the AMS and microstructural study, ii) the Sichuan foreland basin and SGT are well-portrayed, and iii) northwest of the Pengguan complex, high density material (basement) concealed by the Paleozoic rocks display the same thrusted/imbricated pattern as the Pengguan complex (Fig. 4.11). In summary, the data presented in this work document a NW-SE-oriented basement-slice-imbricated structure of the Pengguan complex and adjacent areas.

2) Lateral extent of the basement-slice-imbricated structure

A high resolution seismic profile across the LMTB has been processed by *Guo et al*. (2013) (Figs. 4.10 and 4.11C). The base of the SGT and of the Sichuan foreland basin interpreted in the seismic profile is consistent with our gravity profiles. In the seismic profile, an echelon arrangement of reflectors moderately dipping to the NW corresponds to the place where the hidden high gravity anomaly belt is located (Figs. 4.10 and 4.11C). These reflectors were previously interpreted as pop-up and back thrust structures (*Guo et al*., 2013). However, the reflectors in the seismic profile can be re-interpreted as SE-ward imbrication of basement slices, in agreement with our gravity profiles (Fig. 4.11D). Furthermore, the relatively flat reflectors of the SGT are dissected and benched as well.

At the local scale of the Pengguan complex, the top-to-the-NW shearing and the top-to-the-SE shearing control the southeastward basemen-slice imbrication of the NW part of Pengguan complex. At the regional scale, the top-to-the-NW/N shearing that affects the Pengguan complex, extends from the north of Danba dome, across the north of Kangding complex, the Baoxing complexes, and may extend to the Jiaoziding complex, totalizing more than 300 km in length (Fig. 4.1a) (*Xu et al.*, 2008; *Burchfiel et al.*, 1995; *Li*, 2009; *Tian et al.*, 2016). Thus, it is likely that a first belt of imbricated basement slices represented by the orogen-parallel Neoproterozoic complexes, is regionally developed along the LMTB. Combining the gravity anomaly residual and the seismic profile, a second belt of imbricated basement slices

represented by the hidden high-density material that may be regionally developed to the west of the LMTB as well. These two parallel belts of imbricated basement slices therefore constitute the LMTB and adjacent areas (Fig. 4.10).

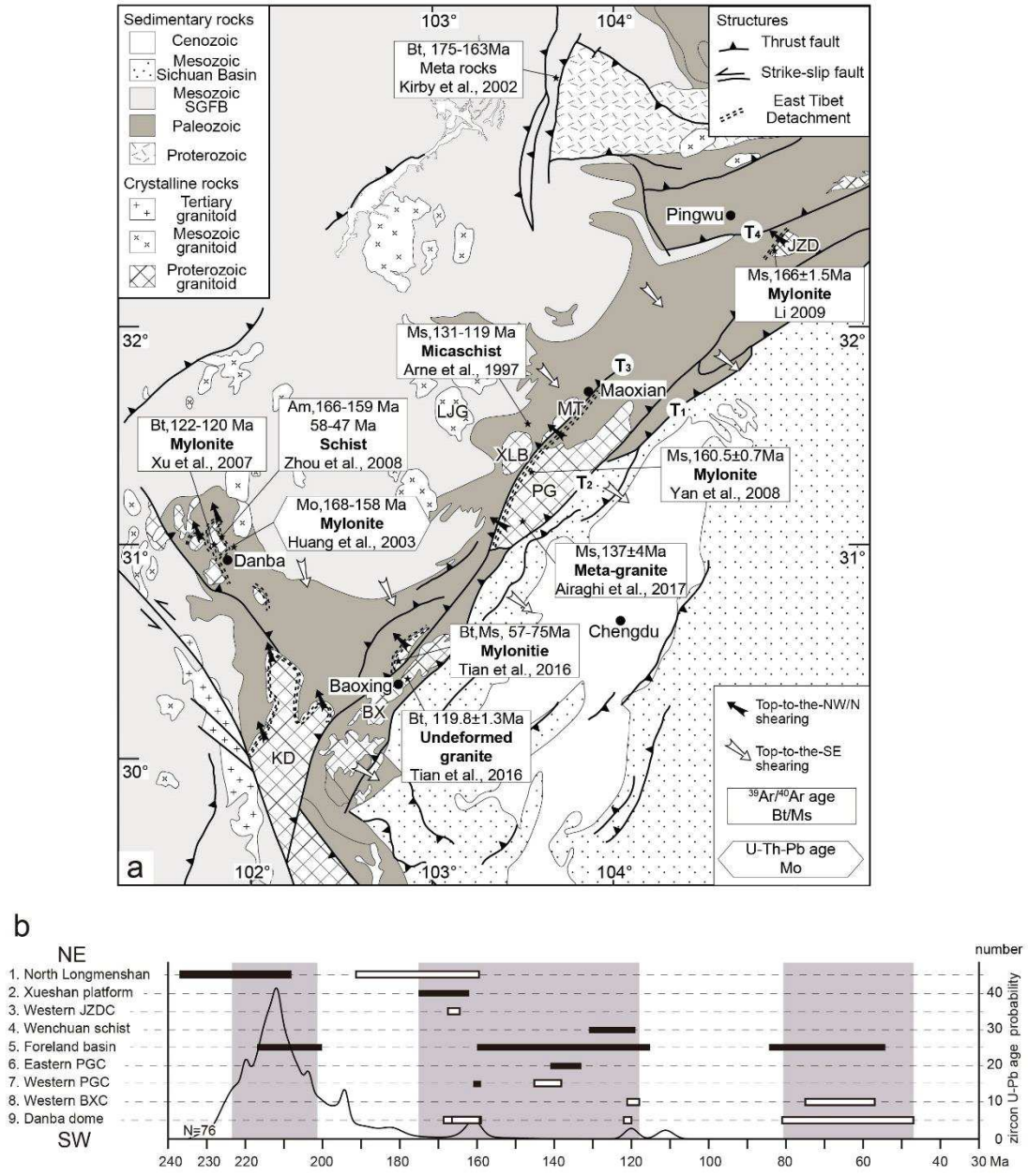

Fig. 4.12 (a) Kinematic map of the Pengguan complex and its adjacent area with the compilation of published geochronological results; (b) 39Ar/40Ar ages from along the LMTB and zircon age probability diagram of the Mesozoic igneous rocks in the SGT.

Black rectangle represents samples from the top-to-the SE/S shearing domain, white rectangle represents samples from the top-to-the N/NW shearing domain. Curve represents the zircon age probability diagram of the Mesozoic igneous rocks in the SGT. 1. Yan et al., 2011; 2. Kirby et al., 2002; 3. Li et al., 2009; 4. Arne et al., 1997; 5. Li et al., 2013; 6. Airaghi et al., 2017; 7. Yan et al., 2008 and Dirks et al., 1994; 8. Tian et al., 2016; 9. Huang et al., 2003b, Zhou et al., 2008 and Xu et al., 2008. Symbols and acronyms are the same as in Fig. 4.1.

3) Geochronological constraints

Published $^{39}Ar/^{40}Ar$ ages measured along the LMTB, on mica, amphibole, and U-Th-Pb dating on monazite from mylonites and micaschists are presented in Fig. 4.12a, and these ages can be roughly divided into three periods (Fig. 4.12b). The first period from 237 to 200 Ma, and the third period from 81 to 47 Ma, correspond respectively to the Early Mesozoic and Late Cretaceous-Cenozoic shortening in the LMTB. The zircon ages of the granites in the SGT reveal one predominant peak at *ca.* 211 Ma that postdates the Early Mesozoic shortening (Fig. 4.12b) (*BGMRSP*, 1991; *Roger et al.*, 2004; *Hu et al.*, 2005; *Zhang et al.*, 2006; *Xiao et al.*, 2007; *Sigoyer et al.*, 2014).

The second group of $^{39}Ar/^{40}Ar$ ages span over a large period between 175 and 118 Ma (Fig. 4.12). For the belt displaying the top-to-the-NW/N shearing distributed at the NW/N-boundary of the Neoproterozoic complexes, the micas from NW boundary of the Jiaoziding complex yield an $^{39}Ar/^{40}Ar$ age of *ca.* 166 Ma (*Li*, 2009). $^{39}Ar/^{40}Ar$ dating on amphibole and U-Th-Pb dating on monazite from mylonite and micaschists in the north of the Danba dome yield ages between 168-158 Ma (*Huang et al.*, 2003b; *Zhou et al.*, 2008). Younger ages, at *ca.*120 Ma, have also been reported at the northwest boundary of the Baoxing complex and the north boundary of the Danba dome (*Xu et al*., 2008; *Tian et al.*, 2016). For the top-to-the-SE shearing, $^{39}Ar/^{40}Ar$ dating on muscovite from the Pengguan mylonitic rocks yields ages of 166-140 Ma (*Airaghi et al*., 2017; *Yan et al*., 2008). West of the Pengguan complex, the age of the micaschists involved in the top-to-the-SE shearing has been constrained between 131-119 Ma by $^{39}Ar/^{40}Ar$ dating on muscovite (*Arne et al.*, 1997). A period of flexural subsidence in the Sichuan foreland basin during J_3-K_1 is probably coeval with the SE-thrusting of the LMTB (*Dirks et al*., 1994; *Li et al*., 2013). Thus the top-to-the S/SE shearing and the top-to-the N/NW shearing that control the imbrication of the first belt of basement slices occurred during J_3-K_1.

Detailed geochronology studies on the metamorphic and magmatic rocks of the SGT indicates a slow regional cooling history during 203-30Ma (*Huang et al.*, 2003a, 2003b; *Roger et al.*, 2011). Meanwhile, the Mesozoic Laojungou granite (224±5Ma) in the SGT experienced a rapid exhumation between 172-140 Ma (*Yuan et al.*, 1991; *Zhao*, 2007). The Laojungou granite was probably popped up by the imbrication of

the underlying basement slices, resulting in localized fast exhumation (Model B-B' in Fig. 4.11). This was contemporary to the localized fast exhumation (168-158 Ma) recorded in the Danba area (*Huang et al.*, 2003b).

In Fig. 4.12b, the zircon age distribution of the granites in the SGT also displays two weak peaks at *ca.* 162 and *ca.* 120 Ma, which could be the magmatic response to the imbrication of the basement slices. In summary, we argue that this basement-slice-imbricated structure formed during the Late Jurassic-Early Cretaceous times.

4) Evolution model of the LMTB and its tectonic implications

Several models have been invoked to interpret the emplacement of the orogen-parallel Neoproterozoic complexes and associated top-to-the-NW/N shearing (*Burchfiel et al.*, 1995; *Li*, 2006; *Xu et al.*, 2008; *Zhou et al.*, 2008; *Tian et al.*, 2016). The crustal wedge extrusion or lower crust flow bounded by a thrust on the foreland side and a normal fault on the hinterland side has been suggested (*Xu et al.*, 2008; *Burchfiel et al.*, 2008). In these models, alike the Himalayan with the Main Boundary Thrust and South Tibetan Detachment, an extensional basin would be expected in the hanging wall side of the normal fault (*Royden et al.*, 1997), whereas, no basin has been reported in the hinterland of the LMTB. This model of the lower crust flow considers that the partially melted lower crust is driven by the topography loading and surface denudation (*Royden et al.*, 1997). However, the partially melted material, such as the leucogranitic magmatism in south Tibet, is absent in the LMTB. Another crust duplex model under contractional tectonics has been proposed to explain the southwestern LMTB (*Tian et al.*, 2016), but failed to explain the top-to-the-NW shearing and the imbrication of the Neoproterozoic basement. All three models mentioned above did not incorporate the second belt of imbricated basement slices in the SGT.

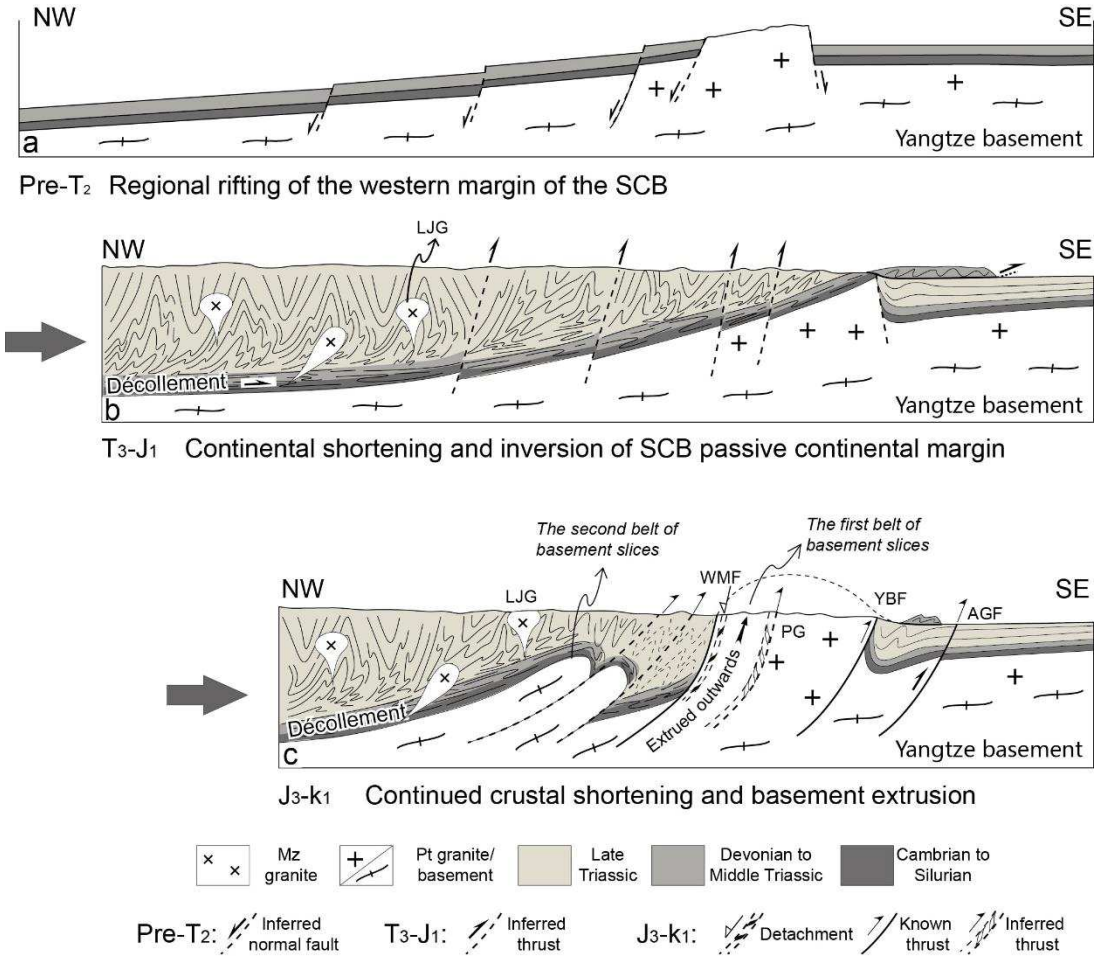

Fig. 4.13 A possible evolution scenario of the LMTB.

(a) A Pre-middle Tricassic rift along the South China Block (SCB); (b) During the Late Triassic-Early Jurassic continental shortening and inversion of SCB passive continental margin; (c) During the Late Jurassic-Early Cretaceous, Continued crustal shortening and basement slice extrusion. The symbols and acronyms are the same as in Fig. 4.1.

The imbricated Neoproterozoic complex and the hidden imbricated structure leads us to propose a basement slice imbrication model. The first belt of basement slices is exposed on the surface as the orogen-parallel Neoproterozoic complexes, while the second belt of basement slices is concealed to the west of the LMTB. Fig. 4.13 presents a general evolution scenario of the LMTB and adjacent areas. During T_3-J_1, the Mesozoic shortening led to large-scale southeastward thrusting and folding of the Paleozoic-Triassic formation of the SGT, along a regional décollement located in the low-strength Silurian shale and pelite, and the latter was transported southeastwards to the Sichuan foreland basin as nappes (*Xu et al*., 1992; *Calassou*, 1994; *Burchfiel et al*., 1995; *Roger et al*., 2004). At the same time, the passive margin of the South China Block was inverted and formed a step-like basement surface in the Longmenshan area (Figs. 4.13a and b) (*Long*, 1991; *Chen et al.*, 1994a; *Burchfiel et*

al., 1995). These crustal thickening and shearing events were responsible for the widespread intrusion of granites in the SGT and the initiation of the Sichuan foreland basin (*Calassou*, 1994; *Roger et al.*, 2004; *Harrowfield and Wilson*, 2005; *Hu et al.*, 2005; *Sigoyer et al.*, 2014).

During J_3-K_1, the basement was cut into slices by several faults and transported southeastwards probably due to the collision between the Lhasa and Qiangtang blocks (Fig. 4.13b) (*Yin and Harrison, 2000*). The first belt of imbricated basement slices represented by the Jiaoziding, Pengguan, Baoxing, Kangding complexes and the Danba dome is located in the proximal continental margin of the Yangtze Block, part of the South China Block. These slices accumulated the highest strain and were 'squeezed' outwards, which formed the contemporaneous top-to-the-NW shearing and top-to-the-SE shearing along their NW and SE boundaries, respectively (Fig. 4.13c). The second belt of basement slices underlies and sustains the SGT so that no extensional basin developed at the hanging-wall side of the NW-normal fault (Fig. 4.13c).

Coeval top-to-the hinterland shearing and top-to-the foreland thrusting are generally developed in orogens with thickened crust though their thickening mechanisms are fundamentally in variance, such as in the Miocene Himalaya (introduced above), the Alpine orogen (e.g., Tavarnelli, 1999; Schmid et al., 2004; Selverstone, 2005), the Late Devonian Appalachians (e.g., Pinet et al., 1996; Castonguay et al., 2007), the Scandinavian Caledonides (e.g., Hartz and Andresen, 1997; Grimmer et al., 2015) and the central East Greenland Caledonides (e.g., White and Hodges, 2002; Johnston et al., 2010). It is therefore reasonable to suggest that the Longmenshan crust had reached a significant thickness by the Late Jurassic-Early Cretaceous, probably due to the imbrication of basement slices. This inference is consistent with the contemporaneous development of Barrovian metamorphism west of the WMF and migmatization north of the Danba dome (Dirks et al., 1994; Arne et al., 1997; Huang et al., 2013b). Inverse multi-equilibrium thermodynamic approach and in situ 39Ar/40Ar dating indicate that the Pengguan complex was exhumed from ca. 20 km depth and overprinted by greenschist facies metamorphism during 135-140 Ma (Airaghi et al., 2017). If this conclusion is convincible, that is to say, the basement slices were backstopped, piled up and imbricated upwards by listric faults over 20 km thick, this means that the crust of the LMTB had already experienced a certain

amount of thickening in Mesozoic times. Thus, the Cenozoic shortening that gave rise to the present Longmenshan belt might have been less important than often assumed.

4.6 Brief summary

Structural analysis, AMS measurements, petrofabric study and gravity modeling reported in this study depict the bulk architecture of the LMTB and adjacent areas developed as two parallel belts of SE-imbricated basement slices. The first belt of basement slices is bounded by the top-to-the-NW/N shearing and top-to-the-SE shearing that formed the Pengguan complex and other orogen-parallel Neoproterozoic complexes. While, the second belt of imbricated basement slices underlies the SGT and sustains its high topography.

The published geochronological data, the localized fast exhumation rate and lithological characteristics of sediments in the Sichuan foreland basin indicate that the imbrication of the basement slices occurred during Late Jurassic-Early Cretaceous. We therefore suggest that the crust of the LMTB experienced a significant phase of crustal thickening during the Late Mesozoic, reinforcing the idea that the plateau may have a long history of uplifting and growing.

5. Mesozoic tectonic evolution of the Longmenshan and its implications

5.1 Multiphase deformation

The LMTB separates the SGFB to the NW and the Yangtze Block to the SE, as a key geological boundary, which records two important phases of deformation. The Vertical Cleavage Belt (VCB) within the LMTB mainly composed of pelite, silt, displaying vertical cleavage and foliation wrapping tightly rootless intrafolial folds and vertical budin that document intensive shortening in the study area. Along the VCB, no obvious lineation or horizontal striation has been observed on the foliation.

During the D_1 deformation, the VCB, as an boundary of the structural geometry and the kinematics, divides the LMTB into an eastern zone and a western zone. The eastern zone can be further divided into four subunits based on deformation intensity and metamorphic grade, from SE to NW are autochthon, para-autochthon, allochthon and meta-autochthon. The meta-allochthon records the highest grade of metamorphism having exclusively NW-dipping foliation and NW-SE trending mineral and strecthed lineation, indicating top-to-the-SE shearing. Temperature results constrained by the mica-thermometer showing highest temperature in the middle of this unit and gradually decreasing to NW and SE, which depict a giant SE-overturned fold that consistent with the regional kinematics. The allochthon separates from the meta-allochthon by the Wenchuan-Maowen fault and bounded to the SE by the Yingxiu-Beichuan fault, sharing the similar geometry and kinematics with the meta-allichthon. While its nearly unmetamorphosed compare to the meta-allochthon which attain to lower amphibole facies of metamorphism in local place. The allochthon also include the orogen-pallel klippen and nappes in the front of the LMTB. The para-autochthon located between the Yingxiu-Beichuan fault and the Anxian-Guanxian fault, mostly characterized by intensively folded Lata Triassic rocks overturned to the SE developping cleavage in local place. The overturned fold, layer-parallel slide and shearing budins exclusively indicate top-to-the-SE shearing. Fron NW to SE, from meta-allochthon to autochthon, it is actually the materials located at different place exhumated to the suface during the D_1 deformation. This phase of deformation developed in the whole LMTB that involve the pre-Late Triassic rocks.

The autochthon almost unconformaty cover on the deformation involved rocks that indicate the termination of the D_1 deformation.

D_1 期事件中，西部带位于松潘-甘孜褶皱带东部边缘以及碧口地块南缘，变形层次南北段出现差异：在南段松潘-甘孜东缘，西部带的变形层次较浅，表现为大型向 NW 的倒转褶皱、强烈褶皱的灰岩夹石英脉等，轴面劈理一致倾向 SE，指示上部向 NW 的剪切变形；在北段碧口地块南缘，变形层次加深，面理一致向 S 倾，面理面上可见新生云母矿物定向指示 N-S 的线理，在 XZ 面上，即垂直面理平行线理的切面，从宏观到微观的剪切指向均指示西部带上部向 N 的剪切作用，实质上西部带的变形是 D_1 期变形向 SE 逆冲过程中同时产生的向 NW/N 的反冲。

相比 D_1 的广泛分布，D_2 期事件仅在 D_1 期事件影响范围的东部带局部地区有所表现，主要围绕龙门山呈线分布的元古代刚性杂岩体分布，并在杂岩体不同位置表现出不同的运动学特征。一方面可能由于 D_2 分布的局限性，几何学形态上，野外并未观察到 D_2 与 D_1 明显的叠关系。D_2 变形层次与 D_1 变形层次相近，均为绿片岩相变形层次，因而新生矿物组合并不能明确地区分这两期变形。D_2 最典型的表现即在龙门山沿线元古代杂岩体 NW 缘以一套糜棱岩产出，沿 XZ 面的定向薄片观察，给出非常明显上部向 NW 的剪切变形，明显不同于 D_1 变形期东部带上部向 SE 逆冲的运动学特征。在东部带元古代杂岩 SE 侧，侏罗纪-白垩纪地层虽然不整合覆盖在褶皱变形的晚三叠世及之前的地层之上，但侏罗纪地层自身也经历了褶皱变形，在龙门山北段侏罗纪地层甚至向 SE 倒转，指示向 SE 的剪切变形。而龙门山中段和南段，侏罗纪地层同样卷入褶皱变形，并作为安县-灌县断裂下盘卷入到向 SE 的逆冲推覆变形中。这些侏罗-白垩地层的变形可能对应元古代基底杂岩向 SE 的逆冲推覆。因而 D_2 期事件在地表的表现与基底杂岩的产出密切相关，我们解释为基底杂岩体作为刚性块体向 SE 挤出的过程中，产生 NW 侧向 NW 的正断和 SE 侧向 SE 的逆冲。典型剖面重力模拟结果表明在松潘-甘孜褶皱带底部基底岩片表现为 SE 逆冲堆叠形态。因此 D_2 期事件可能对应龙门山地区广泛的基底岩片逆冲-挤出构造，属于基底岩片卷入变形的薄皮构造(Pfiffner, 2016)，挤出地表的基底岩片构成现今龙门山

沿线分布的元古代基底杂岩一部分，另一部分隐藏在松潘-甘孜下面的基底岩片，造成龙门山地区地壳增厚并支撑着高的地势。

前人多认为龙门山地区的构造变形先由松潘-甘孜 NE-SW 向强烈挤压缩短，在龙门山地区产生左行走滑，再逐渐演变成向 SE 的逆冲推覆(Dirks et al., 1994; Chen et al., 1995; Worley and Wilson, 1996; Arne et al., 1997)。在这个模式中，沿龙门山的左行走滑对龙门山的构造格架的建立起决定性作用。左行走滑的证据包括：1)褶皱形迹在潘-甘孜褶皱带内为 NW-SE 走向，向 SE 靠近龙门山先向南凸出，然后逐渐松转变为 NE-SW 平行龙门山走向(Harrowfield and Wilson, 2005)；2)垂直龙门山面理的水平面上发育指示左行走滑的剪切布丁(Chen et al., 1995)；3)石榴子石内包裹体径迹指示左行走滑分量(Worley and Wilson, 1996)；4)理县地区枢纽近直立的褶皱。但是基于我们的工作，D_1 期事件主要以相向而倾的面理以及 NW-SE 走向的线理为几何学特征(Figure 3.2)，运动学主要以极性向 SE 逆冲和 NW 的反冲为主。尽管在劈理直立带密集发育直立的面理，但整个研究区并未见到明显的水平矿物拉伸线理，因而左行走滑的构造几何学证据不充分。

D_2 期事件在彭灌杂岩 NW 缘向 NW 的正断，被解释为青藏高原下地壳通道流向 SE 逃逸，遭遇冷的刚性四川盆地后向地表挤出时产生的地表构造样式(Royden et al., 1997; Burchfiel et al., 2008; Royden et al., 2008)。但在论文研究中，重力模拟剖面并未揭示出中下地壳存在低密度的塑形流物质，不支持 channel flow 模式；另一方面，前人对元古代杂岩体 NW 缘糜棱岩同构造矿物 $^{40}Ar/^{39}Ar$ 定年结果在 68-166 Ma 之间(Burchfiel et al., 2008; Xu et al., 2008; Zhou et al., 2008; 李佐臣, 2009; Tian et al., 2016)，时间上与 channel flow 发生在新生代并不吻合。

5.2 Geological constraints of the multiphase deformation

在龙门山逆冲推覆带 NW 侧，松潘-甘孜褶皱带内巨厚的上三叠统西康群复理石发生强烈褶皱变形，随后被晚三叠世末期的八宝山组山间磨拉石不整合覆盖(Chen et al., 1995; Chen and Wilson, 1996; 岳远刚, 2014)，标志着松潘-甘孜带内早中生代强烈造山事件的结束。造山后广泛的岩浆活动，切穿松潘-甘孜褶皱带内的褶皱形迹，并围绕岩体发育完好的环状接触变质带(四川省地质矿产局,

1991; Chen and Wilson, 1996; Worley and Wilson, 1996)，这些岩浆岩锆石 U-Pb 年龄统计结果给出 211.7 Ma 的峰值年龄，很好地将松潘-甘孜褶皱变形时间限定在晚三叠世之前。

在龙门山逆冲推覆带 SE 侧，在其强烈的逆冲推覆下，发育四川周缘前陆盆地，沉积巨厚的上三叠统须家河组磨拉石，为晚三叠世晚期以来形成的，理由有以下几点：1)从时间上对比，须家河组相当于松潘-甘孜褶皱带中晚三叠世末期不整合覆盖的八宝山组，后者代表松潘-甘孜褶皱带封闭以后的沉积，前者代表四川周缘前陆盆地稍晚的沉积，表明晚三叠世变形从松潘-甘孜褶皱带向四川盆地逐渐传递的过程(陈社发等, 1994b; Chen et al., 1995)；2)上三叠统须家河组的沉积环境发生显著变化，由上三叠统以前的海相碳酸盐为主的沉积转变为须家河组以陆相碎屑为主的沉积，随后一直保持着陆相沉积环境，另外整套前陆盆地沉积表现为西厚东薄的楔形，向四川盆地方向逐渐尖灭，反映龙门山晚三叠世强烈的逆冲推覆作用(崔秉荃和龙学明, 1991; Chen et al., 1994a; 刘树根等, 1995; 曾允孚和李勇, 1995; 李勇, 1998, 2010, 2011; Li et al., 2003, 2013, 2014)；3)须家河组的沉积范围严格受控于北川-映秀断裂，仅在断裂带东南侧沉积须家河组地层，表明北川-映秀断裂至少在须家河组沉积之前开始逆冲并对四川盆地西缘加载形成前陆盆地，此外在晚三叠世早期沉积的马鞍塘组也卷入到逆冲推覆变形中，汶川 1 号钻钻孔结果显示马鞍塘组、小塘子组和须家河组二段卷入到映秀-北川断裂的逆冲推覆变形中，说明四川周缘前陆盆地在龙门山逆冲推覆作用下，向 SE 方向有所消减(Li et al., 2003, 2014)。因此，四川周缘前陆盆地的沉积特征将龙门山广泛的逆冲推覆时间限定在晚三叠世时期，即 D_1 期事件的起始时间，并且从松潘-甘孜褶皱带向四川盆地方向构造事件体现出滞后性。

在四川周缘前陆盆地内，在龙门山北段，下侏罗统白田坝组不整合覆盖在褶皱变形的上三叠统须家河组地层之上，向南逐渐过渡为须家河组四段与须家河组三段之间的不整合，标志着 D_1 期事件的结束。绝大多数学者认为在龙门山山前广泛分布的推覆体和飞来峰与龙门山广泛的逆冲推覆作用密切相关，只是龙门山中段的塘坝子飞来峰狭长拖尾不整合盖在协调变形的侏罗-新生代地层之上，这个地层学证据让很多学者将飞来峰的最终就位时间延后到新生代以后

(Burchfiel et al., 1995; Meng et al., 2006)。孢粉年代学抹除了这个飞来峰新生代就位的地层学证据后，使 D_1 期变形以及相关的广泛逆冲晚三叠世-早侏罗世的时间更加确定。

与 D_1 期变形相关的西部带-平武地区，木皮岩体表现出典型的同构造岩体特征，岩体南部发生韧性剪切变形，与围岩的几何学和运动学特征一致，向岩体北部逐渐过渡为块状未变形，表明在岩体就位还未完全固结的情况下发生了与 D_1 期向北的反冲运动。对木皮岩体岩浆锆石 U-Pb 定年给出 219 Ma 的谐和年龄。

D_2 期变形最重要的年龄约束便是来自龙门山广泛的同构造矿物的 $^{40}Ar/^{39}Ar$ 冷却年龄。除北段碧口地区以外，在龙门山沿线以及松潘-甘孜褶皱带南部丹巴地区，无论是元古代杂岩体 NW 缘正断层内角闪石和云母 $^{40}Ar/^{39}Ar$ 冷却年龄还是松潘-甘孜内自生伊利石 K/Ar 年龄，以及独居石 U-Th-Pb 年龄都在 170-120 Ma 之间(四川省地质矿产局, 1991; 夏宗实, 1993; Dirks et al., 1994; Huang et al., 2003; Xu et al., 2008; Yan et al., 2008b; Zhou et al., 2008; 李佐臣, 2009; Airaghi et al., 2017)，明显不同于 D_1 期早中生代的年龄。在四川周缘前陆盆地内，沉积物质周期性过饱和沉积和饥饿沉积阶段与 $^{40}Ar/^{39}Ar$ 冷却年龄很好对应起来。此外，在松潘褶皱带内，晚三叠世侵位的老君沟岩体(224 Ma)(赵永久, 2007)，位于 D_2 期相关的隐藏叠置基底岩片之上，局部地区经历 172-140 Ma 期间的快速隆升(袁海华等, 1991)，从侧面印证了 D_2 期变形的时间。

综上所述，在构造解析基础上，从沉积学、同位素年代学、孢粉年代学、热演化历史等证据，将龙门山地区 D_1 期变形时间限定在晚三叠世-早侏罗世之间 219 Ma 左右，略晚于松潘-甘孜褶皱带的变形时间；而 D_2 期变形在龙门山逆冲推覆带及松潘-甘孜褶皱带东南边缘具有穿时性，时间范围在 170-120 Ma 之间(章节 4.6.2 和图 4.18)。

5.3 Mesozoic tectonic evolution of the Longmenshan

前人对龙门山早中生代构造研究多关注区域上大规模向 SE 的逆冲推覆和松潘-甘孜褶皱带通过龙门山与四川盆地的耦合关系，具体表现为松潘-甘孜区域上部向 S 的大规模缩短变形过程中，通过龙门山地区产生左行压扭作用，进

而产生广泛的向 SE 的逆冲推覆作用(Dirks et al., 1994; Chen et al., 1995; Worley et al., 1995; Chen and Wilson, 1996; Worley and Wilson, 1996; Arne et al., 1997; Harrowfield and Wilson, 2005)。但该构造模式与本文所阐述的构造几何学形态不相符合，最重要的是，在龙门山地区并未观察到水平的线理构造。

龙门山地区早中生代另一显著的构造样式即在西部带地区均一的上部向 NW 的反冲，这点是前人研究中并未很好解释的构造现象。向 NW 的逆冲严格受控于劈理直立带，无论是在西部带还是东部带，都未观察到向 NW 的逆冲与向 SE 的逆冲相互叠加现象，因此我们将向 NW 的逆冲解释为与向 SE 方向逆冲同期的反冲构造。反冲构造在挤压造山带中比较常见，如喜马拉雅、阿尔卑斯、雪峰山中均可见到明显的反冲构造，且都发育于同一期连续的构造事件中(Willett et al., 1993; Godin et al., 1999; Chu et al., 2012a, c)。

Yan et al. (2011)通过褶皱形态、变形层次、面理发育方式和叠加关系将龙门山地区广泛的上部向 SE/S 剪切的构造分为三期变形：1)早中生代华南向华北俯冲过程中，在俯冲板片上部地幔角流作用下产生上部向 SE 的剪切变形，伴随右行剪切分量；2)加厚松潘-甘孜由于华南板块俯冲回撤产生垮塌，形成地壳尺度的“通道流”，并在龙门山沿线元古代基底杂岩顶部产生上部向 SE 的剪切变形；3)由于新生代青藏高原向 NE 方向扩展，在龙门山地区产生一系列向 SEE 方向的逆冲推覆，使伴随龙门山山前一系列飞来峰和推覆体就位。大量同位素年代学数据将这三期变形时间分别限定在 237-208 Ma，193-159 Ma，晚白垩世至今(Yan et al., 2003a, 2008a, b, 2011; Huang et al., 2003; Zhou et al., 2006; Zhou et al., 2008)。但本文野外实地考察过程中，龙门山线理方向在龙门山地区都表现为 NW-SE 方向，局部地区会有微弱角度变化，我们更倾向解释为由于造山带局部不均一性造成线理方向在区域上的小范围内不协调，并不能作为多期变形的证据。岩性的差异同样能影响褶皱产生的形态，因而褶皱形态多样性并不是多期变形的充分条件。龙门山地区变质作用确实由腹陆向前陆(SE)方向有由高到低的变化，我们更倾向解释为造山带向 SE 方向传播过程中将深部-浅部的物质依次抬升到地表，而不能作为多期构造变形的证据。更重要的是，该模式并不能解释元古代基底杂岩 NW 缘稳定存在的向 NW 的正断。

在松潘-甘孜褶皱带，详细构造解析表明元古代扬子基底与上覆古生代-中生代地层中间存在一条区域滑脱带，滑脱带主要发育与震旦-寒武纪岩石中，在丹巴地区出露，表现为强烈剪切带和糜棱岩带(Calassou, 1994; 王宗秀等, 1997; Roger et al., 2004; Harrowfield and Wilson, 2005)。沿着滑脱带，巨厚的松潘-甘孜复理石在阿尼玛卿缝合带闭合过程中，产生强烈的 N-S 向收缩应变，整体上向 S 运移，形成松潘-甘孜内向南凸出的弧形褶皱形迹(Calassou, 1994; 王宗秀等, 1997; Harrowfield and Wilson, 2005)。在松潘-甘孜褶皱带 SW 边界，晚三叠世时期松潘-甘孜块体南缘古特提斯洋南支沿甘孜-理塘缝合带向羌塘块体下面俯冲，俯冲相关的淡色花岗岩及同构造岩体均表明甘孜-理塘闭合时间略晚于阿尼玛卿向北俯冲以及松潘-甘孜广泛褶皱的时间(Roger et al., 2003; Reid et al., 2005a, b, 2007)，与龙门山逆冲推覆带 D_1 期事件具有同时性。

在四川前陆盆地内，伴随龙门山 D_1 期事件向 SE 的逆冲推覆作用，中三叠世地层中的石膏层和煤层等软弱层充当前陆盆地广泛变形的滑脱层，从而吸收整个前陆盆地的构造缩短(Yan et al., 2003b; Tang et al., 2008; Wang et al., 2014)。高精度地震反射剖面表明，在四川前陆盆地内，强烈褶皱地层下部滑脱层向盆地内延伸，并在龙泉山出露，滑脱层向 NW 延伸与安县-灌县断裂汇合，并向龙门山腹陆基底杂岩下延伸(Hubbard and Shaw, 2009; Hubbard et al., 2010; Feng et al., 2015)。

本文研究表明，龙门山 D_1 期事件东部带从腹陆到前陆盆地各个单元变形层次由深至浅变化，与空间几何顺序相反，即变形层次最高的单元在空间位置的最上部，表明在向 SE 逆冲推覆过程中将深部的物质依次折返至地表，这种构造样式的堆叠需要三个条件：1)先存的沉积空间接收沉积；2)后期强烈的挤压造山，使沉积的物质在构造作用下变质，随后通过边界逆冲断层逆冲至地表。龙门山地区，作为扬子板块的 NW 缘，从元古代 Rodinia 大陆裂解以来，一直经受着局部的伸展和稳定断陷沉积作用。包括志留纪、泥盆纪以及二叠纪三个伸展阶段。志留纪局部裂谷产生局部分布的巨厚的志留系沉积，并伴随同时期的碱性火山岩活动(李佐臣, 2009; 李佐臣等, 2011)；地震反射剖面也表明在龙门山前陆盆地下封存着二叠纪以前的古老裂陷盆地(Chen and Wilson, 1996; Jia et al., 2006)；二叠纪时期，龙门山地区的伸展达到顶峰状态，对应峨眉山玄武岩

喷发，在龙门山地区沉积深水硅质岩、深水碳酸盐重力流等(龙学明, 1991; 罗志立和龙学明, 1992; 罗志立, 1994; Chang, 2000)。元古代-晚三叠世早期，龙门山地区并未发生明显的挤压缩短作用，持续的伸展裂陷使早期志留系沉积物沉积。强烈的伸展作用，导致扬子西北缘龙门山地区发生岩石圈地壳减薄，形成一个平行龙门山走向潜在的薄弱带 (Figure 5.1 a)。

根据章节 5.2 的分析，龙门山逆冲推覆带 D_1 期事件略晚于松潘-甘孜巨厚复理石盖层向南运移褶皱变形时间，而与走向近南北，俯冲极性为 SW 的甘孜-理塘缝合带时间相一致。松潘-甘孜褶皱带内，与甘孜-理塘闭合相关近 N-S 走向的褶皱叠加在与阿尼玛卿闭合相关近 E-W 走向的褶皱之上，进一步表明后者时间上早于前者(许志琴等, 1992)。松潘-甘孜块体向 SWW 方向俯冲过程中产生向 NEE 方向的作用力，可能使刚性基底发生消减，盖层伴随基底消减的过程中发生大规模缩短，裂谷中不同层次的物质沿早期正断层，反转逆冲折返至地表，并产生同期向 NW 的反冲形成西部带。鉴于龙门山地区向 SE 逆冲的东部带范围远大于向 NW 逆冲的西部带范围，我们倾向认为四川盆地基底向松潘-甘孜块体下面消减(Figure 5.1 b)。大地电磁测量剖面和地震反射剖面表明龙门山下部冷的块体呈舌形向松潘-甘孜下部嵌入(罗志立和龙学明, 1992; Zhang et al., 2009)。基底消减导致盖层强烈缩短的同时使早期的正断层发生反转，形成龙门山一系列的逆冲断裂、推覆体和飞来峰构造，基底沿着早期的正断被切割成陡坎状，并未卷入变形，整体以薄皮构造为主(Figure 5.1 b)。龙门山逆冲推覆带，并不发育与主变形同期的岛弧岩浆岩、蛇绿岩、弧后扩张等洋壳活动表现，为典型的陆内造山带。

龙门山地区晚中生代构造除了上述“地壳流”的伸展模式外，许志琴等(2007)在整个松潘-甘孜褶皱带东南缘识别出近 200 km 长的上部向 NW 的拆离断层，提出白垩纪以来由于扬子板块对松潘-甘孜地体的陆内俯冲作用产生地壳尺度向 SE 方向挤出的楔形体。该模式很好地解释了元古代杂岩 NW 缘向 NW 的正断以及 SE 缘向 SE 的逆冲。但是地壳尺度楔形体的挤出，会使龙门山腹陆及松潘-甘孜地区下部物质缺失从而出现局部的伸展应力场，而诱发伸展盆地。但事实上整个松潘-甘孜和龙门山腹陆地区，均未观察到与伸展相关的断裂盆地。

本文研究表明 D_2 期晚中生代变形事件与基底岩片向 SE 挤出叠置相关。龙门山地区，由于处在松潘-甘孜块体与扬子板块界线，在扬子板块向西发生陆内俯冲过程中可能是应力最集中的位置，导致基底岩片向 SE 方向挤出，作为外来岩片叠置在四川前陆盆地上，因此，无论是宝兴杂岩还是彭灌杂岩，均表现出西北部强烈变形，而东南部的原地基底杂岩依然保持着块状未变形特征。松潘-甘孜内部，持续的挤压使基底在早期陡坎的基础上被切割成独立的岩片，并向 SE 方向逆冲叠置。这些被巨厚的复理石覆盖的基底叠置岩片，保持着龙门山腹陆持续的挤压背景，即使前缘的基底岩片向 SE 挤出，腹陆也不会因为物质缺失而发生伸展断陷(Figure 5.1 c)。

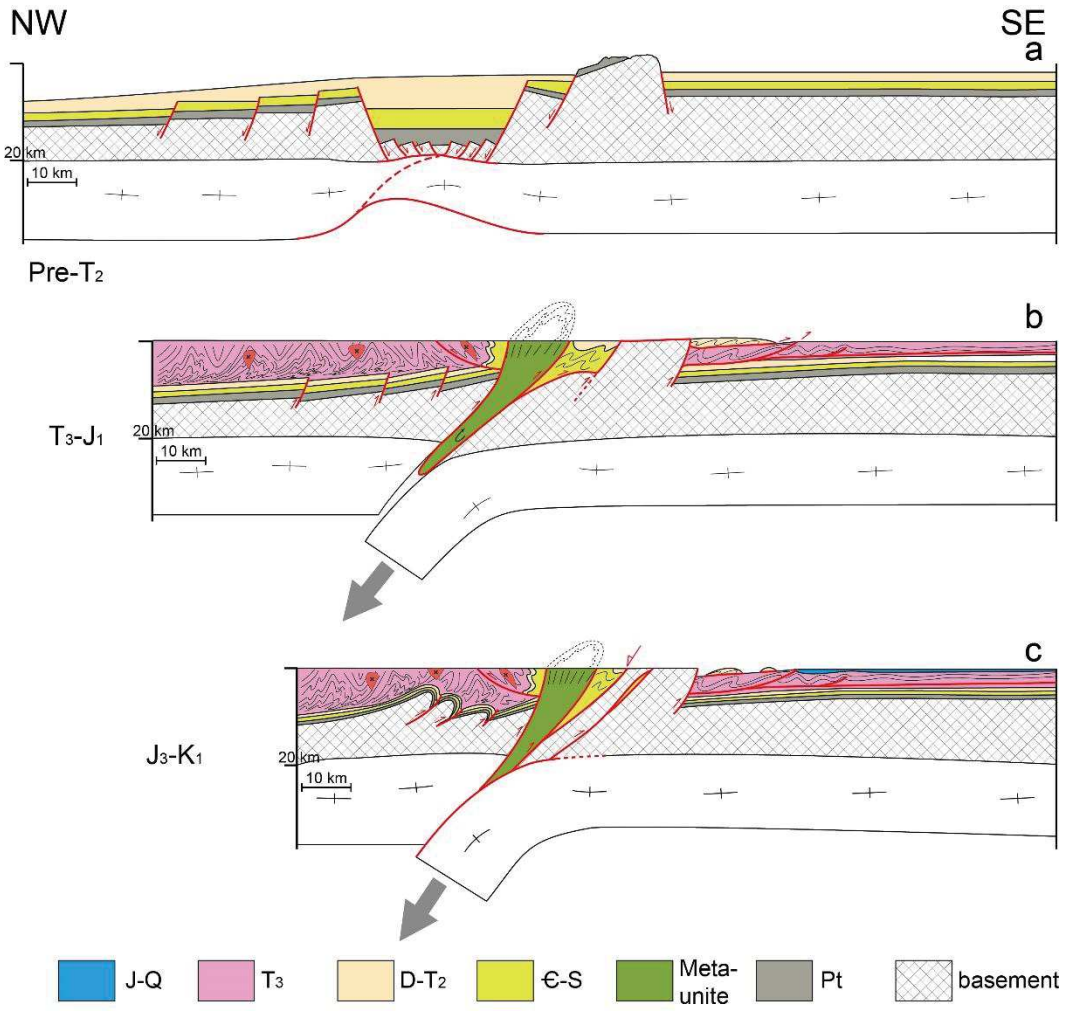

Figure 5.1 Simplified profile show the Mesozoic evolutionary history of the Longmenshan thrust belt.

(a) Pre-T_2 rift system along the NW margin of the Yangtze Block, a array of normal fault developed on each side of the rift; (b) The position where the rift closed offer a potential intracontinental soften zone, and the Yangtze basement subducted along the soften zone under the effect of Paleo tethy obliteration during T_3-J_1, the cover has been strippled from the

basement and thrusted to both SE and NW, the normal fault been reversed to thrust and cut the Yangtze basement to slices; (c) During J_3-k_1, due to the amalgamation of the Lhasa block to Qiangtang block, the basement slices extruded southeastward leading the early stage of the crustal thickening and formed part of the orogen-parallel Proterozoic complexes.

5.4 Implications for the intraplate orogen

陆内造山作用存在两个热点问题：1)陆内造山的力学机制；2)陆内造山带发生的位置(张长厚, 1999)。尽管陆内造山的力学机制还存在较大的争议，但地幔柱活动、平板俯冲和远程效应成为较常用的解释机制(Dickinson and Snyder, 1978; Martin, 1983; English and Johnston, 2004)。Kroner 在研究南非 Damara 造山带时，提出先有 840 Ma 的地幔柱活动导致岩石圈地壳伸展减薄，产生的大规模拗陷接受巨厚沉积，导致早期减薄的岩石圈发生破裂，破裂的岩石圈在自身重力作用下下沉消减，伴随混合岩化作用和广泛的岩浆活动，在地壳表层强烈挤压完成造山过程。这种陆内造山模式强调地壳物质变形对深部岩石圈地幔物质活动的响应，为板内自身物质调整的影响，与板缘活动没有关系。龙门山逆冲推覆带沿线并未观察到混合岩及后造山岩浆活动，因而不太可能是此种类型的板内造山。

与板缘俯冲-碰撞相关的平板俯冲和远程效应强调板缘应力场对造山带的影响。在龙门山及邻区，古松潘-甘孜块体分别沿阿尼玛卿缝合带向北俯冲及沿甘孜-理塘缝合带向 SW 方向俯冲为同期最近的板缘活动，均不符合平板俯冲模式。板块闭合碰撞似乎是龙门山陆内造山的主要动力来源。前陆盆地磨拉石时代及同构造岩体表明阿尼玛卿在晚三叠世末期之前闭合，略早于龙门山 D_1 期陆内造山作用(岳远刚, 2014)，因此龙门山早中生代陆内造山动力学机制不太可能来自阿尼玛卿缝合带。同构造岩体和同构造变形矿物表明甘孜-理塘缝合带末次闭合时间为 211 Ma 左右(Reid et al., 2005a; Reid et al., 2005c; Reid et al., 2007)，与龙门山 D_1 期陆内变形时间相吻合。

除地幔柱活动引发陆内造山外，典型的陆内造山带刚性板内的先存软弱带是发生陆内造山的理想位置。在板块边界，随着板块俯冲-碰撞导致地壳不断加厚，在达到临界值后，挤压作用与地壳加厚产生的重力达到平衡，接下来便很难通过板块增生或碰撞的方式释放两个板块间的应力，导致应力累积。当应力累积到一定程度向板内传递时，板内先存的薄弱带则成为应力释放最理想的场

所而发生构造活化，因而形成远离板块边界上千公里的陆内造山作用。先存薄弱带可以是古老造山带，也可以是闭合后的裂谷。像我国华南雪峰山陆内造山过程中，先存的板内薄弱带可能是扬子和华夏地块拼合的古缝合带，在古太平洋板块西向俯冲产生的远程力向板内传递过程中活化造山(Chu et al., 2012a; Chu et al., 2012c)；又如澳大利亚的 Alice Springs 造山带，在古老的 Petermann 造山带基础上巨厚的沉积物，导致下部岩石圈地温升高发生活化造山；又如中国天山新生代陆内造山以及北美的 Laramide 陆内造山，都是在古老造山带基础上活化而成(Dickinson and Snyder, 1978; Tapponnier and Molnar, 1979; Sandiford et al., 2001)。

龙门山地区早中生代的造山过程正是在这种机制下形成的。与上述典型陆内造山带不同的是，龙门山地区的薄弱带并非古老的造山带，而是广泛的裂谷作用使岩石圈减薄的结果。晚三叠世以前多期次的伸展断陷使龙门山地区在接受广泛沉积的同时，岩石圈地壳也发生减薄，形成潜在的陆内薄弱带。晚三叠世随着甘孜-理塘缝合带的闭合向龙门山方向传递应力，扬子基底沿岩石圈减薄的位置发生消减，裂谷闭合形成大规模的逆冲推覆构造。地表的构造表现和地震反射剖面似乎都支持四川盆地下的扬子基底向松潘-甘孜块体下俯冲(罗志立, 1991; Zhang et al., 2009)。因此，陆内造山过程中，陆内薄弱带不一定局限于先存的古老造山带，长期的伸展-断裂导致岩石圈减薄也可以成为陆内薄弱带诱发陆内造山作用。

5.5 Implications for the thick-skinned and thin-skinned structure

薄皮构造和厚皮构造作为造山带地壳缩短变形的两种不同表现形式，在造山带作用中起着重要作用。典型的薄皮构造仅有盖层卷入变形，盖层通过滑脱面与基底拆离，吸收巨大的缩短变形，如阿尔卑斯外带的 Helvetic 推覆体；典型的厚皮构造指整个上地壳都卷入变形，如南阿尔卑斯的推覆体，由于中生代裂谷作用和埋藏升温作用，导致整个上地壳都卷入变形；第三种基底卷入变形的薄皮构造指在逆冲推覆过程中，基底岩片卷入变形发生堆叠，如阿尔卑斯外带的 Penninic 推覆体(Coward and Dietrich, 1989; Ziegler et al., 1995; Pfiffner, 2016)。

在龙门山地区晚中生代的变形也可以解释为基底岩片卷入变形的薄皮构造。本文研究表明，沿龙门山逆冲推覆带出露的基底杂岩由变形层次明显不同的块体组成。龙门山南段宝兴杂岩，以五龙断裂为界，SE 侧的基底杂岩基本为未变形的块状，NW 侧的杂岩体则记录了明显的韧性变形；龙门山中段彭灌杂岩，尽管杂岩体内部并未识别出明显的断裂带，但岩石显微组构特征也表明彭灌杂岩由 SE 侧块状未变形部分和 NW 侧经历韧性变形的部分组成；在龙门山北段轿子顶地区，地震反射剖面表明轿子顶杂岩为无根的杂岩体，同样经历了较强的韧性变形(Jia et al., 2006; 李佐臣, 2006)。在松潘-甘孜褶皱带内部，重力模拟结果表明高密度物质以岩片叠置的形态存在，可能对应基底岩片的堆叠构造。基底岩片的的挤出或堆叠构造与扬子基底边缘位置密切相关，在扬子板块边缘，应力最集中的位置表现为基底岩片的挤出构造，而在松潘-甘孜内部，远离扬子边缘则仅表现为堆叠构造。根据上述划分三种构造类型，晚中生代龙门山构造样式属于基底岩片卷入变形的薄皮构造。Jia et al.(2006)通过地震反射剖面和前陆盆地演化特征研究表明，龙门山北段为中生代的薄皮构造，而南段宝兴地区为新生代基底卷入变形的厚皮构造。但龙门山北段的轿子顶基底杂岩的出现，表明龙门山北段并非完全意义上的薄皮构造；尽管龙门山南段宝兴杂岩 NW 缘向 NW 正断的糜棱岩云母 $^{40}Ar/^{39}Ar$ 年龄在晚白垩世-早第三纪之间，但是未变形花岗岩内云母仍然给出 120 Ma 的冷却年龄，表明宝兴基底岩片可能在早白垩世便经历了基底岩片的逆冲活动，而新生代的年龄可能为后期重置的年龄(Jia et al., 2006; Tian et al., 2016)。阿尔卑斯的基底岩片卷入变形的薄皮构造与早期中生代广泛发育的正断层密切相关(Pfiffner, 2016)，而龙门山地区晚三叠世之前的伸展使基底被切割成陡坎状，为晚中生代基底岩片的逆冲叠置提供可能的条件。

龙门山作为青藏高原地势最陡的边缘之一，地震反射剖面表明，从四川盆地到松潘-甘孜褶皱带，莫霍面在龙门山下面从 45 km 深陡降至 60 km 深(Robert et al., 2010; Robert et al., 2010; Guo et al., 2013)，因而，无论是地表构造还是深部结构特征都表明龙门山及其西部地区地壳发生了显著增厚。前人对高原增厚的机制提出深入地壳尺度的逆冲断裂和 channel flow 两种端元模式(Tapponnier et al., 1990; Royden et al., 1997; Tapponnier et al., 2001; Royden et al., 2008)，低温年

代学结果和河流侵蚀等都认为青藏高原地壳增厚发生在新生代印度-欧亚板块碰撞之后(Harrison, 1992; Tapponnier et al., 2001; Clark et al., 2005, 2010; Wang et al., 2012; Cook et al., 2013; Tian et al., 2013, 2014)。然而 Wallis et al.(2003)在丹巴地区夕线石变质带内独居石进行电子探针定年，得出 65 Ma 的年龄，提出松潘-甘孜的增厚在新生代之前就已发生，早于印度-欧亚大陆的碰撞。本文研究表明，松潘-甘孜褶皱带内，晚中生代发生的基底叠置岩片，同样可能导致龙门山地区早期地壳增厚，地壳的增厚并非完全成就于新生代印度-欧亚大陆的碰撞作用。

6. Conclusions and unsettled issues

6.1 Conclusions

This thesis focused on the structural architecture and geological evolution of the Longmenshan thrust belt (LMTB), firstly, outlines the Early Mesozoic intrinsic bulk architecture based on robust structural geometry, kinematics analysis, then chooses the Proterozoic Pengguan massif located at the middle segment of the LMTB to unravel its multiphase deformation on the base of structural analysis, Anisotopy Magnetic Susceptibiliy (AMS) and gravity modeling, and finally attains conclusions as following:

1. The stablly developed vertical cleavage belt divides the LMTB into a Western zone and an Eastern zone. All the foliations within the Eastern zone dip to NW and show the top-to-the-SE shearing along NW-SE lineation, while the Western zone has the SE-dipping foliation with the top-to-the-NW shearing along the NW-SE lineation. The Western zone and Eastern zone express as a flower-liking structure that is typical thin-skinned structure.

2. According to defromation intensity and structural level, with the boundries of the three main thrusts of the LMTB, the Eastern zone can be further divided into four subunits, from SE to NW are, autochthon, para-autochthon, allochthon and meta-allochthon.These four subunits present enhancing deformation intensity and deepening metamorphic grade from SE to NW. The meta-allochthon records the highest metamorphism of low amphibole grade loated at a core of SE-ward overturned anticline.

3. Pollen analysis and geochronology dating on syntectonic granite constrain the thrusting timing of the LMTB to the Early Mesozoic around 219 Ma.

4. AMS, microscopic observation and gravity modeling reveal that the Pengguan massif consists of a deformed NW part and a relatively undeformed SE part, the NW extrudes SE-wards and overrides the SE part and stacking together, which is the surface expressions of the basement slice extrusion constrained by the NW-normal fault and SE-thrust on each side of the massif. Two orogen-parallel basement slices belts constitute the present architecture of the LMTB. In-situ Ar/Ar dating of Mica

from the NW-normal fault and SE-thrust with basin sediment characters constrain the extrusion of the basement slices at the Late Mesozoic between Late Jurassic to Early Cretaceous.

5. The LMTB is far away from the contemporaneous plate boundary, lack of ophiolitic rocks and arc-related magmatism, therefore it could be an intracontinental orogen. The closure of a pre-T_2 rifting offers an intraplate soften zone where the Yangtze basement could subdcte along this weak zone, and produce the pervasive shortening to constitute the bulk architecture of the LMTB in the Early Mesozoic. During the Late Mesozoic, basement slices extrude southeastwards, backstopped by the Yangtze block and piled up, and formed the thick-skinned structure that led the early stage crustal thickening of along the LMTB.

6.2 Unsettled issues

在前人研究基础上，本文通过多手段对龙门山中生代事件解析后，还有以下问题需要解决：

1. 碧口地块的来源及变形层次问题。碧口地块的物质化学成分表明其为一套元古代时期在板块俯冲体制下的岛弧火山岩、浊积岩沉积(闫全人等, 2003; 闫全人等, 2004)。前人通过对碧口地块南北缘的边界走滑断层研究认为，碧口地块可能为华南-华北板块碰撞过程中从西秦岭挤出来的块体(Burchfiel et al., 1995; Meng et al., 2005)。但本文研究表明，碧口地块内部并不发育 E-W 向水平的线理，相反都表现为倾向 S 的面理面以及 S-N 向的矿物拉伸线理，运动学剪切指向指示上部向 N 的剪切变形。本文野外考察过程中，碧口地块西部边界的虎牙断裂并未表现出明显向 W 逆冲的构造特征，并不支持碧口地块从西秦岭挤出的模式。此外，碧口地块整体经历了绿片岩相变质作用，如果碧口地块作为元古代的古隆起遭受向 N 的逆冲变形，并不能解释碧口地块整体较深层次的变形特征(刘鹤等, 2008)。章节 3.5.7 江油-平武剖面的解析中将碧口地块和和古生代地层解释为整体向 N 逆冲的推覆体，叠置在原地系统晚三叠系地层之上。如果碧口地块整体都是在 D_1 期变形事件中通过陆内造山推覆至地表，则需要元古代时期的岛弧物质在龙门山持续的裂陷期间有个埋深过程。然而碧口地块的构造属性和物质来源有待开展进一步工作；

2. 从 Figure 2.1 可以看出，青川断裂以南，东部带的外来系统相比龙门山南段出露面积更窄，而同等层次的绢云母片岩在西部带-碧口地块南缘分布面积更广，如果碧口地块物质确实经历埋藏和逆冲抬升，根据地表较深层次物质分布范围，龙门山北段基底消减极性可能由 NW 向 SE，不同于龙门山南段四川盆地扬子基底向 NW 松潘-甘孜块体下俯冲极性。在碧口地块西部边界虎牙断裂表现为 NNW-SSE 的构造形迹，野外观察也表现为 NNW-SSE 走向近直立的面理，可能对应扬子基底在龙门山北段和南段不同陆内消减极性产生的“转换断层”；

3. 本文在解析龙门山造山 D_1 期变形事件时，认为松潘-甘孜褶皱带整体向 S 的剪切变形与龙门山的陆内造山事件属于先后不同的两期事件。在龙门山并未观察到明显的水平线理，表明龙门山地区早中生代左行走滑并不明显，从侧面证明这两期事件的不同时性。那么龙门山逆冲推覆带西部带向 NW 的逆冲与松潘-甘孜早期区域上向 S 的剪切构造是怎样的叠加关系以及西部带在松潘-甘孜褶皱带东缘的影响范围需要更进一步的构造解析来完成。

References

Airaghi, L., J. d. Sigoyer, P. Lanari, S. Guillot, O. Vidal, P. Monié, B. Sautter, and X. Tan. Total exhumation across the Beichuan fault in the Longmen Shan (eastern Tibetan plateau, China): constraints from petrology and thermobarometry. Journal Asian Earth Sciences, 2017, 140, 108-121.

Allen, M. B., S. J. Vincent, and P. J. Wheeler. Late Cenozoic tectonics of the Kepingtage thrust zone: Interactions of the Tien Shan and Tarim Basin, northwest China. Tectonics, 1999, 18(4): 639-654.

Arne, D., B. Worley, C. Wilson, et al. Differential exhumation in response to episodic thrusting along the eastern margin of the Tibetan Plateau. tectonophysics, 1997, 280(3): 239-256.

Avouac, J. P., P. Tapponnier, M. Bai, et al. Active thrusting and folding along the northern Tien Shan and late Cenozoic rotation of the Tarim relative to Dzungaria and Kazakhstan. Journal of Geophysical Research: Solid Earth, 1993, 98(B4): 6755-6804.

Bellahsen, N., F. Mouthereau, A. Boutoux, et al. Collision kinematics in the western external Alps. Tectonics, 2014, 33(6): 1055-1088.

Bonvalot, S., Balmino, G., Briais, A., M. Kuhn, Peyrefitte, A., Vales, Biancale, R., Gabalda, G., Moreaux, G., Reinquin, and F. Sarrailh, M., World Gravity Map, 1:50000000 map, 2012, Eds. : BGI-CGMW-CNES-IRD, Paris.

Borradaile, G. J., and M. Jackson. Anisotropy of magnetic susceptibility (AMS): magnetic petrofabrics of deformed rocks. Geology Society London Special Publications, 2004, 238(1): 299-360.

Borradaile, G. J., and M. Jackson. Structural geology, petrofabrics and magnetic fabrics (AMS, AARM, AIRM). Journal of Structural Geology., 2010, 32(10): 1519-1551.

Borradaile, G., and B. Henry. Tectonic applications of magnetic susceptibility and its anisotropy, Earth Science Review, 1997, 42(1): 49-93.

Bouchez, G.. Two-stage deformation of the mount-Louis-Andorra granite pluton (Variscan Pyrenees) inferred from magnetic susceptibility anisotropy. Journal of Geological Society, 1995, 152: 669-679.

Bouchez, J. L. Anisotropie de susceptibilité magnétique et fabrique des granites. Comptes Rendus de l'Académie des Sciences-Series IIA. Earth and Planetary Science, 2000, 330(1): 1-14.

Bouchez, J. L., D. Hutton, and W. E. Stephens. Granite: from segregation of melt to emplacement fabrics. 2013, Springer Science & Business Media.

Brendan Murphy, J., and R. Damian Nance. Supercontinent model for the contrasting character of Late Proterozoic orogenic belts. Geology, 1991, 19(19): 469-472.

Bruguier, O., J. Lancelot, and J. Malavieille. U–Pb dating on single detrital zircon grains from the Triassic Songpan–Ganze flysch (Central China): provenance and tectonic correlations. Earth and Planetary Science Letters, 1997, 152(1): 217-231.

Burchfiel, B. C., L. H. Royden, R. D. van der Hilst, et al. A geological and geophysical context for the Wenchuan earthquake of 12 May 2008, Sichuan, People's Republic of China. GSA Today, 2008, 18(7): 4-11.

Burchfiel, B. C., Z. Chen, Y. Liu, et al. Tectonics of the Longmen Shan and Adjacent Regions, Central China. International Geology Review, 1995, 37(8): 661-735.

Sengör C., B. A. Natal'in, et al. Evolution of the Altaid tectonic collage and Palaeozoic crustal growth in Eurasia. Nature, 1993, 364(6435): 299-307.

Calassou, S. Etude tectonique d'une chaîne de décollement. A- Tectonique triasique et tertiaire de la chaîne de Songpan Garzê(Est Tibet). B- Géométrie et cinématique des déformations dans les prismes d'accrétion sédimentaire: Modélisation analogique, 1994.

Castonguay, S., G. Ruffet, and A. Tremblay. Dating polyphase deformation across low-grade metamorphic belts: An example based on 40Ar/39Ar muscovite age constraints from the southern Quebec Appalachians, Canada, Geological Society of America Bulletin, 2007, 119(7–8): 978–992.

Cawood, P. A., and C. Buchan. Erratum to “Linking accretionary orogenesis with supercontinent assembly” by P.A. Cawood and C. Buchan [Earth-Science Reviews 82 (2007) 217–256]. Earth-Science Reviews, 2007, 85(1–2): 82-83.

Chang, E. Z. Geology and Tectonics of the Songpan-Ganzi Fold Belt, Southwestern China. International Geology Review, 2000, 42(9): 813-831.

Chen, J., R. Ma, L. Zhang, X. Li, et al. Zircon U-Pb dating and geochemical characters of diabase in the Shuimo area, Northern section of the Longmen Shan. Geology Exploration, 2015, 51(1): 133-142.

Chen, S., and C. J. K. Wilson. Emplacement of the Longmen Shan Thrust-Nappe Belt along the eastern margin of the Tibetan Plateau. Journal of Structural Geology, 1996, 18(4): 413-429.

Chen, S., C. J. L. Wilson, and B. A. Worley. Tectonic transition from the Songpan-Garzê Fold Belt to the Sichuan Basin, south-western China. Basin Research, 1995, 7(3): 235-253.

Chen, S., C. J. L. Wilson, Z. Luo, et al. The evolution of the Western Sichuan Foreland Basin, southwestern China. Journal of Asian Earth Sciences, 1994a, 10(94): 159–168.

Chen, S., Q. Deng, X. Zhao, et al. Deformational characteristics, evolutionary history, and deformation mechanism of the middle Longmenshan thrust - nappes and related tectonics. Seismology and geology, 1994b, 16(4): 413-421.

Chen, Z. Permian carbonate gravity flow sediments in the west margin of the Yangtze block. Canadian Journal of Earth Sciences, 1985, 1(43-50).

Choukroune, P. Tectonic evolution of the pyrenees. Annual Review of Earth and Planetary Sciences, 1992, 20: 143-158.

Chu, Y., M. Faure, W. Lin, et al. Early Mesozoic tectonics of the South China block: Insights from the Xuefengshan intracontinental orogen. Journal of Asian Earth Sciences, 2012a, 61: 199-220.

Chu, Y., M. Faure, W. Lin, et al. Tectonics of the Middle Triassic intracontinental Xuefengshan Belt, South China: new insights from structural and chronological constraints on the basal décollement zone. International Journal of Earth Sciences, 2012c, 101(8): 2125-2150.

Chu, Y., W. Lin, M. Faure, et al. Phanerozoic tectonothermal events of the Xuefengshan Belt, central South China: Implications from UPb age and LuHf determinations of granites. Lithos, 2012b, 150: 243-255.

Clark, M. K., and L. H. Royden. Topographic ooze: Building the eastern margin of Tibet by lower

crustal flow. Geology, 2000, 28(8): 703-706.

Clark, M. K., J. W. M. Bush, and L. H. Royden. Dynamic topography produced by lower crustal flow against rheological strength heterogeneities bordering the Tibetan Plateau. Geophysical Journal International, 2005, 162(2): 575-590.

Clark, M. K., K. A. Farley, D. Zheng, et al. Early Cenozoic faulting of the northern Tibetan Plateau margin from apatite (U–Th)/He ages. Earth and Planetary Science Letters, 2010, 296(1-2): 78-88.

Cook, K. L., L. H. Royden, B. C. Burchfiel, et al. Constraints on Cenozoic tectonics in the southwestern Longmen Shan from low-temperature thermochronology. Lithosphere, 2013, 5(4): 393-406.

Coward, M., and D. Dietrich. Alpine tectonics — an overview. Geological Society London Special Publications, 1989, 45(1): 1-29.

Dewey, J. F., and J. M. Bird. Mountain belts and the new global tectonics. Journal of Geophysical Research Atmospheres, 1970, 75(14): 2625-2647.

Dickinson, W. R., and W. S. Snyder. Plate tectonics of the Laramide orogeny. Geological Society of America Memoirs, 1978, 151: 355-366.

Dirks, P., C. Wilson, S. Chen, et al. Tectonic evolution of the NE margin of the Tibetan Plateau; evidence from the central Longmen Mountains, Sichuan Province, China. Journal of Southeast Asian Earth Sciences, 1994, 9(1): 181-192.

Dunlop, D. J. Theory and application of the Day plot (Mrs/Ms versus Hcr/Hc) 1. Theoretical curves and tests using titanomagnetite data. Journal of Geophysical Research: Solid Earth, 2002, 107(B3): EPM 4-1-EPM 4-22.

English, J. M., and S. T. Johnston. The Laramide orogeny: what were the driving forces? International Geology Review, 2004, 46(9): 833-838.

Enkelmann, E., L. Ratschbacher, R. Jonckheere, et al. Cenozoic exhumation and deformation of northeastern Tibet and the Qinling: Is Tibetan lower crustal flow diverging around the Sichuan Basin? Geological Society of America Bulletin, 2006, 118(5-6): 651-671.

Faure, M., W. Lin, Y. Chu, et al. Triassic tectonics of the southern margin of the South China Block. Comptes Rendus Geoscience, 2015, 348(1): 5-14.

Feng, S., P. Zhang, B. Liu, et al. Deep crustal deformation of the Longmen Shan, eastern margin of the Tibetan Plateau, from seismic reflection survey and finite element modelling. Journal of Geophysical Research: Solid Earth, 2015, 121: 767-787.

Ferré, E. C.. Theoretical models of intermediate and inverse AMS fabrics. Geophysical Research Letter, 2002, 29(7): 31-31–31-34.

Fu, B., P. Shi, H. Guo, et al. Surface deformation related to the 2008 Wenchuan earthquake, and mountain building of the Longmen Shan, eastern Tibetan Plateau. Journal of Asian Earth Sciences, 2011, 40(4): 805-824.

Furlong, K. P., and E. Kirby. Reconstructing the growth of high topography across eastern Tibet in space and time, paper presented at EGU General Assembly Conference Abstracts, 2013.

Godard, V., J. Lavé, J. Carcaillet, et al. Spatial distribution of denudation in Eastern Tibet and regressive erosion of plateau margins. Tectonophysics, 2010, 491(1-4): 253-274.

Godard, V., R. Pik, J. Lavé, et al. Late Cenozoic evolution of the central Longmen Shan, eastern Tibet: Insight from (U-Th)/He thermochronometry. Tectonics, 2009, 28(5): n/a-n/a.

Godin, L., R. L. Brown, S. Hanmer, et al. Back folds in the core of the Himalayan orogen: An alternative interpretation. Geology, 1999, 27(2): 151-154.

Goleby, B. R., R. D. Shaw, C. Wright, et al. Geophysical evidence for thick-skinned crustal deformation in central Australia. Nature, 1989, 337(6205): 325-330.

Grimmer, J. C., J. Glodny, K. Druppel, et al. Early- to mid-Silurian extrusion wedge tectonics in the central Scandinavian Caledonides. Geology, 2015, 43(4): 347–35.

Guo, X., G. R. Keller, R. Gao, et al. Irregular western margin of the Yangtze block as a cause of variation in tectonic activity along the Longmen Shan fault zone, eastern Tibet. International Geology Review, 2014, 56(4): 473-480.

Guo, X., R. Gao, G. Randy Keller, et al. Imaging the crustal structure beneath the eastern Tibetan Plateau and implications for the uplift of the Longmen Shan range. Earth and Planetary Science Letters, 2013, 379: 72-80.

Guo, X., R. Gao, H. Wang, et al. Crustal architecture beneath the Tibet-Ordos transition zone, NE Tibet, and the implications for plateau expansion. Geophysical Research Letters, 2015: n/a-n/a.

Hand, M., and M. Sandiford. Intraplate deformation in central Australia, the link between subsidence and fault reactivation. Tectonophysics, 1999, 305(1–3): 121-140.

Harrison, T. M. Raising Tibet. Science, 1992, 255(5052): 1663-1670.

Harrison, T. M., W. Chen, P. H. Leloup, et al. An Early Miocene Transition in deformation regime within the Red River Fault Zone, Yunnan, And its significance for Indo-Asian tectonics. Journal of Geophysical Research Solid Earth, 1992, 97(B5): 7159–7182.

Harrowfield, M. J., and C. J. Wilson. Indosinian deformation of the Songpan Garzê fold belt, northeast Tibetan Plateau. Journal of Structural Geology, 2005, 27(1): 101-117.

Hartz, E. H., and A. Andresen. From collision to collapse: Complex strain permutations in the hinterland of the Scandinavian Caledonides. Journal of Geophysical Research, 1997, 102(24): 697–711.

He, L. Permian to Late Triassic evolution of the Longmen Shan Foreland Basin (Western Sichuan): Model results from both the lithospheric extension and flexure. Journal of Asian Earth Sciences, 2014, 93: 49-59.

Heller, P. L., C. L. Angevine, N. S. Winslow, et al. Two-phase stratigraphic model of foreland-basin sequences. Geology, 1988, 16(6): 501-504.

Hendrix, M. S., S. A. Graham, A. R. Carroll, et al. Sedimentary record and climatic implications of recurrent deformation in the Tian Shan: Evidence from Mesozoic strata of the north Tarim, south Junggar, and Turpan basins, northwest China. Geological Society of America Bulletin, 1992, 104(1): 53-79.

Hu, J., Q. Meng, Y. Shi, and H. Qu (2005), SHRIMP U-Pb dating of zircons from granitoid bodies in the Songpan-Ganzi terrane and its implications, Acta Petrol. Sin., 21(3), 867-880.

Huang, M. H., I. S. Buick, L. W. Hou, et al. Tectonometamorphic evolution of the eastern Tibet plateau: Evidence from the central Songpan-Garze orogenic belt, western China. Journal of Petrology, 2003, 44(2): 255-278.

Huang, M., R. Maas, I. S. Buick, et al. Crustal response to continental collisions between the Tibet, Indian, South China and North China Blocks: geochronological constraints from the Songpan-Garzê Orogenic Belt, western China. Journal of Metamorphic Geology, 2003, 21(3): 223-240.

Hubbard, J., and J. H. Shaw. Uplift of the Longmen Shan and Tibetan plateau, and the 2008 Wenchuan (M = 7.9) earthquake. Nature, 2009, 458(7235): 194-197.

Hubbard, J., J. H. Shaw, and Y. Klinger. Structural Setting of the 2008 Mw 7.9 Wenchuan, China, Earthquake. Bulletin of the Seismological Society of America, 2010, 100(5B): 2713-2735.

Jelinek, V.. Characterization of the magnetic fabric of rocks. Tectonophysics, 1981,79(3-4): T63-T67.

Jelinek. Costs of synthetic fuels in relation to oil prices. Report for the Committee on Science and Technology, US House of Representatives, March 1981. 1981.

Jia, D., G. Wei, Z. Chen, et al. Longmen Shan fold-thrust belt and its relation to the western Sichuan Basin in central China: New insights from hydrocarbon exploration. AAPG bulletin, 2006, 90(9): 1425-1447.

Jia, D., Y. Li, A. Lin, et al. Structural model of 2008 Mw 7.9 Wenchuan earthquake in the rejuvenated Longmen Shan thrust belt, China. Tectonophysics, 2010, 491(1-4): 174-184.

Jin, W., L. Tang, K. Yang, et al. Segmentation of the Longmen Mountains thrust belt, Western Sichuan Foreland Basin, SW China. Tectonophysics, 2010, 485(1-4): 107-121.

Jin, W., L. Tang, K. Yang, et al. Transfer zones within the Longmen Mountains thrust belt, SW China. Geosciences Journal, 2009, 13(1): 1-14.

Johnston, S. M., E. H. Hartz, H. K. Brueckner, et al. U–Pb zircon geochronology and tectonostratigraphy of southern Liverpool Land, East Greenland: Implications for deformation in the overriding plates of continental collisions. Earth Planetary Science Letters, 2010, 297(3–4): 512–524.

Jordan, T. E. Retroarc foreland and related basins. Tectonics of Sedimentary Basins, 1995.

Kirby, E., P. W. Reiners, M. A. Krol, et al. Late Cenozoic evolution of the eastern margin of the Tibetan Plateau: Inferences from 40Ar/39Ar and (U‐Th)/He thermochronology. Tectonics, 2002, 21(1): 1-1-1-20.

Kruckenberg, S. C., E. C. Ferré, C. Teyssier, et al. Viscoplastic flow in migmatites deduced from fabric anisotropy: An example from the Naxos dome, Greece. Journal of Geophysical Research Atmosphere, 2010, 115(B9): 1-18.

Leloup, P. H., and J. R. Kienast. High-temperature metamorphism in a major strike-slip shear zone: the Ailao Shan—Red River, People's Republic of China. Earth & Planetary Science Letters, 1993, 118(1-4): 213-234.

Li, H., H. Wang, G. Yang, et al. Lithological and structural characterization of the Longmen Shan fault belt from the 3rd hole of the Wenchuan Earthquake Fault Scientific Drilling project (WFSD-3). International Journal of Earth Sciences, 2015.

Li, H., Z. Xu, J. Si, et al. Wenchuan Earthquake Fault Scientific Drilling program (WFSD): Overview and Results. paper presented at AGU Fall Meeting, 2012.

Li, H., Z. Xu, J. Si, et al. Characteristics of the Fault-Related Rocks, Fault Zone Structures and the Principal Slip Zone of the Wenchuan Earthquake in WFSD Drilling Cores. American

Geophysical Union, 2010.

Li, Y., D. Jia, J. H. Shaw, et al. Structural interpretation of the coseismic faults of the Wenchuan earthquake: Three-dimensional modeling of the Longmen Shan fold-and-thrust belt. Journal of Geophysical Research, 2010, 115(B4): 1-26.

Li, Y., D. Su, R. Zhou, et al. Episodic orogeny deduced from coeval sedimentary sequences in the foreland basin and its implication for uplift process of Longmen Mountain, China. Journal of Mountain Science, 2013, 10(1): 29-42.

Li, Y., H. Li, R. Zhou, et al. Crustal thickening or isostatic rebound of orogenic wedge deduced from tectonostratigraphic units in Indosinian foreland basin, Longmen Shan, China. Tectonophysics, 2014, 619-620: 1-12.

Li, Y., P. A. Allen, A. L. Densmore, et al. Evolution of the Longmen Shan foreland basin (western Sichuan, China) during the Late Triassic Indosinian orogeny. Basin Research, 2003, 15(1): 117-138.

Li, Z.. Composition, structural characteristics and evolution of back-Longmenshan orogen (north section) in the northwest margin of Yangtze block, Doctoral thesis, 2009, 211 pp, Chang'an university.

Li, Z. X., X. H. Li, P. D. Kinny, et al. The breakup of Rodinia: did it start with a mantle plume beneath South China? Earth & Planetary Science Letters, 1999, 173(3): 171-181.

Lin, A., G. Rao, and B. Yan. Structural analysis of the right-lateral strike-slip Qingchuan fault, northeastern segment of the Longmen Shan thrust belt, central China. Journal of Structural Geology, 2014, 68: 227-244.

Lin, W., N. Charles, Y. Chen, et al. Late Mesozoic compressional to extensional tectonics in the Yiwulüshan massif, NE China and their bearing on the Yinshan–Yanshan orogenic belt: Part II: Anisotropy of magnetic susceptibility and gravity modeling. Gondwana Research, 2013, (0): 78-94.

Lin, W., N. Charles, Y. Chen, K. Chen, et al. Late Mesozoic compressional to extensional tectonics in the Yiwulüshan massif, NE China and their bearing on the Yinshan–Yanshan orogenic belt: Part II: Anisotropy of magnetic susceptibility and gravity modeling, Gondwana Research. 2013, 78-94.

Liu, S., B. Deng, Z. Li, et al. Geological evolution of the longmenshan intracontinental composite orogen and the eastern margin of the Tibetan Plateau. Journal of Earth Science, 2013, 24(6): 874-890.

Liu, Y., J. Deng, G. Zhang, et al. $^{40}Ar/^{39}Ar$ Dating of Xuebaoding Granite in the Songpan-Garze Orogenic Belt, Southwest China, and its Geological Significance. Acta Geologica Sinica, 2010, 84(2): 345-357.

Lu, R., D. He, J. Suppe, et al. Along-strike variation of the frontal zone structural geometry of the Central Longmen Shan thrust belt revealed by seismic reflection profiles. Tectonophysics, 2012, 580: 178-191.

Lu, R., D. He, S. John, et al. Structural model of the central Longmen Shan thrusts using seismic reflection profiles: Implications for the sediments and deformations since the Mesozoic. Tectonophysics, 2014, 630: 43-53.

Lu, R., D. He, X. Xu, et al. Crustal-scale tectonic wedging in the central Longmen Shan: Constraints

on the uplift mechanism in the southeastern margin of the Tibetan Plateau. Journal of Asian Earth Sciences, 2016, 117: 73-81.

Luo, L., J.-F. Qi, M.-Z. Zhang, et al. Detrital zircon U–Pb ages of Late Triassic–Late Jurassic deposits in the western and northern Sichuan Basin margin: constraints on the foreland basin provenance and tectonic implications. International Journal of Earth Sciences, 2014, 103(6): 1553-1568.

Martin, H.. Alternative Geodynamic Models for the Damara Orogeny. A Critical Discussion, Springer Berlin Heidelberg, 1983.

Mattauer, M. The Songpan-Garze Triassic belt of west Sichuan and eastern Tibet: a decollement fold belt on a passive margin[La chaine Triasique de Songpan-Garze (Ouest Sechuan et Est Tibet): une chaine de plissement-decollement sur marge passive]. 1992, 314: 619-626.

McQuarrie, N. Crustal scale geometry of the Zagros fold-thrust belt, Iran. Journal of Structural Geology, 2004, 26(3): 519-535.

Meng, Q. R., and G. W. Zhang. Geologic framework and tectonic evolution of the Qinling orogen, central China. Tectonophysics, 2000, 323: 183–196.

Meng, Q., J. Hu, E. Wang, et al. Late Cenozoic denudation by large-magnitude landslides in the eastern edge of Tibetan Plateau. Earth and Planetary Science Letters, 2006, 243(1): 252-267.

Meng, Q.-R., E. Wang, and J.-M. Hu. Mesozoic sedimentary evolution of the northwest Sichuan basin: Implication for continued clockwise rotation of the South China block. Geological Society of America Bulletin, 2005, 117(3-4): 396-410.

Miao, Y., M. Qingquan, F. Xiaomin, et al. Origin and development of Artemisia (Asteraceae) in Asia and its implications for the uplift history of the Tibetan Plateau: A review (CPCI-S). Quaternary International, 2011, 236(1): 3-12.

Molnar, P., and P. Tapponnier. Cenozoic Tectonics of Asia: Effects of a Continental Collision: Features of recent continental tectonics in Asia can be interpreted as results of the India-Eurasia collision. Science, 1975, 189(4021): 419-426.

Nance, R. D., and J. B. Murphy. Orogenic Style and the Configuration of Supercontinents. Cspg Special Publications, 1994, 17: 49-65.

Nédélec, A., and J. L. Bouchez. Genesis of hybrid granitoids: mingling and mixing. 2015, 58-72.

Parsons, A. J., E. C. Ferré, R. D. Law, et al. Orogen-parallel deformation of the Himalayan midcrust: Insights from structural and magnetic fabric analyses of the Greater Himalayan Sequence, Annapurna-Dhaulagiri Himalaya, central Nepal. Tectonics, 2016, 35(11): 2515-2537.

Paterson, S. R., O. T. Tobisch, and T. Bhattacharyya. Regional, structural and strain analyses of terranes in the Western Metamorphic Belt, Central Sierra Nevada, California. Journal of structural geology, 1989b, 11(3): 255-273.

Paterson, S. R., R. H. Vernon, and O. T. Tobisch. A review of criteria for the identification of magmatic and tectonic foliations in granitoids. Journal of structural geology, 1989a, 11(3): 349-363.

Paterson, S. R., T. K. Fowler, K. L. Schmidt, et al. Interpreting magmatic fabric patterns in plutons. Lithos, 1998, 44(1): 53-82.

Pei, X., Z. Li, S. Ding, et al. Neoproterozoic Jiaoziding Peraluminous Granite in the Northwestern

Margin of Yangtze Block: Zircon SHRIMP U-Pb Age and Geochemistry and Their Tectonic Significance. Earth Science Frontiers, 2009, 16(3): 231-249.

Pfiffner, O. A. Basement-involved thin-skinned and thick-skinned tectonics in the Alps. Geological Magazine, 2016, 153(5-6)(Thematic issue: Tectonic evolution and mechanics of basement-involved fold-and-thrust belts): 1085-1109.

Pinet, N., A. Tremblay, and M. Sosson. Extension versus shortening models for hinterland-directed motions in the southern Québec Appalachians. Tectonophysics, 1996, 267(1–4): 239–256.

Prior, D. J., A. P. Boyle, F. Brenker, et al. The application of electron backscatter diffraction and orientation contrast imaging in the SEM to textural problems in rocks. American Mineralogist, 2015, 84(11-12): 1741-1759.

Raimondo, T., A. S. Collins, M. Hand, et al. The anatomy of a deep intracontinental orogen. Tectonics, 2010, 29(4): TC4024.

Read, J. F. Carbonate Platform Facies Models. Aapg Bulletin, 1985, 69(1): 1-21.

Reid, A. J., A. P. Fowler, D. Phillips, et al. Thermochronology of the Yidun Arc, central eastern Tibetan Plateau: constraints from $^{40}Ar/^{39}Ar$ K-feldspar and apatite fission track data. Journal of Asian Earth Sciences, 2005b, 25(6): 915-935.

Reid, A. J., C. J. L. Wilson, and S. Liu. Structural evidence for the Permo-Triassic tectonic evolution of the Yidun Arc, eastern Tibetan Plateau. Journal of Structural Geology, 2005a, 27(1): 119-137.

Reid, A. J., C. J. L. Wilson, D. Phillips, et al. Mesozoic cooling across the Yidun Arc, central-eastern Tibetan Plateau: A reconnaissance $^{40}Ar/^{39}Ar$ study. Tectonophysics, 2005c, 398(1-2): 45-66.

Reid, A., C. J. L. Wilson, L. Shun, et al. Mesozoic plutons of the Yidun Arc, SW China: U/Pb geochronology and Hf isotopic signature. Ore Geology Reviews, 2007, 31(1-4): 88-106.

Richardson, N. J., A. L. Densmore, D. Seward, et al. Extraordinary denudation in the Sichuan Basin: Insights from low-temperature thermochronology adjacent to the eastern margin of the Tibetan Plateau. Journal of Geophysical Research, 2008, 113(B4).

Robert, A., J. Zhu, J. Vergne, et al. Crustal structures in the area of the 2008 Sichuan earthquake from seismologic and gravimetric data. Tectonophysics, 2010, 491(1-4): 205-210.

Robert, A., M. Pubellier, J. De Sigoyer, et al. Structural and thermal characters of the Longmen Shan (Sichuan, China). tectonophysics, 2010, 491(1): 165-173.

Rochette, P., M. Jackson, and C. Aubourg. Rock magnetism and the interpretation of anisotropy of magnetic susceptibility. Review Geophysics, 1992, 30(3): 209-226.

Rochette, P., M. Jackson, and C. Aubourg. Rock magnetism and the interpretation of anisotropy of magnetic susceptibility. Reviews of Geophysics, 1992, 30(3): 209-226.

Roger, F., J. Malavieille, P. H. Leloup, et al. Timing of granite emplacement and cooling in the Songpan–Garzê Fold Belt (eastern Tibetan Plateau) with tectonic implications. Journal of Asian Earth Sciences, 2004, 22(5): 465-481.

Roger, F., M. Jolivet, and J. Malavieille. The tectonic evolution of the Songpan-Garzê (North Tibet) and adjacent areas from Proterozoic to Present: A synthesis. Journal of Asian Earth Sciences, 2010, 39(4): 254-269.

Roger, F., M. Jolivet, R. Cattin, et al. Mesozoic-Cenozoic tectonothermal evolution of the eastern

part of the Tibetan Plateau (Songpan-Garze, Longmen Shan area): insights from thermochronological data and simple thermal modelling. Geological Society of London Special Publication, 2011, 353(1): 9-25.

Roger, F., N. Arnaud, S. Gilder, et al. Geochronological and geochemical constraints on Mesozoic suturing in east central Tibet. Tectonics, 2003, 22(4): 1037.

Roger, F., S. Calassou, J. Lancelot, et al. Miocene emplacement and deformation of the Konga Shan granite (Xianshui He fault zone, west Sichuan, China): Geodynamic implications. Earth & Planetary Science Letters, 1995, 130(1): 201–216.

Royden, L. H., B. C. Burchfiel, and R. D. van der Hilst. The geological evolution of the Tibetan Plateau. science, 2008, 321(5892): 1054-1058.

Royden, L. H., B. C. Burchfiel, R. W. King, et al. Surface deformation and lower crustal flow in eastern Tibet. Science, 1997, 276(5313): 788-790.

Sandiford, M., M. Hand, and S. McLaren. Tectonic feedback, intraplate orogeny and the geochemical structure of the crust: a central Australian perspective. Geological Society, London, Special Publications, 2001, 184(1): 195-218.

Schmid, S., B. Fügenschuh, E. Kissling et al. Tectonic map and overall architecture of the Alpine orogen. Eclogae Geolicae Helvetiae. 2004, 97(1): 93–117.

Schuchert, C. Significance of Taconic Orogeny. Geological Society of America Bulletin, 1925, 36(54): 343-350.

Selverstone, J.. Are the alps collapsing? Annual Review of Earth and Planetary Science, 2005, 33(1): 113–132.

Sengör, A. M. C., and B. A. Natal'in. Paleotectonics of Asia: Fragments of a synthesis. 1996.

Sengor, A. M. C., and B. A. Natalin. Turkic-type orogeny and its role in the making of the continental crust. Annual Review of Earth and Planetary Sciences, 1996, 24: 263-337.

Sigoyer, J., O. Vanderhaeghe, S. Duchêne, et al. Generation and emplacement of Triassic granitoids within the Songpan Ganze accretionary-orogenic wedge in a context of slab retreat accommodated by tear faulting, Eastern Tibetan plateau, China. Journal of Asian Earth Sciences, 2014, 88: 192-216.

Sutton, J., and J. V. Watson. Architecture of the Continental Lithosphere. Philosophical Transactions of the Royal Society A Mathematical Physical & Engineering Sciences, 1986, 317(1539): 5-12.

Talbot, J.-Y., M. Faure, Y. Chen, et al. Pull-apart emplacement of the Margeride granitic complex (French Massif Central). Implications for the late evolution of the Variscan orogen. Journal of Structural Geology, 2005, 27(9): 1610-1629.

Tan, X.-B., Y.-H. Lee, W.-Y. Chen, et al. Exhumation history and faulting activity of the southern segment of the Longmen Shan, eastern Tibet. Journal of Asian Earth Sciences, 2014, 81: 91-104.

Tang, L., K. Yang, W. Jin, et al. Multi-level decollement zones and detachment deformation of Longmenshan thrust belt, Sichuan Basin, southwest China. Science in China Series D: Earth Sciences, 2008, 51(S2): 32-43.

Tapponnier, P., and P. Molnar. Active faulting and Cenozoic tectonics of the Tien Shan, Mongolia,

and Baykal regions. Journal of Geophysical Research: Solid Earth, 1979, 84(B7): 3425-3459.

Tapponnier, P., G. Peltzer, A. Y. L. Dain, et al. Propagating extrusion tectonics in Asia: New insights from simple experiments with plasticine. Geology, 1982, 10(12): 611-616.

Tapponnier, P., R. Lacassin, P. H. Leloup, et al. The Ailao Shan/Red River metamorphic belt: Tertiary left-lateral shear betweenIndochina and South China. Nature, 1990, 343(6257): 431-437.

Tapponnier, P., X. Zhiqin, F. Roger, et al. Oblique stepwise rise and growth of the Tibet plateau. Science, 2001, 294(5547): 1671-1677.

Tapponnier, P., Z. Xu, F. Roger, B. Meyer, N. Arnaud, G. Wittlinger, and Y. Jingsui (2001), Oblique stepwise rise and growth of the Tibet plateau, Science, 294(5547), 1671-1677.

Tarling, D., and F. Hrouda (1993), Magnetic anisotropy of rocks, Springer Science & Business Media.

Tavarnelli, E. Normal faults in thrust sheets: Pre-orogenic extension, post-orogenic extension, or both? Journal of Structural Geology, 1999, 21(8–9): 1011–1018,.

Tian, Y., B. P. Kohn, A. J. W. Gleadow, et al. Constructing the Longmen Shan eastern Tibetan Plateau margin: Insights from low-temperature thermochronology. Tectonics, 2013, 32(3): 576-592.

Tian, Y., B. P. Kohn, D. Phillips, et al. Late Cretaceous–earliest Paleogene deformation in the Longmen Shan fold‐and‐thrust belt, eastern Tibetan Plateau margin: Pre‐Cenozoic thickened crust? Tectonics, 2016: 1-20.

Turrillot, P., M. Faure, G. Martelet, et al. Pluton-dyke relationships in a Variscan granitic complex from AMS and gravity modelling. Inception of the extensional tectonics in the South Armorican Domain (France). Journal of Structural Geology, 2011, 33(11): 1681-1698.

Wang, E., E. Kirby, K. P. Furlong, et al. Two-phase growth of high topography in eastern Tibet during the Cenozoic. Nature Geosci, 2012, 5(9): 640-645.

Wang, E., K. Meng, J. J. Chu, et al. East Tibet Detachment: Evidence for the uplift mechanism of the Longmen Shan fault belt. America Geological Fall Meeting, Abstract, 2012.

Wang, E., K. Meng, Z. Su, et al. Block rotation: Tectonic response of the Sichuan basin to the southeastward growth of the Tibetan Plateau along the Xianshuihe-Xiaojiang fault. Tectonics, 2014, 33(5): 686-718.

Wang, H., H. Li, J. Si, et al. Internal structure of the Wenchuan earthquake fault zone, revealed by surface outcrop and WFSD-1 drilling core investigation. Tectonophysics, 2014, 619-620: 101-114.

Wang, W. On the origin and development of Artemisia (Asteraceae) in the geological past. Botanical Journal of the Linnean Society, 2004, 145(145): 331-336.

Wei, W., G. Martelet, N. Le Breton, et al. A multidisciplinary study of the emplacement mechanism of the Qingyang–Jiuhua massif in Southeast China and its tectonic bearings. Part II: Amphibole geobarometry and gravity modeling. Journal of Asian Earth Sciences, 2014b, 86: 94-105.

Wei, W., Y. Chen, M. Faure, et al. A multidisciplinary study on the emplacement mechanism of the Qingyang–Jiuhua Massif in Southeast China and its tectonic bearings. Part I: Structural geology, AMS and paleomagnetism. Journal of Asian Earth Sciences, 2014, 86: 76-93.

Weislogel, A. L., S. A. Graham, E. Z. Chang, et al. Detrital zircon provenance from three turbidite depocenters of the Middle-Upper Triassic Songpan-Ganzi complex, central China: Record of collisional tectonics, erosional exhumation, and sediment production. Geological Society of America Bulletin, 2010, 122(11-12): 2041-2062.

Weislogel, A. L., S. A. Graham, E. Z. Chang, et al. Detrital zircon provenance of the Late Triassic Songpan-Ganzi complex: Sedimentary record of collision of the North and South China blocks. Geology, 2006, 34(2): 97-100.

Weller, O. M., M. R. St-Onge, D. J. Waters, et al. Quantifying Barrovian metamorphism in the Danba Structural Culmination of eastern Tibet. Journal of Metamorphic Geology, 2013, 31(9): 909-935.

White, A. P., and K. V. Hodges. Multistage extensional evolution of the central East Greenland Caledonides. Tectonics, 2002, 21(5): 1048-1071.

Willett, S., C. Beaumont, and P. Fullsack. Mechanical model for the tectonics of doubly vergent compressional orogens. Geology, 1993, 21(21): 371-374.

Windley, and B.F. Uniformitarianism today: plate tectonics is the key to the past. Jornal of the Geological society, 1993, 150(1): 7-19.

Windley, B. Chapter 11 Proterozoic Collisional and Accretionary Orogens. Developments in Precambrian Geology, 1992, 10: 419-446.

Worley, B. A., and C. J. Wilson. Deformation partitioning and foliation reactivation during transpressional orogenesis, an example from the Central Longmen Shan, China. Journal of Structural Geology, 1996, 18(4): 395-411.

Worley, B., C. J. L. Wilson, S. Liu, and Z. Luo. Structural observations from the Wenchuan-Maowen metamorphic belt, Longmen Mountains, China. Journal of Chengdu College Geology, 1995, 22(01): 24-41.

Wu, C. M., and H. X. Chen. Calibration of a Ti-in-muscovite geothermometer for ilmenite- and Al_2SiO_5-bearing metapelites. Lithos, 2015b, s 212–215: 122-127.

Wu, C. M., and H. X. Chen. Revised Ti-in-biotite geothermometer for ilmenite- or rutile-bearing crustal metapelites. Science Bulletin, 2015a, 60(1): 116-121.

Xiao, L., H. Zhang, J. D. Clemens, et al. Late Triassic granitoids of the eastern margin of the Tibetan Plateau: Geochronology, petrogenesis and implications for tectonic evolution. Lithos, 2007b, 96(3-4): 436-452.

Xiao, L., H. Zhang, J. D. Clemens, et al. Late Triassic granitoids of the eastern margin of the Tibetan Plateau: Geochronology, petrogenesis and implications for tectonic evolution. Lithos, 2007, 96(3-4): 436-452.

Xiao, L., H.-F. Zhang, P.-Z. Ni, et al. LA-ICP-MS U–Pb zircon geochronology of early Neoproterozoic mafic-intermediat intrusions from NW margin of the Yangtze Block, South China: Implication for tectonic evolution. Precambrian Research, 2007a, 154(3): 221-235.

Xu, X., X. Wen, G. Yu, et al. Coseismic reverse- and oblique-slip surface faulting generated by the 2008 Mw 7.9 Wenchuan earthquake, China. Geology, 2009, 37(6): 515-518.

Xu, Z., H. Li, L. Hou, et al. Uplift of the Longmen-Jinping orogenic belt along the eastern margin of the Qinghai-Tibet Plateau: Large-scale detachment faulting and extrusion mechanism. Geological Bulletin of China, 2007, 26(10): 1262-1276.

Xu, Z., L. Hou, and Z. Wang Orogenic process of the Songpan-Ganzé Orogenic belt of China. 1st edition, pp. 1-189, Geological Publishing House, Beijing 1992.

Xu, Z., S. Ji, H. Li, et al. Uplift of the Longmen Shan range and the Wenchuan earthquake. Episodes, 2008, 31(3): 291-301.

Yan, D., B. Zhang, M. Zhou, et al. Constraints on the depth, geometry and kinematics of blind detachment faults provided by fault-propagation folds: An example from the Mesozoic fold belt of South China. Journal of Structural Geology, 2009, 31(2): 150-162.

Yan, D., M. Zhou, G. Wei, et al. Collapse of Songpan-Garzê Orogenic Belt Resulted from Mesozoic Middle-crustal Ductile Channel Flow: Evidences from Deformation and Metamorphism Within Sinian-Paleozoic Strata in Hinterland of Longmenshan Foreland Thrust Belt. Earth Science Frontiers, 2008a, 15(3): 186-198.

Yan, D., M. Zhou, G. Wei, et al. The Pengguan tectonic dome of Longmen Mountains, Sichuan Province: Mesozoic denudation of a Neoproterozoic magmatic arc-basin system. Science in China Series D: Earth Sciences, 2008b, 51(11): 1545-1559.

Yan, D., M. Zhou, S. Li, et al. Structural and geochronological constraints on the Mesozoic - Cenozoic tectonic evolution of the Longmen Shan thrust belt, eastern Tibetan Plateau. Tectonics, 2011, 30(6): 1-24.

Yan, D.-P., M.-F. Zhou, H. Song, et al. Structural style and tectonic significance of the Jianglang dome in the eastern margin of the Tibetan Plateau, China. Journal of Structural Geology, 2003a, 25(5): 765-779.

Yan, D.-P., M.-F. Zhou, H.-L. Song, et al. Origin and tectonic significance of a Mesozoic multi-layer over-thrust system within the Yangtze Block (South China). tectonophysics, 2003b, 361(3): 239-254.

Yan, D.-P., M.-F. Zhou, P. T. Robinson, et al. Constraining the mid-crustal channel flow beneath the Tibetan Plateau: data from the Nielaxiongbo gneiss dome, SE Tibet. International Geology Review, 2012, 54(6): 615-632.

Yin, A., and S. Nie. An indentation model for the North and South China collision and the development of the Tan-Lu and Honam fault systems, Eastern Asia. Tectonics, 1993, 12(4): 801-813.

Yin, A., and T. M. Harrison. Geologic evolution of the Himalayan-Tibetan orogen. Annural Review of Earth and Planetary Sciences, 2000, 28, 211-280.

Yuan, C., M.-F. Zhou, M. Sun, et al. Triassic granitoids in the eastern Songpan Ganzi Fold Belt, SW China: Magmatic response to geodynamics of the deep lithosphere. Earth and Planetary Science Letters, 2010, 290(3-4): 481-492.

Yuan, H., Z. Zhang, and P. Zhang (1991), The uplift and cooling histories of Laojungou granite in the western margin of the central Longmen Mountain, J. Chengdu College Geol., 18(1), 17-22.

Zhang, H., L. Zhang, N. Harris, et al. U–Pb zircon ages, geochemical and isotopic compositions of granitoids in Songpan-Garze fold belt, eastern Tibetan Plateau: constraints on petrogenesis and tectonic evolution of the basement. Contributions to Mineralogy and Petrology, 2006, 152(1): 75-88.

Zhang, H., R. Parrish, L. Zhang, et al. A-type granite and adakitic magmatism association in Songpan–Garze fold belt, eastern Tibetan Plateau: Implication for lithospheric delamination.

Lithos, 2007, 97(3-4): 323-335.

Zhang, J., R. Gao, L. Zeng, et al. Relationship between characteristics of gravity and magnetic anomalies and the earthquakes in Longmenshan range and adjacent areas. Chinese Journal of Geophysics. 2009, (02): 572-578.

Zhang, K.J., B. Li, Q.-G. Wei, et al. Proximal provenance of the western Songpan–Ganzi turbidite complex (Late Triassic, eastern Tibetan plateau): Implications for the tectonic amalgamation of China. Sedimentary Geology, 2008, 208(1-2): 36-44.

Zhang, P., Q. Wang, and M. A. Zongjin. GPS velocity field and active crustal deformation in and around the Qinghai-Tibet plateau. Earth Science Frontiers, 2002, 9(2): 442-450.

Zhang, P.-Z., Z. Shen, M. Wang, et al. Continuous deformation of the Tibetan Plateau from global positioning system data. Geology, 2004, 32(9): 809.

Zhang, Y., D. Jia, L. Shen, et al. Provenance of detrital zircons in the Late Triassic Sichuan foreland basin: constraints on the evolution of the Qinling Orogen and Longmen Shan thrust-fold belt in central China. International Geology Review, 2015, 57(14): 1806-1824.

Zhang, Z., Y. Wang, Y. Chen, et al. Crustal structure across Longmenshan fault belt from passive source seismic profiling. Geophysical Research Letters, 2009, 36(17).

Zhao, J. H., and M. F. Zhou. Neoproterozoic Adakitic Plutons and Arc Magmatism along the Western Margin of the Yangtze Block, South China. The Journal of Geology, 2007, 115(6): 675-689.

Zhao, Y.. Mesozoic granitoids in Eastern Songpan-Garze: Geochemistry, petrogenesis and tectonic implications, thesis, Diploma of master, 111 pp, Graduate school Chinese Academy of Sciences, 2007.

Zheng, Y., H. Li, Z. Sun, et al. New geochronology constraints on timing and depth of the ancient earthquakes along the Longmen Shan fault belt, eastern Tibet. Tectonics, 2016, 35: 2781-2806.

Zheng, Y., P. Kong, and B. Fu. Time constraints on the emplacement of klippen in the Longmen Shan thrust belt and tectonic implications. Tectonophysics, 2014, 634: 44-54.

Zhou, M. F., Y. X. Ma, D. P. Yan, et al. The Yanbian terrane (Southern Sichuan Province, SW China): A neoproterozoic are assemblage in the western margin of the Yangtze block. Precambrian Research, 2006, 144(1-2): 19-38.

Zhou, M., and L. C. Michael. Neoproterozoic arc-related mafic intrusions along the northern margin of South China: Implications for the accretion of Rodinia. J. Geol., 2002, 110(5): 611-618.

Zhou, M., D. Yan, A. K. Kennedy, et al. SHRIMP U–Pb zircon geochronological and geochemical evidence for Neoproterozoic arc-magmatism along the western margin of the Yangtze Block, South China. Earth and Planetary Science Letters, 2002, 196(1): 51-67.

Zhou, M., D. Yan, C. Wang, et al. Subduction-related origin of the 750 Ma Xuelongbao adakitic complex (Sichuan Province, China): implications for the tectonic setting of the giant Neoproterozoic magmatic event in South China. Earth and Planetary Science Letters, 2006, 248(1): 286-300.

Zhou, M., D. Yan, P. M. Vasconcelos, et al. Structural and geochronological constraints on the tectono-thermal evolution of the Danba domal terrane, eastern margin of the Tibetan plateau. Journal of Asian Earth Sciences, 2008, 33(5): 414-427.

Zhou, M., D. Yan, P. M. Vasconcelos, J. Li, and R. Hu. Structural and geochronological constraints on the tectono-thermal evolution of the Danba domal terrane, eastern margin of the Tibetan plateau. Journal of Asian Earth Sciences, 2008, 33(5): 414-427.

Ziegler, P. A., S. Cloetingh, and J.D. van Wees. Dynamics of intra-plate compressional deformation: the Alpine foreland and other examples. Tectonophysics, 1995, 252(1-4): 7-59.

边兆祥, 朱夔玉, 金以钟,等. 四川龙门山印支期构造发展特征. 四川地质学报, 1980, (00): 1-10+157.

曾允孚和李勇. 龙门山前陆盆地形成与演化. 矿物岩石, 1995, (01): 40-49.

陈娟, 马润则, 张腊梅,等. 龙门山北段水磨地区辉绿岩锆石 U-Pb 年龄及地球化学特征. 地质与勘探, 2015, 51(1): 133-142.

陈社发, 邓起东, 赵小麟,等. 龙门山中段推覆构造带及相关构造的演化历史和变形机制(二). 地震地质, 1994b, (04): 413-421.

陈社发, 邓起东, 赵小麟,等. 龙门山中段推覆构造带及相关构造的演化历史和变形机制(一). 地震地质, 1994a, (04): 404-412.

陈竹新, 贾东, 张愜,等. 龙门山前陆褶皱冲断带的平衡剖面分析. 地质学报, 2005, (01): 38-45.

褚杨. 早中生代雪峰山造山带的构造演化, 中国科学院研究生院, 2011.

崔秉荃和龙学明. 川西拗陷的沉降与龙门山的崛起. 成都理工大学学报(自科版), 1991, (1): 42-48.

樊春, 王二七, 王刚,等. 龙门山断裂带北段晚新近纪以来的右行走滑运动及其构造变换研究——以青川断裂为例. 地质科学, 2008, (03): 417-433.

高锐, 马永生, 李秋生,等. 松潘地块与西秦岭造山带下地壳的性质和关系——深地震反射剖面的揭露. 地质通报, 2006, (12): 1361-1367.

郭瑞强. 龙门山灌县—安县断裂带的变形特征—汶川地震断裂带科学钻探(WFSD-3P)岩心与井温的研究, 中国地质大学(北京), 2011.

韩建辉, 李忠权,王道永. 龙门山中段清平叠覆式飞来峰的厘定. 成都理工大学学报: 自然科学版, 2009, 36(3): 305-310.

韩建辉, 王道永,李忠权. 龙门山中段清平飞来峰的构造变形特征及形成机制 [J]. 沉积与特提斯地质, 2008, 28(3): 8-14.

韩建辉. 龙门山中段清平飞来峰的厘定及形成演化, 成都理工大学, 2006b.

韩建辉. 论龙门山飞来峰群. 沉积与特提斯地质, 2006a, (01): 55-59.

韩克猷. 龙门山逆掩断裂带成因与油气远景. 天然气工业, 1984, (4): 5+9-16.

韩同林, 何银武,周自隆 (1994), 关于四川彭县“飞来峰”的新见解.

韩同林, 劳雄, 陈尚平,等. 四川彭州葛仙山巨型冰川漂砾的发现及意义. 中国区域地质, 1999, (01): 60-68.

何银武. 论成都盆地的成生时代及其早期沉积物的一般特征. 地质论评, 1992, (02): 149-156.

胡健民, 孟庆任, 石玉若,等. 松潘-甘孜地体内花岗岩锆石 SHRIMP U-Pb 定年及其构造意义.

岩石学报, 2005, (03): 867-880.

黄永健, 张成江, 汪云亮,等. 龙门山造山带中生代花岗岩带成因及其构造意义. 成都理工学院学报, 2002, (01): 69-73.

贾东, 陈竹新, 贾承造,等. 龙门山前陆褶皱冲断带构造解析与川西前陆盆地的发育. 高校地质学报, 2003, 9(3): 402-410.

金文正, 唐良杰, 杨克明,等. 川西龙门山褶皱冲断带分带性变形特征. 地质学报, 2007, 81(8): 1072-1080.

柯小平, 王勇生, 许厚泽,等. 青藏高原地壳三维密度结构的重力反演. 地球物理学进展, 2009, 24(2): 448-455.

赖绍聪, 李永飞,秦江锋. 碧口群西段董家河蛇绿岩地球化学及 LA-ICP-MS 锆石 U-Pb 定年. 中国科学:地球科学, 2007, (S1): 262-270.

李立和金国元. 攀西裂谷带及龙门山断裂带地壳上地幔的大地电磁测深研究. 物探与化探, 1987, (3): 3-11.

李献华, 周汉文, 李正祥,等. 扬子块体西缘新元古代双峰式火山岩的锆石 U-Pb 年龄和岩石化学特征. 地球化学, 2001, 30(4): 315-322.

李勇, 贺佩, 颜照坤,等. 晚三叠世龙门山前陆盆地动力学分析. 成都理工大学学报(自然科学版), 2010, (04): 401-411.

李勇, 苏德辰, 董顺利,等. 龙门山前陆盆地底部不整合面:被动大陆边缘到前陆盆地的转换. 岩石学报, 2011, (08): 2413-2422.

李勇, 徐公达, 周荣军,等. 龙门山均衡重力异常及其对青藏高原东缘山脉地壳隆升的约束. 地质通报, 2005, (12): 1162-1168.

李勇, 周荣军, D. A. L,等. 青藏高原东缘龙门山晚新生代走滑挤压作用的沉积响应. 沉积学报, 2006, 24(2): 153-164.

李勇. 论龙门山前陆盆地与龙门山造山带的耦合关系. 矿物岩石地球化学通报, 1998, (02): 10-14.

李月. 松潘-阿坝及东缘龙门山地区构造特征及动力学分析, 中国石油大学, 2008.

李佐臣, 裴先治, 丁仨平,等. 川西北平武地区南一里花岗岩体地球化学特征及其构造环境. 地质学报, 2009, (02): 260-271.

李佐臣, 裴先治, 刘战庆,等. 扬子地块西北缘后龙门山南华纪-早古生代沉积地层特征及其形成环境. 地球科学与环境学报, 2011, 33(2): 117-124.

李佐臣. 扬子地块西北缘后龙门山造山带(北段)物质组成、构造特征及其形成演化, 长安大学, 2009.

李佐臣. 扬子地块西北缘轿子顶变质核杂岩构造特征及其地质意义, 长安大学, 2006.

林茂炳. 初论陆内造山带的造山模式——以四川龙门山为例. 四川地质学报, 1996, (03): 193-198.

林茂炳和马永旺. 论龙门山彭灌杂岩体的构造属性. 成都理工学院学报, 1995, (01): 42-46.

凌文黎, 高山, 程建萍,等. 扬子陆核与陆缘新元古代岩浆事件对比及其构造意义——来自黄陵和汉南侵入杂岩 ELA-ICPMS 锆石 U-Pb 同位素年代学的约束. 岩石学报, 2006, (02): 387-396.

刘鹤, 颜丹平,魏国庆. 扬子板块西北缘碧口地块变形变质作用序列——松潘-甘孜造山带伸展垮塌事件的意义. Acta Geologica Sinica, 2008, 82(4): 464-474.

刘树根, 罗志立, 庞家黎,等. 四川盆地西部的峨眉地裂运动及找气新领域. 成都理工大学学报(自科版), 1991, (1): 86-93.

刘树根, 童崇光, 罗志立,等. 川西晚三叠世前陆盆地的形成与演化. 天然气工业, 1995, (02): 11-15+108.

刘琰, 邓军, 李潮峰,等. 四川雪宝顶白钨矿稀土地球化学与 Sm-Nd 同位素定年. 科学通报, 2007, (16): 1923-1929.

龙学明. 龙门山中北段地史发展的若干问题. 成都理工大学学报(自科版), 1991, (1): 8-16.

罗志立 (1994), 龙门山造山带的崛起和四川盆地的形成与演化, 成都科技大学出版社.

罗志立和龙学明. 龙门山造山带崛起和川西陆前盆地沉降. 四川地质学报, 1992, (01): 1-17.

罗志立. 龙门山造山带岩石圈演化的动力学模式. 成都理工大学学报(自科版), 1991, (1): 1-7.

罗志立. 试论中国型(C-型)冲断带及其油气勘探问题. 石油与天然气地质, 1984, (04): 315-324.

吕崧, 颜丹平, 王焰,等. 碧口地块麻山、木皮岩体岩石地球化学与地质年代学:对构造属性的指示意义. 岩石学报, 2010, (06): 1889-1901.

马润则, 肖渊甫, 魏显贵,等. 米仓山地区岩浆活动与构造演化. 矿物岩石, 1997, (s1): 79-85.

马永旺, 王国芝,胡新伟. “彭灌杂岩”推覆体的构造变形特征. 四川地质学报, 1996, (2): 110-114.

马永旺和刘顺. 龙门山彭灌地区大鱼洞-九甸坪-龙溪滑覆体的变形特征及形成. 成都理工大学学报(自然科学版), 2003, (05): 462-467.

沙庆安, 温常庆,晋惠娟等. 黔桂地区二叠系综合研究——兼论含油气性. 中国科学院兰州地质研究所, 1992.

石绍清. 彭县地区飞来峰的特征及形成演化. 成都理工学院学报, 1994, (03): 8-13.

四川省地质矿产局 (1991), 四川省区域地质志, 730 pp., 地质出版社, 北京.

王二七, 孟庆任, 陈智樑,等. 龙门山断裂带印支期左旋走滑运动及其大地构造成因. 地学前缘, 2001, (02): 375-384.

王宗秀, 许志琴,杨天南. 松潘-甘孜滑脱型山链变形构造演化模式. 地质科学, 1997, (03): 327-336.

魏春景. 陕甘川交界区碧口群的变质作用及其地质意义. 地质学报, 1994, (03): 241-254.

吴山, 赵兵,胡新伟. 再论龙门山飞来峰. 成都理工大学学报(自科版), 1999, 26(3): 221-224.

吴山和林茂炳. 龙门山唐王寨滑覆构造分析. 成都地质学院学报, 1991b, (01): 56-64.

吴山. 龙门山彭灌杂岩体中韧性剪切带的发现及其构造意义. 矿物岩石, 1993, 13(2): 71-77.

吴山和林茂炳. 龙门山唐王寨滑覆构造分析. 成都理工大学学报(自科版), 1991a, (1): 56-64.

夏宗实. 松潘—甘孜造山带三叠系陆源碎屑岩燕山早期同造山区域近变质作用. 四川地质学报, 1993, (03): 189-192.

许志琴, 侯立炜,王宗秀 (1992), 中国松潘--甘孜造山带的造山过程, 地质出版社.

许志琴, 李化启, 侯立炜,等. 青藏高原东缘龙门-锦屏造山带的崛起——大型拆离断层和挤出机制. 地质通报, 2007, (10): 1262-1276.

许志琴, 王宗秀,候立玮. 松潘-甘孜造山带构造研究新进展. 中国地质, 1991, (12): 14-16.

许志琴, 杨经绥, 姜枚,等. 大陆俯冲作用及青藏高原周缘造山带的崛起. 地学前缘, 1999, (03): 139-151.

闫全人, A. D.Hanson, 王宗起,等. 扬子板块北缘碧口群火山岩的地球化学特征及其构造环境. 岩石矿物学杂志, 2004, (01): 1-11.

闫全人, 王宗起, 闫臻,等. 碧口群火山岩的时代——SHRIMP 锆石 U-Pb 测年结果. 地质通报, 2003, (06): 456-458.

杨光, 李海兵, 张伟,等. 四川龙门山安县-灌县断裂带的特征——以汶川地震断裂带科学钻探 3 号孔(WFSD-3)岩心为例. 地质通报, 2012, 31(8): 1219-1232.

杨光. 龙门山安县—灌县断裂带的断裂岩特征——汶川地震断裂带科学钻探三号孔(WFSD-3)岩芯及地表研究, 成都理工大学, 2012.

袁海华, 张志兰,张平. 龙门山老君沟花岗岩的隆升及冷却史. 成都理工大学学报(自科版), 1991, (1): 17-22.

岳远刚. 东昆仑南缘三叠系沉积特征及其对阿尼玛卿洋闭合时限的约束, 西北大学, 2014.

张季生, 高锐, 曾令森,等. 龙门山及邻区重、磁异常特征及与地震关系的研究. 地球物理学报, 2009, 52(2): 572-578.

张长厚. 初论板内造山带. 地学前缘, 1999, 6(4): 295-308.

张长厚和吴正文. 造山带构造研究中几个重要学术概念问题的讨论. 地质论评, 2002, 48(4): 337-344.

赵永久, 袁超, 周美夫,等. 川西老君沟和孟通沟花岗岩的地球化学特征、成因机制及对松潘-甘孜地体基底性质的制约. 岩石学报, 2007, (05): 995-1006.

赵永久. 松潘—甘孜东部中生代中酸性侵入体的地球化学特征、岩石成因及构造意义, 中国科学院研究生院(广州地球化学研究所), 2007.

周自隆. 四川龙门山国家地质公园“飞来峰”成因研究的新进展. 四川地质学报, 2006, 26(1): 7-9.

周自隆和阮明德. 龙门山国家地质公园飞来峰成因的新证据. 地质论评, 2006, 52(4): 501-509.

朱同兴和蒲心纯. 扬子台地西缘二叠纪深水碳酸盐沉积作用及其环境意义. 沉积与特提斯地质, 1994: 88-103.

Appendix table 3.1 SEM data of mica geothermometer

		Chemical compositions of biotite											
	Input P												T
Sample	(GPa)	SiO_2	TiO_2	Al_2O_3	FeO(tot)	MnO	MgO	CaO	Na_2O	K_2O	Cr_2O_3	NiO	(^oC)
cx10-2Bt	0.4	38.66	1.545	17.461	14.256	0.054	13.03	0.462	0.108	9.515	0.036	0	512
cx10-2Bt	0.4	38.74	1.519	17.664	14.005	0.034	13.24	0.531	0.166	9.387	0.023	0	511
cx10-2Bt	0.4	38.57	1.481	17.664	14.066	0.006	12.94	0.389	0.137	9.608	0.037	0	511
cx10-2Bt	0.4	38.42	1.489	17.491	14.345	0.019	13.19	0.37	0.107	9.424	0.015	0.032	506
cx10-2Bt1	0.4	38.95	1.546	17.228	14.11	0.026	13.13	0.285	0.137	9.26	0.02	0	513
cx10-2Bt2	0.4	38.89	1.52	17.437	13.856	0.019	13.13	0.298	0.123	9.454	0.006	0.004	514
cx10-2Bt3	0.4	38.7	1.479	17.225	14.189	0.047	13.22	0.312	0.099	9.385	0.047	0	506
cx10-2Bt4	0.4	38.84	1.647	17.142	14.188	0.025	13.66	0.442	0.13	8.294	0	0	515
cx10-2Bt5	0.4	38.79	1.571	17.54	13.882	0.041	13.19	0.223	0.109	9.586	0.021	0.017	517
cx10-3Bt	0.4	39.67	1.532	17.365	13.264	0.049	12.8	0.099	0.117	9.393	0.031	0	525
cx10-3Bt	0.4	39.33	1.499	17.253	13.685	0.025	13.28	0.193	0.135	9.306	0.002	0	512
cx10-3Bt	0.4	38.81	1.565	17.17	13.888	0.024	13.31	0.121	0.115	9.478	0.005	0	514
cx10-3Bt	0.4	38.38	1.498	17.223	13.766	0.034	13.49	0.183	0.093	9.36	0.027	0.009	507
cx10-3Bt	0.4	37.53	1.456	16.838	13.578	0.037	13.33	0	0.111	9.594	0.016	0	504
cx10-4bt	0.4	38.24	1.519	17.665	14.334	0.029	13.53	0.055	0.196	9.14	0.017	0	506
cx10-4bt	0.4	37.96	1.498	17.535	14.562	0.025	13.51	0.061	0.094	9.395	0.011	0	502
cx10-4bt	0.4	38.12	1.497	17.734	14.404	0.038	13.41	0.046	0.178	9.49	0.02	0.008	505
cx10-4bt	0.4	38.26	1.449	17.717	14.395	0.037	13.41	0.106	0.066	9.682	0.03	0.049	501

cx10-4bt	0.4	37.96	1.494	17.919	14.124	0.017	13.32	0.026	0.109	9.819	0.038	0.001	508
cx10-5bt	0.4	38.44	1.476	17.688	14.274	0.014	13.31	0.188	0.176	9.312	0.049	0	506
cx10-5bt	0.4	38.95	1.57	17.46	14.228	0.061	13.08	0.162	0.126	9.284	0.041	0.028	516
cx10-5bt	0.4	38.25	1.583	17.709	14.3	0.052	13.45	0.2	0.17	9.461	0.04	0	511
cx10-1bt	0.4	36.94	1.323	17.847	14.447	0.054	13.49	0.215	0.117	9.002	0.032	0	488
cx10-1bt	0.4	37.55	1.285	17.651	14.824	0.057	13.19	0.327	0.103	9.107	0.043	0.01	486
cx10-1bt	0.4	38.1	1.476	17.891	14.68	0.043	13.11	0.166	0.065	9.412	0.03	0.01	505
cx10-1bt	0.4	37	1.443	17.492	13.624	0.016	14.04	0.347	0.053	7.231	0.031	0	500
cx10-1bt	0.4	38.46	1.436	17.438	14.034	0.025	13.1	0.14	0.128	9.504	0.037	0.035	505
cx10-6bt	0.4	38.24	1.469	17.492	14.284	0.041	13.23	0.084	0.078	9.442	0.02	0.026	505
cx10-6bt	0.4	37.95	1.46	17.753	14.249	0.045	13.47	0.059	0.13	9.157	0.024	0.033	503
cx10-6bt	0.4	37.88	1.498	17.789	14.745	0.06	13.35	0.039	0.07	9.639	0.049	0.006	503
cx10-6bt	0.4	37.77	1.395	17.895	14.551	0.029	13.21	0.057	0.082	9.431	0.013	0	498

cx32-2bt	0.4	38.07	1.991	15.366	14.759	0.058	13.53	0.074	0.055	9.149	0.088	0.025	526
cx32-2bt	0.4	38.1	2.126	15.45	14.651	0.066	13.67	0.081	0.046	8.887	0.076	0.054	534
cx32-2bt	0.4	38.45	1.946	15.306	14.596	0.061	13.71	0.058	0.038	9.244	0.045	0.033	523
cx32-2bt	0.4	38.3	1.937	15.125	14.616	0.053	13.59	0.102	0.182	9.109	0.107	0.024	522
cx32-2bt	0.4	38.07	2.02	15.5	14.833	0.079	13.48	0.025	0.041	9.319	0.063	0.033	528
cx32-3bt	0.4	38.22	2.008	15.139	14.47	0.076	13.59	0.144	0.066	8.982	0.078	0.027	528
cx32-3bt	0.4	38.33	1.935	15.1	14.665	0.099	13.78	0.097	0.023	9.001	0.092	0.06	520
cx32-3bt	0.4	38.27	2.061	15.324	14.546	0.076	13.63	0.08	0.038	9.313	0.117	0.018	531
cx32-3bt	0.4	38.42	2.018	15.434	14.614	0.043	13.56	0.053	0.048	9.331	0.085	0.076	529
cx32-4bt	0.4	38.94	1.981	15.485	14.826	0.051	13.77	0.063	0.021	9.27	0.095	0.02	525
cx32-4bt	0.4	38.24	1.976	15.267	14.542	0.056	13.51	0.156	0.104	9.082	0.111	0.026	526

cx32-4bt	0.4	38.5	2.036	15.425	14.645	0.063	13.52	0.109	0.066	9.307	0.124	0.007	530
cx32-5bt	0.4	38.09	2.243	15.321	14.54	0.056	13.2	0.053	0.034	9.19	0.121	0.047	546
cx32-5bt	0.4	38.28	2.1	15.589	14.833	0.056	13.15	0.059	0.056	9.182	0.107	0.005	537
cx32-5bt	0.4	38.29	2.077	15.45	14.6	0.066	13.22	0.064	0.041	9.047	0.092	0.047	537
cx32-6bt	0.4	37.97	2.032	15.29	14.532	0.07	13.43	0.019	0.006	9.183	0.108	0.03	531
cx32-6bt	0.4	37.86	2.017	15.737	14.631	0.093	13.42	0.003	0.024	9.237	0.101	0.036	531
cx32-6bt	0.4	37.83	2.076	15.424	14.95	0.061	13.56	0.023	0.031	9.186	0.128	0.044	529
cx6A-1bt	0.4	38.3	1.765	17.701	17.931	0.083	10.85	0	0.142	9.229	0.028	0	535
cx6A-1bt	0.4	37.81	1.782	17.791	17.786	0.077	10.85	0.014	0.186	9.219	0.023	0	537
cx6A-1bt	0.4	37.84	1.842	17.944	17.9	0.082	10.55	0.029	0.182	9.043	0.021	0	546
cx6A-1bt	0.4	37.28	1.816	17.351	17.842	0.071	10.72	0.027	0.143	8.938	0.014	0.006	538
cx6A-1bt	0.4	38.02	1.735	17.549	17.744	0.069	10.83	0.009	0.138	9.215	0.034	0.02	533
cx6A-2bt	0.4	37.32	1.89	17.31	17.759	0.095	10.7	0.007	0.177	9.328	0.009	0	543
cx6A-2bt	0.4	37.41	1.794	17.122	18.144	0.057	10.91	0.014	0.139	9.384	0.015	0.019	531
cx6A-2bt	0.4	37.24	1.803	17.281	18.263	0.087	10.73	0	0.142	9.328	0.003	0.011	534
cx6A-2bt	0.4	37.08	1.804	17.315	17.892	0.05	10.9	0.001	0.173	9.363	0.01	0.005	533
cx6A-2bt	0.4	37.47	1.807	17.64	18.209	0.073	10.85	0.034	0.169	9.301	0.032	0	535
cx6A-2bt	0.4	37.1	1.757	17.681	17.552	0.045	10.72	0.033	0.171	9.357	0	0	536
cx6A-3bt	0.4	38.03	1.728	17.287	17.381	0.068	10.83	0.052	0.169	9.002	0.019	0.011	534
cx6A-3bt	0.4	37.99	1.778	17.153	17.465	0.088	10.97	0.044	0.17	9.112	0.021	0	534
cx6A-3bt	0.4	38.19	1.645	17.027	17.204	0.066	11.03	0.111	0.112	9.215	0.007	0.013	525
cx6A-3bt	0.4	36.28	1.502	16.362	17.089	0.086	10.62	0.022	0.138	9.021	0.044	0	514
cx6A-3bt	0.4	37.24	1.667	17.675	17.639	0.067	10.98	0.011	0.116	9.381	0.015	0	526
cx6A-4bt	0.4	37.92	1.823	17.215	17.963	0.092	10.92	0.055	0.152	9.013	0.016	0	536

cx6A-4bt	0.4	37.36	1.818	17.13	17.929	0.059	10.64	0.008	0.185	8.976	0.029	0	538
cx6A-4bt	0.4	38.02	1.773	17.251	17.965	0.069	10.61	0.008	0.143	9.228	0.028	0	537
cx6A-4bt	0.4	37.49	1.901	17.239	18.333	0.07	10.65	0.007	0.166	9.302	0.034	0.017	542
cx6A-4bt	0.4	36.98	1.644	17.442	17.958	0.06	10.89	0.023	0.152	9.466	0.024	0.011	522
cx6A-5bt	0.4	36.99	1.763	17.666	18.003	0.064	10.74	0.048	0.197	9.295	0.008	0.007	533
cx6A-5bt	0.4	37.55	1.87	17.334	17.967	0.059	10.92	0.087	0.148	9.287	0.019	0	538
cx6A-5bt	0.4	37.69	1.807	17.246	18.024	0.044	10.93	0.087	0.129	9.282	0	0	533
cx6A-5bt	0.4	37.82	1.882	17.549	17.938	0.074	10.74	0.041	0.122	9.332	0.001	0	543
cx6A-5bt	0.4	37.84	1.739	17.356	17.723	0.054	10.99	0.055	0.149	9.008	0.011	0.049	530
cx6A-6bt	0.4	37.69	1.735	17.496	17.899	0.06	10.72	0.021	0.182	9.112	0.006	0.015	533
cx6A-6bt	0.4	38.56	1.788	17.571	17.692	0.041	10.59	0.028	0.185	8.971	0.001	0.038	543
cx6A-6bt	0.4	37.4	1.82	17.632	17.95	0.046	10.83	0.066	0.123	9.154	0.017	0	537
cx6A-6bt	0.4	37.68	1.689	17.799	17.4	0.052	10.63	0.019	0.177	9.33	0.023	0.011	535
cx6A-6bt	0.4	37.19	1.813	17.422	17.971	0.078	10.88	0.003	0.138	9.334	0.042	0.022	534
cx6A-6bt	0.4	37.48	1.699	17.226	17.793	0.068	10.98	0.12	0.129	9.175	0.023	0	526

cx9A-2bt	0.4	36.71	3.256	16.166	22.187	0.394	6.542	0.115	0.03	9.494	0.024	0	690
cx9A-2bt	0.4	36.24	3.225	16.411	22.526	0.395	6.511	0.07	0.085	9.477	0.02	0.013	688
cx9A-2bt	0.4	36.2	3.319	16.197	22.73	0.398	6.544	0.042	0.065	9.387	0.024	0	689
cx9A-2bt	0.4	36.68	3.237	16.345	23.048	0.395	6.825	0.05	0.056	9.579	0.024	0.005	676
cx9A-2bt	0.4	36.46	3.378	16.289	23.057	0.386	6.672	0.067	0.053	9.647	0	0.002	687
cx9A-1bt	0.4	36.16	3.399	16.301	22.749	0.413	6.524	0.06	0.029	9.486	0	0	694
cx9A-1bt	0.4	36.41	3.327	16.502	22.551	0.371	6.503	0.022	0.064	9.52	0.01	0.001	694
cx9A-1bt	0.4	36.78	3.143	16.151	22.664	0.393	6.669	0.057	0.061	9.348	0.015	0	678
cx9A-1bt	0.4	37.27	3.22	17.085	21.525	0.369	7.08	0.041	0.05	9.584	0.028	0.022	679

cx9A-4bt	0.4	36.78	3	16.414	22.813	0.387	6.91	0.142	0.057	9.568	0.018	0.008	662
cx9A-4bt	0.4	36.83	3.202	16.594	22.934	0.396	6.572	0.121	0.063	9.513	0.013	0	685
cx9A-4bt	0.4	37.19	3.01	16.439	22.624	0.397	6.887	0.081	0.054	9.506	0	0.012	666
cx9A-4bt	0.4	37.26	3.262	16.261	22.198	0.415	7.107	0.088	0.029	9.338	0	0.028	673
cx9A-4bt	0.4	37.03	3.29	16.482	22.343	0.382	6.894	0.078	0.052	9.461	0	0.043	681
cx9A-4bt	0.4	36.89	3.15	16.205	22.572	0.382	7.2	0.072	0.055	9.53	0.007	0.008	661
cx9A-3bt	0.4	36.87	3.355	16.611	22.127	0.402	6.708	0.094	0.098	9.405	0.011	0.026	692
cx9A-3bt	0.4	36.71	3.365	16.301	22.078	0.404	6.871	0.105	0.081	9.546	0.005	0.011	684
cx9A-3bt	0.4	36.29	3.384	16.045	22.377	0.398	6.666	0.096	0.122	9.551	0.026	0.051	688
cx9A-3bt	0.4	35.88	3.248	15.874	22.24	0.41	6.764	0.079	0.083	9.415	0.049	0.011	677
cx9A-5bt	0.4	35.81	2.962	16.794	22.613	0.439	7.115	0.088	0.029	9.443	0	0.012	654
cx9A-5bt	0.4	36.04	3.111	16.764	22.637	0.397	7.023	0.127	0.067	9.396	0.019	0.031	665
cx9A-5bt	0.4	36.32	2.947	16.596	22.737	0.389	7.054	0.107	0.051	9.485	0	0.022	655
cx9A-5bt	0.4	36.48	3.38	16.216	22.972	0.417	7.176	0.081	0.056	9.576	0	0.012	670
cx9A-5bt	0.4	36.46	3.173	16.928	22.117	0.399	7.033	0.056	0.04	9.616	0.012	0.026	672
cx9A-5bt	0.4	36.22	2.965	16.751	22.263	0.385	7.131	0.063	0.055	9.414	0.001	0	657
cx9A-6bt	0.4	35.58	3.068	16.435	22.819	0.377	7.001	0.113	0.056	9.141	0.017	0.02	661
cx9A-6bt	0.4	35.92	2.801	16.884	22.305	0.404	7.058	0.075	0.056	9.399	0.013	0	650
cx9A-6bt	0.4	32.83	3.044	16.224	21.582	0.379	6.412	0.091	0.053	9.069	0.011	0	676
cx9A-6bt	0.4	33.56	3.097	16.618	21.931	0.381	6.686	0.07	0.072	9.228	0.019	0.021	672
cx9A-6bt	0.4	29.93	3.002	15.904	22.074	0.406	6.367	0.088	0.132	8.966	0.014	0.027	663
cx16-9bt	0.4	38.79	1.592	16.222	15.444	0.04	13.14	0.053	0.071	8.989	0	0.034	504
cx16-9bt	0.4	38.38	1.564	16.237	15.503	0.048	12.93	0.149	0.104	9.019	0	0.006	503
cx16-9bt	0.4	37.83	1.579	16.593	15.542	0.052	12.86	0.08	0.081	9.004	0	0.013	505

cx16-9bt	0.4	37.77	1.622	16.385	15.726	0.038	12.84	0.05	0.061	8.967	0.002	0.03	507
cx16-9bt	0.4	38.35	1.668	16.382	15.49	0.046	13.15	0.041	0.081	8.993	0.023	0.025	509
cx16-8bt	0.4	39.35	1.618	16.084	15.526	0.02	12.7	0.041	0.074	8.978	0.017	0.028	511
cx16-8bt	0.4	39.41	1.656	15.981	15.544	0.025	12.91	0.053	0.082	9.096	0	0.007	511
cx16-8bt	0.4	39.29	1.617	15.977	15.767	0.037	13.1	0.04	0.046	9.088	0.017	0.035	505
cx16-8bt	0.4	39.27	1.608	16.165	15.802	0.046	12.84	0.045	0.079	9.097	0	0.035	507
cx16-8bt	0.4	39.46	1.658	15.86	15.872	0.022	12.77	0.045	0.049	9.046	0.014	0	511
cx16-8bt	0.4	39.38	1.563	16.374	15.821	0.02	12.74	0.034	0.054	9.091	0.002	0	506
cx16-5bt	0.4	38.44	1.582	16.355	15.503	0.039	12.85	0.045	0.089	9.016	0.04	0.034	506
cx16-5bt	0.4	38.62	1.559	16.094	15.32	0.045	12.66	0.094	0.149	8.987	0.019	0	507
cx16-5bt	0.4	38.92	1.578	16.192	15.58	0.009	12.75	0.073	0.078	8.921	0.013	0.007	507
cx16-5bt	0.4	38.44	1.558	16.079	15.659	0.032	12.68	0.078	0.074	8.972	0.009	0.02	504
cx16-5bt	0.4	38.24	1.705	16.266	15.724	0.036	12.81	0.04	0.058	9.193	0.024	0.033	513
cx16-7bt	0.4	39.22	1.719	16.333	15.704	0.034	13.1	0.011	0.043	9.004	0.005	0.004	514
cx16-7bt	0.4	39.33	1.766	16.374	15.906	0	13.03	0.028	0.055	8.933	0.033	0.009	517
cx16-7bt	0.4	38.77	1.615	16.403	15.714	0.039	12.86	0.024	0.097	9.019	0.016	0	508
cx16-7bt	0.4	38.37	1.647	16.336	15.761	0.009	12.7	0.023	0.063	9.102	0	0.023	511
cx16-6bt	0.4	38.83	1.664	16.262	15.741	0	12.87	0.027	0.037	9.018	0.016	0.01	511
cx16-6bt	0.4	38.52	1.717	16.215	15.762	0.035	12.68	0.088	0.068	8.98	0.037	0.011	516
cx16-6bt	0.4	38.49	1.586	16.098	15.77	0.051	12.81	0.117	0.054	8.959	0	0	504
cx16-6bt	0.4	38.14	1.79	16.364	15.963	0.039	12.59	0.042	0.055	8.999	0.005	0.042	520
cx16-6bt	0.4	37.53	1.51	16.367	15.798	0.015	12.53	0.083	0.068	9.075	0.027	0	501
cx16-6bt	0.4	37.24	1.615	16.275	15.519	0.014	12.37	0.05	0.05	8.954	0.008	0	512
cx16-6bt	0.4	36.86	1.616	16.145	15.746	0	12.62	0.038	0.065	9.066	0	0.003	506
cx16-1bt	0.4	38.35	1.557	16.102	16.169	0.022	12.74	0.077	0.059	8.893	0	0	501

cx16-1bt	0.4	38.79	1.684	15.79	15.739	0.047	12.91	0.069	0.048	8.947	0.008	0.008	510
cx16-1bt	0.4	39.15	1.762	15.947	15.171	0.036	12.58	0.054	0.057	8.921	0.032	0.031	524
cx16-4bt	0.4	38.45	1.643	16.382	15.786	0.022	13.02	0.009	0.079	9.121	0.036	0.012	507
cx16-4bt	0.4	38.62	1.638	16.454	15.769	0.041	12.91	0.015	0.069	9.157	0	0.009	509
cx16-4bt	0.4	38.62	1.57	16.284	15.855	0.023	12.84	0.002	0.098	9.126	0	0.002	503
cx16-4bt	0.4	38.67	1.741	16.111	15.901	0.018	12.85	0.01	0.038	9.109	0.022	0	515
cx16-3bt	0.4	39.33	1.684	16.232	15.556	0.015	12.8	0.004	0.058	8.889	0.015	0.018	516
cx16-3bt	0.4	39.66	1.585	16.174	15.579	0.021	12.8	0.037	0.077	8.849	0.028	0	509
cx16-3bt	0.4	39.14	2.075	16.088	15.508	0.008	12.62	0.012	0.108	8.952	0.007	0.005	542
cx16-3bt	0.4	38.69	1.607	16.341	15.639	0.018	12.74	0.024	0.043	9.242	0.049	0	509
cx16-2bt	0.4	39.1	1.528	15.991	15.654	0.026	12.82	0	0.075	8.838	0.027	0.052	502
cx16-2bt	0.4	38.78	1.578	16.232	15.43	0.021	12.52	0	0.058	9.01	0.041	0.025	510
cx16-2bt	0.4	38.76	1.628	16.082	15.366	0.004	12.74	0	0.053	9.043	0.047	0.018	511
cx16-2bt	0.4	39.29	1.592	15.855	15.022	0.037	12.76	0.004	0.046	8.879	0	0.026	511

cx8A-3bt	0.4	37.78	1.975	17.491	18.334	0.082	10.64	0	0.147	9.082	0.041	0.003	549
cx8A-3bt	0.4	37.68	1.924	17.717	18.236	0.088	10.66	0	0.159	9.499	0.019	0	546
cx8A-3bt	0.4	37.81	2.069	17.676	18.02	0.08	10.55	0	0.184	9.105	0.051	0.047	558
cx8A-3bt	0.4	37.74	2.011	17.718	17.87	0.067	10.55	0.004	0.185	9.154	0.046	0	556
cx8A-3bt	0.4	37.89	2.067	17.48	18.317	0.087	10.45	0.045	0.184	9.205	0.005	0.036	557
cx8A-4bt	0.4	38.13	2.036	17.51	18.202	0.114	10.34	0.022	0.189	8.991	0.028	0.015	559
cx8A-4bt	0.4	37.63	2.083	17.614	18.068	0.087	10.63	0	0.193	9.127	0.014	0.004	557
cx8A-4bt	0.4	38.02	2.03	17.678	17.972	0.065	10.33	0.015	0.18	9.187	0.014	0.004	560
cx8A-4bt	0.4	37.24	2.111	17.613	18.18	0.099	10.52	0	0.132	9.301	0.019	0.004	559
cx8A-5bt	0.4	37.18	1.964	17.921	18.152	0.107	10.64	0	0.215	9.197	0.051	0.015	549

cx8A-5bt	0.4	37.34	1.975	17.667	18.197	0.101	10.63	0.024	0.169	9.124	0.01	0	549
cx8A-5bt	0.4	37.75	2.019	17.718	17.884	0.099	10.5	0.064	0.175	9.006	0.04	0	557
cx8A-5bt	0.4	38.28	1.953	17.517	17.556	0.095	10.42	0.062	0.206	8.991	0.019	0	556
cx8A-1bt	0.4	38.71	1.853	17.208	18.009	0.088	10.41	0.08	0.081	9.186	0.03	0.027	547
cx8A-1bt	0.4	37.36	1.923	17.768	18.406	0.082	10.54	0.047	0.141	9.227	0	0.017	547
cx8A-1bt	0.4	38.66	1.916	17.457	17.899	0.094	10.31	0.037	0.128	9.295	0.036	0.005	554
cx8A-1bt	0.4	37.35	1.71	17.899	17.699	0.09	10.99	0.046	0.149	8.824	0.073	0.036	530
cx8A-1bt	0.4	37.75	1.81	17.605	17.948	0.08	10.82	0.08	0.154	9.112	0.046	0.025	537
cx8A-2bt	0.4	36.98	1.715	17.785	18.088	0.128	10.52	0.205	0.166	9.113	0.042	0.02	533
cx8A-2bt	0.4	36.91	1.825	17.51	18.18	0.101	10.83	0.139	0.162	8.993	0.012	0	535
cx8A-2bt	0.4	37.73	1.827	17.545	18.068	0.088	10.76	0.184	0.175	9.268	0.017	0	538
cx8A-2bt	0.4	37.3	1.776	17.752	17.909	0.105	10.81	0.129	0.172	9.26	0.01	0	535
cx8A-2bt	0.4	37.31	1.814	17.999	17.99	0.099	10.58	0.191	0.192	9.181	0.071	0	541
cx8A-6bt	0.4	37.96	1.768	17.027	17.309	0.069	10.24	0.118	0.251	9.097	0.006	0	545
cx8A-6bt	0.4	35.81	1.879	16.993	17.945	0.075	10.7	0.233	0.195	9.052	0.045	0	536
cx8A-6bt	0.4	37.32	1.904	17.812	17.538	0.052	10.67	0.134	0.182	9.292	0.03	0.017	548
cx8A-6bt	0.4	36.06	1.938	17.803	17.081	0.086	9.918	0.069	0.166	9.254	0	0.003	562

Chemical compositions of muscovite

Sample	Input P (GPa)	SiO_2	TiO_2	Al_2O_3	FeO(tot)	MnO	MgO	CaO	Na_2O	K_2O	Cr_2O_3	NiO	T (ºC)
cx7-5ms	0.4	48.79	0.365	34.355	1.261	0	1.16	0.216	0.935	9.432	0.007	0	511
cx7-5ms	0.4	48.97	0.409	34.849	1.173	0.005	1.001	0.224	0.952	9.502	0.021	0	526
cx7-5ms	0.4	48.25	0.431	35.172	1.133	0.015	0.863	0.238	1.037	9.42	0.025	0	532

cx7-5ms	0.4	48.11	0.383	34.124	1.208	0	1.109	0.313	0.987	9.537	0.011	0.004	520
cx7-5ms	0.4	46.95	0.344	33.14	1.256	0.031	1.038	0.204	0.853	9.64	0.044	0.013	505
cx7-5ms	0.4	45.99	0.391	32.821	1.306	0.007	1.048	0.163	0.827	9.8	0	0	526
cx7-5ms	0.4	46.74	0.429	33.131	1.23	0.017	1.012	0.057	0.878	9.72	0.02	0	539
cx7-5ms	0.4	46.69	0.246	34.496	1.118	0.016	0.713	0.024	0.992	9.607	0.023	0.009	453
cx7-6ms	0.4	47.52	0.528	34.412	1.116	0.009	0.885	0.173	0.984	9.306	0.044	0	568
cx7-6ms	0.4	48.03	0.726	34.056	1.151	0.008	1.022	0.127	0.928	9.241	0.025	0.006	625
cx7-6ms	0.4	47.68	0.421	33.617	1.165	0.018	1.12	0.105	0.926	9.337	0.026	0.029	537
cx7-6ms	0.4	48.41	0.421	34.137	1.12	0.006	1.092	0.211	0.925	9.324	0.014	0	535
cx7-6ms	0.4	47.29	0.407	34.682	1.028	0	0.878	0.075	0.963	9.318	0.058	0	529
cx7-8ms	0.4	48.01	0.35	34.032	0.906	0	0.793	0.122	0.918	9.231	0.021	0.002	507
cx7-8ms	0.4	48.31	0.41	33.425	1.248	0	1.142	0.014	0.831	9.474	0.018	0.005	531
cx7-8ms	0.4	47.9	0.399	33.601	1.148	0.007	0.92	0.025	0.911	9.402	0.013	0	525
cx7-8ms	0.4	46.87	0.389	34.314	1.186	0	0.88	0.038	0.913	9.446	0.034	0	520
cx7-7ms	0.4	48.25	0.344	33.7	1.296	0.003	1.085	0.022	0.889	9.483	0.024	0	503
cx7-7ms	0.4	48.32	0.382	33.84	1.289	0	0.949	0.027	0.928	9.515	0.024	0.003	515
cx7-7ms	0.4	47.98	0.384	34.559	1.371	0.002	0.887	0.031	0.976	9.385	0.024	0.014	513
cx7-7ms	0.4	47.75	0.381	33.692	1.487	0	1.148	0	0.869	9.763	0.01	0	517
cx7-7ms	0.4	48.53	0.389	33.585	1.256	0.005	1.049	0.155	0.888	9.579	0.014	0.009	520
cx7-9ms	0.4	47.81	0.389	33.684	1.243	0	1.084	0.003	0.922	9.568	0.03	0.02	522
cx7-9ms	0.4	49.68	0.364	33.138	1.203	0	1.057	0.125	0.895	9.325	0.026	0.015	510
cx7-9ms	0.4	47.93	0.354	34.373	1.095	0	0.825	0.068	0.916	9.382	0.037	0	505
cx7-9ms	0.4	48.84	0.37	33.508	1.165	0	0.971	0.267	0.882	9.48	0.033	0.014	513
cx7-9ms	0.4	47.63	0.344	33.496	1.131	0.017	0.851	0.134	0.89	9.462	0.021	0.028	502
cx7-9ms	0.4	47.87	0.327	32.856	1.469	0	1.233	0.14	0.824	9.552	0.01	0.007	497

cx7-9ms	0.4	47.73	0.373	33.278	1.18	0	0.991	0.108	0.909	9.48	0.003	0	516
cx7-9ms	0.4	48.16	0.381	33.703	1.188	0	1.048	0.1	0.71	8.865	0	0	520

Appendix table 3.2 Zircon SHRIMP U-Pb dating of the Mupi granite

Sample/	[Pb]	[U]	[Th]	Th/U	$^{207}Pb/^{206}Pb$ Age	±σ Age	$^{207}Pb/^{235}U$ Age	±σ Age	$^{206}Pb/^{238}U$ Age	±σ Age	207-corr Age	±σ Age
CX48@1	60	1489	516	0.346	230.2	20.0	219.2	3.5	218.2	3.3	218.1	3.3
CX48@02	18	412	292	0.708	237.2	38.4	217.9	4.4	216.1	3.2	216.0	3.2
续表 3.2												
CX48@03	46	1163	355	0.305	229.8	20.6	216.7	3.4	215.5	3.2	215.4	3.2
CX48@04	37	954	261	0.274	224.0	23.4	218.4	3.6	217.9	3.2	217.9	3.3
CX48@05	20	115	137	1.194	746.9	30.1	733.8	10.9	729.5	10.4	729.0	10.7
CX48@06	35	919	206	0.224	188.9	29.6	215.2	3.8	217.6	3.2	217.8	3.2
CX48@07	24	566	289	0.510	207.0	35.2	215.7	4.2	216.5	3.2	216.6	3.2
CX48@08	20	89	169	1.896	790.2	30.5	808.7	11.9	815.4	11.8	816.2	12.2
CX48@09	32	765	235	0.307	256.7	32.3	232.5	4.3	230.1	3.4	229.9	3.4
CX48@10	51	1252	416	0.332	244.0	24.5	224.5	3.7	222.7	3.3	222.6	3.3
CX48@11	47	1031	220	0.213	368.5	29.6	258.4	4.6	246.4	3.7	245.6	3.7
CX48@12	53	1277	577	0.452	205.6	33.1	218.5	4.1	219.7	3.2	219.7	3.3
CX48@13	42	1075	277	0.258	208.9	21.9	218.6	3.5	219.6	3.3	219.6	3.3
CX48@14	65	1560	829	0.532	296.6	17.7	221.8	3.4	214.8	3.2	214.3	3.2
CX48@15	32	172	180	1.046	799.8	22.8	806.1	10.4	808.3	11.5	808.6	11.9

CX48@16	37	945	260	0.275	252.9	31.0	221.2	4.0	218.3	3.2	218.1	3.2
CX48@17	45	1136	300	0.264	221.0	47.9	220.7	5.2	220.7	3.3	220.6	3.4
CX48@18	51	1277	311	0.244	156.3	46.6	216.9	5.0	222.5	3.4	222.9	3.4
CX48@19	51	1275	289	0.227	249.4	46.7	224.8	5.2	222.5	3.3	222.3	3.4
CX48@20	106	175	110	0.631	2473.9	16.1	2438.4	17.0	2396.0	31.1	>1200	
CX48@21	51	1297	265	0.204	327.8	46.2	229.7	5.3	220.2	3.3	219.5	3.3
CX48@22	26	155	249	1.606	765.0	77.6	638.6	19.5	603.5	8.7	599.9	9.0
CX48@23	47	1183	304	0.257	311.2	47.3	226.5	5.3	218.4	3.3	217.8	3.3

Appendix table 4.1 Measurements of anisotropy magnetic susceptibility and microscopic observation

点号	经纬度		n	Km	P_j	T	K_1				K_3				变形级别
	Latitude(ºN)	Longitude(ºE)		10^{-6}SI			Dec(º)	Inc(º)	α_{95max}	α_{95min}	Dec(º)	Inc(º)	α_{95max}	α_{95min}	
LM01	31.278	103.472	5	103	1.046	-0.16	317	70.8	15.8	2.7	142	19.2	4.7	1.5	中等变形
LM02	31.260	103.482	6	11000	1.201	0.047	259.3	67.9	8.9	4.3	161.6	3.1	9.9	8.0	中等变形
LM03	31.275	103.474	10	479	1.04	-0.067	336.6	70.8	7.1	4.3	136.6	18.1	8.6	6.5	中等变形
LM04	31.373	103.510	6	208	1.115	-0.136	213.3	72.5	10.7	4.3	100.9	6.8	15.0	4.0	强变形
LM05	31.403	103.527	7	468	1.015	0.076	153.6	71.2	11.3	5.3	257.2	4.5	6.7	2.8	
LM06	31.182	103.495	7	240	1.066	0.344	19.9	60.7	5.7	5.2	137.5	14.5	13.4	3.3	
LM07	31.153	103.486	6	**138000**	1.378	0.463	67.9	4.7	10.8	3.2	202.5	83.4	5.4	2.7	岩浆组构
LM08	31.073	103.487	5	608	1.196	-0.09	274.3	26.8	6.7	3.5	169.4	27	8.5	4.0	弱变形
LM09	31.092	103.485	5	679	1.043	0.116	40.7	51.2	8.7	2.0	281.5	21.5	6.6	1.4	岩浆组构

LM10	31.111	103.481	5	326	1.032	-0.109	283	22.7	10.8	3.8	16.9	9.3	27.5	5.3	
LM11	31.073	103.458	7	421	1.008	-0.132	86.2	74	8.5	6.5	288.8	14.9	18.0	6.6	
LM12	31.077	103.435	9	498	1.078	0.423	259.6	31.1	20.9	6.9	152.9	25.5	8.5	5.1	弱变形
LM13	31.061	103.410	8	**58400**	1.19	-0.03	91.5	85	7.1	3.3	195.9	1.2	9.2	3.3	岩浆组构
LM14	31.063	103.386	8	404	1.116	0.476	49.5	46.7	13.3	3.0	173.9	29.5	12.5	3.8	弱变形
LM15	31.066	103.369	7	443	1.042	0.039	52	19.7	9.4	4.5	179.4	59.5	10.2	6.5	
LM16	31.059	103.347	9	336	1.055	0.127	290.8	37.9	20.0	9.1	183.6	20.9	14.2	5.7	强变形
LM17	31.072	103.324	7	223	1.067	-0.327	344.6	56.6	10.8	1.7	132.2	29.2	12.7	3.4	
LM18	31.097	103.563	5	68	1.028	0.451	358.7	3.1	16.3	8.8	267.9	14.8	9.2	6.9	弱变形
LM19	31.142	103.578	5	466	1.066	-0.012	63.3	69.3	6.7	2.5	177.3	8.8	13.3	3.8	
LM20	31.118	103.558	5	21100	1.022	-0.201	338.3	36.8	33.8	0.3	133.5	50.5	16.7	1.1	岩浆组构
LM21	31.193	103.653	8	796	1.025	-0.106	294.6	28.7	6.8	5.5	167.9	47.6	57.1	5.8	
LM22	31.208	103.640	5	1020	1.038	-0.025	299.3	62.8	17.5	4.5	109.8	26.9	27.3	11.7	弱变形
LM23	31.215	103.643	10	1320	1.06	-0.378	69.2	34.6	15.6	10.1	308.8	36.2	50.5	14.8	
LM24	31.180	103.658	10	2330	1.058	0.301	333.3	12.3	32.7	10.7	81.3	54.9	49.4	8.4	
LM25	31.344	103.880	10	737	1.073	-0.081	246.1	61	13.8	7.3	101.9	24.2	9.5	6.2	弱变形
LM26	31.410	103.537	9	448	1.052	0.105	225.7	76	15.2	5.2	327.4	2.9	11.5	4.5	
LM27	31.395	103.549	5	325	1.047	0.274	21.1	61.1	24.1	2.2	280.3	5.9	19.2	4.6	
LM28	31.379	103.559	8	974	1.052	0.451	282.3	17.6	12.6	6.7	23.3	31.1	12.3	6.5	
LM29	31.429	103.574	5	30	1.053	0.145	36.2	75.9	16.6	4.2	143.7	4.3	9.5	3.9	弱变形
LM30	31.413	103.588	6	1250	1.023	0.167	237.2	46.9	36.3	10.0	30.5	39.9	32.1	6.2	
LM31	31.399	103.603	5	7720	1.058	-0.198	51.1	68.7	14.1	7.1	176.9	12.9	29.9	7.1	
LM32	31.308	103.527	5	24100	1.044	0.08	219.3	60.1	12.0	8.1	124.5	2.8	14.6	7.9	
LM33	31.291	103.525	8	4130	1.059	-0.437	332.1	74.3	10.9	6.1	157.2	15.6	64.2	8.1	
LM34	31.272	103.525	5	89	1.04	-0.378	321.1	78.5	25.1	2.3	86.6	6.7	18.0	6.2	

LM35	31.271	103.521	7	3540	1.118	0.153	283.6	79.6	7.8	3.9	166.8	4.8	7.4	1.4	Moderate
LM36	31.264	103.504	6	145	1.072	-0.276	296.7	64.7	15.4	6.7	169.3	16	12.5	6.7	

Appendix table 4.2 Micas $^{40}Ar/^{39}Ar$ step heating results

Temp. (℃)	$^{40}Ar/^{39}Ar$	$^{37}Ar/^{39}Ar$	$^{36}Ar/^{39}Ar$	$^{40}Ar^*/^{39}Ar_k$	$^{40}Ar^*$ (%)	$^{39}Ar_k$ (%)	Age Ma	2σ Ma
CX12	**Muscovite**		**J = 0.0051030 0.0000127**					
550 ℃	6.73597	0.04926	0.00165	6.248673	92.77	1.69	56.76	2.29
600 ℃	7.49569	0.00943	0.00043	7.368774	98.31	7.67	66.75	0.95
640 ℃	8.16821	0.00748	0.00031	8.075419	98.86	9.18	73.02	0.87
680 ℃	9.05993	0.00622	0.00022	8.994102	99.27	12.79	81.15	0.88
720 ℃	10.32311	0.00490	0.00024	10.250465	99.30	14.77	92.20	1.02
760 ℃	11.40751	0.00411	0.00023	11.339405	99.40	17.62	101.72	1.07
800 ℃	12.11562	0.00701	0.00034	12.015472	99.17	11.86	107.61	1.13
860 ℃	12.76397	0.01563	0.00037	12.653956	99.14	4.40	113.15	1.33
920 ℃	12.16340	0.00703	0.00043	12.036533	98.96	10.30	107.79	1.13
980 ℃	13.22234	0.00766	0.00052	13.069387	98.84	8.03	116.75	1.38
1040 ℃	15.05591	0.04266	0.00236	14.359161	95.37	1.70	127.87	5.59
CX33	**Muscovite**		**J = 0.0050970 0.0000127**					
550 ℃	16.63693	0.07714	0.00845	14.140233	84.99	1.47	125.85	3.14

620 ℃	16.41009	0.01464	0.00223	15.749784	95.98	7.41	139.63	1.53
670 ℃	15.80785	0.00955	0.00072	15.596131	98.66	11.36	138.32	1.44
720 ℃	15.85828	0.00689	0.00046	15.722224	99.14	14.45	139.40	1.46
770 ℃	16.69821	0.00492	0.00035	16.595155	99.38	20.22	146.83	1.69
810 ℃	16.89711	0.00686	0.00033	16.798076	99.41	15.17	148.56	1.50
850 ℃	16.93453	0.00943	0.00068	16.734147	98.82	10.07	148.01	1.60
890 ℃	16.98031	0.01001	0.00088	16.719430	98.46	8.13	147.89	1.88
930 ℃	17.48967	0.01464	0.00174	16.975290	97.06	5.56	150.06	1.84
1000 ℃	19.50428	0.02307	0.00353	18.461742	94.65	3.92	162.63	1.89
1300 ℃	36.51985	0.03603	0.00949	33.715529	92.32	2.26	286.77	59.38

Acknowlegement

“少儿学，然后吾亲”，这句话用来形容我此时此刻的心情再贴切不过，从初中开始，整整 19 年我没有陪在父母身边，我已记不清他们头发乌黑的模样。现在我的学生时代终于要画上句号，感觉人生仿佛按了快进按钮，我一夜间完成了为人子向为人夫的转变，而父母还是那样的父母，唯一变化的是头上越结越厚的霜。爸爸妈妈，谢谢你们含辛茹苦养育我、无微不至照顾我，于岁月无声处陪伴我，往后的生活中，我身上哪怕有一丝优秀的品德，那都是你们给我的馈赠，作为父母亲，你们很棒，谢谢你们！

2011 年，我以无比激动的心情踏入中国科学院地质与地球物理研究所，从此有个新的头衔，自我介绍的时候都说，我是薛振华，是林伟老师的学生。6 年的时间里，提到我的老师，我身边的人都说“林老师构造做的真棒！”“林老师人真的很不错”，然而事实远不止于此。有时候老师为我们的事情夜不能寐，有人劝他说“这些学生又不是你的孩子，你干嘛这么玩命上心”，我不记得他是怎样回答，只知道他仍然一如既向地为我们操心。6 年的时间里，我从最开始被老师训哭，到后来有点抵触，到后来每次和老师交流都能学到好多东西，到现在我甚至开始怀念与老师交流的日子。师母经常劝老师批评我们的时候不要太直白，但我现在打心底里喜欢这样的直截了当、并心怀感激。以后的日子，可能再也不会碰到这样的老师，在学习上对我谆谆教诲，在我受挫折的时候加油鼓劲，在我犯错的时候耳提面命。林老师，“为人师表、言传身教、传道解惑”短短十二个字，您在我 6 年求学生涯里作了完美的诠释。作为您的学生，人生之幸，谢谢您！

2015 年底，我与谢梦女士结为夫妻，欣喜地步入已婚人士行列，明白钱老先生的“围城爱情论”并非放之四海皆准，明白博士不单只有学习，还有风花雪月的浪漫。谢梦，你的温文尔雅、兰质蕙心常让我如获至宝，就连偶尔的任性无赖都那么可爱，谢谢你这些年来的相伴相守、鼎力支持，我会铭记于心。

在法国求学期间，感谢奥尔良大学陈岩教授、Michel 教授对我学习上悉心的指导和生活上的帮助。两位导师严谨的治学风范、一丝不苟的工作态度、渊博的学识让我受益匪浅。每一次的论文修改，两位导师都会在文稿上挂满红灯，那是我论文提升和进步的基石，也是我一步步进步的见证。谢谢两位导师在异国他乡给予我的帮忙和照顾，让我始终感受到家的温暖。感谢法国地调局 Guillaume 教授对我专业知上的指导和帮助，他的乐观豁达、毫无保留在我心中给法国的老师们画上厚重的一笔。

感谢课题组王清晨老师在我攻读学位期间的鼎力支持，王老师的学识、豁达、豪爽、可亲，让我获益匪浅。

感谢课题组李金雁师傅，带着我这些年走南闯北。牛顿是站在巨人的肩膀上看世界，而我是坐在李师傅的车上学地质，他娴熟的车技保证了我的野外高效、安全完成，更多时候他用毕生阅历给我的生活参考建议，让我在生活上不那么迷茫。李师傅，谢谢您！

感谢所有的师兄们，感谢褚杨、陈科、陶辉飞、冀文斌、卫巍、王军、陈泽超、刘飞、王镇远、徐建强、姜林、邱振，谢谢你们在生活、学习中的指导和帮忙；感谢所有的师弟们，感谢黎乐、孙萍、邱华标、孟令通、任志恒、曾继培在生活中的陪伴和帮助，谢谢你们。感谢刘洪升、黄芳芳、黄旭栋、陈进宇、朱鑫、向路、方婷、陆昀乔、马莹莹在法留学期间的陪伴和帮助，让我在异国他乡也有个温暖的大家庭。感谢室友杨磊、刘军港、丁阔、何万通六年的陪伴，感谢同班同学对我的关心和帮助。

感谢所里的老师为我们创造了良好的科研环境，感谢教育处和图书馆老师为我们提供了良好的生活条件和学习环境。

以前觉得现在社会博士很多很多，没什么了不起的，现在我终于快要成为 Dr. XUE 了，我觉得博士还是了不起的，博士求学的六年时间，将是我人生中最值得纪念和铭记的阶段之一。

谨以此论文献给我所有的亲人、师长、朋友、同学和所有帮助我关心我的人！

作者：薛振华

Xue Zhenhua

L'évolution tectonique du Mésozoïque de la ceinture orogénique de Longmenshan, l'Est du Tibet

La ceinture orogénique de Longmenshan (LMTB) constitue la frontière orientale du plateau tibétain, qui est reconnue par sa topographie escarpée, son activité tectonique intensive ainsi ses la complexité de ses structures. Comme une orogène typique, le LMTB a subi une forte déformation intracontinentale au cours du Mésozoïque. Ainsi, la connaissance sur l'évolution tectonique du Mésozoïque de la LMTB est cruciale pour comprendre l'orogenèse intracontinentale et la surrection du plateau tibétain.

Une ceinture de clivage verticaux divise la LMTB en une zone occidentale et une orientale. La Zone orientale présente un top-to-SE cisaillement tandis que la zone occidentale présente un top-to-NW cisaillement. La zone orientale peut être subdivisée en quatre sous-unités avec de foliations orientées du SE au NW. Le granite syntectonique et les données géochronologiques contraignent cette déformation principale au Mésozoïque inférieur (environ 219 Ma).

L'analyse structurale, l'AMS, l'étude microstructurale et la modélisation gravimétrique sur le complexe de Pengguan, l'un des complexes de l'orogène néoprotérozoïques au milieu de segment de la LMTB), révèlent une structure des slices du socle imbriquées de la LMTB et la zone adjacente. Les âges connus, l'exhumation rapide localisée et la subsidence du bassin flextual suggèrent que les slices du socle sont imbriquées au cours du Mésozoïque supérieur (166-120 Ma).

La LMTB se trouve loin de la limite de la plaque contemporaine, et est absence de matériel ophiolitique, donc elle peut être considéré comme une orogène intracontinentale. Pendant le début du Mésozoïque, le Yangtze plate subductait vers l'ouest en fermant l'océan paléo-Téthys. Cette tectonique a exhumé des matériaux de différentes profondeurs en surface par des chevauchements vers le SE et chevauchements arrières vers le NW. Au cours de la fin du Mésozoïque, le socle a été soulevé davantage en raison de la collision entre les blocs de Lhasa et de l'Eurasie, qui a conduit à une imbrication des slices du socle et épaissi la croûte.

Mots clés : Tibétain Plateau, intracontinentale orogenèse, Mésozoïque tectonique,

Mesozoic tectonic evolution of the Longmenshan thrust belt, East Tibet

The Longmenshan Thrust Belt (LMTB), constituting the eastern boundary of the Tibetan Plateau, is well known by its steep topography, intensive tectonic activities and the complicated structures. As a typical composite orogen, the LMTB experienced extensive intracontinental deformation during the Mesozoic. The knowledge on the Mesozoic tectonic evolution of the LMTB therefore is crucial to understand the intracontinental orogeny and uplifting of the Plateau.

The vertical cleavage belt divides the LMTB into a Western Zone and an Eastern Zone. The Eastern Zone displays a top-to-the-SE shearing while the western zone a top-to-the-NW shearing. The Eastern Zone can be further divided into four subunits with foliations deepening from SE to NW. The syntectonic granite and published geochronologic data constrain this main deformation to the Early Mesozoic around 219 Ma.

Structural analysis, AMS and microstructural study and gravity modeling on the Pengguan complex, one of the orogen-parallel Neoproterozoic complexes located in the middle segment of the LMTB, reveal a basement-slice imbricated structure of the LMTB and adjacent areas. Published ages, localized fast exhumation rate and flexural subsidence of the foreland basin suggest that the basement-slices imbricated southeastwards during Late Mesozoic (166-120 Ma).

The LMTB is far away from the contemporaneous plate boundary and devoid of ophiolite-related material, therefore, it is supposed to be an intracontinental orogen. During the Early Mesozoic, the Yangtze basement underthrusted westwards due to the far-field effect of the Paleo-Tethys' obliteration, and the materials in different structural levels have been exhumated to the surface by southeastward thrusting and contemporaneous backward thrusting. During the Late Mesozoic, the basement is further underthrusted due to the collision between the Lhasa and Eurasia blocks, which led to SE-ward imbrication of the basement-slices that may thicken the crust.

Keywords: Longmenshan, intracontinental orogeny, Mesozoic tectonics, thin skinned structure

UNIVERSITE D'ORLEANS

Institut des Sciences de la Terre d'Orléans, 45067 Orléans, France

Institut des Géologie et Géophysique (CAS), 100029 Pékin, Chine